Identification of TeV γ-ray sources through multi-wavelength studies

Identifikation von
TeV-Gammastrahlungsquellen durch
Studien in einem breiten
Wellenlängenbereich

Der Naturwissenschaftlichen Fakultät
der Friedrich-Alexander-Universität Erlangen-Nürnberg
zur Erlangung des Doktorgrades Dr. rer. nat.

vorgelegt von
Peter Alfred Eger
aus Hanau

Als Dissertation genehmigt von der Naturwissenschaftlichen Fakultät
der Friedrich-Alexander-Universität Erlangen-Nürnberg

Tag der mündlichen Prüfung: 20. Juli 2011

Vorsitzender der Promotionkommission:	Prof. Dr. Rainer Fink
Erstberichterstatter:	Prof. Dr. Christian Stegmann
Zweitberichterstatter:	Prof. Dr. Jörn Wilms
Drittberichterstatter:	Prof. Dr. Thomas Lohse

Abstract

The aim of this work is to demonstrate the powerful synergies that arise from combining data from various wavelength regimes to identify sources of very-high-energy (VHE, E >100 GeV) γ-rays detected by H.E.S.S. After the underlying radiation mechanisms as well as the observatories used for the analyses are introduced, this work focuses on two very different kinds of astrophysical objects.

In the first part of this work, multi-wavelength observations of the surroundings of the previously unidentified VHE γ-ray source HESS J1626−490 are presented. This object is particularly interesting as it could not be associated to any obvious source of highly energetic radiation, such as a powerful pulsar or a young supernova remnant. A detailed analysis of data of an archival *XMM-Newton* observation does not yield any X-ray counterpart that can be associated with HESS J1626−490. The derived upper limit for radiation in the 1–10 keV band makes it unlikely that the observed VHE γ-ray signal is purely based on leptonic processes. Observations of ^{12}CO ($J = 1 - 0$) molecular line emission performed with the NANTEN telescope show the presence of a molecular cloud in good morphological agreement with the VHE γ-ray signal. Furthermore, based on H I data from the Southern Galactic Plane Survey the shell-type supernova remnant SNR G335.2+00.1 could be identified as a potential source of hadronic cosmic rays that might illuminate the molecular cloud. The application of a detailed model for cosmic-ray diffusion and interaction confirms that this SNR could indeed provide a sufficiently large cosmic-ray density at the location of the molecular cloud to give rise to the observed VHE γ-ray flux via the decay of neutral pions.

The second part of this thesis focuses on Globular clusters (GCs). These gravitationally bound systems of highly evolved stellar populations feature extremely dense cores with high stellar encounter rates. According to several theoretical models, the large abundance of millisecond pulsars (MSPs) in GCs could give rise to γ-ray emission in the MeV to TeV regime. Particularly for the highest energies, the γ-ray flux is expected to come from inverse Compton (IC) up-scattering of low-energy photons by relativistic electrons. These electrons could be accelerated in the magnetospheres of individual MSPs or in the shocks of colliding pulsar wind nebulae. Such a scenario would also predict synchrotron emission in the X-ray band produced by the same population of leptons. In this work, data from VHE γ-ray and X-ray observations of several Galactic GCs were searched for the presence of such signals. The GC Terzan 5 stands out as the only cluster where significant excess emission could be detected in both energy bands. Even though synchrotron/IC scenarios for the observed X-ray and γ-ray signals are viable, also different origins of the VHE γ-ray emission, such as a recent type Ia supernova or a short gamma-ray burst, are discussed. Most likely, only future observations with more sensitive VHE γ-ray observatories as well as more detailed multi-wavelength studies will yield the decisive clues to explore the non-thermal processes at work in GCs.

Kurzfassung

Das Ziel der vorliegenden Arbeit ist es aufzuzeigen, welcher Nutzen sich daraus ergibt Informationen aus verschiedenen Wellenlängen-Bereichen zusammenzutragen, um Quellen höchstenergetischer γ-Strahlung zu untersuchen. Zunächst werden sowohl die zugrundeliegenden nicht-thermischen Strahlungsmechanismen, als auch die Observatorien vorgestellt, die die Daten für diese Arbeit geliefert haben. Der Hauptteil dieser Dissertation beschäftigt sich mit zwei sehr verschiedenen Klassen astrophysikalischer Objekte. Im Folgenden sind die Ergebnisse der Beobachtungen kurz zusammengefasst.

Die TeV-Gammastrahlungsquelle HESS J1626−490, die mit dem H.E.S.S.-Teleskopsystem entdeckt wurde, konnte bisher nicht mit einem bekannten Quelltyp höchstenergetischer Gammastrahlung assoziiert werden, wie z.B. einem energiereichen Pulsar oder einem Supernovaüberrest. Die Auswertung von Daten, die mit dem Röntgenteleskop *XMM-Newton* aufgenommen wurden, zeigt, dass keine signifikante Emission im Energiebereich von 1–10 keV mit HESS J1626−490 in Verbindung gebracht werden kann. Die abgeleitete obere Grenze für den möglichen Röntgenfluss schließt rein leptonische Prozesse zur Erzeugung der beobachteten Gammastrahlung nahezu aus. Eine Analyse von Radio-Daten beim Frequenzbreich des molekularen Rotationsübergangs ^{12}CO ($J = 1 - 0$) lässt auf eine Molkekülwolke schließen, die sehr gut mit dem Emissionsgebiet der TeV-Gammastrahlung übereinstimmt. Durch H I-Beobachtungen und durch die Auswertung eines physikalischen Modells zur Diffusion und Interaktion von hochenergetischer kosmischer Strahlung lässt sich ein nahe gelegener schalenartiger Supernovaüberrest identifizieren, der eine ausreichende Dichte an relativistischen Protonen am Ort der Molekülwolke liefern könnte, um den gemessenen Fluss an TeV-Gammastrahlung durch den Zerfall neutraler Pionen zu erklären.

Der zweite Teil dieser Arbeit beschäftigt sich mit Kugelsternhaufen (KHn). Diese gebundenen Systeme aus weit entwickelten Sternen weisen sehr dichte Kerne auf, in denen die Rate für nahe Begegnungen zweier Objekte sehr hoch ist. Aktuellen Modellen zufolge könnten die zahlreichen Millisekundenpulsare (MSPe) für Gammastrahlung mit Energien von 1 MeV bis 10 TeV verantwortlich sein. Insbesondere die Photonen höchster Energien könnten durch inverse Compton-Streuung (IC) von relativistischen Elektronen an niederenergetischen Photonen entstehen. Die hochenergetischen Elektronen könnten in den Magnetosphären einzelner MSPe oder auch in kollidierenden Pulsarwindnebeln beschleunigt werden. In einem solchen Szenario wäre auch Synchrotronstrahlung im Röntgenbereich zu erwarten, die von der selben Population relativistischer Leptonen herrührt. In dieser Arbeit wurden Daten aus Beobachtungen von Gammastrahlung als auch von Röntgenstrahlung einer ganzen Reihe Galaktischer KHn nach entsprechenden Signalen untersucht. Terzan 5 ist der einzige KHn, bei dem in beiden Energiebereichen signifikante Emission entdeckt wurde. Neben alternativen Szenarien für die Erzeugung der TeV-Gammastrahlung, wie ein Typ-Ia-Supernovaüberrest oder ein kurzer Gammastrahlungsausbruch, ist auch ein Synchrotron-IC Modell zur Erklärung der gemessenen Röntgen- und Gammastrahlung

in der Lage. Möglicherweise aber wird der verantwortliche Mechanismus erst durch Beobachtungen künftiger Gammastrahlungs-Obervatorien und detailliertere Multi-Wellenlängen Studien aufgeklärt werden können.

Contents

1 Introduction

Almost 100 years ago Victor Hess discovered the existence of cosmic rays (CRs), a highly energetic radiation from space which is mainly comprised of charged particles. This discovery made it clear that the Universe has more to offer than is detectable within the narrow energy regime accessible by our naked eyes. Today we know from measurements of cosmic-ray-induced air showers, as performed, e.g., by the *Pierre Auger Observatory*, that the spectrum of these cosmic particles extends up to energies of at least 10^{21} eV (see, e.g., Mariş et al. 2007). Such particles are about eight orders of magnitude more energetic than those produced in man-made accelerators. Thus, the physics related to these particles and their cosmic accelerators lies at the edge of our current understanding.

In 1949 and the following years, the first concepts of possible production mechanisms of CRs were introduced by H. Primakoff, and later by various other scientists such as I.B. Hutchinson and P. Morrison (see, e.g., Morrison 1958). Right from the beginning it was clear that purely thermal mechanisms would be far too inefficient to provide the observed CR flux at energies beyond a few keV, unless the temperatures of astrophysical sources exceeded 10 million Kelvin by several orders of magnitude. Such high temperatures seemed rather unrealistic, and thus, energetic CRs were considered to be of some non-thermal origin. A good candidate for such a process was, and still is a concept which was originally developed by Enrico Fermi in the 1940s (see Sect. 2.3). In this theory a charged particle is repeatedly reflected by moving "magnetic clouds" gaining large amounts of energy under certain conditions. However, for this process to be efficient, very high velocities of the reflecting clouds would be needed, and thus large amounts of available kinetic energy. Therefore, it was thought that only in the most extreme and violent environments of the Universe, such as in the vicinity of recent supernova explosions (see, e.g., Fig. 1.1) or in regions close to compact objects like neutron stars, stellar-mass or supermassive black holes, the physical conditions are set to accelerate particles up to the highest energies.

In measuring the energy spectrum of CRs, much can be learned about their origin and acceleration mechanisms (see chapter 2, in particular Sect. 2.1). However, it is very difficult to identify individual astrophysical accelerators by observing CRs. This is due to the fact that charged particles, such as leptons, protons and heavier nuclei are deflected by interstellar and intergalactic magnetic fields before they arrive at a distant observer. Therefore, it is impossible to deduce the location of the original CR source from measuring the arrival directions of these particles at Earth. A solution for this problem lies in the observation of neutral messengers, such as neutrinos and γ-rays. As this work considers only the latter, the remaining part of this introduction

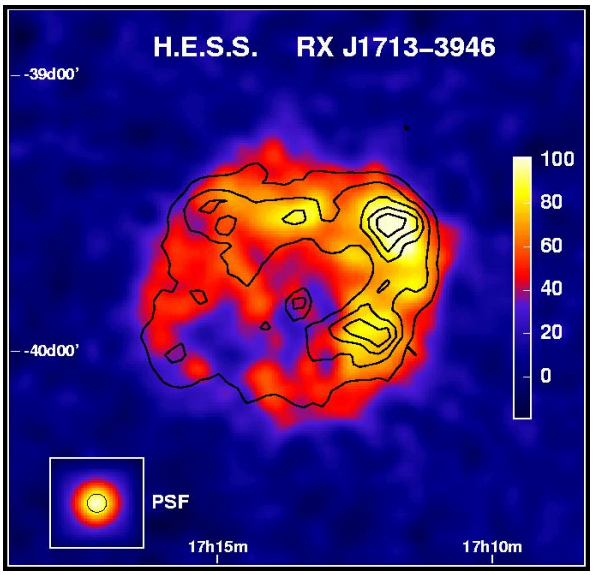

Figure 1.1: Image of very-high-energy γ-ray emission of the supernova remnant RX J1713−3946. The data were recorded with the H.E.S.S. array of imaging Cherenkov telescopes. The size of the instrument's point spread function is shown in the bottom left panel. Black contours show regions of enhanced X-ray emission as seen with the ASCA satellite (Uchiyama et al. 2002). Image credit: H.E.S.S. collaboration.

will focus on high-energy photons, and what they can contribute to our understanding of cosmic particle accelerators.

The astrophysical processes of high-energy γ-ray emission are inelastic collisions of hadronic cosmic rays with nuclei of the interstellar medium, or the interaction of relativistic leptons with interstellar magnetic and radiation fields. Thus, the detected γ-ray flux should be enhanced towards the direction of individual cosmic-ray sources and/or regions of dense interstellar matter. In particular the Galactic center and disc fulfill both these requirements as most of the Galactic objects as well as the bulk of the interstellar gas are concentrated there. Indeed, in 1967 enhanced γ-ray emission from the Galactic center was detected by the OSO-3 satellite (Kraushaar et al. 1972), confirming the early predictions. By contrast, it came as a surprise as the first extragalactic γ-ray sources were discovered between 1969 and 1979 by the Vela satellites (Metzger et al. 1974) which were originally designed to detect terrestrial γ-ray flashes caused by nuclear weapon tests. These detected astronomical sources were called Gamma-Ray-Bursts (GRBs) due to their transient nature. Even today the origin of GRBs is still not settled yet, but it is assumed that extremely violent and energetic types of supernova explosions called "hyper-novae" might be the origin of some of these γ-ray flashes (see, e.g., Georgy et al. 2009).

As γ-radiation is absorbed by the Earth's atmosphere, balloon-borne experiments and later detectors aboard satellites were needed to confirm the presence of extraterrestrial γ-rays. To detect this highly penetrating radiation a large and massive detector volume

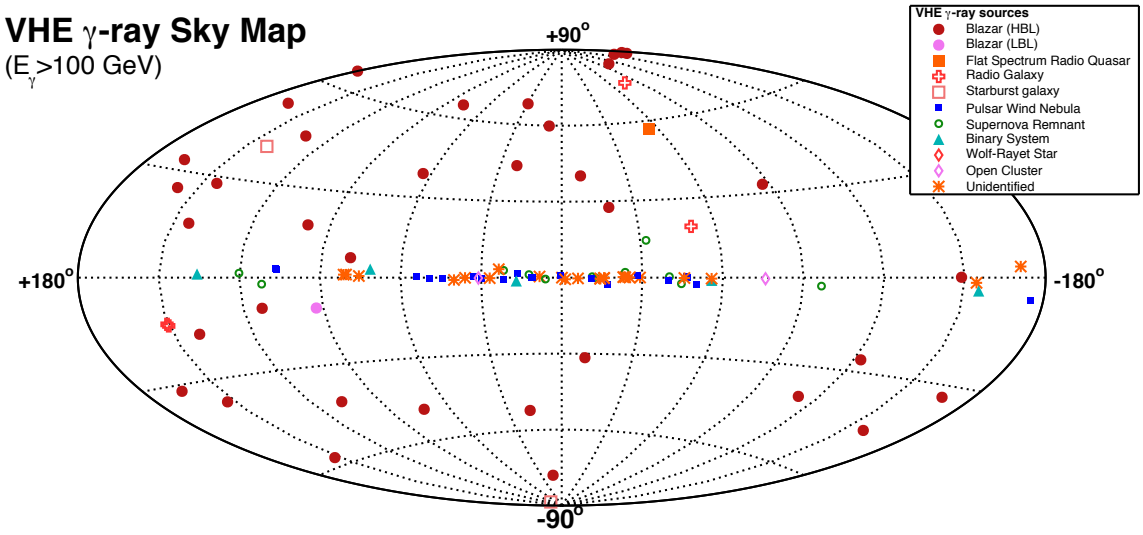

Figure 1.2: Map of the sky in Galactic coordinates showing all known VHE sources (date: 2011-01-08). Source classes are indicated by different markers. Image credit: Robert Wagner/MPPMU/MPG.

is needed. However, the dimensions and weight of satellite payloads are very limited, which poses a natural constraint for the capabilities of space-borne γ-ray detectors. A new era in γ-ray astrophysics came with the advent of ground based Imaging Atmospheric Cherenkov Telescopes (IACTs, see Sect. 3.5) which are visible light telescopes that do not detect the γ-ray photons directly but observe the Cherenkov light emitted by particles of the air showers induced by both cosmic rays and γ-ray photons. These telescopes do not suffer from the same limitations as their space-borne counterparts and opened a new window at the highest γ-ray energies between 100 GeV and 100 TeV which lies beyond the reach of compact satellite detectors. This energy range is often referred to as "Very-High-Energy" (VHE), in contrast to "High-Energy" (HE, MeV to GeV) which is still best accessible by space-borne instruments, as e.g. the recently launched *Fermi*[1] satellite. Since the current generation of IACTs, such as H.E.S.S.[2], MAGIC[3], and VERITAS[4], is in operation, well more than 100 individual VHE γ-ray sources have been discovered.

Figure 1.2 shows all known sources of the current VHE γ-ray sky. A large portion of these sources are of extragalactic origin and are most likely associated to accreting supermassive black holes at the centers of active galaxies. The most common class of Galactic VHE γ-ray sources are pulsar wind nebulae. These are regions around energetic pulsars that are filled with a highly relativistic plasma of leptons which accelerate low-energy photons to very high energies via the inverse Compton (IC) process. An-

[1] for a summary of *Fermi*/LAT results from the first year of operation, see Michelson et al. (2010)
[2] A review of recent H.E.S.S. results: Gallant, Y. A. for the H. E. S. S. Collaboration (2010)
[3] Scientific highlights and status of the MAGIC Telescope: López Moya (2010)
[4] for a review of recent results from VERITAS, see LeBohec, S. for the VERITAS Collaboration (2009)

other class of objects are young supernova remnants (SNRs, Fig. 1.1) that are also very bright and often extended γ-ray sources. Here, leptons as well as hadrons might be accelerated in the expanding supernova shocks and could produce γ-rays by interaction with surrounding photon fields or dense interstellar matter, respectively. As can be seen in Fig. 1.2, a large fraction of Galactic VHE γ-ray detections still lack conclusive identification. Such objects are often referred to as "dark" accelerators which means that they could not be associated to any object seen at lower energies. It is because of these unidentified objects that in some cases a γ-ray astronomer can not be content with sticking to the regime of highest energies and has to make a detour to radio, X-ray, and infrared astronomy to uncover the mysteries of a particular source. The aim of this work is to give a glimpse at how powerful multi-wavelength (MWL) studies can be and what each energy regime can contribute to the understanding of the Universe at highest energies. The following two examples will demonstrate this briefly.

In pulsar wind nebulae the same population of relativistic electrons is thought to be responsible for VHE γ-ray emission via IC up-scattering of low-energy photon fields as well as for synchrotron radiation in the X-ray band (see Fig. 1.3, *Left*). Each of

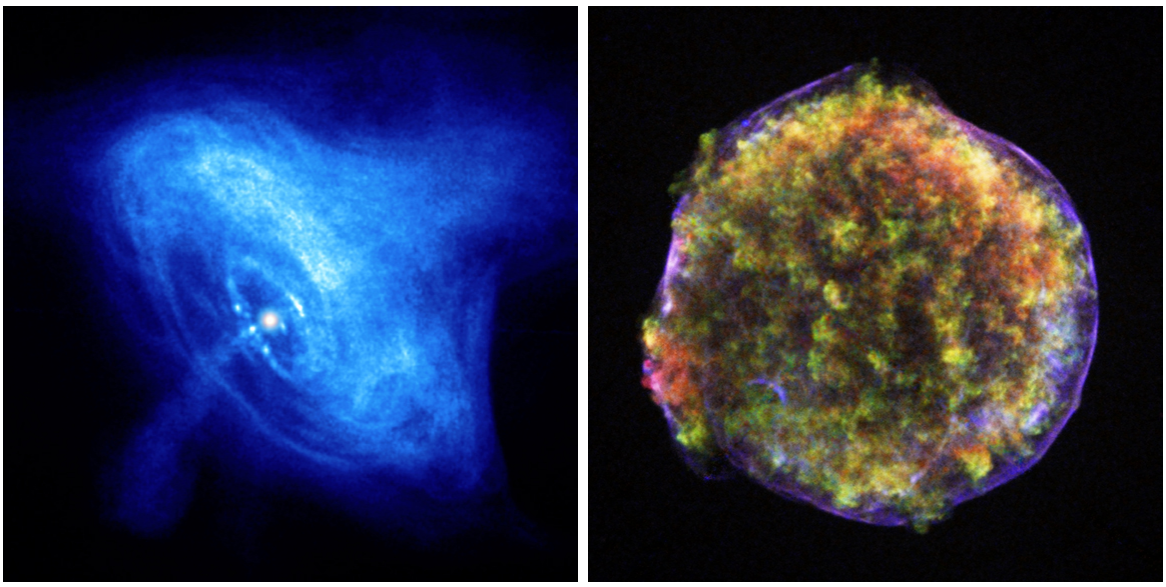

Figure 1.3: *Left:* *Chandra* X-ray image of the Crab nebula which is a pulsar wind nebula around a very young and powerful pulsar. Visible are the pulsar itself as a point-like source at the center, as well as toroidal structures and perpendicular jets. The emission in the X-ray band is most likely produced by synchrotron radiation of extremely relativistic leptons. Image credit: NASA/CXC/ASU/J. Hester et al. *Right:* Multi-wavelength image of Tycho's supernova remnant (SN 1572). The image is a composite of an X-ray image taken by *Chandra* (blue), an infrared image taken by the *Spitzer* Space Telescope (red), and an optical image taken by the 3.5-meter Calar Alto telescope (green). Image Credit: X-ray: NASA/CXC/SAO; Infrared: NASA/JPL-Caltech; Optical: MPIA, Calar Alto.

these two processes depends on different parameters of the astrophysical environment of the pulsar and its nebula. The most important quantity for synchrotron radiation is the strength of the magnetic field, whereas for the IC process the spectra and energy densities of the ambient photon fields, such as Cosmic Microwave Background, starlight, and infrared dust emission, have the largest influence on the up-scattered photon distributions. Thus, if the target photon fields are reasonably well known, the ratio of fluxes in VHE and X-ray may allow to measure the magnetic field strength, which in turn gives insights into the evolution of the pulsar and its nebula. In a similar way, also X-ray observations of SNRs yield decisive insights into the distribution of the magnetic field and its strength. In strong B-fields, the synchrotron cooling timescale for energetic leptons is very short, which means that these particles will only fill very small volumes as they diffuse away from their acceleration site. By measuring the extent of thin X-ray filaments at the rims of young SNR shocks, it was possible to derive quite accurate values of the magnetic field strength right at the supposed production site of high-energy cosmic rays (see Fig. 1.3, *Right*).

Another example for the power of MWL analyses are young SNRs interacting with dense molecular clouds. Here highly relativistic protons, accelerated in the SNR shock, may escape the shock and diffuse through the interstellar medium until they hit dense target material in the form of molecular clouds. Neutral pions created in the inelastic collisions decay into two γ-ray photons that can be detected by HE and VHE instruments. The properties of the target material, such as its mass, its density and even its distance can be derived with radio observations at mm/sub-mm wavelengths. Similar to the first example, the search for X-ray emission will allow to determine or constrain the contribution from an additional leptonic component through its synchrotron radiation. If any piece of the puzzle is missing it is impossible to identify the source. Comparing the broad-band emission of the SNR–molecular cloud complex to physical models gives insights into the cosmic-ray diffusion coefficient which so far is a very poorly known quantity.

In this dissertation two unidentified VHE γ-ray sources, detected by H.E.S.S., are investigated in their broad MWL context to uncover the underlying physical processes. In chapter 2 the relevant non-thermal radiation mechanisms are introduced, followed by a detailed description of all observatories (chapter 3) whose data were used for the presented analyses. In chapter 4 the origin of VHE γ-ray emission from the unidentified H.E.S.S. source HESS J1626−490 is explored, in particular in the context of a SNR–molecular cloud interaction scenario. The second main topic of this work is presented in chapter 5. Here, Globular Clusters (GCs) are discussed as a potential new source class of non-thermal emission in the X-ray and VHE γ-ray regimes, with a particular focus on the GC Terzan 5. The dissertation is closed by a brief summary in chapter 6.

2 Cosmic rays and high-energy astrophysical processes

This chapter provides an overview of our current understanding of the origin of cosmic rays (CRs), their sources, as well as subsequent non-thermal radiation mechanisms that may give rise to VHE γ-ray emission. In the first section (2.1) the CR spectrum is discussed, followed by a Section describing the evolution of supernova remnants, which are our best candidates as sources of Galactic CRs (Sect. 2.2). The next section introduces the process of diffusive shock acceleration, which is one scenario how SNRs and other energetic sources could efficiently accelerate particles to relativistic energies (Sect. 2.3). Depending on the nature of these particles, they can give rise to intense γ-ray emission via *leptonic* or *hadronic* mechanisms. Both scenarios are discussed in the last two sections of this chapter (Sect. 2.4 and 2.5).

The electromagnetic radiation is produced in the interaction of relativistic particles with ambient magnetic fields, photon fields, or interstellar matter and can span the whole spectrum from radio to γ-ray wavelengths. Thus, by observing the electromagnetic radiation one can explore the nature of the underlying high-energy particle population. This knowledge can then be used to investigate the astrophysical sources themselves and the physical conditions present in their environments.

2.1 The cosmic-ray spectrum

CRs can be divided into two groups. "Primary" CRs are those particles that are directly accelerated in astrophysical sources, whereas "secondary" CRs are produced in the interaction of primaries with the ISM or interstellar photon fields. Typical primaries are electrons, protons and nuclei of isotopes synthesized in stars (see e.g. D'Urso 2007). The observation of primaries, in particular their composition and energy spectra, provides a direct window into the acceleration mechanism itself. However, all primaries are charged particles and are therefore deflected by interstellar magnetic fields, which makes it hard to deduce the position of their source in measuring their arrival directions at Earth. Only primary CRs with extreme energies ($\sim$EeV) may be used to locate cosmic accelerators, as their deflection is less pronounced. The low-energy ($\lesssim$GeV) particles incident on the atmosphere are heavily influenced by the solar activity and the geomagnetic field. Their flux is therefore dependent on the direction and the activity state of the sun. CRs can either be detected directly by satellites or

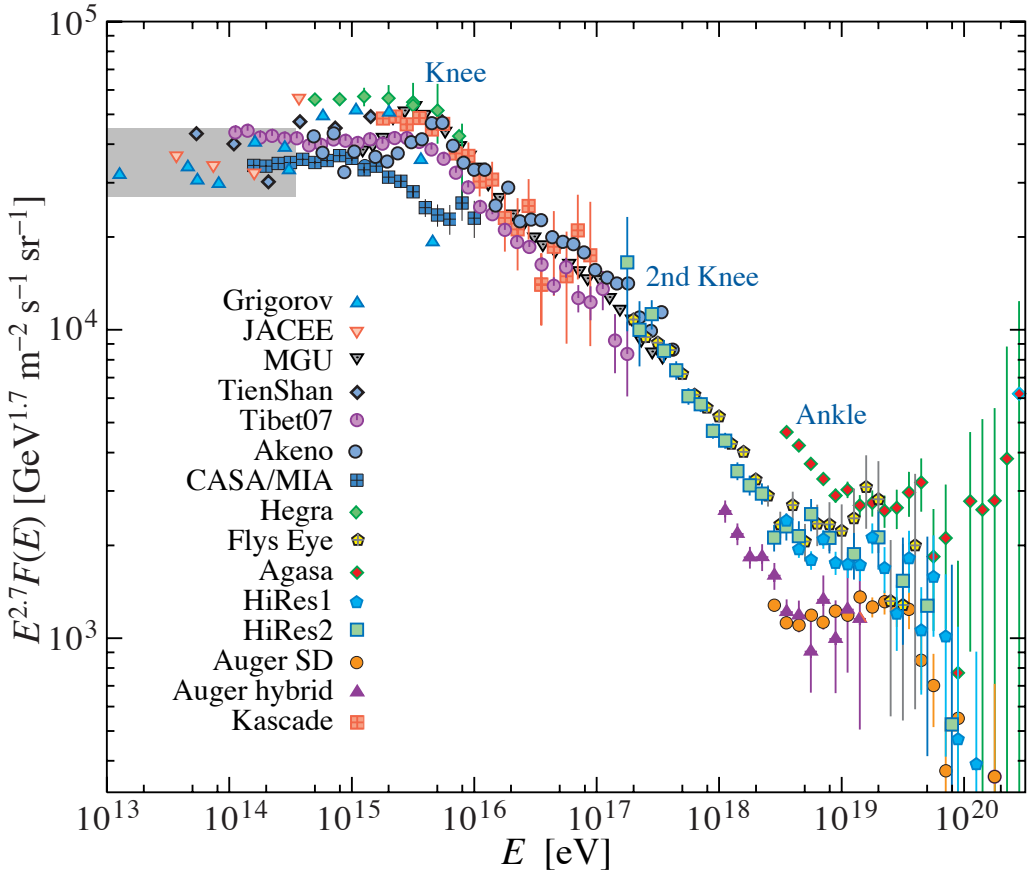

Figure 2.1: The all-particle CR spectrum from air shower measurements. The shaded area shows the range of the direct CR spectrum measurements. Image credit: Particle Data Group and D'Urso (2007).

balloons in space ($E \lesssim$1–10 GeV) or via air shower measurements from the ground (10 GeV$< E <10^{21}$ eV).

The detection of secondary particles, like photons, neutrinos, and nuclei like lithium or beryllium, gives insights into the interaction of CRs with various targets of the ISM, and only provides indirect evidence for the underlying particle acceleration process. Therefore, to explore cosmic accelerators through the observation of secondaries, one needs a detailed understanding of the particle interaction mechanisms as well. Some of the secondary species (γ-rays, neutrinos) are neutral and are thus not affected by intra- and extragalactic magnetic fields. In contrast to primaries, these messengers can therefore be used to locate CR sources, independent of the particles' energy.

Figure 2.1 shows the high-energy end of the all-particle CR energy spectrum, multiplied by $E^{2.7}$ to make the deviations from a pure powerlaw shape at high-energies more pronounced. Up to energies of about 10^{15} to 10^{16} eV the CR spectrum follows a powerlaw distribution with index -2.7. At larger energies the spectrum is steeper and the transition is referred to as the "knee". One interpretation for this steepening is that CRs up to this energy are of Galactic origin and that the location of the knee indicates

the maximum energy achieved by these sources. Also, CRs with energies larger than 10^{16} eV might not be confined within Galactic magnetic fields and could escape into intergalactic space (Ptuskin et al. 1993). At energies of about 10^{19} eV the CR spectrum begins to flatten again, which is called the "ankle". A common interpretation for this feature is that at these energies the spectrum of an extragalactic population of CRs with a larger high-energy cut-off, starts to dominate over the Galactic flux. Sources for these extra-galactic CRs could be nearby active galactic nuclei. If these high-energy particles are indeed of extra-galactic origin, from sources at distances beyond 100 Mpc, then a rapid steepening of the CR spectrum at $\sim 5 \times 10^{19}$ eV is expected (the GZK cut-off, Greisen 1966; Zatsepin and Kuz'min 1966) due to the onset of inelastic collisions of ultra-high-energy CRs with the cosmic microwave background (CMB). However, current measurements in that energy range do not provide sufficient statistical quality to favor or disfavor such a scenario.

2.2 Evolution of supernova remnants

Supernova remnants (SNRs) are our prime candidates for Galactic CR sources, as they are among the most energetic and violent environments in the Galaxy. However, to discuss possible particle acceleration scenarios, first a basic understanding of the evolution of SNRs is required. This section provides a brief summary of our current phenomenological understanding of SNR evolution (see also Woltjer 1972). In a supernova explosion a bubble of hot gas of mass M, initial velocity $v \sim 10^9$ cm s^{-1} and a typical total energy $E \approx 10^{51}$ erg is ejected into the surrounding cold interstellar medium (ISM) with density $\rho \approx 1$ cm^{-3}. When the bubble starts to interact with the ISM, a shell with radius R, preceded by a shock is formed. Initially, the shell is hot and pressure forces dominate over radiative cooling effects (cooling rate $(\mathrm{d}\epsilon/\mathrm{d}t)_{\mathrm{rad}}$, where ϵ is the current kinetic energy of the ejecta). Ultimately, when a large amount of interstellar matter has been swept up, the velocity of the shell becomes comparable to the random motion of interstellar clouds and the shell is completely absorbed into the ISM, losing its identity. Following Woltjer (1972), the hydrodynamic evolution of SNRs can be divided into four phases:

- Phase I: $M \gg (4\pi/3)\rho R^3$
  Here the SNR expands freely into the surrounding gas (*free expansion phase*), as the mass of the swept up material is negligible.

- Phase II: $M \lesssim (4\pi/3)\rho R^3$, $\int (\mathrm{d}\epsilon/\mathrm{d}t)_{\mathrm{rad}} \mathrm{d}t \ll E$
  As the mass of the swept up material becomes comparable to the mass of the ejecta, the SNR enters the so-called *Sedov phase* (Sedov 1959). This happens after a time

$$t_{\mathrm{Sedov}} \approx 200 \left(\frac{E}{10^{51}\ \mathrm{erg}}\right)^{1/3} \cdot \left(\frac{\rho}{\mathrm{cm}^{-3}}\right)^{-1/3} \cdot \left(\frac{v}{10^9\ \mathrm{cm\,s}^{-1}}\right)^{-5/3} \text{years.} \quad (2.1)$$

Then the velocity and the shock radius scale with time as $R \propto t^{2/5}$ and $v \propto t^{-3/5}$, respectively. As radiative losses are still negligible the total energy of the bubble remains constant. If the downstream ISM is cold the limit of strong shocks (with Mach numbers $\gg 1$) is reached and the *compression factor*, i.e the ratio between post- and pre-shock density, is approximately $s = 4$. A typical interstellar magnetic field of ~ 3 μG could be increased due to the compression to $B \lesssim 12$ μG in the post-shock medium. Then the magnetic energy density is $B^2/8\pi = 6 \times 10^{-12}$ erg cm^{-3}. For a shock velocity $v = 100$ km s^{-1} the hydrostatic pressure behind the shock is equal to $(3/4)\rho v^2 = 1.9 \times 10^{-10}$ erg cm^{-3}, which is almost two orders of magnitude larger than the magnetic field energy density. Thus, the influence of the magnetic field on flow dynamics is negligible in Phase II, and B just follows the motion of the gas.

Due to the expansion, the density behind the shock gradually decreases, while the temperature increases. When the density of the matter inside the shell becomes sufficiently low due to the adiabatic expansion, a reverse shock forms that is driven back into the interior of the SNR, further heating the gas (Ardavan 1973). At a certain temperature, radiative cooling starts to become effective. For $T > 5 \times 10^6$ K free-free absorption of H and He is the dominant radiation process. At lower temperatures line emission from heavier elements, such as iron, is more important. To estimate the duration of Phase II one can calculate the radiative timescale, i.e. the time after which half of the initial energy E is lost due to radiative processes. Following Woltjer (1972) this time can be calculated as:

$$t_{\rm rad} = 1.1 \; E^{4/17} \; \rho^{-9/17} \text{ years.} \tag{2.2}$$

- Phase III: $t > t_{\rm rad}$
  The matter behind the shock has cooled down significantly and the shell now moves at constant momentum, i.e. $(4\pi/3)\rho R^3 v =$ constant. Due to the cooling, the post-shock density increases further by probably also increasing the magnetic field strength. The latter is only true in the case of the magneto-hydrodynamic limit, where the magnetic field is coupled to the motion of the plasma and the magnetic field strength is directly related to the density. For a shock traveling transverse to the magnetic field the upper limit for B is given by $\rho v^2 = B^2/8\pi$, which corresponds to $B = 80$ μG for a pre-shock density $\rho = 1$ cm^{-3} and $v = 100$ km s^{-1}. This suggests a compression factor of $s = 26$, giving an upper limit for the post shock-density of 26 cm^{-3}. Larger densities, as observed, e.g. from the Cygnus Loop, an SNR with an age between 5000 and 8000 years, are of course possible if the shock is moving along the magnetic field lines.

- Phase IV: $v \approx 10$ km/s
  When the expansion speed becomes comparable to the random motion of interstellar clouds the bubble of ejecta merges into the ISM. Now the shell is heavily distorted and can no longer be distinguished from the ISM.

The model above is only valid if the shock expands into a homogeneous medium. However, if a dense cloud lies along the way, the shock reaching the cloud will be slowed

down due to the increased density. The shock outside of the cloud will propagate undisturbedly and compress the medium behind the cloud. Therefore, the cloud is then surrounded by regions with high pressure, leading to a uniform compression. If the radiative cooling timescale for the cloud medium compared to the time it takes for the shock to traverse the cloud is large, the cloud may heat up and disperse. For short cooling timescales, the cloud will remain a coherent object, compressed by the surrounding gas. In the latter case a dense molecular cloud is maintained that could provide target material for CRs accelerated in the SNR shock (see Sect. 2.5).

As discussed in the next section, magneto-hydrodynamic shocks could be able to accelerate particles to relativistic energies. For SNRs both leptonic and hadronic particle populations are discussed in the interpretation of high-energy observational data. The presence of relativistic particles inside the shell can lead to an accelerated expansion during the free expansion phase (Phase I) or can hinder the deceleration during later phases. This effect should become important if the total energy of the CRs becomes comparable to the kinetic energy of the ejecta. Particularly during Phase III where the kinetic energy varies as R^{-3}, this might be the case and could lead to a significantly different behavior of the shock radius with time: $R \propto t^{1/3}$, in contrast to $R \propto t^{2/5}$, as expected without the additional CR pressure (Kahn and Woltjer 1967).

Up to now, we only discussed the evolution of the expanding shell, but not a possible compact object remaining at the center of core-collapse supernovae. In the case of a spinning, magnetized neutron star, i.e. a pulsar, a population of relativistic particles is injected into the medium inside the cavity created by the supernova blast wave. These particles interact with the unshocked material and form a *termination shock* at a radius of $\sim$0.01–0.1 pc. Similarly to the outwards propagating forward shock of the SNR, also at this termination shock particles may be accelerated to high energies (see next section). These particles propagate outwards and fill the interior of the SNR shell, forming the so-called Pulsar Wind Nebula (PWN). The evolution of such a PWN is tightly connected to the dynamics of the shell and can be divided into three distinct phases. First the radius of the PWN is much smaller than that of the shell and the wind expands freely. When the PWN encounters the reverse shock of the SNR it is compressed, followed by a re-expansion. This might eventually lead to the "stripping" of the pulsar from its wind. In the third phase the pulsar forms a new, more compact PWN, in addition to the "relic" PWN of particles injected at much earlier times. As a PWN is not a very likely scenario for the γ-ray sources discussed in this work, only a brief summary of PWN evolution is given here. For a detailed review on the structure and evolution of PWNe, the reader is referred to Gaensler and Slane (2006).

2.3 Diffusive shock acceleration

In the previous section our current picture of the evolution of SNRs was discussed, including some references to possible particle acceleration mechanisms that are supposed

to be present in these environments. There is much observational evidence, such as synchrotron emission in the radio to X-ray energy regime or HE/VHE γ-ray emission, that SNRs are indeed sources of relativistic particles. Even though the exact acceleration mechanism is unknown, there are physical models that reproduce the measurements surprisingly well. If high-energy CRs originated right from the supernova explosion itself, they would be trapped in the expanding plasma bubbles and lose their energy adiabatically (see, e.g., Eq. (130) in Kulsrud 2005). Therefore, CRs are unlikely to be accelerated in the explosion itself, but have to be created in their remnants, when the expansion rate has slowed down significantly. The most common model for this case is diffusive shock acceleration, also referred to as *Fermi acceleration*, a concept that dates back to the 1940s. Originally, these considerations were made for the development of nuclear bombs to model the effects of shock fronts propagating through the atmosphere. In this section the *Fermi acceleration* scenario is motivated, and it is shown that this scenario can reproduce some of the observed properties of the CR spectrum.

Following Fermi (1949), particles can gain energy when they are reflected multiple times by moving interstellar clouds. When a particle with energy E and momentum p collides with a cloud,moving with velocity $u \ll c$, with a mass much larger than that of the particle, the energy (E') and momentum (p') of the particle in the frame of the cloud are:

$$E' = E + up \tag{2.3}$$

$$p' = p + \frac{uE}{c^2}. \tag{2.4}$$

After the collision p' is reversed to $-p'$ and E' is unchanged. Transferring back to the rest frame we get:

$$E'' = E' - (-p')u = E' + up' = E + 2up + \mathcal{O}\left(\frac{u^2}{c^2}\right), \tag{2.5}$$

and the CR is now moving in the opposite direction. If it encounters another moving cloud it will be reflected again, gaining energy in the process. Therefore, particles could be trapped between two approaching clouds, and if the escape probability of the particles is sufficiently small they could gain large amounts of energy. The two approaching clouds will eventually be penetrated or reflected by each other. Thus, the particles the particles would be trapped between two receding clouds at later times. If the escape probability of the particles is too small they would lose again the same amount of energy that they gained before. Therefore, this scenario was at first deemed rather unlikely, as the dwell time of the particles inside the acceleration region would have to be just right, to transfer a significant amount of energy from the clouds to CRs.

Even though the above particle acceleration mechanism is viable under certain conditions, still a scenario has to be established how this could be realized in an astrophysical context. Following Drury (1983) (and references therein), the strong hydrodynamic shocks in expanding SNR shells can provide a suitable environment for efficient *Fermi* acceleration. Here the moving magnetic clouds are represented by the upstream and downstream fluid. In the limit of strong shocks the compression factor is $s = 4$, which is also the ratio between the up- and downstream bulk velocities. For a shock moving with velocity $\vec{u}_{\rm sh}$, the upstream fluid velocity u_- equals $|\vec{u}_{\rm sh}|$ and the downstream fluid velocity is $u_+ = |\vec{u}_{\rm sh}|/4$, when transforming into the rest frame of the shock. The CR particle crosses the discontinuity and bounces off the downstream flow, losing an energy of $2u_+E/c = (2|\vec{u}_{\rm sh}|/4)E/c$. It is then reflected back and bounces off the upstream flow, gaining an energy of $2u_-E/c = 2|\vec{u}_{\rm sh}|E/c$. After these two reflections the net energy gain of the CR particle is $2 \times \frac{3}{4}|\vec{u}_{\rm sh}|E/c$. Because the up- and downstream flow are formed by the same fluid which traverses the shock region, the "mirrors" are stable and the relative direction of u_+ and u_- will not change with time, in contrast to the scenario of colliding clouds. Therefore, only the total number of collisions, and thus the maximum energy gain, depends on the particles' dwell time in the acceleration region, and not the energy gain per collision.

With the observed energy release of supernova explosions ($\sim 10^{51}$ erg) and their rate in the Galaxy (one per 30 years) a conversion efficiency of $\sim$0.1 from the kinetic energy of the ejecta into particle acceleration is required to account for all the observed Galactic CRs (Baade and Zwicky 1934). Even though this might seem plausible, apart from this total energy balance, also other CR characteristics need to be reproduced by the model. Of course, the qualitative description in the previous paragraph is not sufficient to investigate more detailed properties of the CR spectrum, e.g. its spectral shape. For a general approach the CR transport equation has to be solved (e.g. Drury 1983):

$$\frac{\partial f}{\partial t} - \nabla D \nabla f + \vec{u}\nabla f = \frac{\nabla \vec{u}}{3} p \frac{\partial f}{\partial p}. \tag{2.6}$$

Here $f(\vec{r}, \vec{p})$ denotes the particle distribution function, $\vec{u}$ the bulk velocity and D the diffusion coefficient in the acceleration region. With the shock moving along the x-axis and assumed to be at $x = 0$ in frame of the shock, $\nabla \cdot \vec{u}$ equals $(u_+ - u_-)\delta(x)$. For the stationary case ($\frac{\partial f}{\partial t} = 0$) equation 2.6 then reads:

$$u\frac{\partial f}{\partial x} - \frac{\partial}{\partial x}\left(D\frac{\partial f}{\partial x}\right) = \frac{1}{3}(u_+ - u_-)\delta(x)p\frac{\partial f}{\partial p}. \tag{2.7}$$

This equation can be solved for the up- and downstream regions separately, where the right-hand side is zero. Furthermore, the equation can be integrated for a small region around the shock and matched to the up- and downstream solutions. To obtain solutions for the up- and downstream particle distribution functions f_+ and f_-, respectively, we assume as boundary conditions $f(x, p) \to f_-(p)$ and $\partial f/\partial x \to 0$ as $x \to -\infty$,

and $f(x,p) \to f_+(p)$ and $\partial f/\partial x \to 0$ as $x \to +\infty$. The up- and downstream solutions inserted into equation 2.7 integrated over a small region around $x = 0$ gives:

$$(f_+ - f_-)u_- = \frac{u_+ - u_-}{3} p \frac{\partial f_+}{\partial p}. \tag{2.8}$$

This is a differential equation for the downstream distribution f_+ when the upstream distribution function f_- is assumed to be known. The solution is:

$$f_+ = \frac{q}{p^q} \int_0^p f_- p'^{(q-1)} dp', \tag{2.9}$$

with $q = 3s/(s-1)$ and $s = u_-/u_+$. If f_- is very steep, i.e. mainly dominated by low-energy particles, f_+ asymptotically follows a powerlaw distribution in p with index $-q$ for high energies. For strong shocks $q = s = 4$, which is, quoting Drury (1983), "encouragingly similar to the observed CR spectrum". A more detailed derivation of the above solution is given by Kulsrud (2005).

The above solution is only an approximation, as in efficient accelerators the CRs themselves can have a significant impact on the shock structure. In particular, CRs can make the shock more compressible, increasing the compression factor s. This makes the spectrum of accelerated particles harder with indices $q \approx 3.7$, as recent observations and theoretical calculations for the SNR RX J1713.7−3946 have shown (Berezhko and Völk 2006).

2.4 Leptonic radiation mechanisms

In the previous section one possible particle acceleration mechanism was discussed that might be present in shell-type SNRs or at the termination shock of PWNe. Such a mechanism works similarly well for hadrons and leptons, and in fact either of the two might be dominant in different kinds of sources. Now taking the presence of high-energy particles for granted, this section discusses possible electromagnetic radiation processes that arise from a leptonic population of particles (i.e. electrons and positions).

2.4.1 Inverse Compton scattering

Compton scattering, in particular the scattering of a high-energy electron off a low-energy photon (= "inverse Compton", IC), is a common phenomenon in astrophysics and may give rise to emission in the HE and VHE energy regimes. The IC process in general is very complicated, however, there are two limiting cases where the cross sections simplify. These are the Thomson limit, where the photon energy is negligible with respect to the electron rest mass ($E_\gamma \ll mc^2$), and the Klein-Nishina limit, which

describes the opposite case ($E_\gamma \gg mc^2$). Following Blumenthal and Gould (1970), in the Thomson limit the total electron energy loss rate is given by:

$$-\frac{\mathrm{d}E_e}{\mathrm{d}t} = \frac{4}{3}\sigma_\mathrm{T} c \gamma^2 \epsilon_\gamma, \tag{2.10}$$

where

$$\sigma_\mathrm{T} = \frac{8\pi}{3}\left(\frac{e^2}{4\pi\epsilon_0 mc^2}\right)^2 \tag{2.11}$$

is the Thomson cross section and ϵ_γ denotes the energy density of the photon gas. Furthermore, in the Thomson limit the photon distribution function prefers low energy photons, where not much energy is transferred from the electron to the photon (see Fig. 2.2). Things change in the extreme Klein-Nishina limit. Here the energy loss rate is no longer proportional to γ^2 but increases only logarithmically with energy ($-\frac{\mathrm{d}E}{\mathrm{d}t} \propto \ln\gamma$). Furthermore, the behavior of the photon distribution function is reversed with respect to the Thomson limit. Now higher energies are favored, meaning that electrons preferentially lose a large portion of their total energy in single collisions (see Fig. 2.2).

When assuming a powerlaw distribution for the electron energy spectrum ($N_e \propto E^{-p}$) and a black-body spectrum for the photon field, which is reasonable as most of the relevant photons originate from thermal sources (CMB, dust and starlight), the spectrum of IC up-scattered photons in the Thomson limit also follows a powerlaw distribution with index $-(p+1)/2$. The IC spectrum in the extreme Klein-Nishina case is a powerlaw spectrum as well, however with a much steeper index of $-(p+1)$ (Blumenthal and Gould 1970). Thus, towards higher energies in the lepton spectrum the photon field with the softest spectrum (e.g. the CMB) dominates. In many cases it is therefore sufficient to only consider the CMB as target photon field. However, if the electron population is embedded in very intense additional photon fields originating from infrared dust emission or starlight, other components might play a significant role in the IC spectrum. This could be the case in regions close to the Galactic center or in γ-ray binaries with a bright companion star.

2.4.2 Synchrotron radiation

In astrophysics synchrotron radiation (SR) may account for non-thermal emission in the radio to X-ray wavelength regimes. The SR flux and spectral shape mainly depend on the underlying population of leptons and on the magnetic field. An electron with energy $E = \gamma mc^2$ spirals along a magnetic field line with an angular frequency of $\Omega = eB/\gamma mc$, which is independent of the angle between its velocity and the magnetic field lines. The spectrum of emitted SR photons can be calculated by transforming into the lepton rest frame and studying the Compton scattering of the electrons with

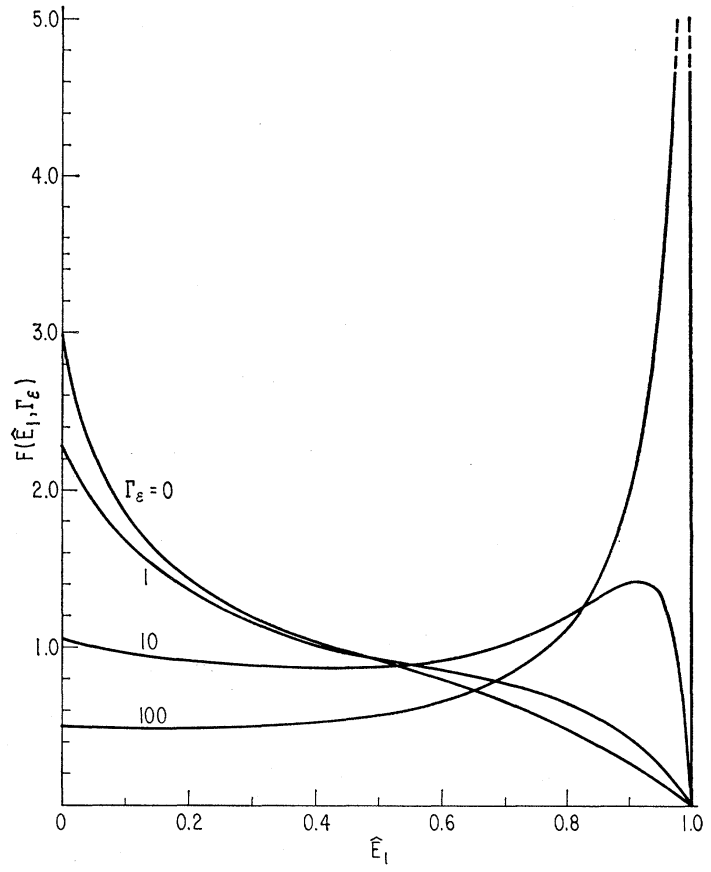

Figure 2.2: Distribution function of the IC scattered photon in the general case. $\hat{E}_\mathrm{I}$ denotes the fraction of the scattered photons energy with respect to the energy of the incident lepton. Γ_ϵ is a dimensionless parameter that determines the *domain* of the scattering. $\Gamma_\epsilon \ll 1$ refers to the Thomson limit and $\Gamma_\epsilon \gg 1$ refers to the extreme Klein-Nishina limit. Image credit: Blumenthal and Gould (1970).

the virtual photons of the magnetic field. Following Blumenthal and Gould (1970), the total energy loss rate due to SR can be written as:

$$\frac{\mathrm{d}E}{\mathrm{d}t} = -\frac{2r_0^2}{3c}\gamma^2 B^2 v^2 \sin^2\alpha, \tag{2.12}$$

with $r_0 = e^2/mc^2$, the lepton velocity v and the pitch angle α between $\vec{v}$ and $\vec{B}$. The opening angle of the emitted radiation is very small for highly relativistic leptons ($\theta \propto \gamma^{-1}$), leading to strong beaming effects in the laboratory frame. Figure 2.3 shows the SR spectrum of a single electron as a function of $x = \nu/\nu_c$, with the critical frequency $\nu_c = 3eB\gamma^3/4\pi mc$. The spectrum is peaked near ν_c with a sharp cut-off towards lower energies and an exponential decline towards higher energies ($\propto e^{-\nu/\nu_c}$). Now assuming a distribution of electrons following a powerlaw shape ($N(\gamma) \propto \gamma^{-p}$) the

shape of the SR spectrum also follows a powerlaw with index $-(p-1)/2$ (Blumenthal and Gould 1970).

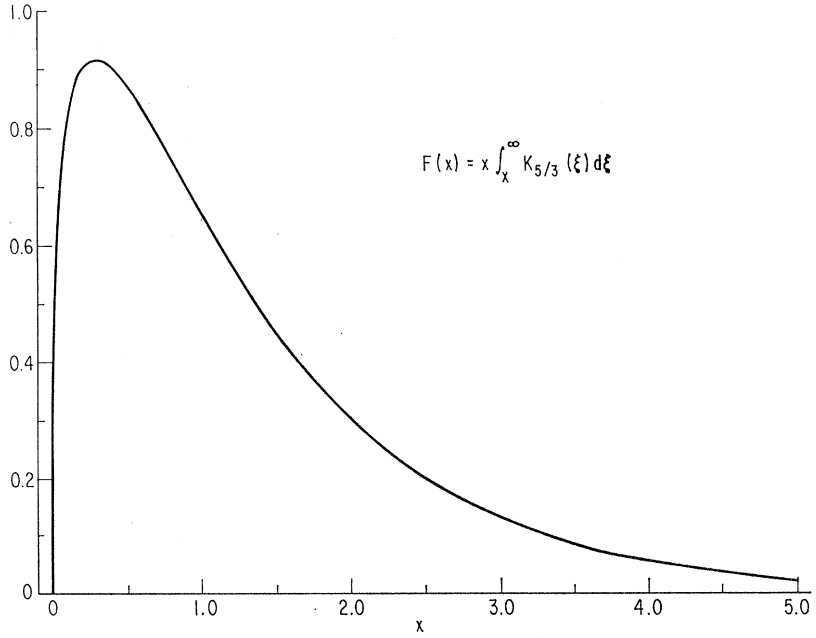

Figure 2.3: SR spectrum of a single electron as a function of $x = v/v_c$. Image credit: Blumenthal and Gould (1970).

As the leptons lose energy via SR, the radiation in turn modifies the lepton energy spectrum, redistributing high-energy leptons to lower energies. This effect is also often referred to as "synchrotron cooling". Following Blumenthal and Gould (1970) SR cooling steepens the lepton spectrum by increasing the index by one: $N(\nu) \propto \nu^{-p} \rightarrow N(\nu) \propto \nu^{-(p+1)}$. Whether this effect becomes important is determined by the age of the electrons with respect to the SR cooling timescale, and it becomes dominant first for larger electron energies. Thus, synchrotron cooling can introduce a spectral break in the observed SR spectrum at a critical energy E_c, which is determined by the magnetic field and the age of the lepton population.

2.5 Hadronic radiation mechanisms

Apart from leptons that were discussed in the previous section, also hadrons may produce VHE γ-rays in the vicinity of cosmic accelerators. Via inelastic collisions of relativistic protons with interstellar matter neutral pions could be created that subsequently decay into two γ-ray photons. The problem of discriminating between leptonic and hadronic processes is not easy, and often only a multi-wavelength approach may

shed light on the issue (as discussed in Sect. 3.4.1). However, hadronic scenarios are preferred when the interaction region is located sufficiently far away from the acceleration region, so that a potential primary leptonic component is efficiently cooled away via SR. Then only secondary leptons that are created in the inelastic hadronic collisions may contribute to the γ-ray signal. Such a scenario is viable for γ-ray emission observed from molecular clouds (MCs) in the vicinity (10 to 100 pc) of SNR shocks. This hadronic mechanism that ultimately leads to γ-ray emission can be divided into three phases, which are all described in this chapter. First the hadrons have to be accelerated to high energies (see Sect. 2.3). Then the relativistic particles diffuse through the ISM until they impinge on the dense target material of the MC (see Sect. 2.5.1). Finally, neutral pions (among other products) are created in the inelastic collisions which decay into γ-ray photons (see Sect. 2.5.2).

2.5.1 Cosmic-ray transport

Following Aharonian and Atoyan (1996); Gabici et al. (2009), this section describes a model to calculate the effects of diffusion on CRs escaping from SNR shocks. Here a SNR in the *Sedov* phase is considered, where the shock radius and velocity scale with time as $R_{\mathrm{sh}} \propto t^{2/5}$ and $|\vec{u}_{\mathrm{sh}}| \propto t^{-3/5}$ (see Sect. 2.2). The transport equation (Eq. 2.6) determines the shape of the CR spectrum originating from SNR shocks. In the general case the diffusion coefficient in the shock region D is a function of energy. The maximum momentum p_{max} achieved by accelerating shocks is given by the confinement condition, i.e. the diffusion length l_{d} should be smaller than the shock radius R_{sh}:

$$l_{\mathrm{d}} = \frac{D(p_{\mathrm{max}})}{|\vec{u}_{\mathrm{sh}}|} \lesssim R_{\mathrm{sh}}. \tag{2.13}$$

In the Bohm limit[1] the diffusion coefficient only depends on the momentum and the magnetic field ($D \propto p/B_{\mathrm{sh}}$). Therefore, the maximum momentum decreases with time as $p_{\mathrm{max}} \propto B_{\mathrm{sh}} t^{-1/5}$. It might decrease even faster since the magnetic field is also expected to decrease with time. For any given time, the spectrum of accelerated CRs f_+ follows a powerlaw distribution for $p < p_{\mathrm{max}}$ (see Eq. 2.9) and has a sharp cut-off at $p > p_{\mathrm{max}}$. All particles with energies above this cut-off escape from the acceleration site. At any given time t the spectrum of runaway particles q_{esc} can therefore be approximated by a delta-functional dependence plus the spectrum of particles with $p > p_{\mathrm{max}}$ that have been accelerated at earlier epochs (Ptuskin and Zirakashvili 2005):

$$q_{\mathrm{esc}} = -\delta(p - p_{\mathrm{max}}) \times \int_0^\infty d^3R \left(\frac{\partial p_{\mathrm{max}}}{\partial t} + \frac{\nabla \vec{u}_{\mathrm{sh}}}{3} p_{\mathrm{max}} \right) f_+(p_{\mathrm{max}}, R). \tag{2.14}$$

[1] Bohm diffusion describes the transport of charged particles in magnetized plasmas by introducing a relation between the gyroradius r_{g} and the particles' mean free path λ. The ratio between these two quantities was empirically found to be $\lambda/r_{\mathrm{g}} = 16$ (see, e.g., Spitzer 1960).

The determination of $p_{\rm max}$ requires the knowledge of the diffusion coefficient, which in turn is determined by the level of magnetic turbulence that is generated by the CRs themselves. This problem is therefore non-linear, and its solution is not straightforward. For this model the evolution of the maximum momentum is parametrized as $p_{\rm max} \propto t^{-\delta}$. This is motivated by the fact that most of the kinematic parameters that describe the shock in the *Sedov* phase, such as $R_{\rm sh}$ and $|\vec{u}_{\rm sh}|$, also feature a powerlaw dependence. To determine δ a value of $p_{\rm max} = 5$ PeV/c is assumed at early ($t = 200$ yr) and $p_{\rm max} = 1$ GeV/c at late ($t = 5 \times 10^4$ yr) epochs, which requires $\delta \approx 2.48$. The lower energy threshold is motivated by the fact that at energies below 1 GeV ionization losses dominate over the nuclear interaction cross section. The upper energy threshold corresponds to the location of the *knee* in the CR spectrum, which might indicate the maximum energy achieved by Galactic accelerators (see Sect. 2.1). According to Ptuskin and Zirakashvili (2005), if the maximum momentum has a powerlaw shape, then also the spectrum of escaping particles follows a powerlaw distribution of the form $\propto p^{-4}$. Following these authors, the distribution of escaping particles $f_{\rm out}$ for a given distance from the shock R satisfies the following diffusion equation:

$$\frac{\partial f_{\rm out}}{\partial t}(R,p,t) = D_{\rm ISM}(p)\nabla^2 f_{\rm out}(R,p,t) + q_{\rm esc}(p,t)\delta(R). \tag{2.15}$$

The diffusion coefficient $D_{\rm ISM}(p) = D_{10}(pc/10\,{\rm GeV})^s$ describes the transport of relativistic particles in the Galactic ISM, with D_{10} being the coefficient at a momentum of $p = 10$ GeV/c. Note that $D_{\rm ISM}$ describes the diffusion through the ISM outside the acceleration region, and should not be confused with the shock diffusion coefficient D that is used, e.g., in Eq. 2.6. The parameters $s \approx 0.5$ and $D_{10} \approx 10^{28}$ cm^{2}s^{-1} can be constrained by CR measurements (Berezinskii et al. 1990). However, the quoted values are only an average over the whole Galaxy and might differ quite substantially in the vicinity of individual CR accelerators. Therefore, exact measurements of the high-energy particle population in these regions may provide insights into CR transport mechanisms and magnetic field turbulence. If $p_{\rm max}$ indeed scales as a powerlaw with time, Eq. 2.15 can be solved analytically for any given distance R from the SNR shock, time t and energy $E \geq c \times p_{\rm max}(t)$ (Gabici et al. 2009):

$$f_{\rm out}(t,R,E) = \frac{\eta E_{\rm SN}}{\pi^{3/2}\ln(E_{\rm max}/E_{\rm min})}\frac{e^{-(R/R_{\rm d})^2}}{R_{\rm d}^3}E^{-2}. \tag{2.16}$$

Here $E_{\rm SN}$ is the total energy released by the supernova explosion and η is the fraction that is converted into CRs. $E_{\rm max} = 5$ PeV and $E_{\rm min} = 1$ GeV are the maximum and minimum energies of CRs escaping during the whole *Sedov* phase. The diffusion length $R_{\rm d}$ is given by:

$$R_{\rm d} = \sqrt{4D(E)(t-\chi(E))}, \tag{2.17}$$

where

$$\chi(E) = t_{\mathrm{Sedov}} \left(\frac{E}{E_{\mathrm{max}}} \right)^{-1/\delta} . \tag{2.18}$$

Here t_{Sedov} (see Eq. 2.1) is the time after which the SNR enters the *Sedov* phase. With Eq. 2.16 the spectrum of CRs that arrive at a MC located at a distance R from the shock and at a time t after the explosion can be calculated[2]. Figure 2.4 shows the energy density of CR spectra calculated with Eq. 2.16 for $R = 50$ pc, $\eta E_{\mathrm{SN}} = 10^{50}$ erg, $D_{10} = 10^{28}$ cm^{2}s^{-1}, and evaluated for various times t. Please note that the CR spectra shown in Fig. 2.4 only comprise hadrons that originate from the nearby SNR shock. Of course each MC is also embedded in the "sea" of CRs that are generated by the whole population of Galactic and extragalactic particle accelerators (with a flux of $J_{\mathrm{sea}} = 2.2 \left(\frac{E}{\mathrm{GeV}}\right)^{-2.75} \mathrm{cm}^{-2}\mathrm{s}^{-1}\mathrm{GeV}^{-1}\mathrm{sr}^{-1}$, Dermer 1986). However, for sufficiently young SNRs and if the distance between MC and SNR is not too large, the local particles dominate over the energy density of the sea. The ratio between local CR

[2]Please refer to Gabici et al. (2009) for a more detailed discussion of each step of the above derivation.

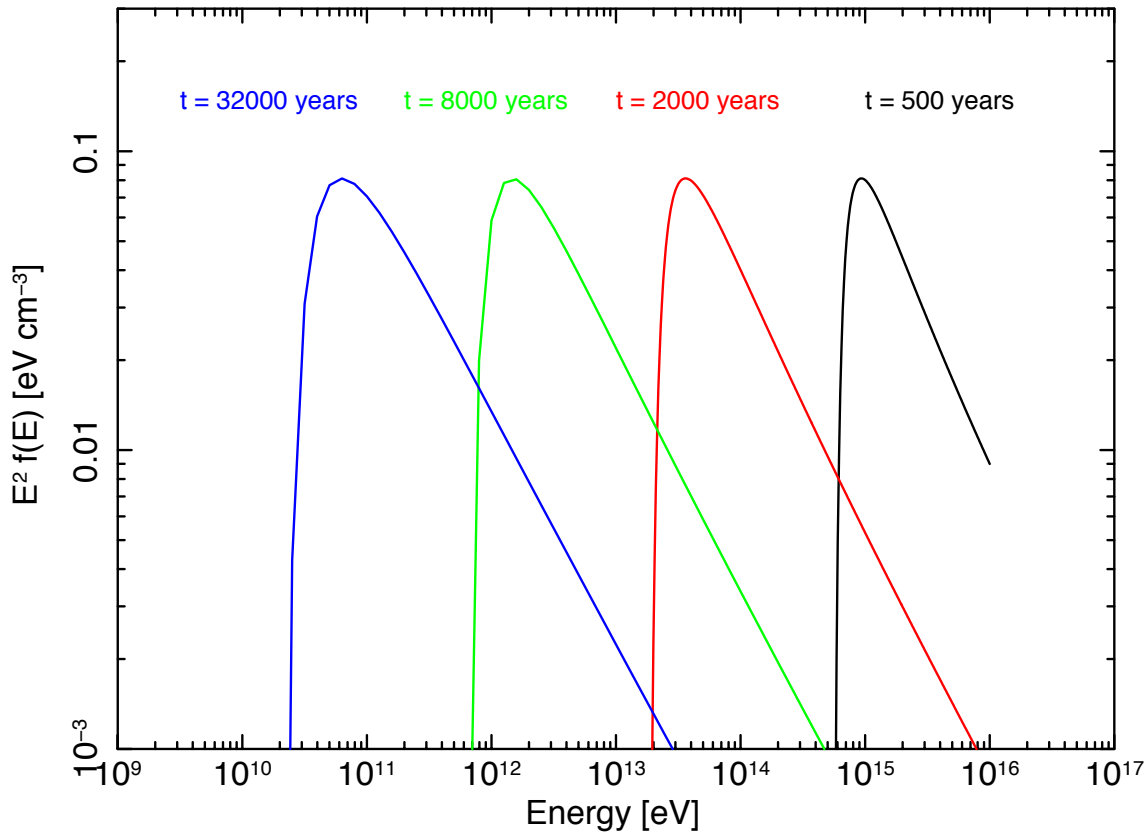

Figure 2.4: Energy density of CRs ($\eta E_{\mathrm{SN}} = 10^{50}$ erg) at a distance of 50 pc from the SNR shock. The different colors refer to different times after the supernova explosion, as indicated in the figure.

density and CR density observed at Earth, which is assumed to be representative for the mean Galactic sea value, is also referred to as the *Cosmic ray enhancement factor* k_{CR}.

2.5.2 The emissivity of π^0-decay γ radiation

In the previous section a model to calculate the time dependent energy density of CRs incident on a MC located at a certain distance from the SNR shock was introduced. MCs mainly consist of molecular hydrogen (H_2) and we therefore have to consider "fixed target" proton–proton collisions. To calculate the expected γ-ray flux due to π^0-decay one first has to know the neutral pion emissivity $q_\pi(E_\pi)$, i.e. the number of created pions produced per second per hydrogen atom. Following e.g. Dermer (1986), the π^0-emissivity can be calculated as:

$$q_\pi(E_\pi) = 4\pi \int_{E_{\min}}^{\infty} \mathrm{d}E_p \; J_p(E_p) \; \frac{\mathrm{d}\sigma(E_\pi, E_p)}{\mathrm{d}E_\pi}, \tag{2.19}$$

where E_p, E_π denote the energy of the proton and the pion, respectively, $J_p = c/4\pi f_{p,\mathrm{out}}$ is the incident proton flux and $\mathrm{d}\sigma(E_\pi, E_p)/\mathrm{d}E_\pi$ the differential cross section for the production of a neutral pion with energy E_π in a fixed target collision of a proton with energy E_p. In the GeV to TeV energy range the fraction of the incident proton energy that is transferred to the π^0 is nearly constant ($f_\pi \approx 0.17$, see Gaisser 1990). Now assuming that every created pion gets exactly that fraction of the proton's energy in the collision, Eq. 2.19 can be simplified to (Aharonian and Atoyan 1996):

$$q_\pi(E_\pi) = 4\pi \int_{E_{\min}}^{\infty} \mathrm{d}E_p \delta(E_\pi - f_\pi E_p) \sigma_{pp}(E_p) J_p(E_p), \tag{2.20}$$

where $\sigma_{pp}(E_p)$ is the total inclusive cross section for π^0-production in proton–proton collisions, which is well known from accelerator experiments. Below 10 GeV σ_{pp} shows a rather strong energy dependence. Here, the parametrization given by Dermer (1986) is used for this energy range. For higher energies the cross section is only mildly energy-dependent and can be approximated as $\sigma_{pp} \approx 30 \times (0.95 + 0.06 \log(E/\mathrm{GeV}))$ mb (Aharonian and Atoyan 1996).

Each π^0 decays into two γ-ray photons and in an isotropical case the γ-ray emissivity then is:

$$q_\gamma(E_\gamma) = 2 \int_{E_{\min}}^{\infty} \frac{q_\pi(E_\pi)}{\sqrt{E_\pi^2 - m_\pi^2 c^4}} \mathrm{d}E_\pi, \tag{2.21}$$

with the photon energy E_γ and $q_\pi(E_\pi)$ from Eq. 2.20.

In the particular case of a powerlaw proton spectrum with index $-\alpha$ Eq. 2.21 can be written as (Gaisser 1990; Aharonian and Atoyan 1996):

$$q_\gamma(E_\gamma) \approx \frac{16\pi f_\pi^{\alpha-1}}{\alpha^2}\sigma_{pp}(10E_\gamma)J_p(E_\gamma)\eta_{\mathrm{A}}. \tag{2.22}$$

Here $\eta_{\mathrm{A}} \approx 1.5$ is a correction factor to take into account the contribution from heavier nuclei. Also note that σ_{pp} is here formally evaluated at 10 times the photon energy, which roughly corresponds to the energy of the primary proton. To predict the γ-ray flux observed from a MC at a distance R from the SNR and at a distance d from the observer we assume that the cloud acts as a passive target, i.e. that no additional particle acceleration is present inside the cloud. In this case the γ-ray flux is given by

$$F_\gamma = \frac{\int_V n(\vec{r})q_\gamma(\vec{r})\mathrm{d}^3r}{4\pi d^2}, \tag{2.23}$$

where $n(\vec{r})$ is the gas number density and V the volume of the cloud. If the CRs can freely penetrate the MC, the γ-ray emissivity is constant over the whole volume, and Eq. 2.23 reads

$$F_\gamma = \frac{Mq_\gamma}{m_p 4\pi d^2}, \tag{2.24}$$

where M is the total mass of the MC inside the volume V and m_p is the proton rest mass (Aharonian and Atoyan 1996). In this work (chapter 4) Eq. 2.24 is used to model the VHE γ-ray emission of HESS J1626−490 in the context of a SNR–MC interaction scenario.

3 Observatories

The techniques to measure extraterrestrial light at different wavelengths are almost as diverse as the physical mechanisms responsible for the emission. Figure 3.1 shows the electromagnetic spectrum together with typical observatories at each band. The atmosphere's degree of opacity at each frequency allows ground-based (e.g. visible light, radio: 10 cm to ∼10 m) or requires space-borne (e.g. infrared, X-ray) observation. Visible, UV, infrared and X-ray wavelengths today are mainly recorded with semiconductor CCD cameras; yet camera operating modes and mirror optics are greatly different among the various energy bands. Due to the long wavelengths radio observatories require huge telescope dishes and/or long baselines in interferometric mode to achieve good angular resolutions. To detect highly penetrating γ-radiation above ∼0.1 MeV classical optical concepts are not applicable and therefore γ-ray instruments resemble more the detectors used in high-energy particle physics (as, e.g., the recently launched *Fermi* satellite). At energies beyond 100 GeV ground based Imaging Atmospheric Cherenkov Telescopes (IACTs) even use the atmosphere itself as detection medium to gain huge effective areas.

It is the purpose of this chapter to introduce the different observatories that provided the data necessary for the analyses presented in chapters 4 and 5. Also the detection techniques at the respective frequency regime are described in some detail. As this work is based on two VHE γ-ray sources detected with H.E.S.S., the one thing that all of the observatories have in common is that they can observe the southern sky and are therefore either located somewhere on the southern hemisphere or space-borne. Even though most of these telescopes were not built with γ-astronomy in mind, they can still be powerful tools for our purposes. To demonstrate these synergies, each of the following sections contains a "scientific background" subsection, which introduces the areas of high-energy astrophysics where the respective observatories can contribute to our understanding of the physical processes.

3.1 The Australia Telescope Compact Array (ATCA)

3.1.1 Scientific background: SNRs and the Interstellar Medium

One of ATCA's primary purposes is the study of the Interstellar Medium (ISM) of the southern sky. But how does this link to VHE γ-ray sources detected with H.E.S.S.? Many of the cosmic particle accelerators are connected to supernova explosions and their remnants. These violent events have quite a large impact on the surrounding

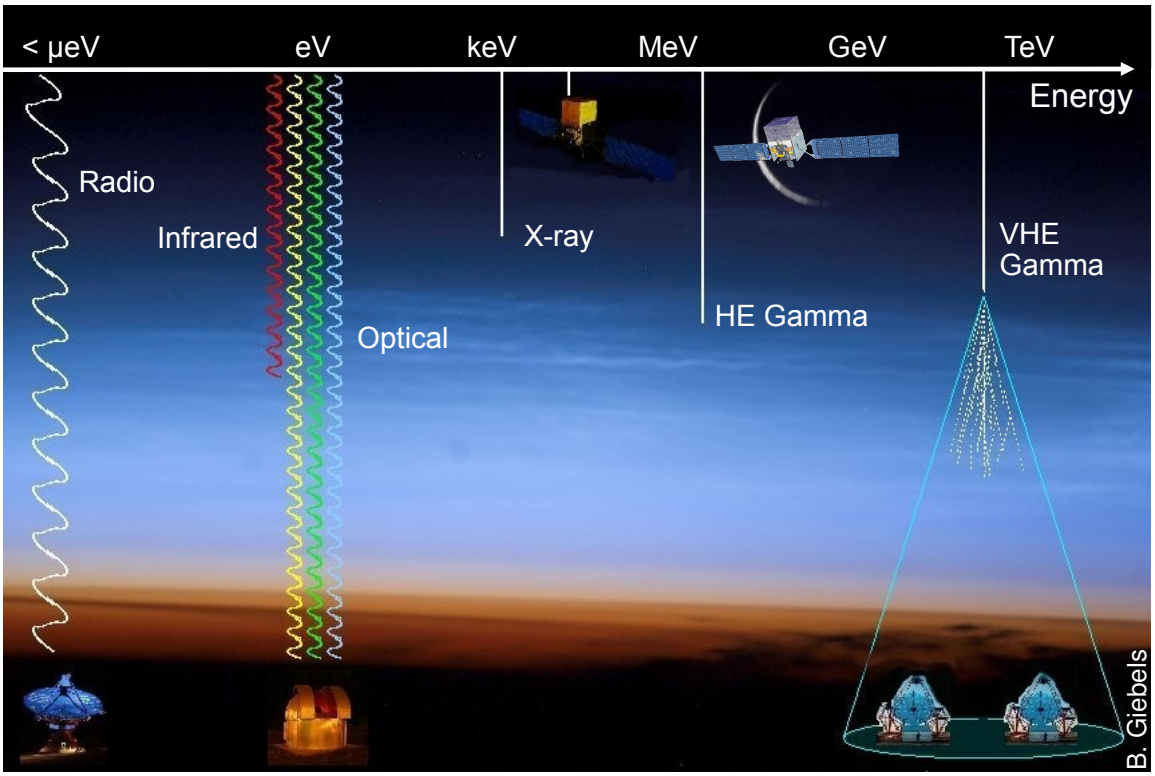

Figure 3.1: Schematic view of the electromagnetic spectrum and the observational techniques for each band. Image credit: Berrie Giebels/CNRS/France

ISM as they deposit their kinetic energy by compressing the surrounding gas, creating large blown-out cavities bordered by dense, shell-like regions with diameters of a few 10 to 100 pc. By searching for such imprints of SNRs in the ISM with radio observations, parameters such as the distance or sometimes the age of the SNR can be derived. This section will give some general information about the ISM, describe how stars and their remnants influence their surroundings, how the ISM can be observed, and what we can learn from that about cosmic ray accelerators in particular.

A significant portion of the total mass of the Milky Way is not yet condensed into stars and exists in the form of gas that occupies the interstellar space. Its average density is about $\rho \sim 0.1$ atom/cm^3 but can increase greatly in the centers of dense clouds where star formation takes place. The ISM features a wide variety of different phases defined by its temperature and density, ranging from cold, dense molecular clouds (T$\approx$10 K, $\rho \leq 10^6$ atoms/cm^3) to hot ionized gas in H II regions (T$\approx 10^4$ K, $\rho \approx 10^2$ atoms/cm^3) where the UV radiation of young stars heats the surrounding gas. The physical condition of the ISM dictates its dominant cooling mechanism. Thus, the gas might be visible at very different wavelengths. Non-ionized atomic hydrogen can be traced by its 21 cm hyperfine transition. As the thermal energy associated with this transition is $\ll$1 K, it can be excited almost in every environment. Hot plasma on the other hand, may be best seen in infrared (Hα emission) or even in the X-rays via thermal continuum and line emission of metals.

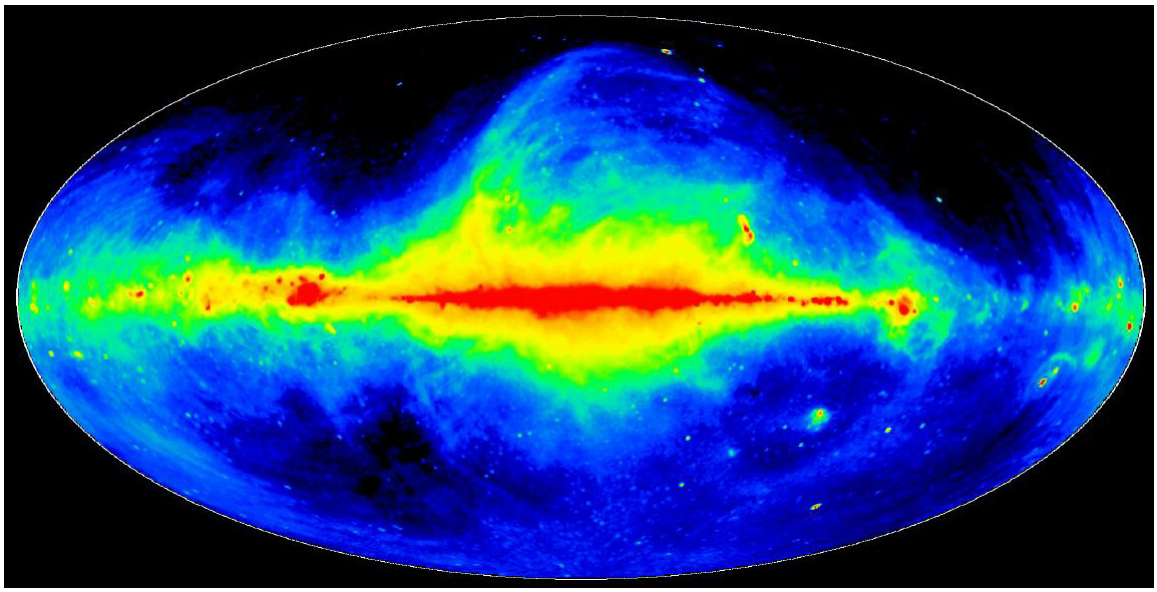

Figure 3.2: All-sky map of 21 cm emission in Galactic coordinates. Most of the radiation comes from the hyperfine transition of neutral hydrogen. Image credit: Reich et al. (2001)/MPIfR.

The ISM plays an important role in the dynamical evolution of a galaxy's stellar population as new stars are formed in the densest parts of the ISM. Stellar winds and outflows, as well as explosions such as novae and supernovae feed the ISM with new matter and energy which can lead to compression and heating of the gas and might trigger new star forming activity. The interplay between the ISM and stellar objects defines the galactic dynamics and the timescale on which all the free gas will be finally condensed into stars which marks the end of its active life-span.

Hydrogen is by far the most abundant element in the Universe. Tracing neutral hydrogen (H I) via the 21 cm hyperfine line intensity over a large fraction of the sky (see Fig. 3.2 for an example) allows to identify ISM structures of Galactic scales down to individual clouds with sizes of only a few parsec. All these size scales are also important for high-energy astrophysics: The γ-ray emission from the Galactic center ridge might be linked to the distribution of matter in that region (Aharonian et al. 2006a). Furthermore, as mentioned above, many individual cosmic ray accelerators, such as young SNRs, influence the surrounding ISM on scales of a few 10 pc.

One can even measure distances by observing the H I line. The Milky Way rotates, and the relative velocity between object and observer depends on their respective positions in the Galaxy. This introduces a Doppler shift of the measured wavelength ($\Delta\lambda$) with respect to the emission that would be observed at rest. This shift translates into a relative line-of-sight velocity (v_{LSR}) via:

$$v_{\mathrm{LSR}} = \frac{\Delta\lambda}{\lambda} c. \tag{3.1}$$

If the Galactic rotation curve is known v_{LSR} can then be used to calculate the distance to the observed object. This basically adds a third coordinate along the line of sight to the data in addition to the two coordinates in the plane of the sky. The gas distribution can then be studied in three dimensions, and the distance to objects seen in other wavelength regimes (e.g. SNRs) connected to certain ISM structures can be measured.

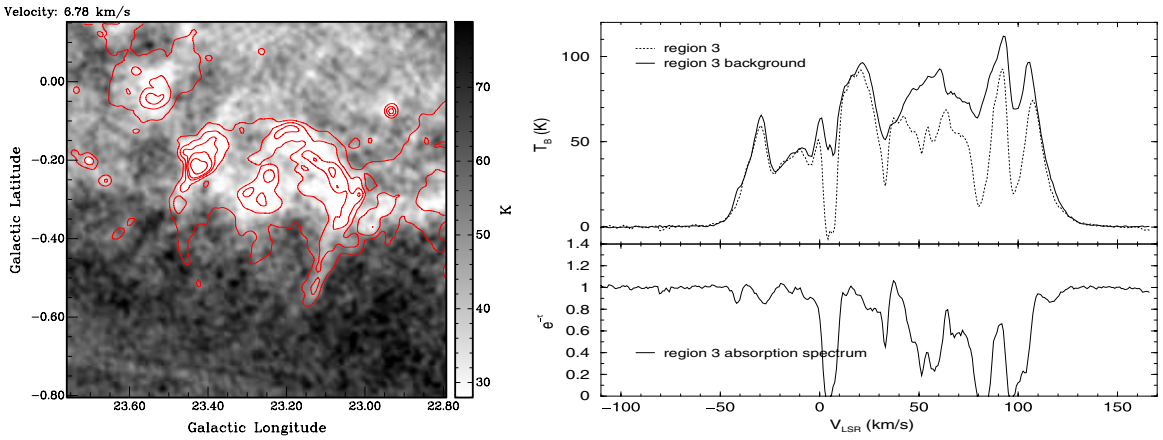

Figure 3.3: *Left:* H I image at 6.78 km/s of the SNR W41. The emission from the continuum source (denoted by red contours) is clearly absorbed, most likely due to foreground clouds. *Right:* H I emission/absorption spectra from a sub-region of the SNR W41 and a background region. It can be clearly seen that up to velocities of ∼100 km/s the source spectrum is absorbed with respect to the background spectrum. Image credit: Leahy and Tian (2008).

As recently shown by Tian et al. (2007, for G18.8+0.3) and Leahy and Tian (2008, for W41), H I absorption measurements can also be a powerful tool to determine the distance of continuum radio sources, such as SNRs. Here the H I line emission spectrum from a continuum source is compared to the H I spectrum from an adjacent background region (as shown in Fig. 3.3). Gas clouds that lie between the continuum source and the Earth lead to absorption dips in the H I spectrum from the on-source region that do not exist in the background region. The maximum line-of-sight velocity up to which such absorption dips occur gives a lower limit for the distance to the SNR, as there must be absorbing matter up to this distance between the observer and the source. An upper limit for the distance to the continuum source can be derived if a prominent gas cloud is located at a larger line-of-sight velocity that does not show up as an absorption dip in the H I spectrum. Otherwise, if such a cloud would indeed be in front of the SNR, a prominent absorption dip in the H I on-source spectrum would be expected. However, one difficulty of this method is that emission in the H I line does not only arise from the continuum source but also from emitting clouds overlapping with the

source in the plane of the sky. If the H I emission varies between background and source regions, fake "absorption" signatures could be generated.

3.1.2 Observation technique: Radio telescopes and interferometry

The radio fluxes of astronomical sources are in many cases very small compared to fluxes in other wavelength regimes and large collecting areas are needed to measure the faint signals. Radio observatories are in a sense non-imaging telescopes as the total light is collected and focused onto one receiver at the focal plane. An image of the intensity distribution on the sky can be created by combining the data from a scan over a larger region. The size of the area on the sky where the radiation can originate from to be focused onto the receiver is referred to as the "beam size" and is mainly determined by the diameter of the mirror area. Similarly to the point spread function of imaging telescopes the beam size determines the angular resolution of the obtained images. Thus, for good angular resolution and large collecting areas radio telescopes need large dishes of tens or even one hundred meters.

A method to increase the angular resolution without increasing the size of individual dishes is the use of several telescopes in an array configuration. Operating the array in interferometric mode allows to observe at an angular resolution that a telescope with the diameter of the separation between the telescopes would have. At radio wavelengths both the amplitude and the phase of the light can be recorded by each individual telescope. Therefore, the combined interferometric information can be gained by an offline analysis. In contrast, in optical and infrared astronomy the light from each telescope has to be propagated and physically combined to record the interference pattern. For a specific distance ("baseline") between two telescopes and position on the sky the measured signal is one point of the so called "coherence function":

$$V = \int I_\nu(\vec{s}) e^{2\pi i \ \vec{s} \ \cdot \ (\vec{r}_i - \vec{r}_j)} \ \mathrm{d}\Omega. \tag{3.2}$$

Here I_ν is the intensity distribution on the sky, $\vec{s}$ is the unit vector in the direction of observation, and $(\vec{r}_i - \vec{r}_j)$ is the separation vector between antenna i and j. Basically, the recorded interferometric signal is the Fourier transform of the intensity distribution. By scanning the Fourier space for many different baselines a high resolution image of the sky can be obtained after Fourier back-transformation of V.

3.1.3 The telescopes

ATCA is an array of six 22-m radio telescopes (Fig. 3.4) with configurable antenna spacings. While one antenna is fixed in position the other five can be positioned at any of 44 stations providing baselines between 30 m and 6 km. The array is operated by the Australia Telescope National Facility (ATNF) together with other radio telescopes

Figure 3.4: A part of the Australia Telescope Compact Array at the Paul Wild Observatory, Narrabri, New South Wales, Australia. Image credit: ATNF/CSIRO.

as the Parkes[1] and MOPRA[2] observatories. ATCA can be used for observations at wavelengths between 27 cm and 3 mm. Many atomic and molecular lines, such as the 21 cm hyperfine line of molecular hydrogen (H I) lie in that frequency range.

This thesis makes use of public ATCA H I data recorded as part of the Southern Galactic Plane Survey (SGPS, McClure-Griffiths et al. 2005). For this survey the southern Milky Way was scanned in a region of Galactic longitude, $l = 253°$ to $l = 358°$ (SGPS I) and $l = 5°$ to $l = 20°$ (SGPS II) covering Galactic latitude $|b| <= 1.°5$. These survey data have an angular resolution of $2'$. Observations were conducted between December 1998 and November 2000 where the ATCA survey region was observed ten times to minimize the systematic effects due to annual variations.

To study high-energy sources connected to SNRs it is particularly important to resolve ISM structures in all three dimensions down to scales of ∼10 pc. Therefore, a good spectral resolution is particularly important to measure also the line-of-sight extent of the gas distribution. For the SGPS the maximum bandwidth for each observed frequency was 8 MHz which was sampled by 2048 channels. This leads to a channel width of 3.9 kHz which translates to a resolution in the line-of-sight velocity of $\Delta v_{\mathrm{LSR}} =$

[1] http://www.parkes.atnf.csiro.au/
[2] http://www.narrabri.atnf.csiro.au/mopra/

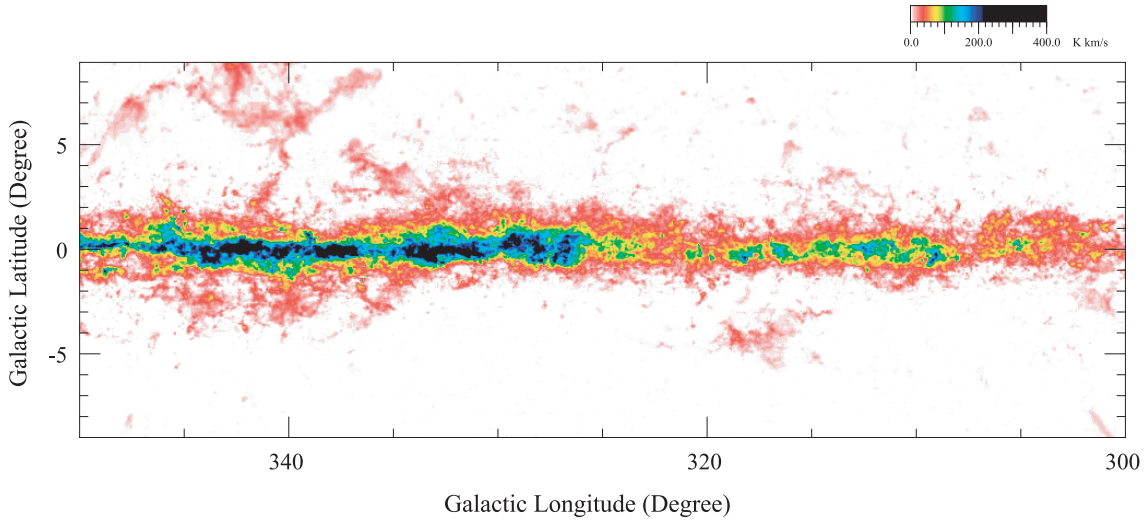

Figure 3.5: Pseudo color NANTEN ^{12}CO ($J = 1 - 0$) total intensity map in galactic coordinates. Image credit: Matsunaga et al. (2001).

0.82 km s^{-1}. The SGPS data are publicly accessible via the world-wide-web[3]. In this work the data are used to study the environment of HESS J1626−490 (Sect. 4.5).

3.2 The NANTEN mm/sub-mm observatory

3.2.1 Scientific background: Molecular Clouds

Hadronic scenarios for high-energy γ-radiation are based on production and decay of neutral pions in a sufficiently massive and dense target medium (see Sect. 2.5). In the previous section (3.1) it was discussed how observations of atomic hydrogen (H I) can help in locating the accelerator itself, i.e. the SNR, based on its signature imprinted on the ISM. This section focuses on the search and characterization of the target medium via observations of molecular gas such as carbon monoxide (CO).

The densest regions of the ISM consist mainly of molecular hydrogen (H_2) and are therefore called "molecular clouds" (MCs). Due to the lack of a dipole moment and the unsuitable conditions within MCs to excite its rotational transitions, H_2 is difficult to observe directly. Carbon monoxide (CO) is the second most abundant molecular species in MCs. It has a dipole moment and its rotational transitions are easily excited at typical MC temperatures (10–100 K) and densities ($\gtrsim$100 cm^{-3}). CO line emission is in most cases the main cooling mechanism for MCs as the transition is efficiently excited by collisions with H_2 molecules.

[3]http://www.atnf.csiro.au/research/HI/sgps/queryForm.html

The frequency of the radiation emitted by a rotational transition from level J to $J-1$ can be calculated as:

$$\nu = \frac{\Delta E_{\mathrm{rot}}}{h} = \frac{\hbar J}{2\pi I}, \tag{3.3}$$

where I is the molecules moment of inertia. The ^{12}CO ($J = 1-0$) transition lies at a frequency of $\nu = 115$ GHz ($\lambda = 2.6$ mm). Depending on the temperature and density at the emission region also higher transitions might be observable, e.g. the $J = 8-7$ is suited to study warmer gas in the denser parts of Molecular Clouds (MCs). Similarly to H I line data (see Sect. 3.1.1), the line-of-sight velocity, and therefore the distance can also be measured with CO line observations.

The observed CO intensity W_{CO} is considered to be a good tracer of the H_2 column density ($N_{\mathrm{H_2}}$) which constitutes most of the total mass of the MC. Large-scale CO surveys (see e.g. Fig. 3.5) were performed to characterize Galactic and extragalactic molecular gas. $N_{\mathrm{H_2}}$ can be estimated from CO observations through a constant "X-factor" (e.g. Dickman 1978):

$$X = \frac{N_{\mathrm{H_2}}}{W}\ \mathrm{cm^{-2}\ K^{-1}\ s}. \tag{3.4}$$

From observations of Galactic MCs this factor was estimated to be $X \approx 10^{20}\ \mathrm{cm^{-2}\ K^{-1}\ s}$ (e.g. Dame et al. 2001). However, if this factor is assumed to be constant there arises a discrepancy between the Galactic distribution of SNRs, believed to be sources of cosmic rays, and the emissivity (= photons / target mass / s) of γ-rays. This could be solved if the X-factor increases by a factor of 5–10 from the inner to the outer Galaxy, as also expected from the Galactic gradient in metallicity (Strong et al. 2004). Furthermore, the ^{12}CO ($J = 1-0$) line intensity is known to be saturated due to extinction for sufficiently massive and dense MCs (e.g. Caselli et al. 2008). Thus, only if the CO intensity is below the saturation level it is a good indicator for the total mass of the cloud. New insights in the issue of determining the correct X-factor might also be gained by simulations of MCs in various conditions (e.g. Shetty et al. 2011).

As already discussed in detail in Sect. 2.5 SNR–MC interactions provide a unique way to probe hadronic cosmic ray transport and γ-ray production. Dense molecular material and young SNRs are strongly connected due to the dynamical evolution of star formation. SNRs are believed to be sources of high-energy cosmic rays, and dense molecular clouds in the vicinity can provide target material for escaping relativistic particles. Leptons are efficiently trapped in regions near their acceleration site due strong magnetic fields, whereas energetic hadrons may survive the trip to the cloud. A part of the cosmic ray flux is converted into γ-rays via the production and subsequent decay of neutral pions. In studying both the VHE and CO emission we can learn more about cosmic ray acceleration, transport and diffusion as well as interaction with the ISM. In chapter 4 the VHE γ-ray source HESS J1626−490 is discussed in such a context.

Figure 3.6: *Left:* The 4-m NANTEN mm/sub-mm telescope (1995–2004) at the Las Campanas-Observatory, Chile. *Right:* The upgraded NANTEN2 telescope (since 2004) on Pampa la Bola, Chile. Image credit: Onishi et al. (2005) and ph 1/Universität Köln.

3.2.2 The telescope

The 4-m NANTEN mm/sub-mm radio telescope (Fig. 3.6, *left*) is in operation since 1994 and was located at the Las Campanas-Observatory (Chile) until 2004. After that period the main and secondary reflector as well as the mount were upgraded and the telescope was moved to a higher location on Pampa la Bola (Fig. 3.6, *right*). The accessible frequency range is 115–880 GHz or 2800–340 μm. Institutes from Japan, South Korea, Germany and Chile participate in the new NANTEN2 project.

NANTEN's primary scientific objective is to map CO emission from the southern Galactic Plane and southern off-plane regions. Previous CO surveys suffered either from low spatial resolution ($8'$–$30'$; Dame et al. 2001) or from small spatial coverage (Sanders et al. 1986). With NANTEN a large part of the Galactic Plane was surveyed $l = 240°$ to $60°$ and $|b| \leq 10°$ (see Fig. 3.5), with a beamsize of only $2\farcm6$ (Mizuno and Fukui 2004). The integration time per point was $\sim$5 s allowing a velocity resolution and coverage of 0.65 km/s and 500 km/s, respectively.

NANTEN's unprecedented capabilities to resolve small-scale molecular structures on the southern sky make it an ideal instrument, in combination with HE and VHE γ-ray instruments, to identify hadronic γ-ray emission processes. The data of the NANTEN Galactic Plane Survey are not publicly accessible, but the necessary data to search for molecular clouds connected to HESS J1626−490 (Sect. 4.4) were kindly provided by the NANTEN collaboration.

3.3 The Spitzer Space Observatory

3.3.1 Scientific background: Star forming regions and their connection to γ-ray sources

A correlation between high-energy γ-rays and star forming regions (SFRs) was proposed already in the 1980s (Casse and Paul 1980; Voelk and Forman 1982; White 1985; Pollock 1987). In particular, massive stars and the interaction of their stellar winds with each other or the surrounding ISM were discussed as potential sources of high-energy radiation. With the Compton Gamma-Ray Observatory (COMPTEL) and the Energetic Gamma-Ray Experiment Telescope (EGRET) a first strong statistical correlation between SFRs and γ-ray emission could be established (e.g. Romero et al. 2000). With the discovery of the VHE γ-ray source TeV J2032+4130 by the HEGRA IACT (Aharonian et al. 2002) an individual VHE γ-ray source could be connected to stellar effects in an SFR for the first time. Recently, a similar source which is probably connected to the SFR Westerlund 2 was discovered with H.E.S.S. (Aharonian et al. 2007a). SFRs harbor large amounts of fast-evolving, massive stars and are thus likely connected to other "classical" types of VHE γ-ray sources such as SNRs and PWNe. Especially because SFRs are embedded in dense molecular clouds, they are good candidates for high-energy γ-ray emission via hadronic processes in SNR–MC interactions.

Star formation is still a very poorly understood process, particularly the mechanisms that originally form molecular clouds, as well as how the cloud collapse is triggered that ultimately leads to densities and temperatures high enough for hydrogen burning. A review of the current phenomenological understanding of star formation is given by Krumholz (2011). What are the observational diagnostics at our disposal to identify regions with star forming activity? Star formation starts at dense cores of molecular clouds and the first young stars ionize the surrounding nebula with their strong UV radiation. Such regions of ionized hydrogen are called H II regions, in contrast to clouds of non-ionized gas (H I). Particularly, the most massive stars form in very compact H II regions featuring relatively small sizes (<0.1 pc), high densities $> 10^7$ cm^{-3}, high temperatures ($T > 100$ K) and high luminosities (10^4–10^6 $L_\odot$). As the first emission from these stars is heavily obscured by the surrounding gas and dust, they are difficult to detect directly. Only at later stages, when the nebula becomes less opaque, the newly formed stars can be observed. However, a large part of the energy is re-radiated in the mid-infrared regime by the envelope comprised of gas and dust. Thus, infrared (IR) surveys combined with radio continuum and molecular line observations are a powerful method to locate SFRs. Furthermore, due to the compact and dense molecular clouds at their centers SFRs become strong absorbers of H I emission and can be identified in H I images from absorption features if they are located between source and observer. This might be particularly useful as a cross check for kinematic distance estimates (see Sect. 3.1.1), as the distances to SFRs can often be independently measured via the parallax of their member stars.

3.3.2 The telescope

Spitzer is a space telescope launched in 2003 designed for IR wavelengths between 3 and 180 microns which includes the near- and far-infrared regimes. To reduce launch costs and to avoid the thermal IR radiation from Earth, *Spitzer* is in an heliocentric orbit, trailing behind Earth (see Fig. 3.7, *left*). As thermal radiation from the telescope itself would pose a huge source of IR background it consists of two thermally decoupled parts. The 85 cm Ritchey-Chrétien telescope and the scientific instruments are cooled by an onboard cryostat to <5.5 K, whereas the rest of the spacecraft, including the solar panels, remains roughly at room temperature. As *Spitzer* was designed to operate for only 5 years, it has run out of coolant by now. However, scientific observations are still possible with "warm" *Spitzer* with one of the three instruments. *Spitzer* has a slightly inclined, fixed heat shield that has to face towards the sun at all times to protect the sensitive telescope and instruments. This restricts *Spitzer's* pointing direction to a maximum inclination of 120° towards the sun.

The three focal plane instruments are the InfraRed Array Camera (IRAC), The InfraRed Spectrograph (IRS) and the Multiband Imaging Photometer for Spitzer (MIPS). Only one instrument can be taking data at any given time and the observations were scheduled in instrument campaigns lasting up to 21 days. *Spitzer* and its instruments are designed to operate either in pointed or scanning mode, meeting the requirements of a large variety of science objectives. The arrangement of the focal plane instruments is shown in Fig. 3.7 (*right*). In the following paragraph each of the science instruments is described briefly.

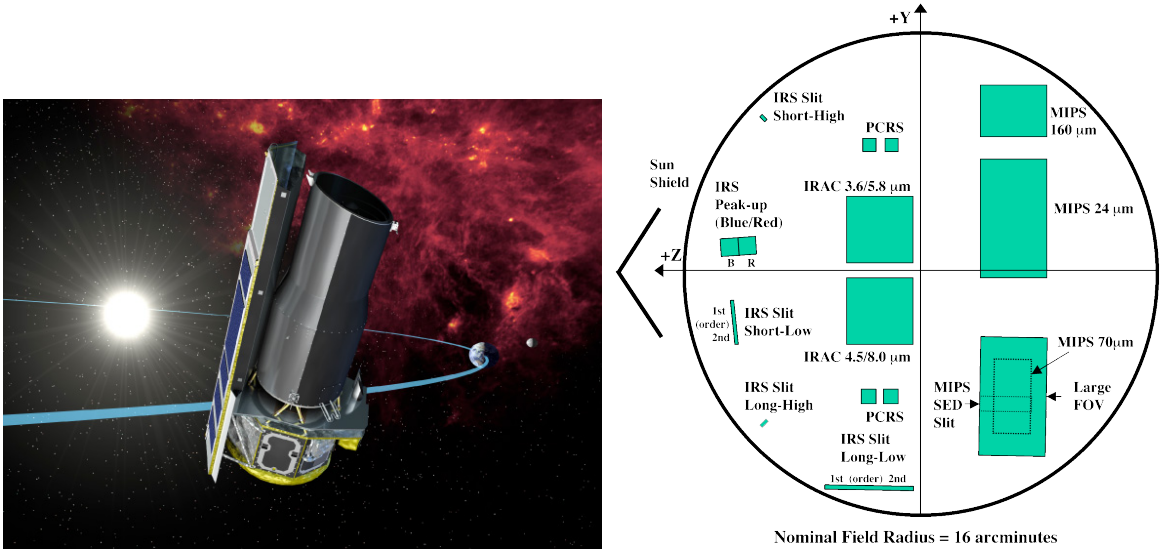

Figure 3.7: *Left:* Artists impression of *Spitzer* in its Earth-trailing orbit. Image credit: JPL/CalTech/NASA. *Right:* The arrangement of *Spitzer's* science instruments in the FoV of the telescope. Image credit: Spitzer telescope handbook/Spitzer Science Center/CalTech.

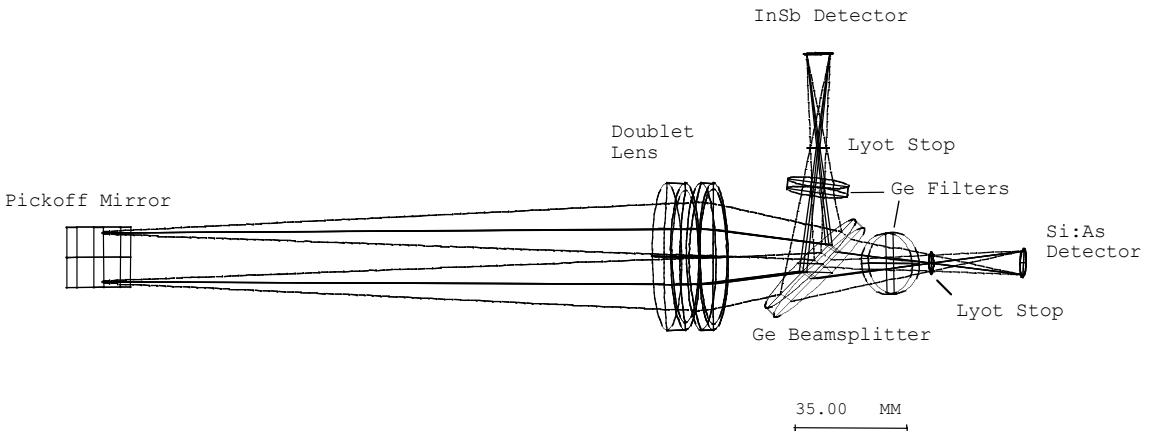

Figure 3.8: IRAC optical layout, top view. The layout is similar for both pairs of channels; the light enters the doublet and the long wavelength passes through the beamsplitter to the Si:As detector (Channels 3 and 4) and the short wavelength light is reflected to the InSb detector (Channels 1 and 2). Image credit: IRAC instrument handbook.

IRAC is a four-channel camera with a field of view (FoV) of $5.2' \times 5.2'$. Four wavelengths can be observed simultaneously (3.6, 4.5, 5.8 and 8 microns) in two different windows in the FoV, offset by $1\farcm5$. To select these narrow bands, the light from the telescope is guided by a dichroic beamsplitter onto the cameras (see Fig. 3.8). The four 256×256-pixel semiconductor detectors are made of InSb (3.6 and 4.5 μm) and Si:As (5.8 and 8 μm), respectively. On "warm" *Spitzer* only the two cameras for the smaller wavelengths can still operate at peak performance. IRAC is an excellent survey instrument due to its high sensitivity, relatively large FoV and simultaneous four-color imaging capabilities. The second instrument onboard *Spitzer* is the IRS, which is an IR spectrometer consisting of four modules that provide low (R=60–130) and moderate (R∼600) spectroscopic resolution between 5.2 and 38 μm. The spectra are recorded by 128×128-pixel cameras. One of them has a "peak-up" function which allows to position the sources on the slit with sub-arcsecond precision, but also has an imaging mode in the 13.5 to 26 micron band. MIPS is *Spitzer's* third focal plane instrument, which consists of three semiconductor cameras, designed to provide photometry and super resolution imaging at 24, 70 and 160 microns, respectively. The instrument is equipped with a scan mirror that allows changing the cameras FoV without moving the spacecraft. MIPS is a multi-purpose instrument, which can image large areas of the sky quickly or take low-resolution spectra from a small area in the FoV, as well as measure total surface brightnesses in Total Power Mode. Detailed information about every aspect of the telescope and the whole payload is compiled in the *Spitzer* telescope handbook[4].

[4]http://ssc.spitzer.caltech.edu/spitzermission/missionoverview/spitzertelescopehandbook/

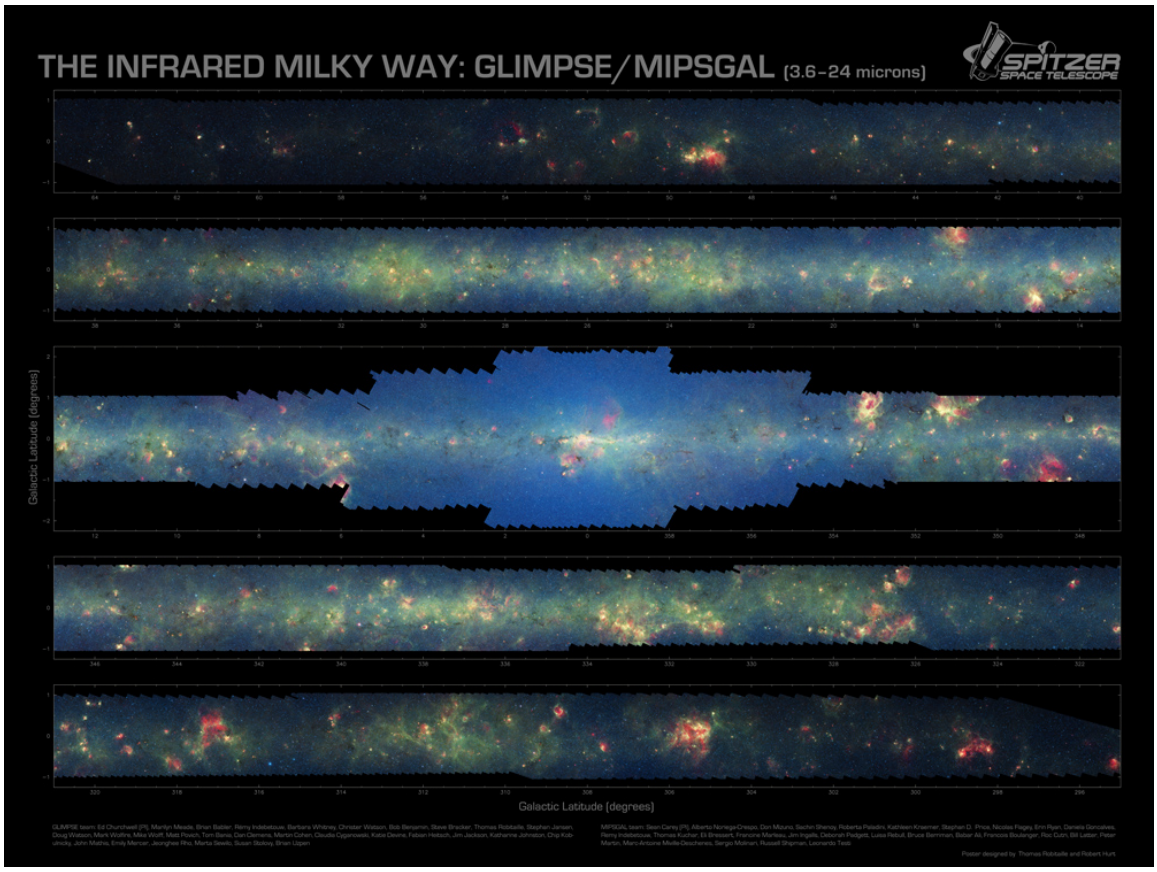

Figure 3.9: A combined color-coded image from the *Spitzer* GLIMPSE (3.6 μm) and MIPSGAL (24 μm) surveys in Galactic coordinates. Image credit: Space Science Institute.

Two large Galactic plane surveys were performed with *Spitzer's* imaging instruments: The Galactic Legacy Infrared Mid-Plane Survey Extraordinaire (GLIMPSE[5], with IRAC) and the MIPS Galactic survey (MIPSGAL[6], with MIPS). The surveys encompass a large fraction of the Galactic Plane over a latitude range of $\pm 139°$. Most parts of the surveys extend over a longitude range of $|b| < 1°$, except for regions close to the Galactic Center with $|b|$ of up to 3° (see Fig. 3.9). The MIPSGAL survey was performed in the two wavelength bands centered at 24 and 70 microns, whereas the GLIMPSE data were recorded for all four of the IRAC bands (3–9 microns). The main science goals were to identify and study massive stars forming in the inner Galaxy and to investigate the distribution and energetics of interstellar dust in our Galaxy. For this thesis the public GLIMPSE and MIPSGAL data were used to search for H II regions connected to HESS J1626−490 (Sect. 4.5).

[5]For a detailed description of the GLIMPSE survey as well as its scientific motivation and outcome see: Churchwell et al. (2009)

[6]A review and motivation of the GLIMPSE survey: Carey (2008)

3.4 The X-ray observatories XMM-Newton and Chandra

3.4.1 Scientific background: Leptonic vs. hadronic γ-ray emission

In this section the problem of identifying the origin of γ-ray emission detected from SNRs and PWNe is discussed, particularly emphasizing the diagnostic power of observations of non-thermal X-ray emission.

With the current generation of space-borne HE and ground based VHE γ-ray telescopes a number of γ-ray emitting SNRs were discovered. These include G347.3-0.5, Vela Jr., RCW 86, and SN 1006 (see references in Reynolds 2008). As described in detail in chapter 2 both leptonic (IC) and hadronic (production and decay of π^0s) processes can in principle lead to γ-ray emission in these energy bands. Up to now it is still not settled yet which of both scenarios is dominant. Furthermore, it may be possible that the relative contribution from both effects may vary between core-collapse and Type I supernovae (see, e.g., Reynolds 2010, for a recent review).

The presence of high-energy charged particles in SNRs was established long before the detection of the first γ-rays. Since the 1950s some SNRs were known to be radio and optical continuum emitters, most likely due to synchrotron emission of electrons with GeV energies (e.g. Cas A, Minkowski 1957). In ASCA observations of SN 1006, featureless X-ray emission, spatially decoupled from the thermal line-emitting regions, was

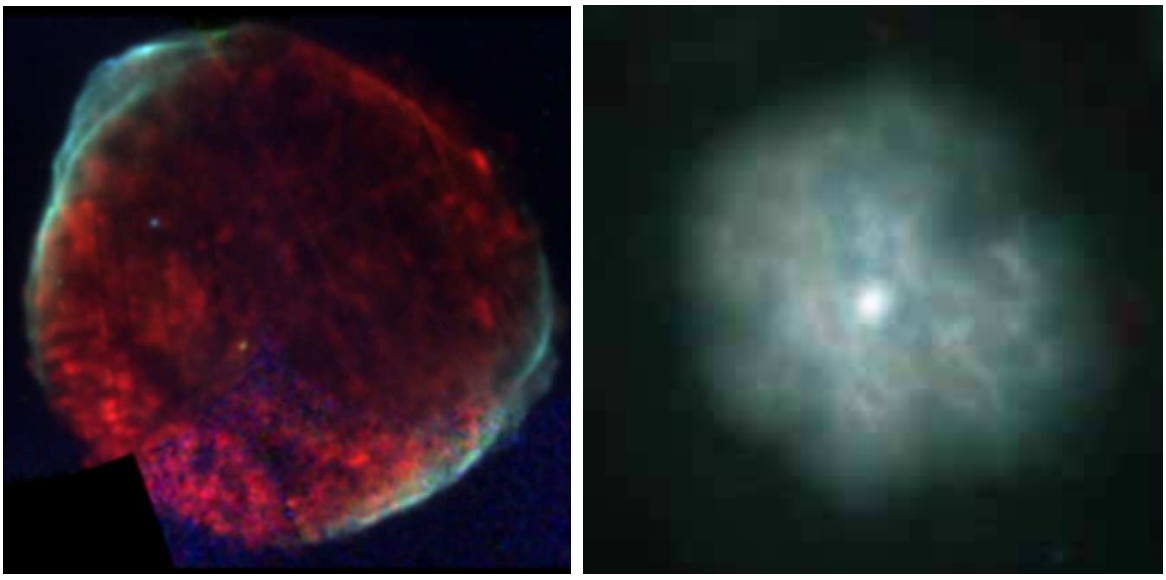

Figure 3.10: *Left: XMM-Newton* image of SN 1006. The colors represent energies of 0.7–2 keV (red) and 2–7 keV (blue), respectively. *Right: Chandra* image of the PWN G21.5-0.9. Red corresponds to 0.2–1.5 keV, green to 1.5–3.0 keV, and blue to 3.0–10.0 keV. Image credit: Vink (2004) / Matheson and Safi-Harb (2005).

detected from an SNR for the first time (*XMM-Newton* image: Fig. 3.10, *left*). This was interpreted as the high-energy end of the synchrotron peak, suggesting that relativistic electrons with energies of up to ∼100 TeV are present in SNR shocks (Koyama et al. 1995). This population of electrons is expected to emit IC radiation in the VHE γ-ray regime with the Cosmic Microwave Background (CMB), and potentially other additional components, as target photon fields. However, it still remains unclear whether the IC radiation is the dominant process giving rise to the observed γ-ray fluxes from SNRs.

If the magnetic field is large ($\gtrsim$10 μG) the amount of electrons required for the observed synchrotron emission is greatly reduced with respect to environments with moderate magnetic fields. Thus, also the expected VHE γ-ray flux via IC scattering is rather low, due to the small electron population. Furthermore, this would suggest a lower high-energy cut-off ($<$ 10 TeV) in the IC spectra arising from the more efficient synchrotron cooling of high-energy electrons. However, with the data of current VHE γ-ray telescopes the location of spectral cut-offs is often very poorly defined. Therefore, only extremely deep observations or next generation telescopes will be able to sufficiently constrain this feature to test the validity of IC scenarios for large magnetic fields. Furthermore, for high magnetic field strengths the expected IC flux would be too low to account for the total flux observed from VHE γ-ray bright SNRs. Thus, in these cases a significant contribution from hadronic processes is needed for the interpretation of the observational data.

Indeed, the presence of strong magnetic fields ∼100 μG in SNR shock regions is supported by the detection of extremely thin non-thermal X-ray rims in Tycho's SNR (see Fig. 1.3, and Bamba et al. 2003). These rims indicate that the synchrotron cooling timescale for leptons is very short requiring large magnetic fields to be present in the shock region. Such large magnetic fields can not be explained by simple compression of the ISM magnetic field with typical shock compression factors of ∼4 for strong shocks (e.g. Reynolds 2010). One explanation for this large amplification may be cosmic ray driven instability (Bell 2004). This instability requires high-efficiency ion acceleration, which would lead to predominantly hadronic γ-ray emission. On the other hand, if the magnetic field strength is small (∼5 μG), IC emission could indeed be the dominant γ-ray emitting process for some SNRs (see e.g. Berezhko et al. 2002). As only the synchrotron component couples to the magnetic field directly, further observations in the radio, and especially in the X-ray regime are needed to shed light on the shock-conditions of more members of the γ-ray emitting SNR population. Furthermore, for a hadronic scenario sufficiently dense target material needs to be present in the interaction region. This could be tested by measuring the intensity of X-ray thermal bremsstrahlung components, which is directly connected to the ISM density (as suggested by Katz and Waxman 2008).

More direct hints suggesting a hadronic component are provided by SNRs interacting with dense MCs. If the γ-ray emission is not observed from the SNR directly but from nearby MCs, a possible primary leptonic component is most likely cooled away via synchrotron emission, even for moderate magnetic fields. This makes a purely hadronic

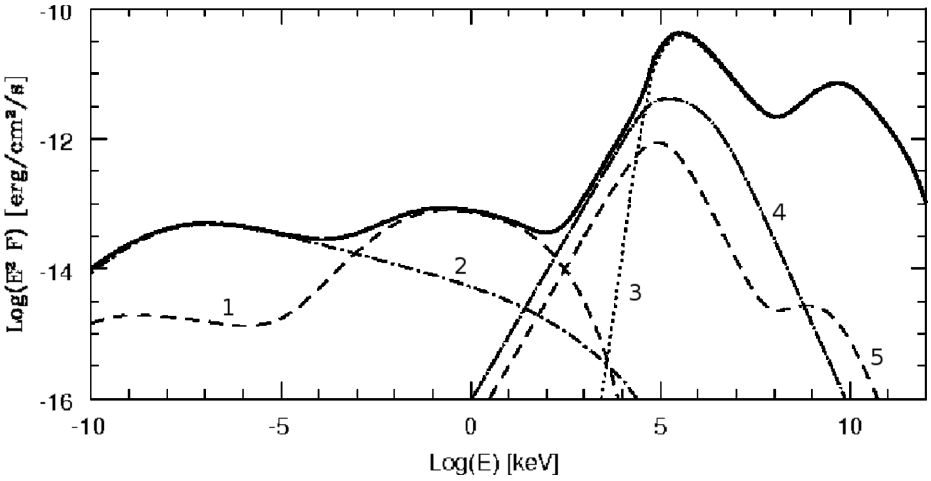

Figure 3.11: Broad-band spectrum of a SNR–molecular cloud interaction. The dotted line shows the emission from π^0-decay (curve 3), the dot-dashed lines represent the synchrotron (curve 2) and bremsstrahlung (curve 4) emission from background cosmic ray electrons that penetrate the molecular cloud, and the dashed lines the synchrotron (curve 1) and bremsstrahlung (curve 5) emission from secondary electrons. Image credit: Gabici et al. (2009).

scenario more plausible for these sources. However, secondary leptons, produced in the decay of charged pions, give rise to broad-band non-thermal emission via synchrotron or bremsstrahlung emission. These spectra are peaked in the X-ray and radio band, respectively (Gabici et al. 2009, see also Fig. 3.11). The observation of non-thermal X-rays thus provides insights into the hadronic processes, as well. However, the expected X-ray fluxes are quite low compared to primary leptonic scenarios. This makes a significant detection challenging, especially due the often very extended emission regions.

Apart from SNRs there are also other types of cosmic particle accelerators where the observation of non-thermal X-rays can be a powerful diagnostic tool. Following Berezhko et al. (2002) SNRs may indeed be the prime sources of hadronic cosmic rays in the case of large magnetic fields and efficient ion acceleration. But then SNRs may not account for the total leptonic component observed in the local cosmic ray spectrum. Therefore, additional accelerators, such as PWNe, of primarily leptonic particles are needed. In these sources a powerful pulsar injects energetic particles into the surrounding medium which are stopped by the ISM at the so-called "termination shock". Leptons can be accelerated in the shock and diffuse outwards, cooling via synchrotron and IC emission as well as through adiabatic losses (see e.g. Slane 2010). The emission from PWNe encompasses the whole electromagnetic spectrum, with peaks in the X-ray (see Fig. 3.10, *right*) and γ-ray bands. Even though this thesis does not focus on these types of objects in particular, they are still discussed in the interpretation of the data. The three main ingredients for the understanding of PWNe are the synchrotron spectrum (radio to X-rays), the IC spectrum (HE, VHE γ-rays), and the target photon fields for the IC

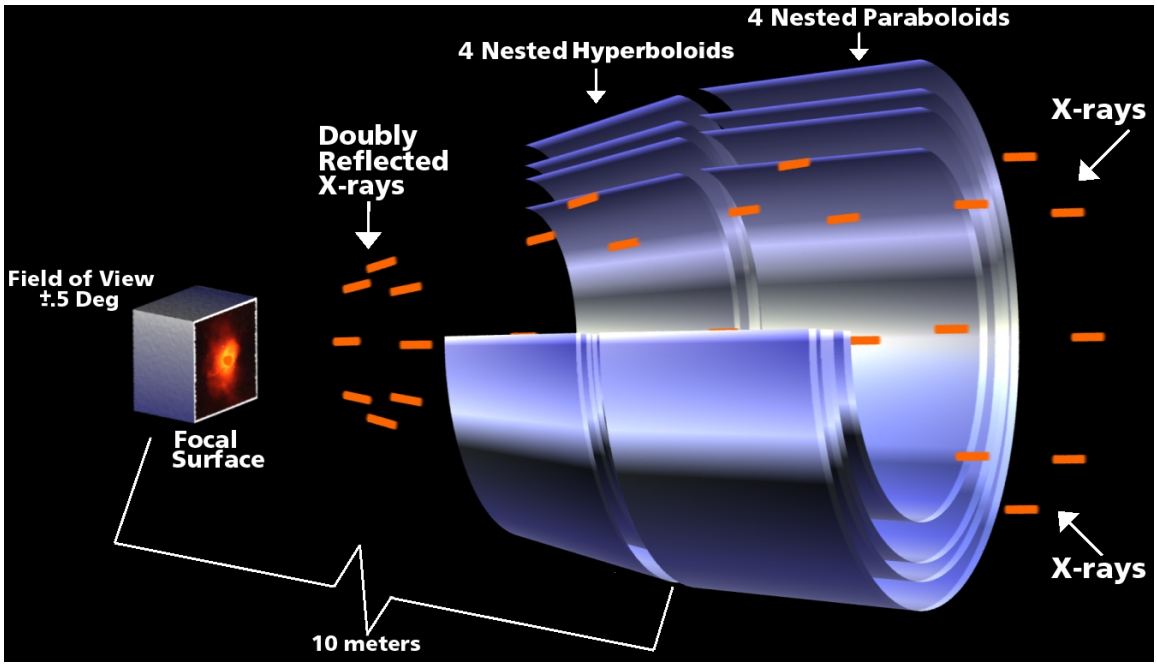

Figure 3.12: Schematic illustration of the grazing incidence technique with four nested mirror shells. Image credit: NASA/CXC/D.Berry.

process (CMB, starlight, IR). Spatially resolved spectroscopy can provide insights into the cooling mechanisms of the leptonic population as well as into the physical conditions present at the termination shock. Just recently, we have shown that a spatially resolved spectroscopic analysis and subsequent modeling of the X-ray emission of the PWNe MSH 15-5*2* (Schöck et al. 2010) and G 09+0.1 (Holler et al. 2011) can constrain parameters such as the conversion efficiency or the magnetization.

Now that we are convinced that X-rays provide a helpful window to the high-energy phenomena present in cosmic particle accelerators, the next section focuses on the detection methods of this radiation. As Earth's atmosphere is opaque for wavelengths shorter than those of ultra-violet light, all X-ray telescopes are either balloon-born or aboard satellites.

3.4.2 Observation technique: Wolter optics

Since X-rays are either transmitted or absorbed and not reflected when hitting mirrors at large angles, the classical focusing techniques that are used in optical and infrared astronomy can not be applied here. Instead one uses the so called *Wolter* telescope which focuses X-rays by reflecting them two times at grazing incidence angles on metal-coated surfaces. In imaging X-ray astronomy only *Wolter* type-I telescopes are currently used. Here the light is first reflected on a paraboloidal surface followed by a hyperboloidal one (Fig. 3.12). As the maximum grazing incidence angle and thus the inclination angle of one such mirror shell is very small, single mirrors provide very small collecting areas.

To increase the effective area one can combine many such mirror shells with different radii and the same focal length, nested on a common mounting structure. As each shell can only be aligned with a certain precision, a drawback of large shell counts is that the accumulated adjustment errors lead to a deteriorated point spread function (PSF) of the full telescope with respect to single mirrors. Thus, depending on the scientific goals of each X-ray observatory the number of nested mirrors varies. The *Wolter* focusing technique works only for photon energies $\lesssim$10 keV, because at shorter wavelengths the grazing incidence reflectivity of single layer coated surfaces drops off rapidly. However, this may be remedied in future missions when using multi-layer surface coatings.

Also present in these types of telescopes are losses in effective area for off-axis sources due to geometrical vignetting and variation in the grazing incidence angle on the mirrors. This basically means that the telescopes are less sensitive for sources at a certain distance from the optical axis with respect to the on-axis position. In particular when studying extended sources that cover a large part of the FoV this effect has to be understood in detail, as the vignetting change within the emission region becomes significant. Furthermore, the vignetting is energy dependent, because the maximum reflection angle is smaller for photons with shorter wavelengths. The effective collecting cross section, i.e. the total area from where photons can reach the mirrors via double reflection, is thus reduced for higher photon energies. An example measurement of energy-dependent vignetting in X-ray telescopes is shown in Fig. 3.13. In Sect. 4.3 an analysis technique is presented that accurately takes into account the energy-dependent vignetting effects when extracting a spectrum from a large region in the FoV.

3.4.3 The telescopes

In the previous section the grazing incidence technique for imaging X-ray telescopes was discussed. The analyses presented in chapters 4 and 5 rely on data from the X-ray observatories *XMM-Newton* and *Chandra*, which are described in this section.

The X-ray Multi-Mirror Mission (*XMM-Newton*, Jansen et al. 2001) was launched by the European Space Agency (ESA) on December 10th 1999. It carries three *Wolter* telescopes with 58 nested mirror shells, each with a focal length of 7.5 m, and features the largest effective area among all imaging X-ray telescopes. The *Chandra* Space Observatory (Weisskopf et al. 2002) was launched by NASA on July 23, 1999 and is equipped with one X-ray telescope consisting of four mirror shells. Both spacecrafts are on highly eccentric orbits with periods $\gtrsim$2 days that allow for long uninterrupted observations far from Earth's radiation belts. Even though both observatories employ similar techniques they are quite complementary in their capabilities. With only few mirror shells aligned with unprecedented precision *Chandra* features sub-arcsecond angular resolution, which is about one order of magnitude better than *XMM-Newton*. However, with its significantly larger collecting area ($\sim$1500 cm^2 at 1 keV) *XMM-Newton* shines in producing high quality spectra and in the detection of faint extended sources. Schematic views of both telescopes are shown in Fig. 3.14. The following two

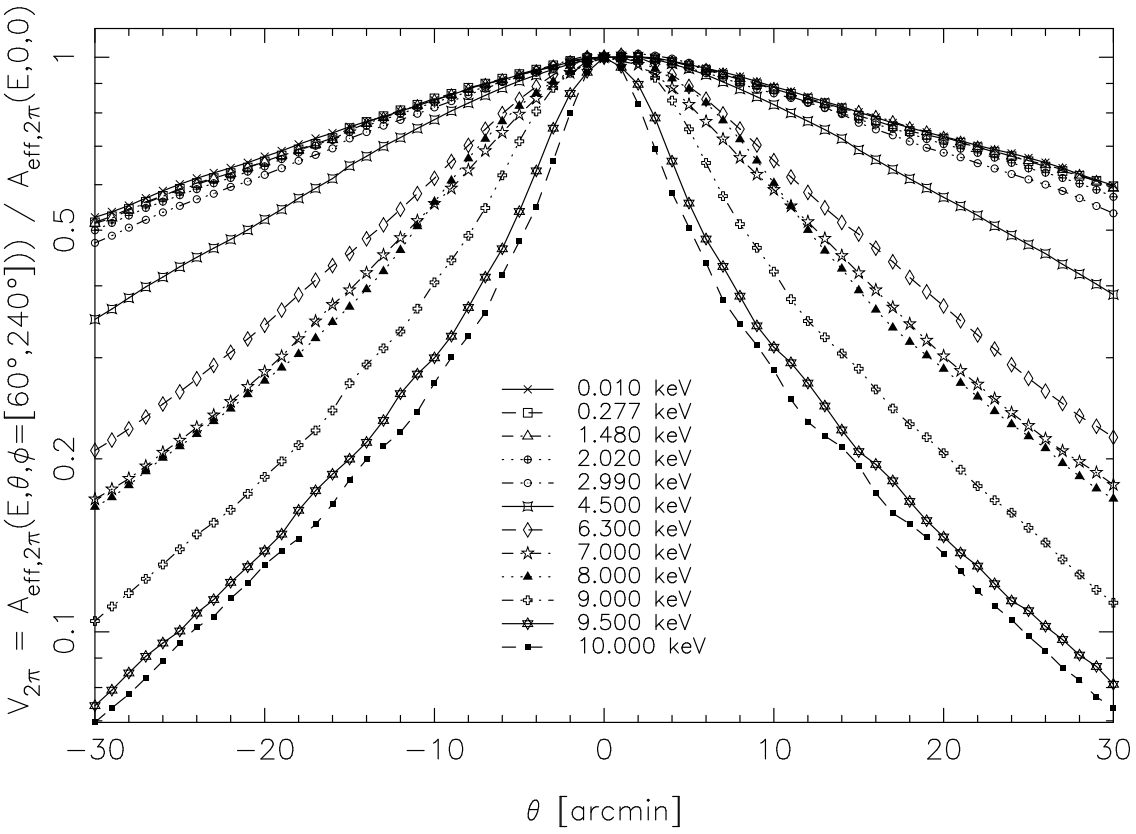

Figure 3.13: The relative mirror vignetting shown for different energies. The data were recorded with the *Chandra* space telescope. Image credit: Gaetz et al. (2000).

sections describe the scientific instruments of both observatories that are relevant for this work.

3.4.4 The scientific instruments of XMM-Newton

Each of *XMM-Newton's* telescopes is equipped with a silicon Charge Coupled Device (CCD) camera, the European Photon Imaging Camera (EPIC). Each of them covers an area of $\sim$36 cm^2 in the focal plane which translates into a FoV of 30′ in diameter. Two CCD cameras are of Metal Oxide Semi-conductor type (MOS, Turner et al. 2001) and one is of pn type (Strüder et al. 2001). The telescopes in front of the MOS instruments both are equipped with the Reflection Grating Spectrometer (RGS), which deflects roughly half of the incoming flux towards the RGS detectors. This results in a reduced effective area with respect to the PN camera. The X-ray absorbing CCDs are operated in single photon counting mode which means the photon properties such as location, energy and arrival time are stored for every single registered event. Of course, this is only true when the observed source is not too bright, i.e. pixels are hit at most once per readout frame. The MOS instruments consist of seven front-illuminated CCDs with a pixel size of 1.″1. They are arranged at different heights to follow the shape of the focal

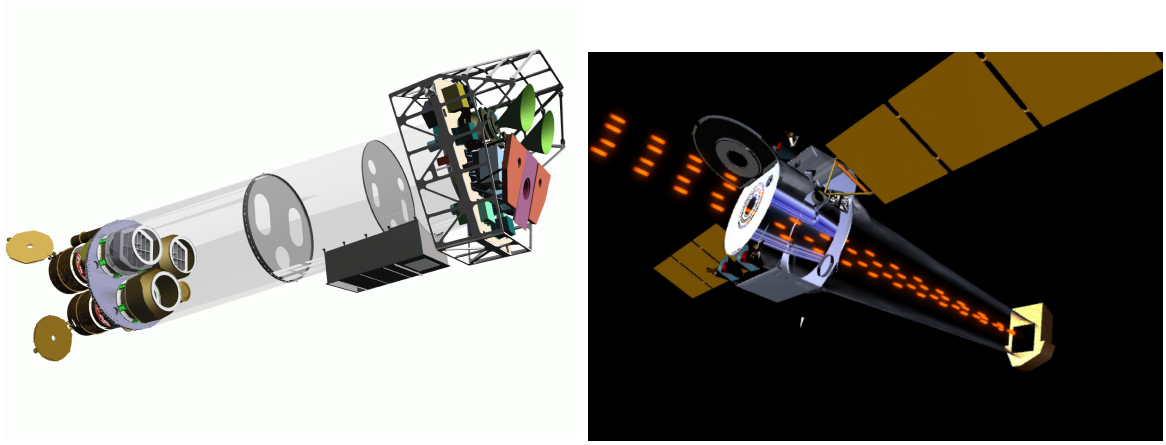

Figure 3.14: Schematic views of the *XMM-Newton* (*left*) and *Chandra* (*right*) payloads. The light path of X-rays through the mirrors onto the detector in the focal plane is indicated by red lines in the *right* image. Image credit: Dornier Satellitensysteme GmbH & ESA; NASA/CXC/D.Berry & A.Hobart.

plane. In contrast, the twelve back-illuminated pn CCDs with a pixel size of $4\farcs1$ are all fabricated out of the same wafer and are therefore in the same plane (Fig. 3.15, *left*). Since both cameras are also sensitive to UV, optical and infrared light three different aluminum coated optical blocking filters are used to reduce the background from those photons. All EPIC cameras can be operated in various modes, e.g. to reduce the frame time by sacrificing parts of the FoV.

Reflection gratings (RGS) are placed behind the two MOS telescopes and deflect 53% of the incoming flux towards a strip of nine back-illuminated CCD detectors offset from the focal plane. Those detectors record the position of the diffracted photons to determine high-resolution spectra. To separate the contributions from overlapping diffraction orders the energy as determined by the CCDs is also detected for each photon. Resolving powers of $\lambda/\Delta\lambda$=150-800 are reached in the energy range from 0.33 to 2.5 keV. RGS spectra require high photon statistics and are only available for the brightest sources, unlike the ones presented in this work.

3.4.5 The scientific instruments of Chandra

Chandra is equipped with two focal plane instruments which can be moved in and out of the FoV of the telescope. It is also possible to adjust their exact position within the focal plane for specific scientific demands. Furthermore, two transmission gratings, the High Energy (HETG) and the Low Energy Transmission Grating (LETG) can be moved in and out of the light-path to allow high-resolution spectral analyses. *Chandra's* first instrument is the Advanced CCD Imaging Spectrometer (ACIS, Garmire et al. 2003) which has a pixel size of $\sim 0\farcs5$. The ACIS detector is quite similar to the EPIC described in the previous section. It consists of four front-illuminated CCDs covering a FoV of $16' \times 16'$ (ACIS-I) designed for wide field imaging. Furthermore, a strip of six CCDs (ACIS-S) is available to record the diffracted light from the spectrometers. One of the ACIS-S chips (S6) is also often used in imaging mode ($8' \times 8'$ FoV) as it has the best energy resolution of all the ACIS chips and is particularly sensitive to soft X-rays as it is back-illuminated. Fig. 3.15 (*Right*) shows all ACIS chips on their mounting structure.

Chandra's second instrument is the High Resolution Camera (HRC). It consists of two CsI-coated microchannel plate arrangements with an angular resolution of $0\farcs4$ which provide the best resolved images of the X-ray sky, but feature only rather low energy resolution (30% at 1.0 keV). Similar to ACIS the HRC comes in two arrangements for imaging with a FoV of $31' \times 31'$ (HRC-I, 90×90 mm) and for spectroscopy (HRC-S, 100×20 mm).

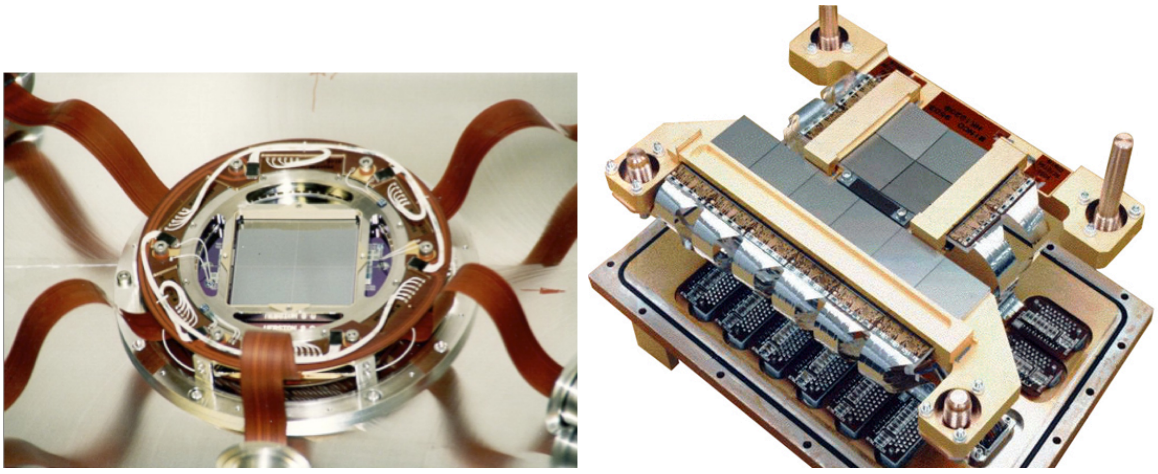

Figure 3.15: *Left:* The *XMM-Newton* EPIC-pn camera, consisting of twelve CCDs that are fabricated out of a single wafer. The camera covers an imaging area of 36 cm^2. *Right:* The *Chandra* ACIS camera on its mounting structure. Image credit: MPI-semiconductor laboratory, MPE, Astronomisches Institut Tübingen, Germany and ESA; CfA/SAO/NASA.

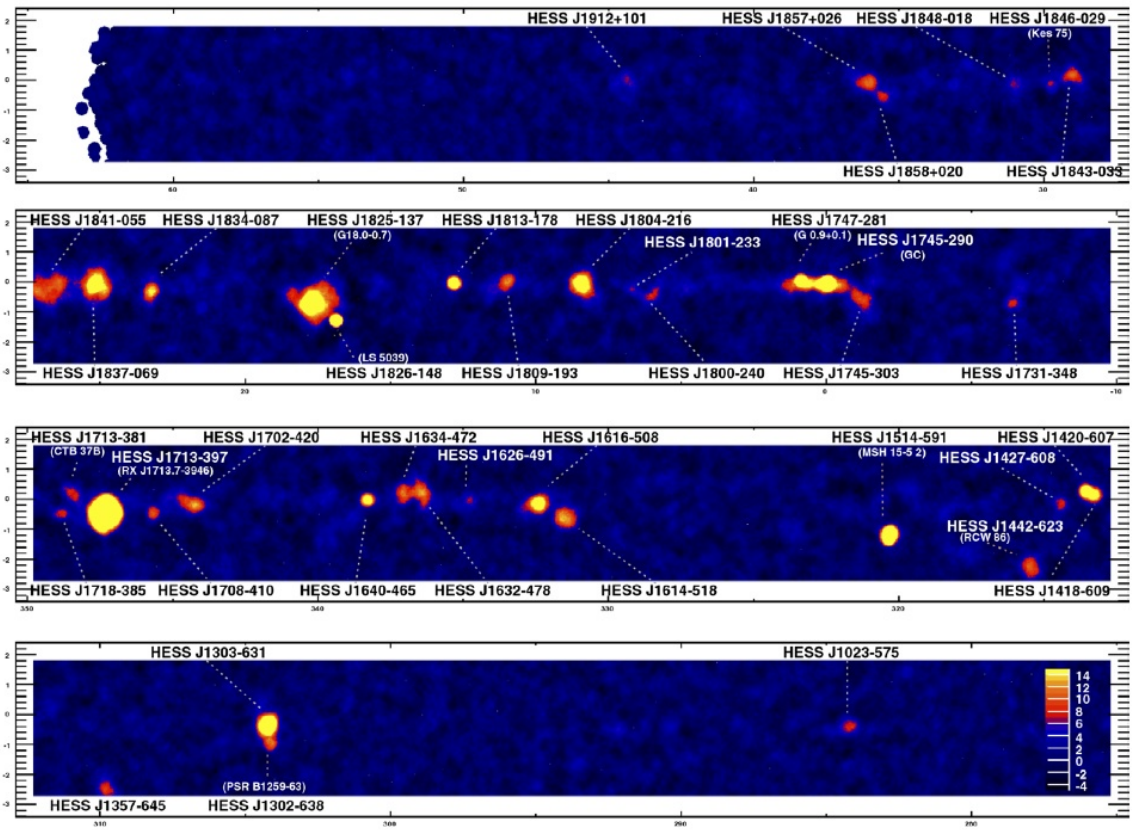

Figure 3.16: The H.E.S.S. survey of the inner galaxy in ∼1 TeV γ-rays. The color scale shows the statistical significance for an excess within 0.22° at each position. Image credit: H.E.S.S. collaboration.

3.5 The H.E.S.S. telescope array

3.5.1 Scientific background: The dawn of VHE γ-ray astronomy

Among high-energy astronomers the past ten to twenty years are often referred to as the "Golden Age of X-ray astronomy", as two powerful X-ray observatories were launched nearly simultaneously in 1999, and are in operation together with quite a number of other X-ray telescopes, such as SWIFT[7], RXTE[8], and Suzaku[9]. These telescopes are still performing exceptionally well, even though many of them long exceeded their estimated lifetimes. However, as no comparable X-ray missions are on the immediate horizon to replace these work horses, the "Golden Age of X-ray astronomy" seems to be nearing its end, at least for now.

But there is still hope on the high-energy frontier, as a new window to the energetic universe is opening up about 9 orders of magnitude shorter in wavelength. The era of

[7] http://www.nasa.gov/mission_ pages/swift/main/index.html
[8] http://heasarc.gsfc.nasa.gov/docs/xte/xte_ 1st.html
[9] http://www.nasa.gov/mission_ pages/astro-e2/main/index.html

VHE (E>100 GeV) γ-ray astronomy effectively started in 1989 as the first source, the Crab Nebula, was detected in this energy regime by the *Whipple* Imaging Atmospheric Cherenkov Telescope (IACT; Weekes et al. 1989). Since then the number of known VHE γ-ray sources as well as that of IACT observatories has grown rapidly. Currently the third generation of IACTs is in operation, namely H.E.S.S., MAGIC, VERITAS, and CANGAROO. The key advantage of ground-based γ-ray observation is the huge effective area which is a factor of $\sim 10^5$ larger than what is realistically attainable in direct detection techniques aboard satellites. Furthermore, IACTs are sensitive to energies between 100 GeV and 100 TeV, extending the HE regime (MeV to GeV) currently accessible with space-borne systems. IACTs also feature the best angular resolution ($\sim 0.1°$) among all high-energy telescopes beyond 0.1 MeV. In this section some recent results in VHE γ-ray astronomy are highlighted, focusing only on Galactic sources. The details of the imaging atmospheric Cherenkov technique are described in the next section (3.5.2).

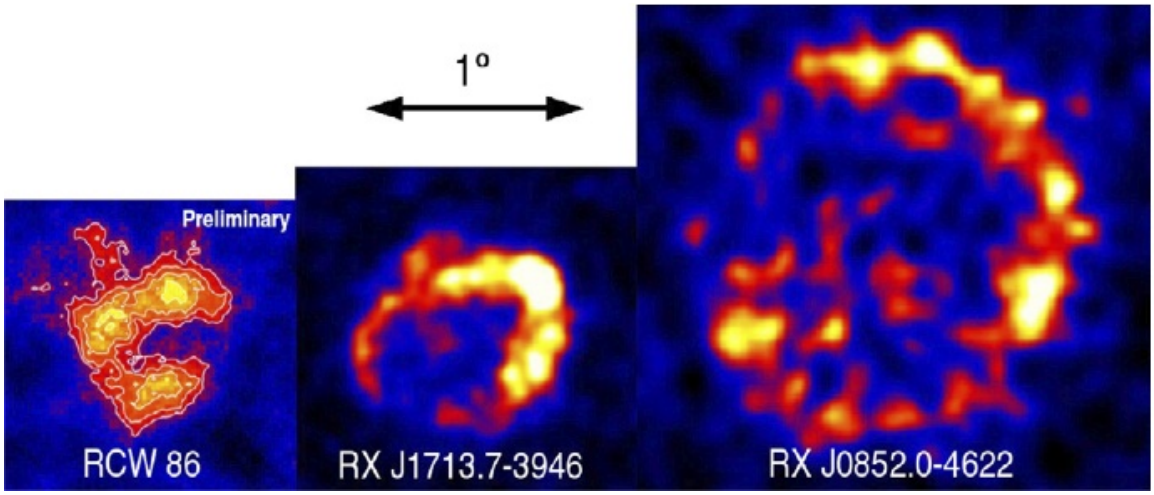

Figure 3.17: Shell-type SNRs as observed with H.E.S.S.: RCW 86, RX J1713−3946 and Vela Junior. Image credit: Hoppe et al. (2008); Aharonian et al. (2007b,c); Hinton (2009).

Shell-type SNRs and PWNe are the two most prominent classes of Galactic VHE γ-ray sources, followed by binary systems, SFRs (see Sect. 3.3.1) and most likely other source classes. The emission mechanisms that are believed to give rise to this extremely high-energy radiation are described in detail in chapter 2. What can IACTs contribute to the understanding of these objects? The number of known Galactic VHE γ-ray sources grew by one order of magnitude during the past few years, mainly due to the H.E.S.S. survey of the Galactic plane (see Fig. 3.16, Aharonian et al. 2005a, 2006b). The survey encompasses nearly the whole inner Galaxy: $-85° < l < 60°, -2.^\circ 5 < b < 2.^\circ 5$. Furthermore, also dedicated observations of promising source candidates were an important step to increase the number of firmly detected sources. Some shell-type SNRs

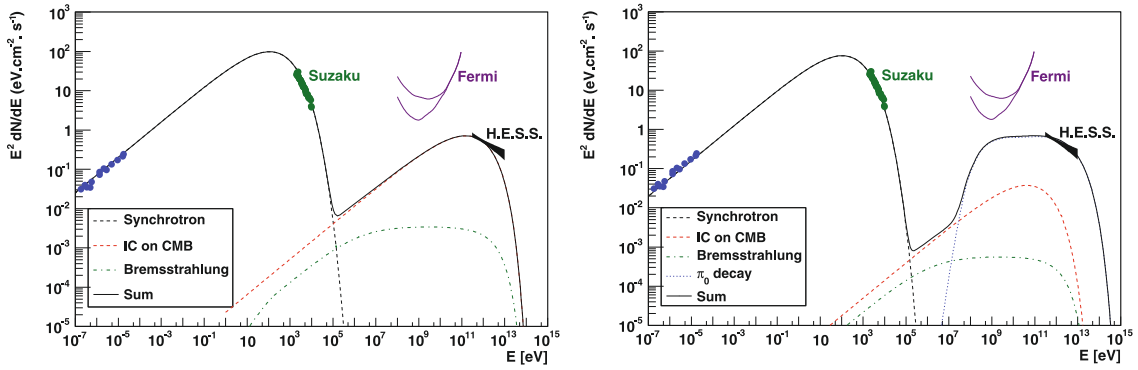

Figure 3.18: Broad-band differential energy spectrum of the SNR SN 1006, together with a leptonic (*left*) and hadronic (*right*) model. Image credit: Acero et al. (2010).

can be resolved as extended objects (see Fig. 3.17) with the high angular resolution of current IACTs. Now for the first time detailed morphological studies in the γ-ray regime are feasible that compare the emission regions over the whole electromagnetic spectrum to explore possible common physical scenarios. Particularly, to discriminate between leptonic and hadronic processes, cross correlations between VHE and X-ray (see Sect. 3.4.1) or molecular line observations (see Sect. 3.2.1) are a powerful tool. Apart from pure morphological analyses, the detailed extraction and modeling of broad-band spectra may also provide new insights into the emission mechanism. Often the cut-off of the high-energy peak lies within the VHE energy range, and a detailed estimation of the cut-off position gives direct evidence of the maximum energy of the relativistic particle population. This information is crucial as it might discriminate between leptonic or hadronic processes (see also Sect. 3.4.1). However, up to now the statistical uncertainties of current measurements in most cases do not allow to favor one over the other (see e.g. Fig. 3.18). Future large IACT arrays as well as advances in the theoretical understanding of these processes are needed to settle the issue.

The largest population of identified Galactic VHE γ-ray sources are PWNe (see also Sect. 2.4 and 3.4.1). A systematic search for VHE γ-ray sources detected in the H.E.S.S. survey coincident with high-spindown radio pulsars was recently conducted by the H.E.S.S. collaboration (Carrigan et al. 2008). Here a clear excess of VHE γ-ray emission from pulsars with $\dot{E}/d > 10^{35}$ erg s^{-1} kpc^{-1} was found, which significantly exceeded the chance coincidence probability. One of the most important results from recent studies of extended PWNe was the discovery of energy-dependent morphology in HESS J1825−137 (Aharonian et al. 2006c). It was found that the γ-ray nebula is more compact for higher energies, a fact that was previously only known from X-ray detections of these extended sources. This gives additional evidence for the presence of $\gtrsim$TeV electrons being efficiently cooled while propagating away from their acceleration site, i.e. the termination shock. Therefore, VHE γ-ray observations provide now an additional tool to probe these effects close to energetic pulsars and to determine parameters, such as the magnetic field.

Apart from these established VHE γ-ray source classes there might be other types of sources not easily identified with their counterparts. One such scenario are clusters of massive young stars. The colliding winds of massive stars are thought to give rise to strong shocks that could accelerate particles to multi-TeV energies (see e.g. Domingo-Santamaría and Torres 2006; Pittard and Dougherty 2006; Reimer and Reimer 2009). Particularly, the collective effects of many such systems in star clusters might be detectable with current γ-ray facilities. One recent example for such a scenario is the VHE γ-ray source HESS J1023−575 which is consistent in position with the cluster Westerlund 2, the second most massive young stellar cluster in the Galaxy (Aharonian et al. 2007a).

3.5.2 Observation technique: IACTs

The previous section provided an overview over the types of Galactic sources observable in VHE γ-rays and what such observations can contribute to the understanding of these sources. Now the technique of ground-based γ-ray detection with IACTs is described. First, cosmic ray induced air showers are discussed, followed by an introduction to the telescope technology.

3.5.3 Air showers and their emission of Cherenkov light

Earth's atmosphere is opaque to γ-rays. The dominant photon absorption process for energies far above twice the electrons rest mass is pair creation. Here the photon is absorbed, distributing its energy among the created electron-positron pair. These leptons produce a next generation of γ-ray photons via bremsstrahlung. Every new generation of photons interacts again via pair creation until they go below the energy threshold for this process. The typical distance scale over which an electron loses all but $1/e$ of its initial energy is called *radiation length* X_0 and strongly depends on the medium. X_0 is directly proportional to the mean free path for pair creation ($= {}^{9}\!/_{7} X_0$). This basically means that roughly each traversed radiation length the number of particles in the shower doubles, giving rise to an exponential growth (see Fig. 3.19). However, at a certain depth the average energy of the shower particles becomes low enough that ionization losses start to dominate over bremsstrahlung processes and the number of shower particles starts to decrease. This "maximum shower depth" $x_{\max}$ depends on the initial energy of the γ-ray photon as well as on atmospheric conditions and can be calculated as:

$$x_{max} = X_0 \, \log \left(E_\gamma / \epsilon_c \right), \tag{3.5}$$

with the primary energy E_γ of the photon and the critical energy ϵ_c at which ionization processes begin to dominate.

Air showers induced by cosmic rays, such as protons and heavier nuclei, are the main source of background for electromagnetic shower detection. Pions with large transverse

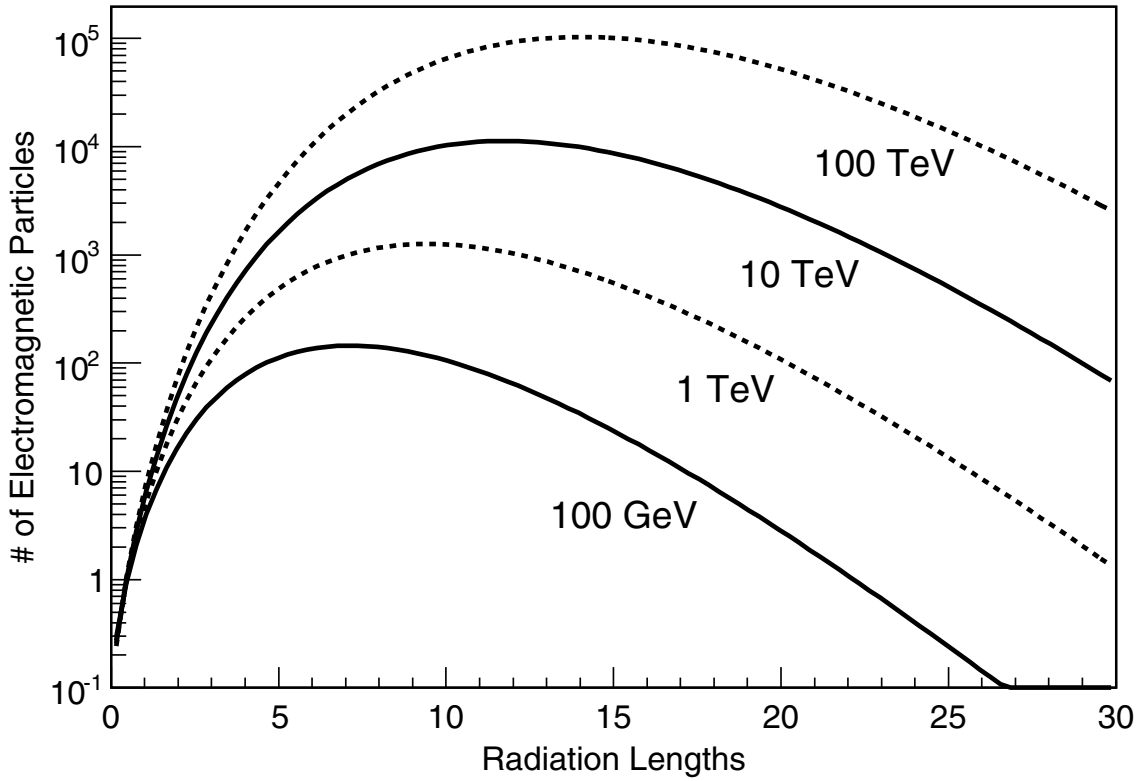

Figure 3.19: The longitudinal development of extensive γ-ray induced air showers, as calculated according to equation 3.5, given for several primary energies. Sea level is ∼28 radiation lengths, 2600 m above sea level is ∼20 radiation lengths. Image credit: Aharonian et al. (2008d).

momenta can be created in the interactions of cosmic rays with atmospheric nuclei. Neutral pions immediately decay into two γ-ray photons, giving rise to electromagnetic sub-showers, very similar to primary photon-induced showers, only different in the depth of first interaction. Charged pions on the other hand decay into muons and neutrinos. Despite their short lifetimes a large portion of the muons (∼20% at 1 GeV) survive the trip down to sea-level due to relativistic time dilation. In general, hadronic showers are much more extended than their electromagnetic counterparts. However, the exact shape of these showers strongly depends on the first few interactions, which are dominated by statistical processes. For example if a large part of the total cosmic ray energy is transferred to a π^0 decaying in turn into photons, hadronic and electromagnetic showers can look quite similar. This is also the case if only an electromagnetic sub-shower is observed by the instruments. A detailed review of our current understanding of air-showers can be found in Aharonian et al. (2008d).

Any of the secondary charged particles can emit Cherenkov light if its velocity exceeds the speed of light in the traversed medium, i.e. $v > c/n(z)$, with the altitude-dependent refraction index $n(z)$.

The angle of the Cherenkov cone is given by:

$$\theta_{\mathrm{c}(z)} = \cos^{-1}\left(\frac{1}{\beta n(z)}\right), \text{ with } \beta = \frac{v}{c}. \tag{3.6}$$

Each secondary electron in the shower emits Cherenkov light until a certain depth where the Cherenkov condition is no longer satisfied. Due to the altitude-dependent refraction index, the Cherenkov angle is smaller for larger altitudes: At a height of 8 km, $\theta_{\mathrm{c}} = 0.74°$, whereas at 10 km, $\theta_{\mathrm{c}} = 0.66°$. Therefore, the Cherenkov cone on the ground is blurry with a typical radius of $\sim$120 m, assuming an altitude of the initial interaction of 10 km. Secondary electrons in the shower suffer from multiple Coulomb scattering which leads to further broadening of the Cherenkov light cone observed at the ground. However, the deflection from the shower axis is exponentially suppressed ($\sim\exp^{-\theta/\theta_0}$, $\theta_0 = 0.83E_{\mathrm{min}}^{-0.67}$) and the Cherenkov cone maximum at a radius of $\sim$120 m is still quite pronounced. The number of Cherenkov photons emitted per particle per unit length is

$$n_{\mathrm{C}} \approx 800(n-1) \approx 0.1 \text{ photons cm}^{-1} \tag{3.7}$$

at sea level. Multiplying n_{C} by N_{max} and the path length of shower particles, one can calculate the total number of Cherenkov photons as $N_{\mathrm{C}} \approx 10^6$ for E_γ=1 TeV. N_{C} is proportional to E_γ and is therefore a good parameter to estimate the primary γ-ray energy. Cherenkov light is strongly peaked in the UV-blue wavelength regime. Therefore, mirrors and detectors can be adjusted to match the emission spectrum to suppress much of the optical background at different wavelengths. The shower development as well as its Cherenkov light is indicated in Fig. 3.20.

3.5.4 Cherenkov light detection and shower reconstruction

Now that we know the basic parameters of photon and cosmic ray induced air showers, the questions remain how to best detect them, how to reconstruct the showers and how to separate electromagnetic and hadronic showers. Basically, there is more than one approach, as one could either detect the secondary particles directly, as it is done by the cosmic ray arrays MILAGRO and AUGER for instance, or one can detect the Cherenkov light emitted by these particles. Here the latter method is described, as it is particularly suited for γ-ray astronomy.

Basically, for ground-based Cherenkov telescopes the atmosphere is used as a very deep calorimeter. Even though the particles deposit their whole energy in the atmosphere, current instruments are rather comparable to sampling calorimeters as only a small part of the total light-pool is covered by detectors. An IACT consists of a large reflective area with a wide FoV and short focal length and a high-speed camera of light sensitive detectors, such as photo-multiplier tubes. The large reflectors and short exposures ($\lesssim$30 ns) are needed to separate the faint flashes of Cherenkov light from

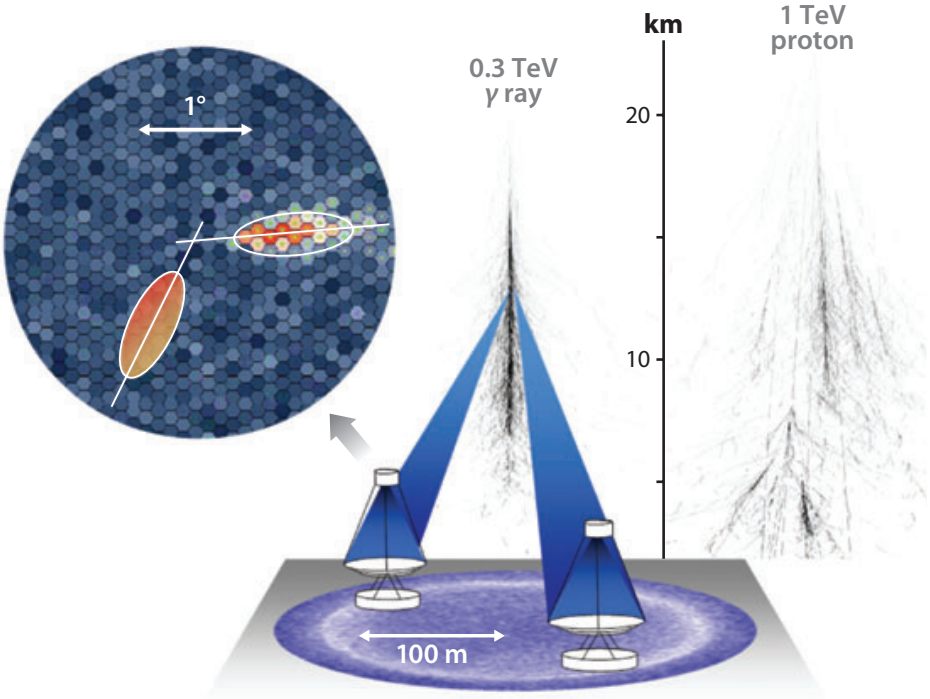

Figure 3.20: Schematic view of the stereoscopic technique when using two or more IACTs simultaneously. The shower images from two or more telescopes can be superimposed to derive the direction of the primary γ-ray. Additionally shown are typical profiles of an electromagnetic shower induced by a 300 GeV photon and a hadronic shower induced by a 1 TeV proton. Image credit: Hinton and Hofmann (2009).

Poisson fluctuations in the night-sky background. Cherenkov Telescopes should also be located at a remote site to avoid man-made background components, and observe only at moonless nights. Furthermore, IACTs are best located at an optimum altitude ($\sim$2000 m) to avoid the atmospheric absorption of the Cherenkov light at low altitudes and to still be able to observe the shower maximum as it would not be possible at very high altitudes. To resolve the typical scale of air shower features, IACTs should at least provide an angular resolution of $\sim$0.1°.

The elliptical air shower images recorded by IACTs depend on various parameters of the primary interacting particle, such as the nature of the particle: γ vs. hadron, the primary energy, or the impact parameter, as well as atmospheric conditions (see Fig. 3.21). Furthermore, another very important parameter is the angle between the zenith and the pointing direction of the telescopes ("zenith angle"). For larger zenith angles the distance the Cherenkov light has to travel in the atmosphere is larger, which gives rise to more pronounced scattering and absorption effects. Therefore, low-energy showers are harder to detect with increasing zenith angle, and the energy threshold of IACTs thus features a strong zenith angle dependence. As there are no TeV-class calibration sources for γ-rays available, neither on Earth nor in orbit, one has to rely on the theoretical understanding of atmospheric shower developments and on monte-

carlo simulations to interpret the recorded data. The three most important shower image parameters are the *width*, the *length* and the angle *alpha*. The *width* refers to the semi-minor axis of the image and gives information about the lateral shower development. The *length* refers to the semi-major axis of the image and is a measure of the longitudinal shower development. It provides information on the parallax angle to the shower maximum and grows with increasing impact parameter. *alpha* is the angle between the major axis and the line between source position and image centroid. Showers originating close to the pointing position should therefore have a very small value of *alpha*.

When using more than one IACT simultaneously, not only the total collection area is increased, but also the accuracy of shower reconstruction itself, due to the stereoscopic view of the shower light. The location of the intersection of the major axes from all recorded images provides a good measure of the origin of the shower (as indicated in Fig. 3.20, left circular panel). Also, the separation power between electromagnetic and hadronic showers is improved in stereoscopic mode, because the same shower is observed from different angles providing a more accurate shower reconstruction. Furthermore, if one telescope observes a leptonic sub-shower of a larger hadronic shower, chances are that one of the other telescopes still detects other components of the shower. This can be used as a veto to suppress the cosmic ray contamination. The spacing between the telescopes needs to be large enough to provide good stereoscopic views of the showers, but small enough to fit multiple telescopes into one light-pool. Therefore, typical telescope spacings are in the range of 70 to 150 m. Current instruments provide an angular resolution of $3'$ to $6'$, depending on the zenith angle, and a cosmic ray rejection factor of $\sim 10^{-2}$. The absolute energy calibration can be challenging for IACTs. Often the Cherenkov light from local muons is used for this purpose, but the number of Cherenkov photons can vary for different atmospheric conditions and for different angles of the shower axis with respect to the geomagnetic field (Bernlohr 2000). This introduces uncertainties of 10% to 20% in the absolute energy response of these systems. Furthermore, the effective area for shower detection is radially symmetric within the FoV of IACTs and decreases with increasing distance between the shower origin and the camera center. This is due to the fact that the fraction of shower images that lie completely in the FoV is larger for sources closer to the on-axis position. For more detailed information on the IACT technique the reader is referred to the recent review of Hinton and Hofmann (2009).

3.5.5 The telescopes

The High Energy Stereoscopic System (H.E.S.S.) is an array of four identical IACTs located in the Khomas highlands of Namibia (*Lat.*$= -23°$, *Lon.*$= 16°$) at an altitude of $\sim$1800 m. The four 13 m (107 m^2) telescopes are arranged in a square layout with a side length of 120 m (see Fig. 3.22). With the Davies–Cotton optical design the telescopes provide a large FoV (5°) together with a reasonably good off-axis point spread function (PSF) of 0.16° at the edge of the FoV. The cameras consist of 960 photomultiplier tube

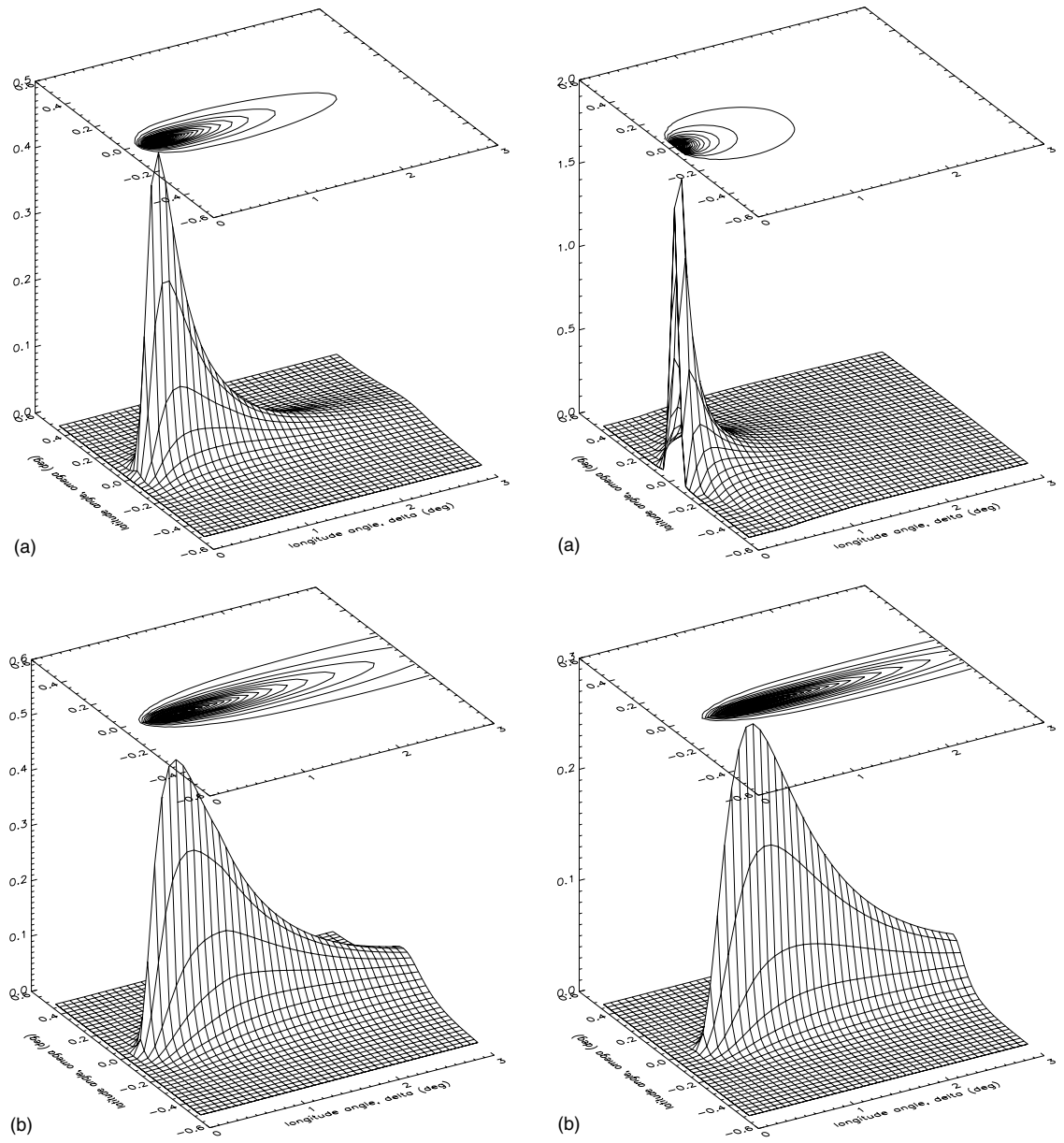

Figure 3.21: *Left:* Analytical calculation of the average angular distribution of a γ-ray shower observed at zenith with an impact parameter of 50 m and an energy of 100 GeV (a) and 10 TeV (b). *Right:* Angular distribution of a 1 TeV γ-ray shower observed at zenith, with an impact parameter of 10 m (a) and 100 m (b). Image credit: Aharonian et al. (2008d).

pixels with a pixel size comparable to the off-axis PSF. Even though the cameras are read out via 1 GHz analogue ring samplers, in normal mode only 16 ns integrated signals are stored to reduce dead time. H.E.S.S. uses an array trigger that requires at least *two* telescopes to meet the required criteria so that the event is accepted (Funk et al. 2004). To define the single telescope trigger criteria the cameras are divided into overlapping sectors containing 64 pixels each. A camera trigger occurs if the signals of a certain amount of pixels (2–4) within one sector exceed a given threshold of a

Figure 3.22: The H.E.S.S. IACT array in Khomas Highland, Namibia.
Image credit: Philippe Plailly/EURELIOS.

few photoelectrons. As discussed in the previous section, due to their inhomogeneous nature hadronic showers distribute their Cherenkov light over a larger area than γ-ray induced showers of the same energy. Therefore, cosmic ray induced showers are less likely to trigger two telescopes at the same time, and thus the array trigger can be used to suppress this background component significantly.

The H.E.S.S. array's energy threshold is about 100 GeV with a limiting point-source sensitivity of 0.7% of the flux of the Crab nebula (5σ at zenith, for a 25 h exposure). Its angular resolution is $\lesssim 0.1^\circ$ and improves with increasing energy due the more accurate reconstruction of larger and brighter showers. In addition to the four existing telescopes, a parabolic 26-m telescope (HESS II) at the array center is under construction to boost the performance of the system at lower energies (Vincent 2005). A description of the H.E.S.S. telescope array and references for each of the sub-systems are given by Hinton (2004).

4 Exploring the nature of the unidentified γ-ray source HESS J1626−490

4.1 Introduction

During scans of the Galactic plane with the H.E.S.S. IACT array a number of new Galactic VHE γ-ray sources were detected (Aharonian et al. 2005a, 2006b). Many of these sources could be identified as PWNe, shell-type SNRs, γ-ray binaries, or MCs. However, there are still a few TeV sources that could not be unambiguously associated with any source detected in lower energy bands (see, e.g., Aharonian et al. 2008a). In recent efforts to investigate these 'dark' VHE emitters, multi-wavelength observations were conducted to probe the environment of these particle accelerators (for recent work, see, e.g., Aharonian et al. 2008b,c).

HESS J1626−490 is another VHE γ-ray source of unknown origin, which so far could not be identified with a source at lower wavelengths (Fig. 4.1, *left*). This object, with an intrinsic extent of $\sim 5'$ (Gaussian FWHM), is located right on the Galactic plane (R.A.: $16^{\rm h}26^{\rm m}04^{\rm s}$, Dec.: -49°05′13″) and was detected by H.E.S.S. with a peak significance of 6.0σ (Aharonian et al. 2008a). Owing to the long tail extending towards the east, it is also stated that the source might be composed of two separate sources. In the energy range between 0.5 TeV and 40 TeV, these authors measured a power-law spectrum with a photon index of $2.2 \pm 0.1_{\rm stat} \pm 0.2_{\rm sys}$ and a flux normalization of $(4.9 \pm 0.9) \times 10^{-12} {\rm cm}^{-2}\,{\rm s}^{-1}\,{\rm TeV}^{-1}$ at 1 TeV. A number of potential counterparts from other wavelengths were discussed by Aharonian et al. (2008a), such as the nearby faint extended ROSAT source 1RXS J162504−490918 (Voges et al. 1999), the shell-type SNR G335.2+00.1 (Whiteoak and Green 1996), and despite their large offsets, the X-ray binaries (XRBs) 4U 1624−490 and IGR 16283−4838 (see Fig. 4.1, *right*). Furthermore, the high-energy (HE) source 1FGL J1626.0−4917c from the one-year *Fermi* source catalog (1FGL, Abdo et al. 2010a) and the SNR G335.2+00.1 lie both in close proximity to HESS J1626−490. As all these potential counterparts do not match very well in size or in position with the VHE γ-ray signal, the source was classified as unidentified.

In this work, we analyzed the data of an archival *XMM-Newton* observation to search for an X-ray counterpart of HESS J1626−490 (Sect. 4.3). Therefore, we classified the detected X-ray point sources in the vicinity of HESS J1626−490 and searched for potential diffuse excess emissions above the expected Galactic background. We also present

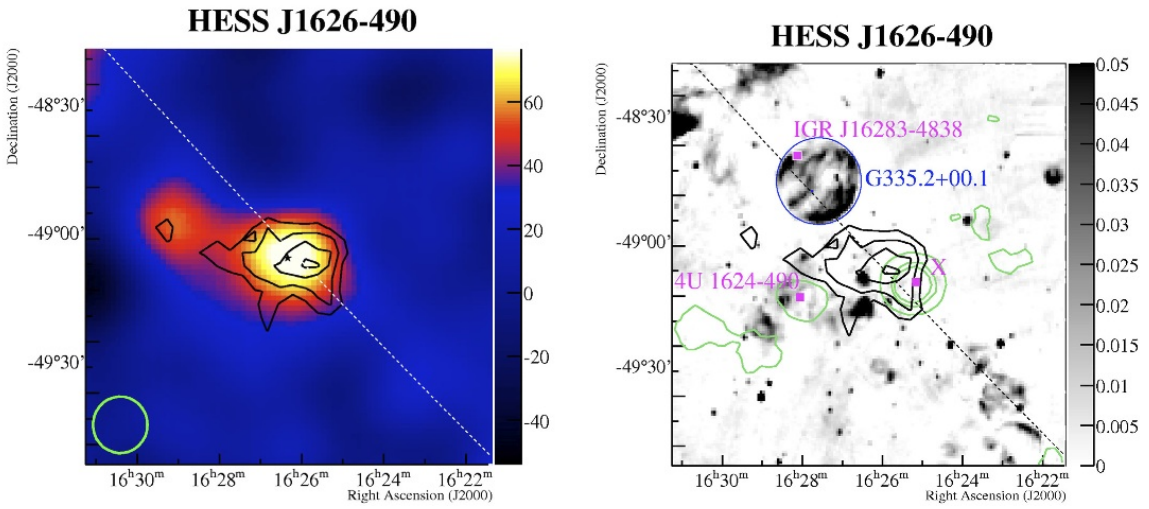

Figure 4.1: *Left:* VHE γ-ray image of HESS J1626−490, with a smoothing radius of 0.1°. The Galactic plane is indicated by the dashed line. The size of the H.E.S.S. PSF is indicated by a solid circle (green). *Right:* MOST radio continuum image (Bock et al. 1999) with overlaid H.E.S.S. significance contours (black) and contours of the faint ROSAT source 1RXS J162504−490918 (green). The two binary systems 4U 1624−490 and IGR 16283−4838 are indicated by squares (magenta). The shell-type SNR G335.2+00.1 is indicated by a circle (black). Image credit: Aharonian et al. (2008a).

^{12}CO ($J = 1 - 0$) molecular line survey data taken with the NANTEN mm/sub-mm observatory to scan for molecular clouds (Sect. 4.4), H I data from the SGPS survey, and infrared data from the *Spitzer* GLIMPSE and MIPSGAL surveys to search for indications of recent star-forming activity (Sect. 4.5). A large part of the work presented in this chapter is already published (Eger et al. 2011). In addition to the published results, a re-analysis of the H.E.S.S. VHE γ-ray data is presented (Sect. 4.2), based on a much larger dataset and a more sensitive analysis method than employed by Aharonian et al. (2008a). Furthermore, the γ-ray emission is compared to a detailed SNR–MC interaction model to test the validity of such a scenario (Sect. 4.7).

4.2 Updated analysis of the H.E.S.S. VHE γ-ray data

The VHE γ-ray source HESS J1626−490 is located directly in projection of the Galactic plane. It was detected in the H.E.S.S. Galactic plane scan with a statistical significance of 6.0 σ during a total exposure of 8 hours (Aharonian et al. 2008a). Due to the large FoV of H.E.S.S. (5°) the position of HESS J1626−490 was also covered by follow-up observations of nearby sources, after the initial detection. The currently available dataset of H.E.S.S. observations pointed within 2.5° of HESS J1626−490 comprises ∼20 hours of good quality data. H.E.S.S. observations are performed in "runs" with a duration of 28 minutes. Before a final source analysis, the runs are selected based on

various quality selection criteria, such as the number of active telescopes, the system trigger rate, atmospheric and weather conditions, and some more (see e.g. Aharonian et al. 2006d). The main reasons why certain runs are excluded from an analysis are:

- The number of active telescopes is too low. For standard analyses only runs are accepted where at least three of the four H.E.S.S. telescopes were participating in the observation. For lower telescope counts the gamma–hadron separation is less efficient and the positional uncertainties in the shower reconstruction are larger.
- The system trigger rate is variable or generally lower than expected. A variable trigger rate indicates that clouds were moving through the FoV during the observation. This leads to strong systematic effects on the shower reconstruction, and such runs are generally excluded. Dust and aerosols in the atmosphere absorb and scatter the Cherenkov light, which leads to systematic errors in the reconstructed energies and fluxes, if not correctly accounted for in the analysis algorithm. Generally, such hazy atmospheres increase the energy threshold of Cherenkov telescopes, which is reflected in a lower trigger rate compared to observations under perfect conditions. Such runs can also be identified and removed from the dataset.
- Parts of the hardware or the readout electronics are broken or not working within normal parameters. Examples for such cases are broken pixels/photomultipliers, problems with the tracking system or power cuts. Runs that are too much affected by such issues can be removed, e.g. by setting a threshold on the maximum number of inactive pixels, or by including information from hardware controller log files in the run selection.

The quoted 20 hours of good quality data for HESS J1626−490 are based on standard run selection criteria employed for H.E.S.S. sources, where no specific scientific demands require more stringent restrictions.

In this work, in addition to a more than twice larger dataset, also an improved analysis method was used with respect to the original detection by Aharonian et al. (2008a). The standard analysis technique, originally used for H.E.S.S. data, is based on second moments of the shower images, which was already applied in the analysis of Crab data recorded by the Whipple IACT (Hillas et al. 1998). Here only a few parameters of the elliptical shower images, such as the length, the width and the angle with respect to the camera center, were used to perform gamma–hadron separation and to derive the energy and direction of the event (*Hillas* analysis). However, for this algorithm to be efficient, an image cleaning has to be performed beforehand. In contrast, one of the more sophisticated methods (*model* analysis), which is quite frequently employed in current analyses, makes use of the full information contained in the images, without previous cleaning. Here the characteristics of air showers are calculated for various energies, directions, impact parameters and zenith angles, based on a semi-analytical model. The expected camera images from these calculated showers are then compared to the actual recorded Cherenkov data, using a maximum likelihood technique. A detailed description of this method is beyond the scope of this work. The reader is

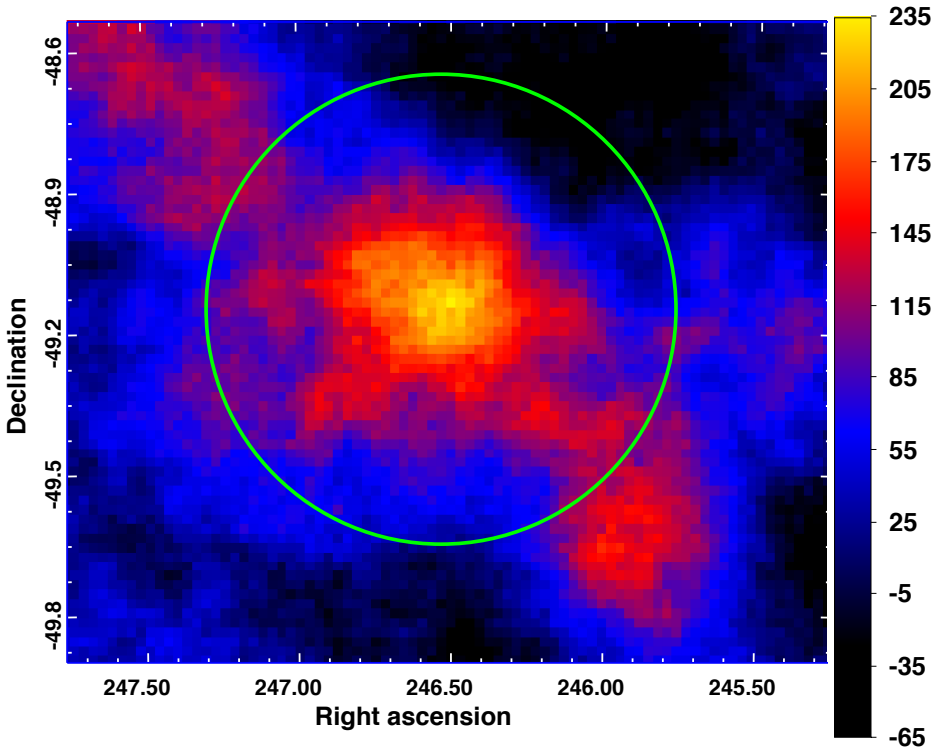

Figure 4.2: H.E.S.S. excess map of HESS J1626−490 above an energy threshold of 200 GeV. The circle (green) has a radius of 0.5° and indicates the region used for the extraction of the VHE spectrum.

referred to de Naurois and Rolland (2009), who describe the model development, as well as an application to the H.E.S.S. data. This method performs exceptionally well, as it increases the sensitivity of H.E.S.S. by almost a factor of 2 for some cases. Particularly for low-energy showers, where the image cleaning in the *Hillas* analysis could eliminate a large part of the information, the model method provides the best improvement.

The latter method was now applied to the analysis of the H.E.S.S. data of HESS J1626−490. Figure 4.2 shows the map of VHE γ-ray excess events above an energy threshold of 200 GeV. To derive the number of excess events at each position the *ring background* method was used (see Berge et al. 2007). Here the number of background events for each position is estimated in each run from events within a ring around the location. Known sources (e.g. just outside the north east of the image) are excluded from the rings (see Fig. 4.3, *left*). The radius of the ring is chosen to be larger than the instrument point spread function ($\sim 0.1°$), to avoid contamination from the source region. The number of counts in the ring is first normalized by the ratio of the areas of test and ring region and then subtracted from the counts within the test region. This method is particularly suited to create excess maps of extended areas, by just sliding the ring over the whole area. As in the analysis presented in the original detection paper, HESS J1626−490 appears to be extended. The intrinsic extent of the emission was determined by fitting an asymmetrical double Gaussian to the two-dimensional excess map. The core of the source seems to be very symmetric

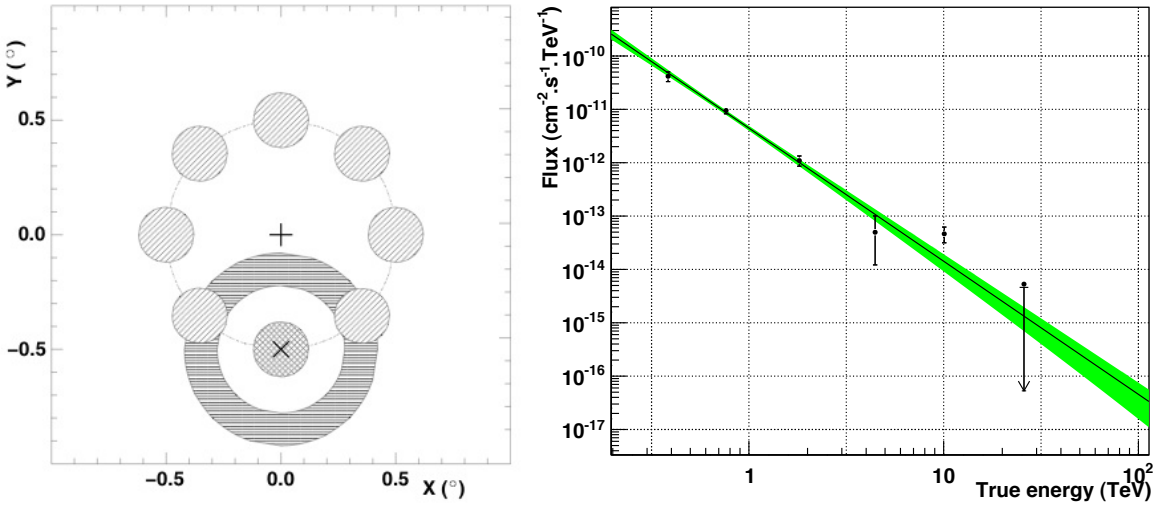

Figure 4.3: *Left:* Illustration of the ring and reflected background methods described in the text. The observation position is denoted by a cross, the test position by an X. The area of the ring background is filled by horizontal lines, the areas of the reflected background regions are filled by inclined lines. Image credit: Aharonian et al. (2006d). *Right:* VHE γ-ray spectrum of HESS J1626−490. The solid line (black) denotes the best fit of a powerlaw model. The colored area (green) shows the 1 σ confidence region.

with an intrinsic extent of $0.1' \pm 0.05'$ on both axes. This is in agreement with the first analysis, where a slightly asymmetric profile was measured: $0.07' \pm 0.02' \times 0.1' \pm 0.05'$. However, the marginally significant tail towards the east (see Fig. 4.1, *left*) is no longer seen in the new image. Furthermore, there is now an apparent extent of enhanced emission from the core towards the south west.

To derive a spectrum of VHE γ-ray emission from HESS J1626−490, the counts within 0.5° from the core were extracted (as indicated in Fig. 4.2). This radius is the same as used by Aharonian et al. (2008a) for the original analysis, and it does not include most of the tail towards the south, as its connection to HESS J1626−490 is not clear. Since the effective area strongly varies within the H.E.S.S. FoV, the ring background method is not very well suited for spectral analyses, as it compares regions with different γ-ray acceptances. As commonly used for H.E.S.S. VHE sources, we relied on the *reflected background* method for spectral extraction (see again Berge et al. 2007). Here only regions with the same distance to the camera center as the source region are used to estimate the background. Because the acceptance for γ-rays is radially symmetric, only regions with the same effective area are compared. This is achieved by rotating the source region around the camera center and fitting as many background regions as possible in the available area (see Fig. 4.3, *left*). Again, known VHE γ-ray emitters are excluded from the background regions. To fit the data a forward folding technique was used, where the model (as a function of true energy) is first convolved with the energy response and then fit to the measured data, as a function of reconstructed energy. A simple powerlaw model ($N_0 \cdot E^{-\Gamma}$) provided a very good fit (χ^2/n.d.f. = 50/50).

Figure 4.3 (*right*) shows the best fit model as a function of true energy together with the 1 σ confidence interval. The derived spectral parameters are consistent within 1 σ errors with the original measurement (see Tab. 4.1).

Table 4.1: VHE Spectral fitting results of HESS J1626−490

	exposure (hrs)	Sign. (σ)	excess (counts)	Γ	$N_0 \cdot 10^{-12}$ ($\mathrm{cm^{-2}s^{-1}TeV^{-1}}$)	E_{min} (TeV)	E_{max} (TeV)
published*	8.0	6.0	167	2.18±0.12	4.9±0.9	0.6	50
this work	19.6	10.2	679	2.30±0.13	4.4±0.5	0.2	113

*Aharonian et al. (2008a)

4.3 XMM-Newton observation

The position of HESS J1626−490 was observed by *XMM-Newton* with all three EPIC instruments in February 2007, for a total duration of 22 ks (Observation ID: 0403280201). For this work we downloaded the dataset from the public archive[1]. We analyzed the data with the *XMM-Newton* Science Analysis System (SAS) version 9.0.0 (Gabriel et al. 2006), supported by tools from the FTOOLS package (Blackburn et al. 1993) and XSPEC version 12.5.0 (Arnaud 1996) for spectral modeling. For all spectra and images presented in the following sections, we selected good (FLAG==0) single and multiple events: PATTERN≤4 (pn), PATTERN≤12 (MOS). For image processing, we used some tools from the CIAO 4.0 software package (Fruscione et al. 2006).

In this section we first discuss the EPIC background components (Sect. 4.3.1), since an accurate understanding of the background is essential for the spectral analysis of very extended sources. Detected X-ray point sources (4.3.2) as well as diffuse X-ray emission (4.3.3) in the vicinity of HESS J1626−490 are then discussed. After a detailed analysis of the diffuse X-ray signal we derived an upper limit for potential extended emission connected to HESS J1626−490 (Sect. 4.3.3.1). In section 4.3.3.2 we discuss a possible contamination of the diffuse signal due to an X-ray dust scattering halo from a binary system just outside the *XMM-Newton* FoV.

4.3.1 Background components

The data recorded by *XMM-Newton* contain background components from a variety of different sources. Before proceeding to the actual analysis, first these background

[1]http://xsa.esac.esa.int:8080/aio/jsp/createPostcards.jsp?obsno=0403280201

contributions and strategies to deal with them are discussed in this section. For point-like sources or extraction regions which are small compared to the total FoV, one usually defines a nearby off-source region to estimate the background contribution in the on-source area. However, as some of the background components vary over the FoV, this approach can lead to significant systematic errors when the source extraction region is very large. In such cases other strategies have to be employed to deal with the background (see below and Sect. 4.3.3). The background can be divided into three separate groups:

- *Electronic noise:* This comes from broken or "hot" CCD pixels and columns, readout noise etc. Pixels and/or whole sections of the CCD chip that show unusually high activity can be identified and removed from the data. This is basically taken care of in the standard processing chain, where a list of bad detector regions is generated.

- *Particle-induced background:* Charged particles directly from the solar wind or trapped in the Earth's radiation belt passing through the detector induce charge signals in the CCD pixels along their track. These can be removed by identifying readout frames containing long, continuous tracks of bright pixels. Furthermore, charged particles that interact with the material surrounding the cameras lead to characteristic X-ray emission, which is subsequently registered by the X-ray sensitive detector. Here the whole detector is affected more or less homogeneously. This background component is highly variable, and many observations feature quiet periods as well as time intervals of strong flaring activity. Therefore, the contamination of the observation can be reduced by restricting the dataset to "good time intervals" (GTIs) where the background activity is low. To identify GTIs one can use the the light-curve at high photon energies (7–15 keV). At these energies the flux from photons originating from astrophysical sources detected in the focal plane is very low, due to the very small effective area of the X-ray mirrors. Thus, the photon flux measured by the camera is dominated by particle-induced X-rays.

  The particle-induced background can also be measured with observations where the filter wheel in front of the camera is in its closed position, blocking the light-path from the telescopes. Such datasets (as provided by Carter and Read 2007) can be used to subtract the remaining particle induced background from already GTI-screened datasets. To account for any systematic differences between source and background observation one can compare the count rates at high energies and re-normalize the background observation to match the source data. For GTI-screened datasets, typical re-normalization factors are in the order of $\sim$10%.

- *Astrophysical background:* The previous two background components are also often referred to as non-X-ray background (NXB), as they do not arise from primary X-ray photons. The third background component arises from unresolved or diffuse astrophysical sources. These could be a population of faint background sources (e.g. AGN) or, particularly in regions close to the Galactic plane, diffuse X-ray emission from hot gas. In contrast to all other background components,

this is the only one that is subject to mirror vignetting (see Sect. 3.4.2), as the photons reach the camera via the telescope. The astrophysical background strongly depends on the observed position and is best estimated from in-field background regions from the same observation. Otherwise, there is also the possibility to request "custom-tailored" blank-sky datasets from the *XMM-Newton* background working group[2]. Here background datasets composed of actual observational data are combined, to match some parameters of the source observation, e.g. the Galactic column density towards the pointing direction. However, there are still possibilities for systematic differences between the background of the observation and the blank-sky dataset, which could be difficult to measure. For instance, even if the total column-density matches between both datasets, the gas temperatures could be different. This would introduce artificial hardening or softening of the extracted spectra.

The *XMM-Newton* observation of HESS J1626−490 was affected by long intervals of strong background flaring. To clean the data we applied a background GTI screening based on the full field-of-view (FoV) 7–15 keV light curve provided by the standard processing chain (see Fig. 4.4). We used thresholds of 8 cts/s for pn and 3 cts/s for MOS and the resulting net exposures are 4.9 ks for pn and 13.2 ks for MOS, respectively.

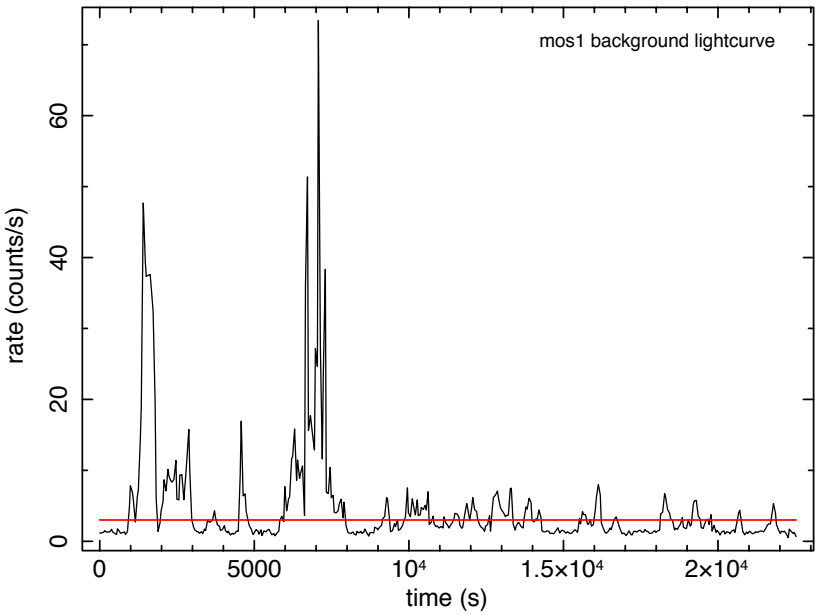

Figure 4.4: MOS1 background light curve in the energy range between 7 and 15 keV. The threshold at a rate of 3 counts/s used for the GTI screening is indicated by a horizontal line (red).

[2]see Carter and Read (2007); the web-form to request a custom-tailored blank-sky dataset can be found at: http://www.star.le.ac.uk/ jac48/BG/UserRequest/blankskyform.html

4.3.2 X-ray point sources

Even though Aharonian et al. (2008a) detected HESS J1626−490 with an intrinsic extent of ∼0.1°, we first characterized potential point-like X-ray counterparts. The SAS standard maximum likelihood technique for source detection was used in several energy bands: 0.2–0.5 keV, 0.5–1.0 keV, 1.0–2.0 keV, 2.0–4.5 keV, 4.5–10.0 keV, and 0.5–10.0 keV. The resulting point source list indicates a detection threshold of 2×10^{-14} erg cm^{-2} s^{-1}. Within (or close to) the 7σ contours of HESS J1626−490, we detected twelve X-ray point sources (see Fig.4.5). For five of these sources (1, 5, 7, 8, and 9) the photon statistics were sufficient to perform a spectral analysis. The remaining seven objects were classified according to their hardness ratio (HR), which we defined as the normalized difference between high-energy (Hi: 2.0–10.0 keV) and low-energy (Low: 0.2–2.0 keV) counts:

$$HR = \frac{Hi - Low}{Hi + Low}. \tag{4.1}$$

The number of counts in the respective energy bands is the sum over all EPIC instruments where the source is detected. A correction for differential vignetting was applied to the HRs. Similar to the Galactic plane X-ray source population studies conducted with *XMM-Newton* (Hands et al. 2004) and *Chandra* (Ebisawa et al. 2005), we classified sources as either soft ($HR < -0.5$), medium ($-0.5 < HR < 0.5$) or hard ($HR > 0.5$). To identify near-infrared (NIR) counterparts, we correlated the X-ray point source positions to the 2MASS all-sky catalog (Skrutskie et al. 2006). Especially for regions on the Galactic plane where the interstellar absorption is very strong, which is the case for HESS J1626−490 ($N_H \sim 2.22\times10^{22}$ cm^{-2}, Dickey and Lockman 1990), the NIR band is particularly suited for probing deep into the interstellar medium (ISM). We classified an X-ray source from this observation as NIR-identified when a 2MASS catalog entry is found within $2''$ of the source position resulting from the SAS source detection algorithm. We classified the detected point sources as either "soft Galactic" (e.g., X-ray active stars), "hard Galactic" (e.g., cataclysmic variables (CVs), X-ray binaries), or "hard extra-galactic" (e.g., background AGN), based on the X-ray spectral characteristics and the NIR counterpart. These classifications are meant to reflect general characteristics such as hard/soft or absorbed/unabsorbed, which helps to derive more accurate fluxes for sources where no spectral analysis was possible.

4.3.2.1 Soft Galactic sources

Owing to coronal activity and/or binary interaction, stars can exhibit strong thermal X-ray emission during a wide variety of evolutionary stages (for a compilation of the 100 brightest X-ray stars detected by ROSAT, see Makarov 2003). Therefore, such objects comprise the vast majority of soft Galactic sources. A typical physical model to describe their X-ray spectra is an absorbed multi-temperature thermal plasma (MEKAL in XSPEC) with temperatures in the range of $kT = 0.5$–2.0 keV. Due to the lack of high

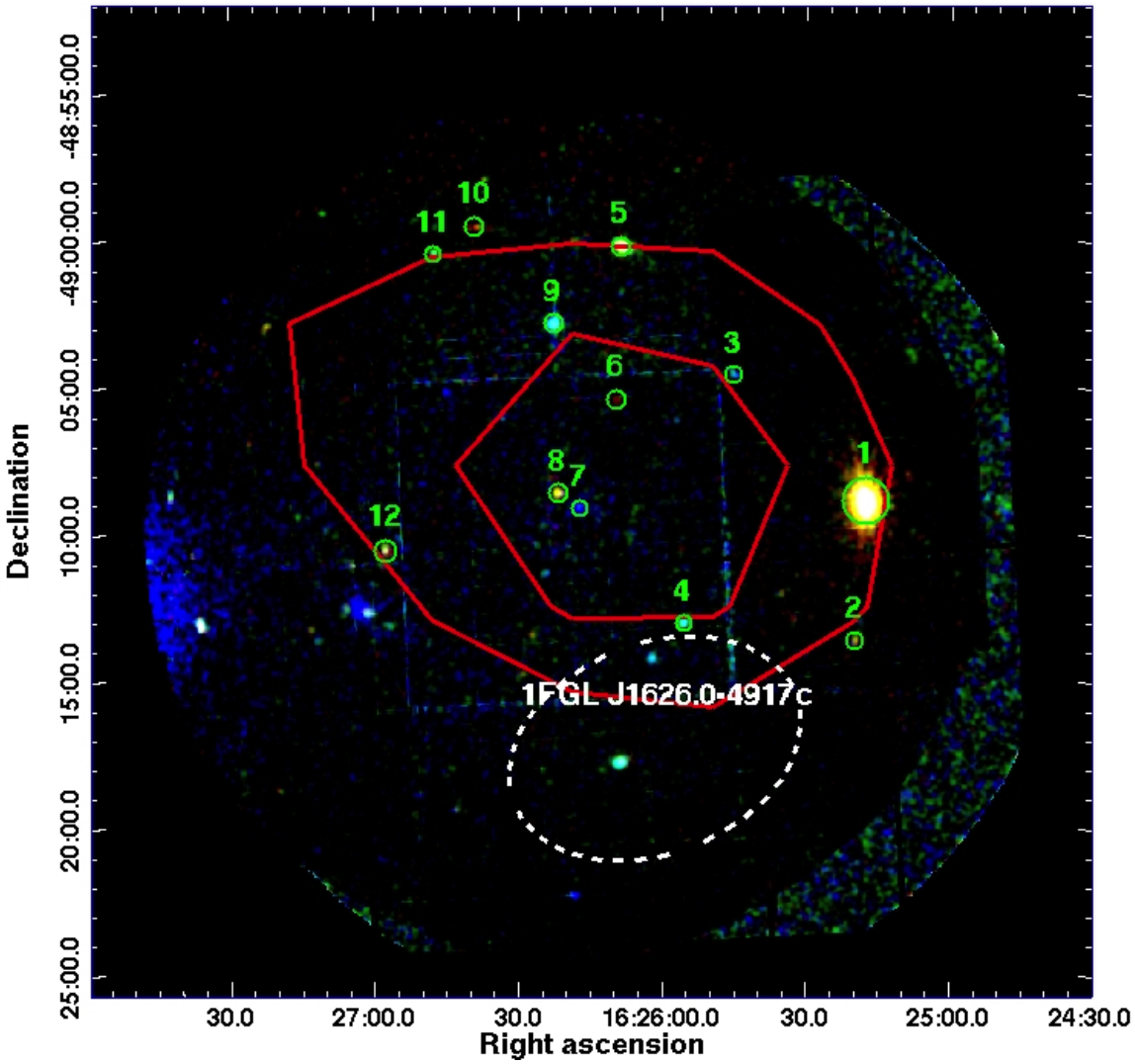

Figure 4.5: Combined color-coded image from the pn and MOS detectors. Energy intervals for the colors are 0.5-1.0 keV (red), 1.0-2.0 keV (green), and 2.0-4.5 keV (blue). The red contours denote the 8 and 7 σ statistical significance levels of the H.E.S.S. detection of HESS J1626−490. Marked are the point sources detected within the 7σ VHE contours (numbered 1 to 12 with increasing R.A.). The dashed ellipse (white) shows the 1σ confidence region of the positional uncertainty of the *Fermi* source 1FGL J1626.0−4917c.

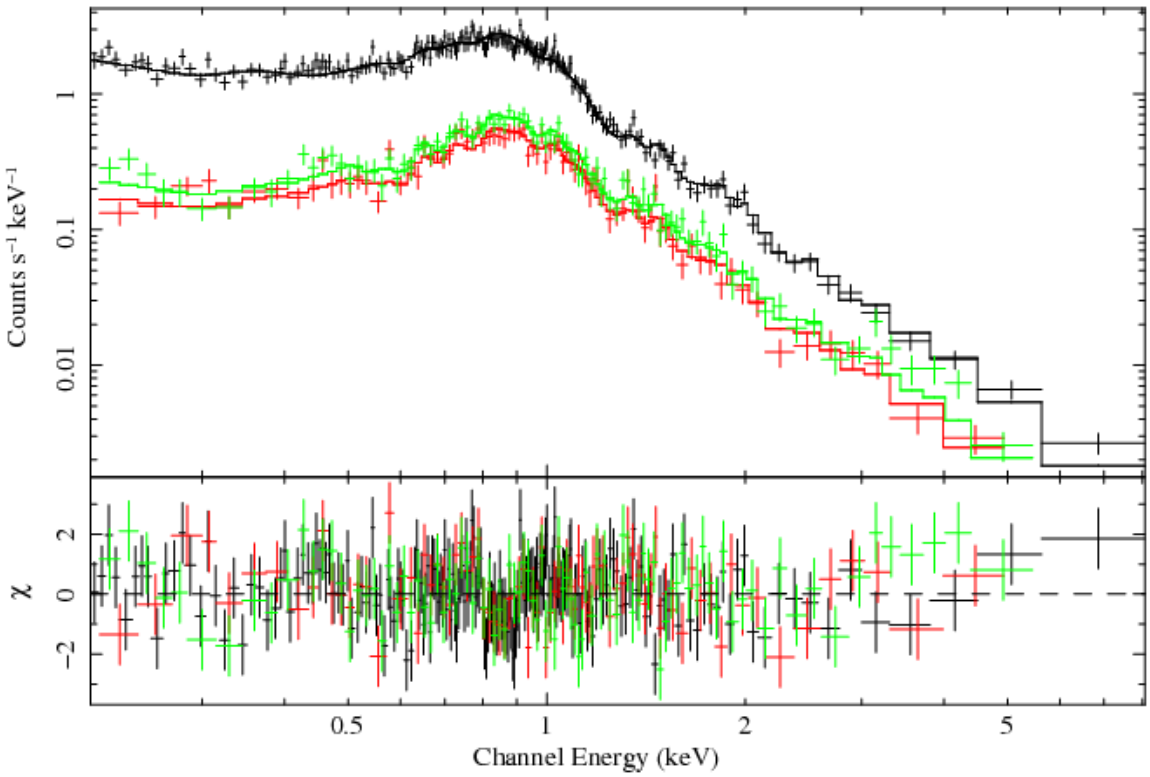

Figure 4.6: EPIC-pn and EPIC-MOS spectra of source No. 1 with a 3-temperature thermal plasma model (MEKAL, $\chi^2/\nu = 1.07$) fit.

interstellar absorption at these short distances and their intrinsically soft spectra, these objects would be classified as *soft*, according to the HR criterion, mentioned in the previous section. Furthermore, we required an NIR counterpart for an identification as a "soft Galactic" source. According to these criteria, eight of the twelve point sources were classified as "soft Galactic", and a spectral analysis could be performed on three of them. We calculated the flux for those sources with no spectrum from the 0.5–10.0 keV count rate assuming an unabsorbed power-law spectrum with photon index 3.0. The X-ray and infrared information for these objects is compiled in Table 4.2.

Source No. 1 is by far the brightest X-ray point source in the FoV (with an unabsorbed flux of $F_{X,unabs} = 8.0{\times}10^{-12}$ erg cm^{-2} s^{-1}) and is spatially coincident with the active triplet system HD 147633 = 1RXS J162517.7−490855 (Makarov 2003). This system contains a close binary of two G-type main sequence stars. The X-ray spectrum (Fig. 4.6) can be well-fit with a 3-temperature thermal plasma emission model (see Table 4.2). The three plasma temperatures resulting from the fit are compatible with temperatures seen, e.g., from the Castor X-ray triplet (Güdel et al. 2001). We therefore conclude that an identification of Source No. 1 with HD 147633 is very likely.

4.3.2.2 Hard Galactic and extra-galactic sources

In contrast to the X-ray emission seen from nearby active stars, the spectra of background AGN and Galactic CVs are intrinsically harder, and, in the case of AGN,

Table 4.2: Classification of X-ray point sources

Source No.	R.A.	Dec.	N_H (10^{21} cm^{-2})	$HR^{(1)}$	kT / $\Gamma^{(2)}$ (for kT: keV)	$F^{(3)}_{X,unabs}$	J$^{(4)}$ (mag)	2MASS name	class
1	16:25:17.5	-49:08:53	<0.08	−0.91	$kT_1 = 0.20^{+0.06}_{-0.02}$ $kT_2 = 0.63^{+0.02}_{-0.01}$ $kT_3 = 2.0^{+0.09}_{-0.09}$	79.5	6.117	J16251768-4908524	soft Galactic
2	16:25:19.6	-49:13:33	–	−0.80	–	0.39	13.458	J16251980-4913341	soft Galactic
3	16:25:45.0	-49:04:30	–	−0.05	–	3.5	–	–	med. extra-galactic
4	16:25:55.4	-49:12:56	–	−0.25	–	2.1	12.895	J16255550-4912576	hard Galactic
5	16:26:08.0	-49:00:09	<1.6	−0.72	$kT_1 = 0.46^{+0.59}_{-0.28}$ $kT_2 = 3.5^{+1.5}_{-1.4}$	3.1	7.884	J16260819-4900103 –	soft Galactic
6	16:26:09.2	-49:05:21	–	−0.82	–	0.044	12.42	J16260907-4905195	soft Galactic
7	16:26:17.2	-49:09:03	88^{+18}_{-4}	+0.92	$\Gamma = 0.41^{+0.9}_{-0.3}$	3.9	–	–	hard extra-galactic
8	16:26:21.6	-49:08:33	<0.9	−0.91	$kT = 0.84^{+0.3}_{-0.1}$	1.9	13.133	J16262176-4908333	soft Galactic
9	16:26:22.3	-49:02:48	6.5±5.0	−0.16	$\Gamma = 2.0 \pm 0.7$	1.4	11.304	J16262255-4902485	med. Galactic
10	16:26:38.1	-48:59:29	–	−0.98	–	0.091	13.47	J16263792-4859277	soft Galactic
11	16:26:47.2	-49:00:22	–	−0.39	–	2.1	12.726	J16264736-4900230	hard Galactic
12	16:26:57.4	-49:10:30	–	−0.73	–	0.35	11.704	J16265766-4910312	soft Galactic

(1)Hardness ratio as defined in the text. (2)Temperature(s) or photon index resulting from a MEKAL or power-law model fit to the spectra; depending on the statistical quality of the thermal spectra, the number of temperature components varies. (3)Unabsorbed flux in the 0.5–10.0 keV band in units of 10^{-13} erg cm^{-2} s^{-1}. The flux is derived from spectral fitting or, for fainter sources, by scaling an assumed spectrum with the count rate depending on the source class (see text). (4)J magnitude from the 2MASS catalog in cases where a counterpart was found within 2″ of the X-ray source.

heavily absorbed by the interstellar medium in the Galactic plane. According to the hardness-ratio classification scheme, these sources would be *medium* or *hard*. For two sources, not classified as "soft Galactic", an X-ray spectrum could be extracted (Nos. 7 and 9). Both feature hard power-law spectra. Source No. 7 shows a very high absorption column density ($N_H = 8.8{\times}10^{22}$ cm^{-2}), which is higher than the Galactic level in that direction ($N_H = 2.1{\times}10^{22}$ cm^{-2}, Dickey and Lockman 1990), so we classify this object as "hard extra-galactic". In contrast, the spectrum of the NIR identified source No. 9 is much less absorbed, indicating a location in the Galactic plane. We therefore classify this source as "hard Galactic". The rest of the *medium* or *hard* sources were classified as "Galactic" if an NIR counterpart is present, otherwise as "extra-galactic". We calculated the flux for sources with no spectrum from the 0.5–10.0 keV count rate assuming an absorbed power-law spectrum with a photon index of 2.0. For "extra-galactic" sources we assumed the total Galactic column density $N_H = 2.1{\times}10^{22}$ cm^{-2}, for "Galactic" sources the somewhat lower value $N_H = 5{\times}10^{21}$ cm^{-2}. The results for all point sources are shown in Table 4.2. We note here that in the rare case of hard Galactic sources with no NIR counterpart, such as PWNe, these objects would have been wrongly classified as "extra-galactic".

4.3.3 Properties of the diffuse X-ray emission

Aharonian et al. (2008a) approximated the morphology of HESS J1626−490 by fitting a 2-D Gaussian to the VHE excess map. The resulting intrinsic (with the effects of the instrument point-spread-function removed) major and minor axes were 0.1° and 0.07°, respectively, with a position angle of 3° west to north. An IC scenario would predict X-ray emission due to the synchrotron cooling of the same population of electrons. Likely candidates for such a scenario are PWNe. For these sources the X-ray nebula is more compact than the VHE source since the high magnetic fields close to the pulsar lead to strong synchrotron cooling. In contrast, the VHE nebula might be dominated by a more extended population of electrons with lower energies and longer cooling timescales. However, as we did not see any obvious extended X-ray counterpart to HESS J1626−490 with *XMM-Newton* (see below), we characterized the diffuse X-ray emission seen from a region comparable to the intrinsic VHE extent.

Before the extraction of events from diffuse regions, we first removed all detected point sources from the dataset. For that purpose we mostly relied on the results from the SAS maximum-likelihood source detection algorithm. Exceptions were very bright sources (e.g. source No. 1), sources at large off-axis angles (e.g. source No. 5), and the out-of-time event column from source No. 1, where we modified or added the respective regions manually. All exclusion regions are shown in Fig. 4.7.

To clean the background data from soft proton flares and to remove contributing observations with a higher general flux level, we applied the same GTI threshold as for the source data. However, due to the non-simultaneity of the source and background observations, the particle-induced background level could still be different. At energies above ∼12 keV the effective area of the X-ray telescope decreases significantly and the

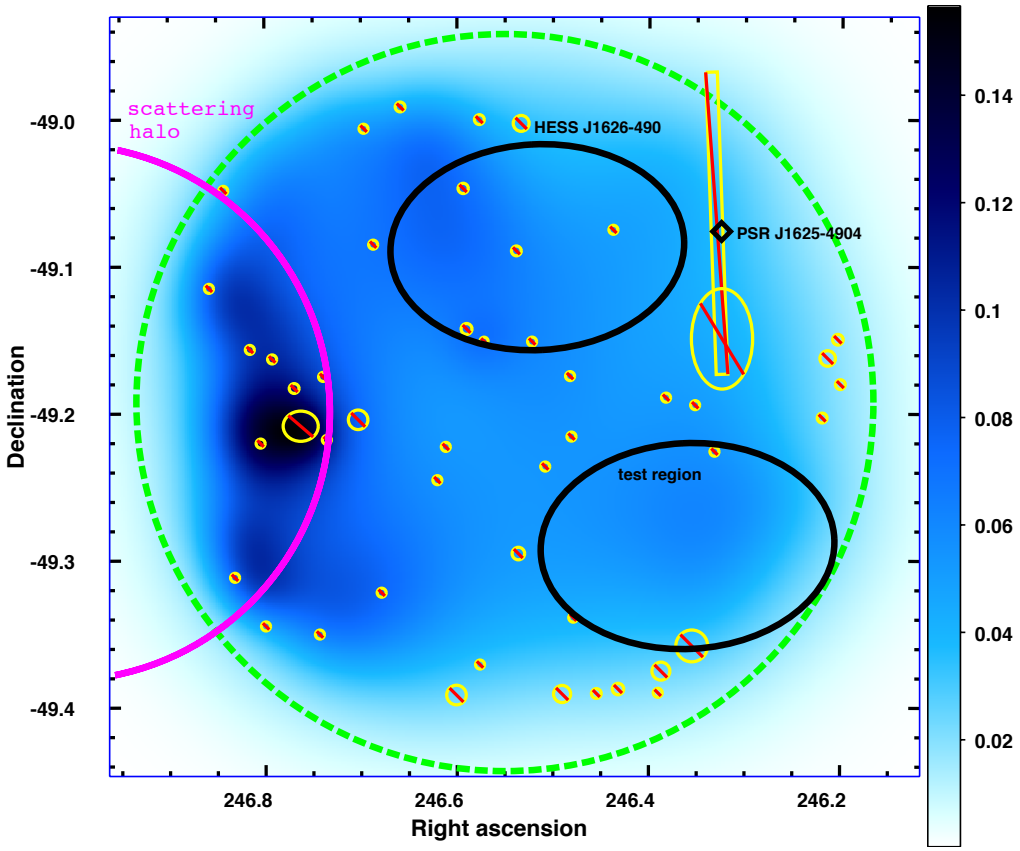

Figure 4.7: Adaptively smoothed EPIC-pn image of diffuse X-ray flux in the 3–7 keV energy band with a linear color scale (arbitrary units). The instrument FoV is shown as a dashed circle (green). The large ellipses (black) denote the extraction regions for HESS J1626−490 and the background test, respectively. The large circle (magenta) to the east gives the approximate extent of the X-ray scattering halo of 4U 1624−490. Excluded regions are shown as crossed-out areas (yellow regions crossed with red lines).

NXB becomes the dominant background component. Thus to improve the estimation of the NXB we derived a scaling factor based on the ratio of the count rate in the 12–15 keV energy bands between source and background observations (similar to De Luca and Molendi 2004).

To check for potential hard diffuse X-ray excess emission, as expected for a synchrotron radiation scenario, we extracted an image in the 3–7 keV energy band. We refilled excluded regions using *dmfilth* and applied the adaptive smoothing algorithm *csmooth* from the CIAO software package (Fig. 4.7). For the kernel size determination of the smoothing we required a minimum significance of 5σ. As background we subtracted the scaled NXB dataset as described in the previous paragraph.

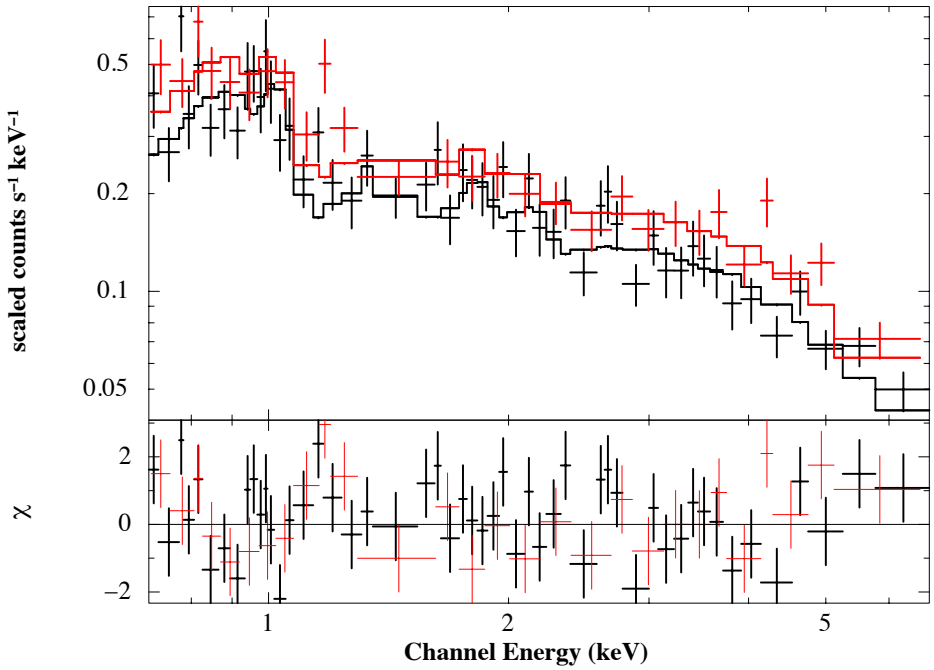

Figure 4.8: NXB-subtracted spectra from the elliptical region centered at HESS J1626−490 (black) and a region in the south of the FoV outside the 4 σ contours of HESS J1626−490 (red). The stepped lines show the best-fit of a 2-temperature NEI model.

4.3.3.1 Upper limit for extended X-ray emission from HESS J1626−490

The difficulties that arise when accurately measuring X-ray spectra from very extended regions can be summarized as follows. Due to the energy dependent mirror vignetting the effective area changes significantly within the extraction region. In principle one could use a *mean* effective area of the whole region. The easiest method would be to simply average over the effective areas of all pixels within the source region. However, this method introduces systematic errors, if the source flux varies within the region. To take this variation into account, one could calculate the mean effective area based on a weighted average, where the contribution from each pixel is weighted by its flux in a certain energy band. However, to determine the flux, one first would have to know the source spectrum, which in turn requires the knowledge of the effective area. As the effective area is not known at this point, this method can also just be an approximation. But it is still commonly used for extended source analyses, as it is very easily implemented with standard analysis tools.

However, for this work we adopted a more accurate method, which was first described for *XMM-Newton* by Arnaud et al. (2001). In this method each event is weighted as if it were measured at the on-axis position. To calculate the weighting factor, we used the vignetting information stored in the calibration database for the exact position and energy of each event. For instance, if a 1 keV event is registered at a distance of $\sim 8'$ from the on-axis position, the weight would be 2, as the attenuation due to

the vignetting at this distance and for this energy would be ∼0.5. Now, we can use the on-axis energy response (RMF) and ancillary response files (ARF) to calculate the correct energy spectrum.

Apart from the problems in extracting the source spectrum, the background subtraction is also a non-trivial issue for extended sources. Due to vignetting, the astrophysical background component significantly differs between the in-field background region and the extended source region. To account for this difference we employed the weighting method described in the previous paragraph for both source and background spectrum. Now if the in-field background is compared to the source spectrum, the astrophysical background component is treated properly. However, the NXB is *not* subject to vignetting, and the weighting method would lead to an over- or underestimation of this component. We dealt with this issue by using a filter-wheel closed dataset, provided by the EPIC background working group (Carter and Read 2007). For both background and source region we also extracted a spectrum from the NXB dataset from the exact same areas in the detector. We again employed the weighting method for the NXB spectra. Now if the respective weighted NXB spectra are first subtracted from the source as well as the in-field background spectra, the NXB component is properly removed, leaving only the (now comparable) astrophysical background and potential source excess emission in the net spectra.

Now that we have a powerful method to extract X-ray spectra from extended regions, we turn again towards the *XMM-Newton* data of HESS J1626−490. The image of diffuse X-ray emission (Fig. 4.7) shows no significant spatial variation, apart from the area at the eastern edge of the FoV, which is discussed in the next section. To derive an upper limit for the total X-ray flux possibly connected to HESS J1626−490 (yellow ellipse in Fig. 4.7) we extracted a spectrum from that area and compared it to a spectrum extracted from the southern part of the FoV outside the 4 σ contours of the VHE detection. For the spectral analysis we used the same exclusion regions as for the extraction of the diffuse image (see Sect. 4.3.3).

Since HESS J1626−490 is right on the Galactic plane, we assumed that the observed emission from both regions is of diffuse Galactic origin. Therefore, we adopted the two-temperature non-equilibrium ionization model (2-T NEI) from Ebisawa et al. (2005, henceforth E05). These authors observed a typical Galactic plane region (Dickey and Lockman 1990) with *Chandra* and analyzed the Galactic diffuse emission in great detail. We fixed most of the model parameters at the values from E05, except for the norm and column densities of both temperature components and the Si abundance of the hard component, which would have been significantly overestimated otherwise. We fitted both spectra in parallel with this model (Fig. 4.8), and we only allowed the normalizations to vary separately. The intrinsic surface fluxes were derived by dividing the unabsorbed fluxes by the effective extraction region, which is the region on the detector minus excluded areas, bad pixels/columns, and CCD gaps. For both regions the details of the fitting parameters are listed in Table 4.3.

The total surface fluxes for both regions agree within 1.5 σ. Here the flux measured from the test region is slightly larger. Therefore, we did not detect any significant X-ray

Table 4.3: Fit results for a 2-temperature NEI model

Parameter	HESS J1626−490	Southern test region
Soft Component		
kT (keV)	0.59 (frozen)	
$\log(n_\mathrm{e}\mathrm{t}/(\mathrm{cm}^{-3}\mathrm{s}))$	11.8 (frozen)	
Abundance (except Ne, Mg, Si)	0.044 (frozen)	
Ne abundance	0.30 (frozen)	
Mg abundance	0.14 (frozen)	
Si abundance	0.25 (frozen)	
$\mathrm{N_H}$ (10^{22} cm^{-2})	0.23±0.09	
Intrinsic surface flux$^{(*)}$ (10^{-7} erg cm^{-2} s^{-1} sr^{-1})	1.4±0.4	1.8±0.5
Hard Component		
kT (keV)	5.0 (frozen)	
$\log(n_\mathrm{e}\mathrm{t}/(\mathrm{cm}^{-3}\mathrm{s}))$	10.6 (frozen)	
Abundance (except Fe)	0.17 (frozen)	
Fe abundance	0.9 (frozen)	
$\mathrm{N_H}$ (10^{22} cm^{-2})	$3.17^{+0.31}_{-0.27}$	
Intrinsic surface flux$^{(*)}$ (10^{-6} erg cm^{-2} s^{-1} sr^{-1})	2.7±0.2	3.6±0.3
χ^2 / ν	102 / 74	

$^{(*)}$ In the 0.7–10.0 keV energy band

excess emission from the direction of HESS J1626−490 with respect to the test region. Assuming that a potential X-ray signal associated to HESS J1626−490 would originate in a region with the same extent as the VHE signal and that an excess flux greater than $4\,\sigma$ above the Galactic diffuse emission would be detectable, we derived an upper limit for the X-ray flux in the 1–10 keV band of $\mathrm{F_{X,excess}} < 4.85{\times}10^{-12}$ erg cm^{-2} s^{-1}. Given the observed background count rate from the ellipse and assuming an absorbed power-law spectral shape with index −2 and column density $1{\times}10^{22}$ cm^{-2}, the formal $4\,\sigma$ confidence level flux upper limit (1–10 keV) would be $\sim 1{\times}10^{-12}$ erg cm^{-2} s^{-1}, somewhat lower than the above value. However, we used the first value as we deem it more realistic for the actual source analysis techniques.

Figure 4.9 shows the VHE spectral energy distribution (SED) of HESS J1626−490, together with this upper limit, assuming a power-law spectrum with index −2 for the X-ray spectrum. In addition, the spectral uncertainty band of the *Fermi* source 1FGL J1626.0−4917c is shown (Abdo et al. 2010a).

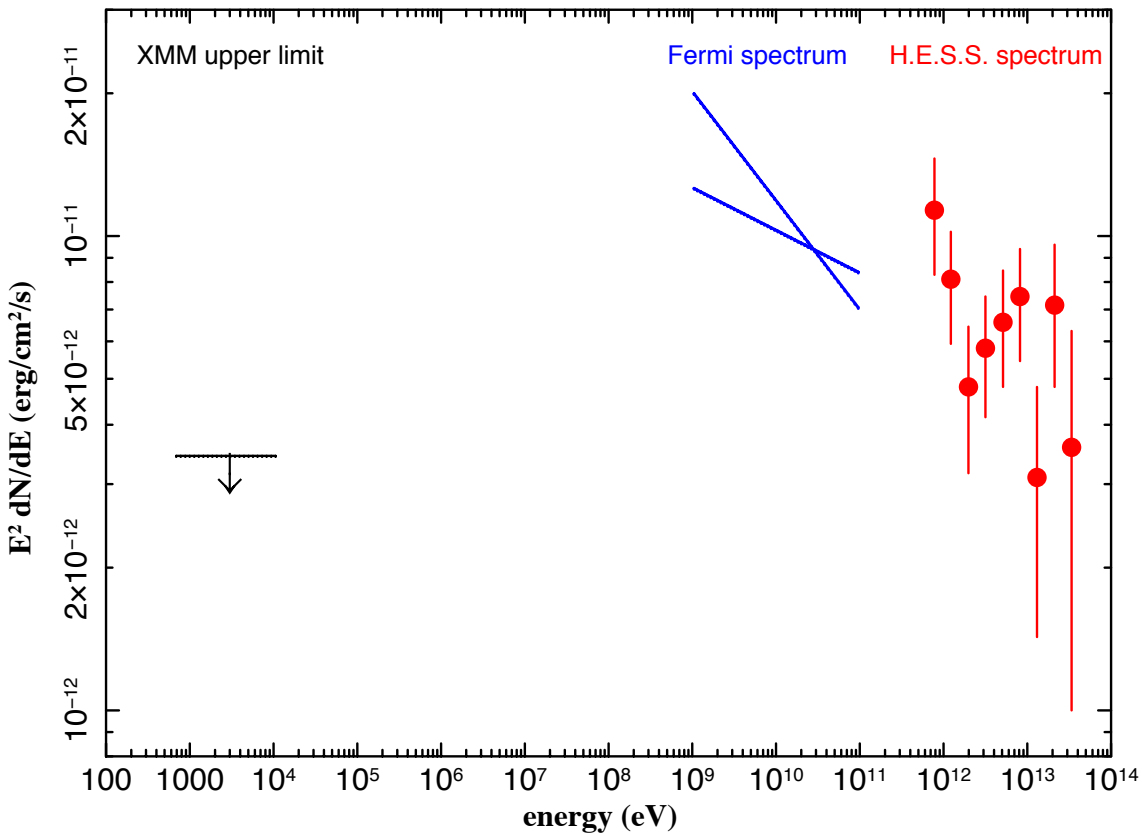

Figure 4.9: Spectral energy distribution of HESS J1626−490, showing the H.E.S.S. spectrum as data points with errors (red) (Aharonian et al. 2008a) together with the spectral uncertainty band of 1FGL J1626.0−4917c (Abdo et al. 2010a). The *XMM-Newton* upper limit from this work is denoted by a horizontal line with an arrow (black).

4.3.3.2 Contamination from the dust-scattering halo of the low-mass X-ray binary 4U 1624−490

As seen in the smoothed image of diffuse X-ray emission in Fig. 4.7, the flux level increases towards the eastern edge of the FoV. The dipping low-mass X-ray binary 4U 1624−490 is located $\sim$270″ outside the *XMM-Newton* FoV, exactly to the east. This source features an extended dust-scattering halo, which was detected with *BeppoSAX* (Bałucińska-Church et al. 2000) and *Chandra* (Xiang et al. 2007). According to these authors the halo shows a hard, highly absorbed spectrum (N_H = 8–9×10^{22} cm^{-2}) and should reach well inside the *XMM-Newton* FoV of this observation as denoted by the eastern yellow circular region in Fig. 4.7. An absorbed power-law fit to the spectrum extracted from the eastern region in the *XMM-Newton* observation gives a column density of $N_H = (8.0\pm2.5)\times10^{22}$ cm^{-2} and a photon index of $\Gamma = 2.3\pm0.7$. These results, together with the apparent circular shape of the excess, confirm the identification of this emission with the dust-scattering halo of 4U 1624−490. The effects of this contamination are very limited to the eastern edge of the FoV and should therefore not influence much the measurements of the diffuse emission from the direction of

HESS J1626−490 and the test region.

4.4 NANTEN ^{12}CO ($J = 1 - 0$) data

To search for molecular clouds, spatially and morphologically coincident with HESS J1626−490, we analyzed ^{12}CO ($J = 1-0$) molecular line observations performed by the 4 m NANTEN mm/sub-mm telescope. These data were taken as part of the NANTEN Galactic Plane Survey (1999 to 2003, Matsunaga et al. 2001, and references therein). The survey grid spacing was $4'$ for the region around HESS J1626−490. For this work the local standard of rest velocity (v_{LSR}) range −240 to +100 km s^{-1} was searched.

Figure 4.10 shows the NANTEN ^{12}CO ($J = 1-0$) image integrated over the v_{LSR} range −31 to −18 km s^{-1}. In this interval we found a ^{12}CO feature partially overlapping

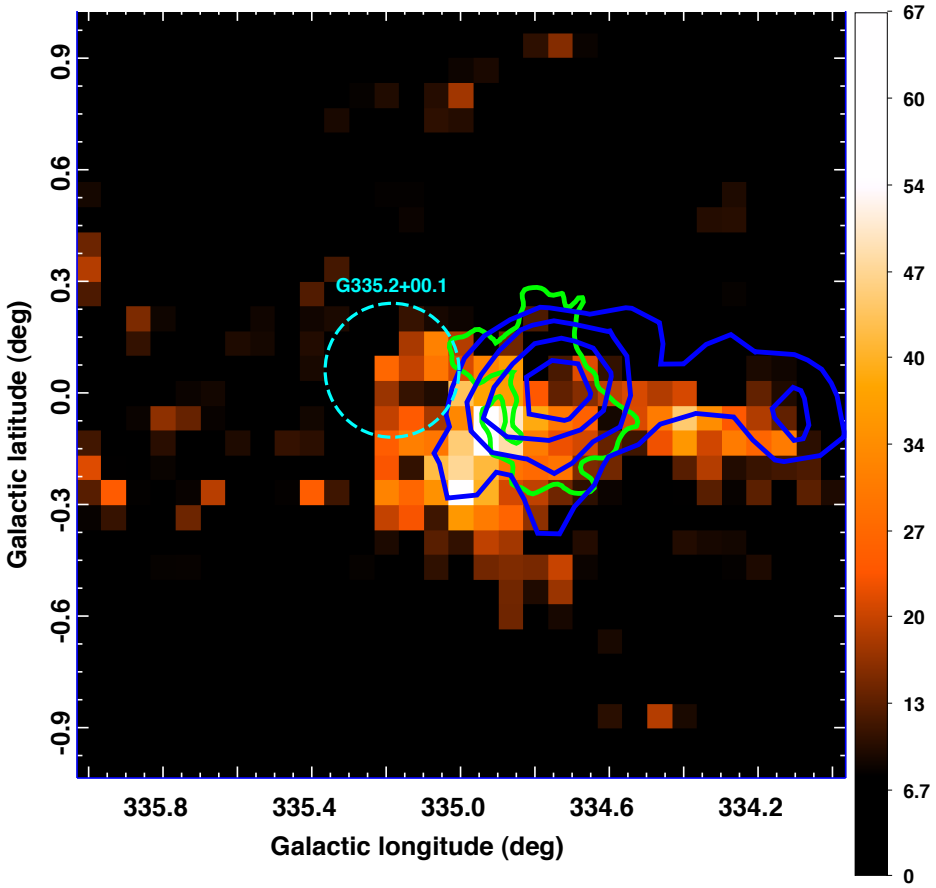

Figure 4.10: NANTEN ^{12}CO ($J = 1-0$) image of the region around HESS J1626−490 (linear scale in K km s^{-1}) integrated over the v_{LSR} range −31 to −18 km s^{-1}. Overlaid are the contours of the VHE emission (blue) and of the H I cloud discussed in Sect. 4.5 (green). The dashed circle (light blue) denotes the position and extent of the SNR G335.2+00.1.

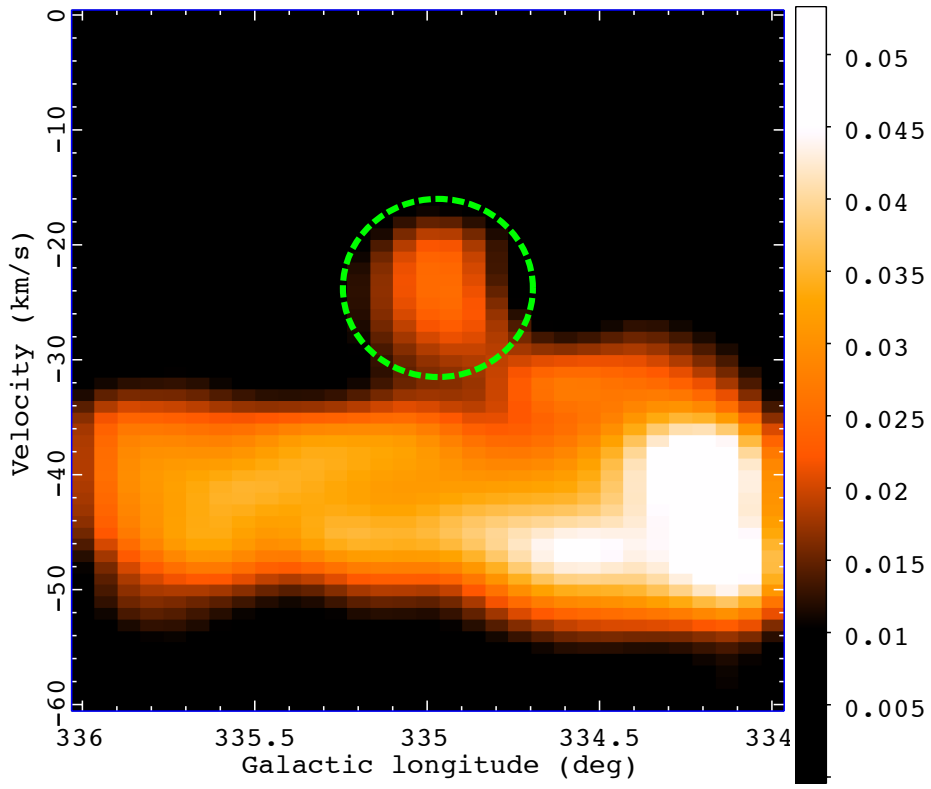

Figure 4.11: NANTEN ^{12}CO ($J = 1 - 0$) Galactic longitude–velocity plot (linear scale in K degrees) integrated over the Galactic latitude range $-0.33°$ to $0.14°$. The ^{12}CO cloud shown in Fig. 4.10 is marked by a dashed circle (green).

with the VHE emission. According to the Galactic rotational model of Brand and Blitz (1993), this v_{LSR} range corresponds to a kinematic distance of 2.2 to 1.5 kpc. As can be seen in the NANTEN position-velocity plot (Fig. 4.11), this CO cloud seems to be connected to a much larger system of clouds at velocities -32 to -50 km s^{-1}. The ^{12}CO emission at these more distant velocities is much more extended, and we did not find any apparent feature particularly matching the VHE morphology or coinciding with the SNR G335.2+00.1.

Using the relation from Strong et al. (2004):

$$\mathrm{N_H} = 1.5 \times 10^{20} \left(\frac{W(^{12}\mathrm{CO})}{\mathrm{K\,km\,s^{-1}}} \right) \tag{4.2}$$

between the hydrogen column density $\mathrm{N_H}$ and the ^{12}CO ($J = 1-0$) intensity W(^{12}CO), we estimated the total mass of this cloud at $1.8{\times}10^4 \mathrm{M}_\odot$ for $d = 1.8$ kpc within an elliptical region centered at $l = 334.78°$, $b = 0.00°$ with dimensions $0.26° \times 0.30°$. The corresponding average density is $2.1{\times}10^2$ cm^{-3}. Both these parameters are important for modeling the VHE γ-ray emission in an hadronic scenario (see Sect. 4.7).

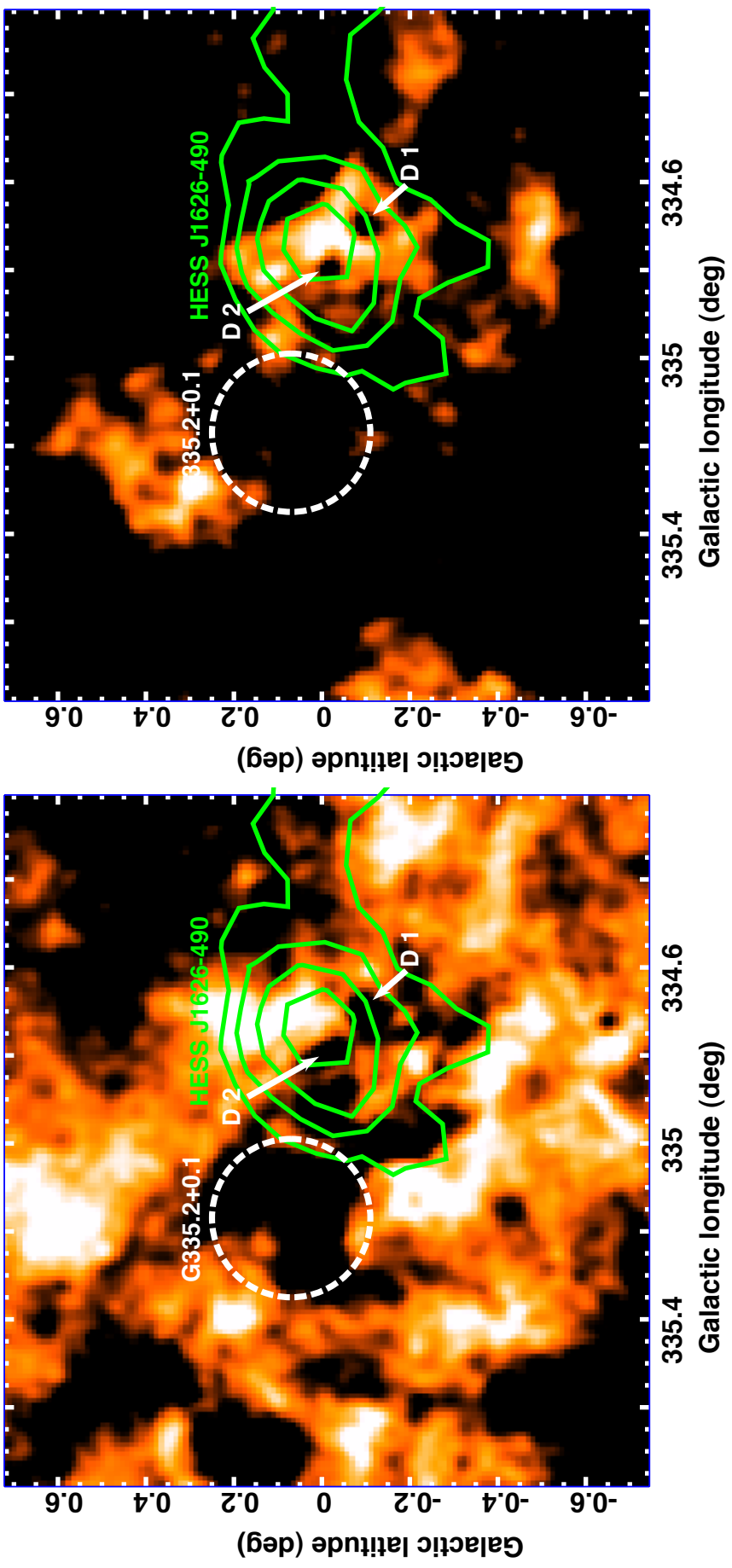

Figure 4.12: H I SGPS images of the region around HESS J1626−490 (linear scale in K km s^{-1}) integrated over the $v_{\rm LSR}$ ranges −23 to −18 km s^{-1} (*Left*) and −31 to −23 km s^{-1} (*Right*), respectively. The dashed circle (white) marks the position and radio extent of SNR G335.2+00.1. Also shown are the H.E.S.S. VHE contours of HESS J1626−490 (green). The arrows (white, labeled D1 and D2) mark two dips, probably due to foreground absorption.

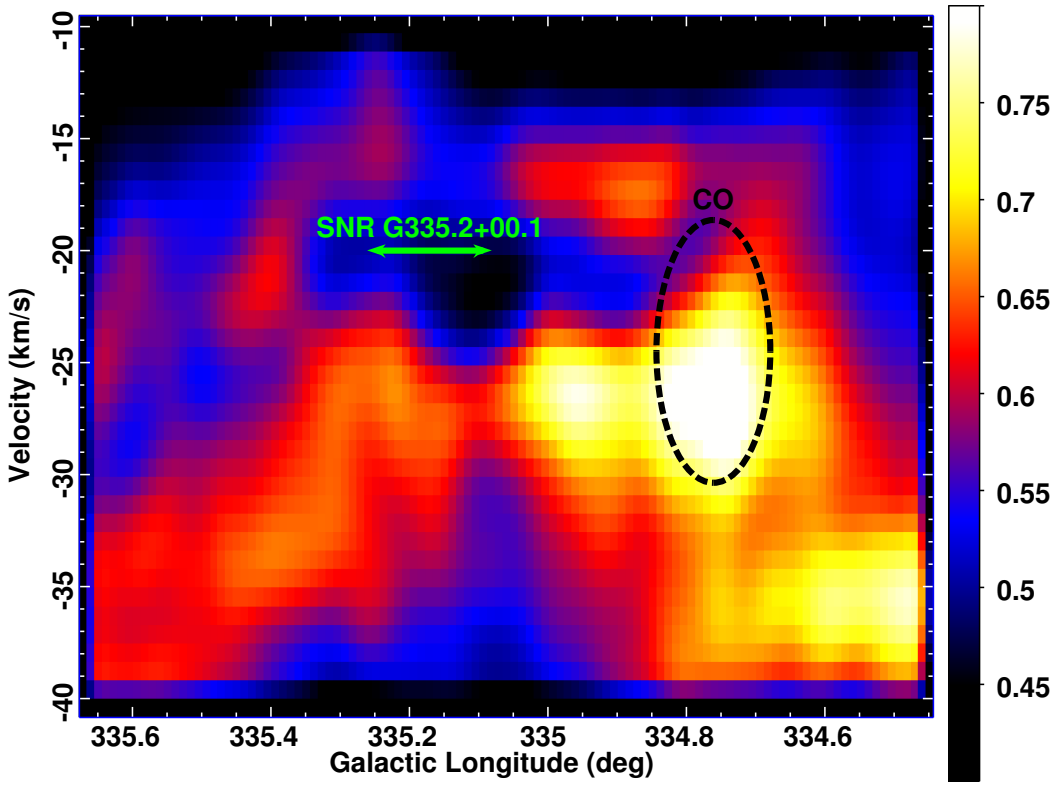

Figure 4.13: H I SGPS Galactic longitude–velocity plot (linear scale in K deg) integrated over the Galactic latitude range -0.11° to 0.24°. The position and extent of the ^{12}CO cloud is denoted by a dashed circle (black). The double arrow (green) shows the Galactic latitude and extent of SNR G335.2+00.1.

4.5 SGPS HI and Spitzer infrared data

Figure 4.12 shows H I images of the region around HESS J1626−490 from the Southern Galactic Plane Survey (SGPS McClure-Griffiths et al. 2005) integrated over the $v_{\rm LSR}$ ranges −23 to −18 $km\,s^{-1}$ (*Left*) and −31 to −23 $\mathrm{km\,s^{-1}}$ (*Right*), respectively. A local H I density depression is seen in the center of the left image at an angular separation of $\sim 21'$ from the CO molecular cloud and HESS J1626−490. It is striking that this feature is consistent in position as well as in angular extent with the SNR G335.2+00.1 (Green 2009; Reach et al. 2006). Furthermore, both images show a region of increased gas density in spatial coincidence with the VHE contours, which is more pronounced in the −31 to −23 $\mathrm{km\,s^{-1}}$ velocity range. Two dips, most likely due to foreground absorption, are marked by arrows (labeled D1 and D2).

We estimated the mass of the dense H I region coinciding with the VHE and ^{12}CO features using the signal within the same elliptical region as for the CO cloud (Sect. 4.4). Using the relation between H I intensity and hydrogen column density from Dickey and Lockman (1990) (X=$1.8\times10^{18}\,\mathrm{cm^{-2}\,K^{-1}\,km/s}$) we estimated the mass of the cloud as $4.9\times10^3\,\mathrm{M_\odot}$ with an average density of 60.1 $\mathrm{cm^{-3}}$. However, we note here that due to

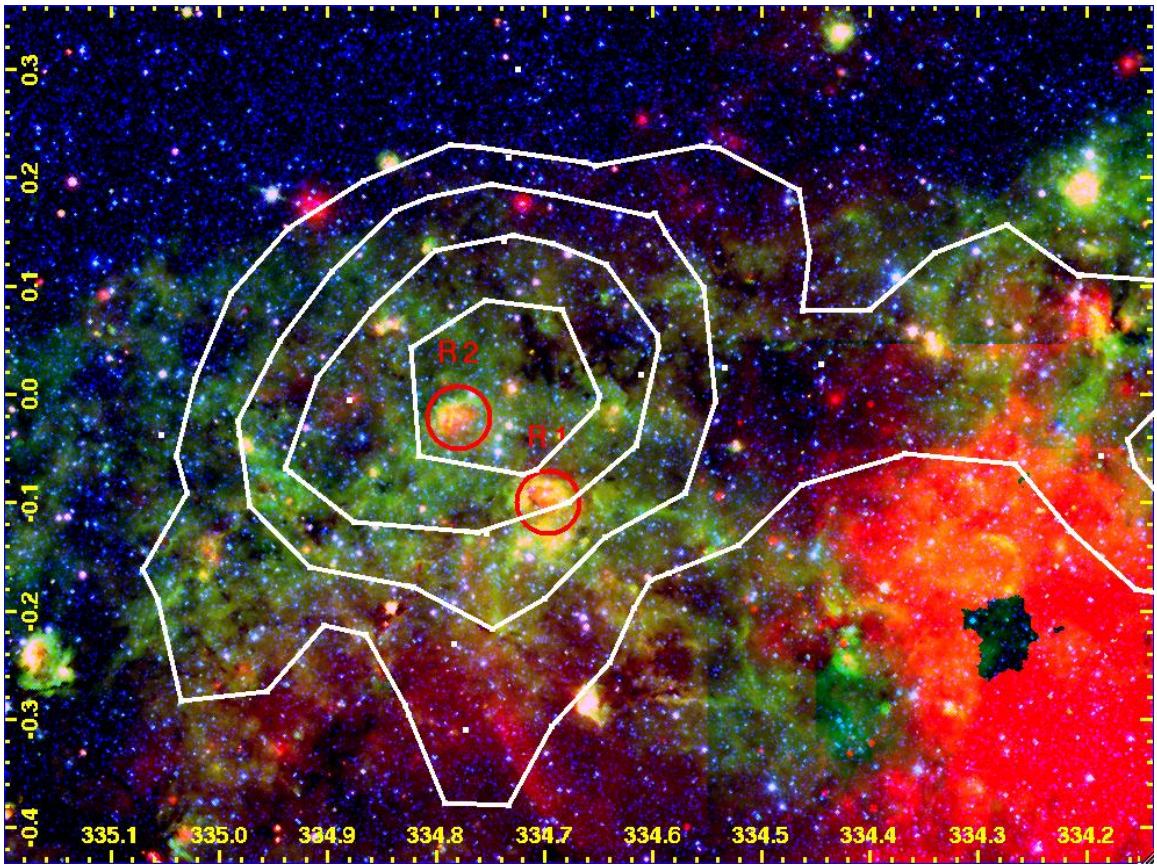

Figure 4.14: Three-color (rgb=24/8/3.6 μm) image from the *Spitzer* GLIMPSE and MIPSGAL surveys in log scale (MJy/sr units) with lower limit clipping at (rgb=30/60/5 MJy/sr) in Galactic coordinates. Shown are the VHE contours of HESS J1626−490 (white) and two H II regions (red, labeled R1 and R2).

the two absorption dips in the region this value should be seen only as a lower limit of the actual mass of the H I cloud.

Figure 4.13 shows the $v_{\rm LSR}$ profile for this region integrated over the Galactic latitude range −0.11° to 0.24°, which is the extent of both the SNR G335.2+00.1 and the VHE emission of HESS J1626−490. Both the region of low density and the H I cloud are clearly visible. The latter is in good agreement with the position of the CO cloud (Sect. 4.4), as indicated by the dashed ellipse.

Figure 4.14 shows a three-color (rgb=24/8/3.6 μm) image from the *Spitzer* GLIMPSE and MIPSGAL surveys in log scale (MJy/sr units) with lower limit clipping at (rgb = 30 / 60 / 5 MJy/sr). Apart from the large-scale diffuse emission in the red and green bands along the Galactic plane, there are two prominent H II regions within the 4 σ H.E.S.S. contours. These two H II regions are coincident with the absorption dips seen in H I (Fig. 4.12), which is a common feature of many H II regions in the Galactic plane (see, e.g., Kuchar and Bania 1990). R1 is listed in the catalog of Russeil (2003) (No. 427) with a systemic distance of 2.4±0.3 kpc. Even though R2 is not

listed, judging from the similarity of the two absorption dips, the distances to both H II regions should be quite similar. Both H II regions are also clearly seen in the Molonglo (Green et al. 1999) 843 MHz radio image shown by Aharonian et al. (2008a, Fig. 2). The differing distance estimates for the H II regions and the H I/CO-complex might indicate systematic differences between both methods. In particular this could mean that a large fraction of the mass of the H I cloud is located at a distance greater than 1.8 kpc.

4.6 Discussion of the emission scenario

In this work we searched for X-ray, sub-millimeter, and infrared counterparts of the unidentified VHE γ-ray source HESS J1626−490 to explore the nature of the particle acceleration process responsible for the observed emission. With a luminosity of 2×10^{33} erg s$^{-1}\times$(d/kpc)^2, HESS J1626−490 is quite typical of Galactic TeV sources detected by H.E.S.S., and we discuss both leptonic and hadronic emission scenarios in this section.

According to Reimer et al. (2006), close binary systems consisting of Wolf-Rayet (WR) and/or OB super-giant stars are expected to effectively produce VHE γ-rays in the colliding wind zone where strong shocks are present and where particle acceleration to multi-TeV energies could take place. The nearby triplet system HD 147633 (source No. 1, Sect. 4.3.2.1) is a strong X-ray emitter. Its spectrum can be well fit by a thermal model with temperatures typical of X-ray binaries showing coronal activity. This system is composed of a close binary of two G-type main sequence stars and a tertiary star orbiting at a greater distance (Makarov 2003) and can therefore most likely be ruled out as an efficient source of highly relativistic particles, which could give rise to VHE γ-ray emission. Apart from that, the extended morphology of HESS J1626−490 makes an identification with an X-ray point source detected by *XMM-Newton* rather unlikely.

In the case of a leptonic scenario where low-energy photons are up-scattered by relativistic electrons via the IC process, X-ray emission is expected to accompany the VHE signal arising from synchrotron cooling of the same population of high-energy electrons (Aharonian et al. 1997). Two examples for such sources detected by H.E.S.S. are the pulsar wind nebulae MSH 15-52 (Aharonian et al. 2005b; Schöck et al. 2010) and HESS J1825-13 (Aharonian et al. 2005c). Even from a first glance at the flux levels in X-rays ($\sim10^{-13}$ erg cm^{-2} s^{-1} for point sources and $\sim10^{-12}$ erg cm^{-2} s^{-1} for diffuse emission) and at VHE energies ($\sim10^{-11}$ erg cm^{-2} s^{-1}), a purely leptonic emission scenario seems unlikely. Following Aharonian et al. (1997) and assuming a typical Galactic magnetic field strength of 3×10^{-6} G, the corresponding synchrotron photon energy for E=1 TeV IC photons is ϵ=0.02 keV. Assuming the same photon index for the synchrotron counterpart as measured from the VHE source (Γ = 2.18) and extrapolating the flux to the 0.5 to 10 keV band, we estimate an integrated source

flux of $\sim 1.110^{-11}$ erg cm^{-2} s^{-1}. This flux is a factor of $\sim$25 more than what we measured from any point source, apart from X-ray source No. 1, which was discussed in the previous paragraph. This makes an identification of HESS J1626−490 with any of these sources unlikely. Our upper limit for diffuse X-ray emission (Sect. 4.3.3.1) is a factor of $\sim$2 lower than the expected value for HESS J1626−490 in a purely leptonic model.

We observed infrared emission from the field around HESS J1626−490 (see Sect 4.5) which could provide an additional target radiation field for the IC process. This would lower the expected synchrotron flux in the X-ray band. On the other hand, these estimates are based on the lowest possible magnetic field found in the Galactic ISM. Magnetic fields in the vicinity of energetic pulsars can be a factor of 10–100 larger, which would increase the expected synchrotron flux accordingly. We therefore conclude that a purely leptonic emission scenario is rather unlikely for HESS J1626−490.

The non-detection of any X-ray source fulfilling the energetic requirements for a purely leptonic scenario favors a hadronic emission process such as dense clouds in the vicinity of a cosmic particle accelerator. Such a scenario will be discussed in the remaining part of this section. As already mentioned in Sect. 4.1, dense molecular clouds are established VHE γ-ray emitters because they provide target material in regions of high cosmic-ray densities. Using data from the NANTEN ^{12}CO ($J = 1 - 0$) Galactic plane survey, we detected a molecular cloud that is morphologically consistent with HESS J1626−490. Particularly, the extended VHE tail, only seen in the updated analysis of the H.E.S.S. data, seems to have a CO counterpart. This additional morphological coincidence, that was not yet seen in our paper, confirms the positive identification of HESS J1626−490 with the observed CO cloud. The MC is located at a mean kinematic distance of $\sim$1.8 kpc. Following Aharonian et al. (1994, Eqs. 2 and 3), we estimated the gas density required to produce the observed VHE γ-ray signal ($F_\gamma(>0.6\,\mathrm{TeV}) = 7.5\times10^{-12}$ ph cm^{-2} s^{-1} and $\Gamma = 2.2$) as $n \approx 10$ cm^{-3} assuming a CR production efficiency of $\theta = 0.1$ and a distance of d = 1.8 kpc. This value is an order of magnitude lower than the measured ^{12}CO mean density. Thus, this environment would be easily suited to provide the observed VHE γ-ray flux.

Following Aharonian (1991) (Eq. 10), assuming that the observed molecular cloud only provides a 'passive' target for cosmic rays originating in a nearby acceleration site, the cosmic-ray enhancement factor for this source would be $k_{\mathrm{CR}} = 333$ for 10 TeV protons. As seen in Fig. 4.12 (*right*) and Fig. 4.13, there is a region of high-density H I gas spatially coincident with HESS J1626−490 located at $v_{\mathrm{LSR}} \approx -25$ km s^{-1}. Taking the additional mass of this H I cloud into account as supplementary target material k_{CR} would be down to $\sim$255, which is an order of magnitude larger than seen from other SNR–ISM interactions (see, e.g., Aharonian et al. 2008c). However, following Aharonian and Atoyan (1996), even CR enhancements of $k_{\mathrm{CR}} > 10^3$ are to be expected from molecular clouds at distances <10 pc from the SNR shell (as in our case, see next paragraph) and for a diffusion coefficient of $D_{10} \approx 10^{26}$ cm^2 s^{-1} if the age of the SNR does not exceed 10^4 to 10^5 years (see Fig. 4.15).

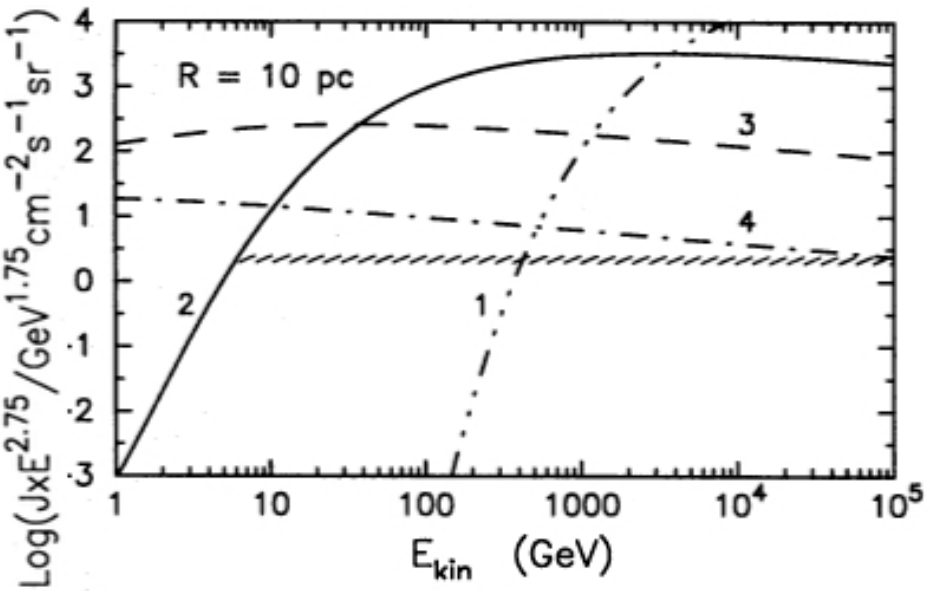

Figure 4.15: The temporal evolution of the energy spectrum of relativistic protons in the vicinity of an impulsive accelerator during their energy-dependent propagation. The index of the powerlaw injection spectrum is assumed to be −2.2, for a total CR energy of 10^{51} erg. Shown is the spectrum at a distance of 10 pc from the source. A powerlaw diffusion coefficient is assumed with s=0.5 and $D_{10} = 10^{26}\mathrm{cm}^2/\mathrm{s}$. The curves plotted by fancy (1), solid (2), dashed (3), and dot-dashed (4) lines correspond to the age of the source $t = 10^3, 10^4, 10^5$, and 10^6 years, respectively. The hatched curve shows the fluxes of the CR protons observed near Earth. Image credit: Fig. 1b in Aharonian and Atoyan (1996).

Now assuming that this ^{12}CO / H I cloud is indeed the source of the observed VHE γ-rays, a nearby accelerator would be needed. The presence of two prominent H II regions at distances consistent with the CO / H I clouds (see Sect. 4.5) indicates massive star formation, hence potential PWNe and SNRs in this area. The nearby density depression seen in H I (see Sect. 4.5) might indicate a recent catastrophic event, such as a supernova explosion, giving rise to strong shocks that would have blown the neutral gas out. At d = 1.8 kpc the edge of this region would be at a distance of 8.1 pc from the ^{12}CO/H I cloud. It is striking that this H I feature is consistent in both position and angular extent with the SNR G335.2+00.1 (Green 2009). Using the Σ-D relation Guseinov et al. (2004) estimated the distance to SNR G335.2+00.1 as d = 5 kpc which, at first glance, conflicts with the identification of SNR G335.2+00.1 with the H I depression seen at a distance of 1.8 kpc. However, the scatter in Σ-D distances for individual sources is quite large (Green 2005) making a positive identification of SNR G335.2+00.1 and the H I depression seen at a kinematic distance of 1.8 kpc very well possible.

We note here that, apart from potential systematic uncertainties in kinematic distance estimates, the projected distance of 8.1 pc should be seen only as a lower limit because

the physical separation of accelerator and target could be larger if both objects are not at the same distance to the observer. A hint that this could be the case for this source is that the center of gravity of the CO cloud is slightly shifted in velocity with respect to the H I density depression. A larger distance between the accelerator, most likely SNR G335.2+00.1, and the molecular cloud would lower the expected CR enhancement.

Even though the angular separation of the *Fermi* source 1FGL J1626.0−4917c and HESS J1626−490 is relatively small, these sources are not coincident within the 3σ significance level of their spatial uncertainties (see Fig. 4.5). Furthermore, we did not find any feature in X-rays, CO, or H I that could explain a displacement between HE and VHE γ-ray emission. 1FGL J1626.0−4917c also shows signs of a slight variability. Based on the variability index listed in the 1FGL catalog (Abdo et al. 2010a), the chance of the source being a constant emitter can be estimated to <11%, which might indicate an extragalactic origin. Thus it remains unclear at this point whether these two sources are physically connected.

4.7 Test of an hadronic model

Following the discussion in the previous section, the VHE γ-ray emission from HESS J1626−490 arises most likely from hadron-dominated mechanisms. This interpretation so far is mainly based on the comparison of flux levels in various energy regimes. However, the spectral shape in the VHE regime did not yet contribute to a detailed understanding of the source. Furthermore, there are still some parameters that are not very well constrained yet. For the distance R between SNR and MC we only have a lower limit of 8 pc, which is the projected distance seen from Earth. Also the age t of the SNR is not known, as well as the diffusion coefficient D_{10} (see Sect. 2.5) in the vicinity of the source. The latter so far was only determined in the Galactic average ($D_{10} \approx 10^{28}\mathrm{cm}^2\ \mathrm{s}^{-1}$, Berezinskii et al. 1990) or for W41, which is an historic SNR with a known age ($D_{10} \approx 10^{26}\mathrm{cm}^2\ \mathrm{s}^{-1}$, Gabici et al. 2010).

Table 4.4: Scanned parameter space

Parameter	lower boundary	upper boundary	step size
Age t (yr)	10^3	10^6	10^3
Radius R (pc)	8	50	1
Diffusion coefficient D_{10} ($\mathrm{cm}^2\ \mathrm{s}^{-1}$)	10^{25}	10^{28}	2×10^{25}

In this section the model for hadronic transport and γ-ray emission described in Sect. 2.5 is used to reproduce the measured VHE spectrum of HESS J1626−490. For

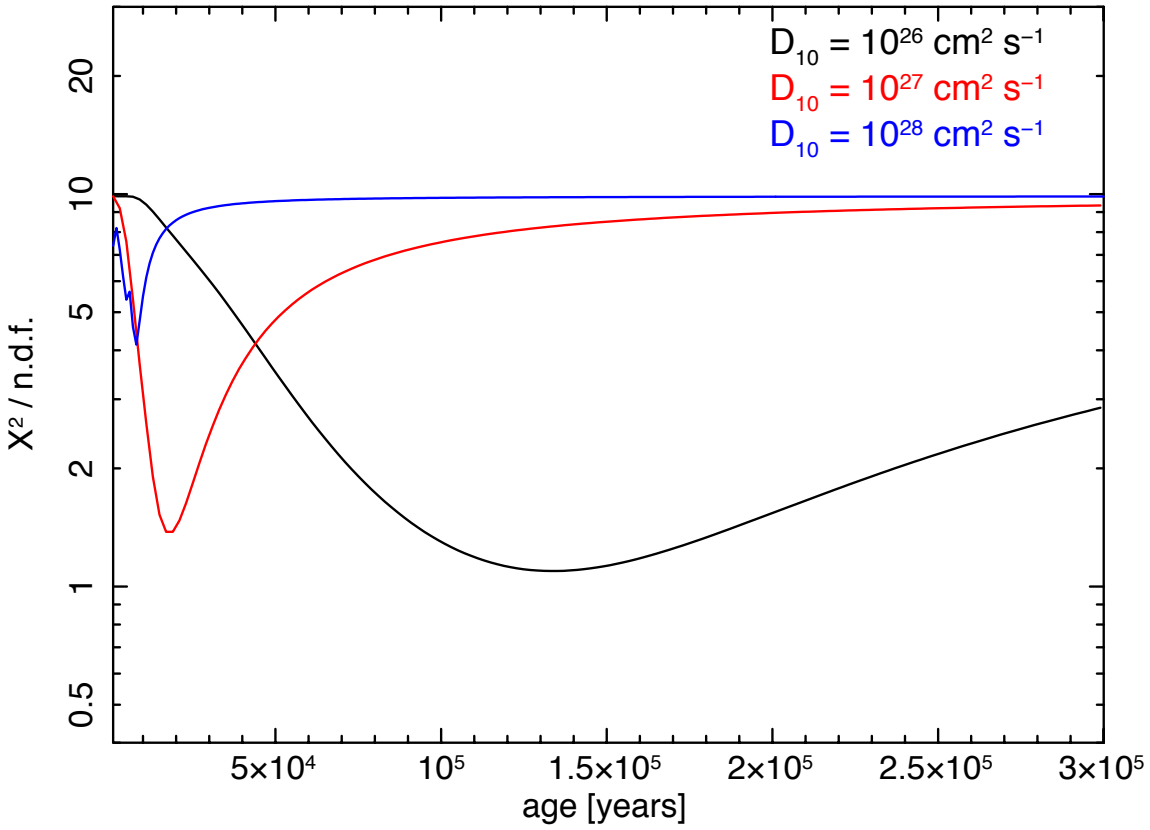

Figure 4.16: Evolution of X^2/n.d.f. as a function of the age t. The three solid lines refer to diffusion coefficient normalizations of $D_{10} = 10^{26}$cm^2 s^{-1} (black), $D_{10} = 10^{27}$cm^2 s^{-1} (red), and $D_{10} = 10^{28}$cm^2 s^{-1} (blue). The Radius was fixed at $R = 35$ pc for all three scans.

this purpose the parameter space of R, t, and D_{10} is scanned within the ranges and with the step-sizes given in Table 4.4. For each parameter combination the model spectrum is calculated, and the deviation from the measured VHE data is quantified by its mean squared deviation (X^2). As it is unlikely or at least unclear that the offset *Fermi* source 1FGL J1626.0−4917c is connected to HESS J1626−490 (see previous section), the model is only compared to the data from H.E.S.S..

To demonstrate how the parameters t and D_{10} influence the spectra, the X^2 value is shown as a function of t for three different values of D_{10} in Fig. 4.16. For each distribution it can be seen that the deviation from the data is very large for young ages. This is because young SNRs are very powerful accelerators for CR energies of up to 5 PeV, and feature high low-energy cut-offs of the CR spectra, as the lower energy particles did not yet have time to reach the MC due to the energy dependent diffusion. Therefore, for these energies the VHE data are extremely over-estimated by the model. Furthermore, the low-energy cut-off of the model spectra are within the range of the measured VHE spectrum, leading to a very poor reproduction of the data. For older modeled SNRs, the X^2 distribution reaches a minimum, followed by a slow rise towards higher values of t. The fact that the minimum is reached earlier

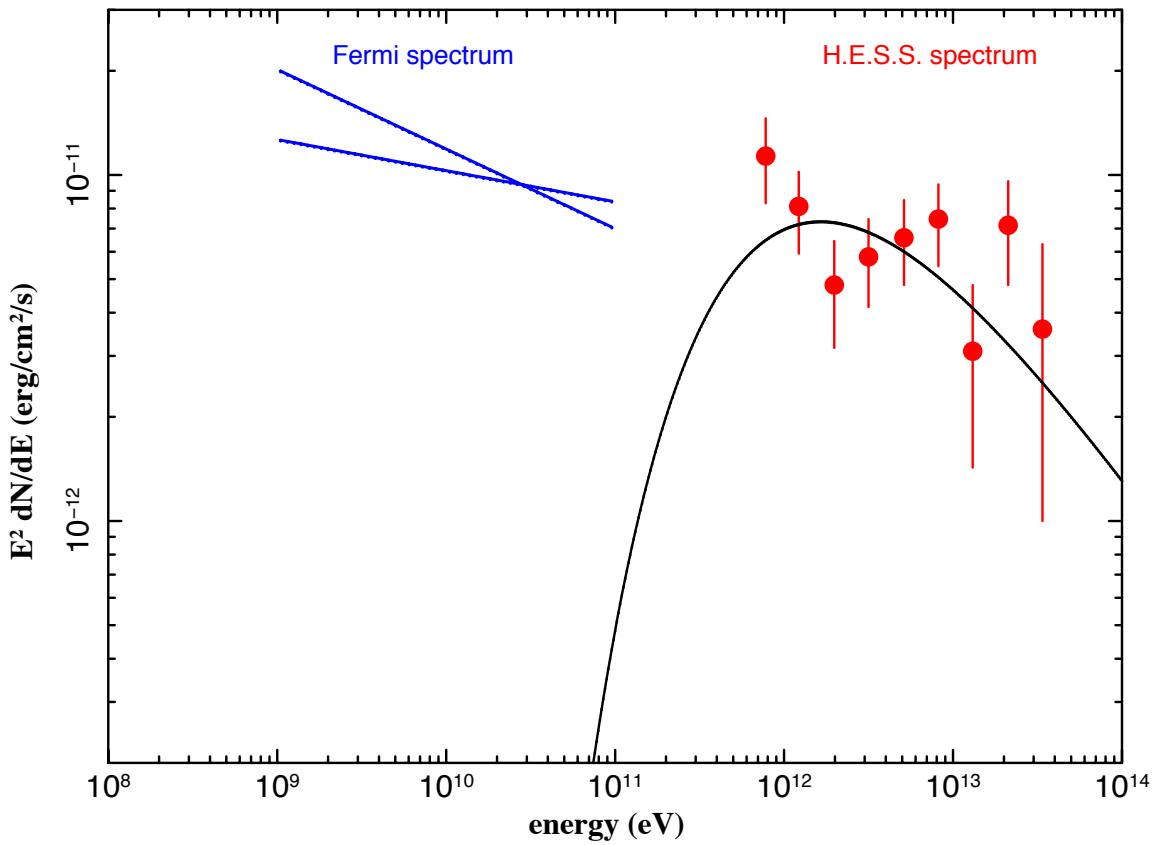

Figure 4.17: Spectral energy distribution of HESS J1626−490 showing the H.E.S.S. spectrum (red) and the spectrum of the *Fermi* source 1FGL J1626.0−4917c (blue). The solid line (black) shows the hadronic model with the parameters that give the lowest value of X^2 ($R = 35$ pc, $t = 1.5 \times 10^5$ yr, $D_{10} = 9 \times 10^{25}\mathrm{cm}^2\ \mathrm{s}^{-1}$).

for larger values of D_{10} can easily be explained by the the correlation between these two parameters. For faster diffusion (i.e. larger D_{10}) the lower energy particles reach the MC earlier. Therefore, the low-energy cut-off of the model spectra passes over the measured data range from high energies towards low energies for younger ages t. The VHE data of HESS J1626−490 obviously do not show a pronounced low-energy cut-off in the probed energy range. Thus, a good fit of the VHE γ-ray data is possible for smaller values of t when D_{10} is larger.

The slow but steady rise of the reduced X^2 distribution after the minimum is due to the fact that with increasing t the peak of the modeled CR spectrum steadily shifts towards lower energies. This leads to a more and more pronounced under-estimation of the measured data in the VHE range. All three X^2 distributions asymptotically reach a constant value of ∼10 for very large SNR ages, which basically reflects the significance of the measured spectrum, as the models predict a flux comparable to zero.

The scan over the full three-dimensional parameter space given in Table 4.4 yields a global minimum of $\frac{X^2}{\mathrm{n.d.f.}} = 1.1$ at $R = 35$ pc, $D_{10} = 9 \times 10^{25}\mathrm{cm}^2\ \mathrm{s}^{-1}$ and $t =$

1.5×10^5 years. Figure 4.17 shows the VHE γ-ray spectrum together with the model spectrum calculated with the these parameters. Similar good results ($\frac{X^2}{\text{n.d.f.}} < 1.2$) are achieved for radii between $R = 31$ pc and $R = 34$ pc, with ages varying between $t = 1.5 \times 10^5$ and $t = 2.0 \times 10^5$ years. The model reproduces the flux as well as the spectral shape of the H.E.S.S. measurement very well. However, it is not compatible with the flux of the *Fermi* source 1FGL J1626.0−4917c. But if 1FGL J1626.0−4917c is indeed not connected to HESS J1626−490, as suggested by the spatial offset and the indications for slight variability (see previous section), this result might explain why no second bright GeV γ-ray source was detected by *Fermi* in this region. The radius of $R = 35$ pc would imply a difference between the line-of-sight distances to the SNR and the MC of ∼34 pc. This is well below the spectral resolution of the cm/mm telescopes and therefore compatible with the observations.

4.8 Conclusion and outlook

This chapter presented a detailed multi-wavelength study of the previously unidentified VHE γ-ray source HESS J1626−490. An updated H.E.S.S. data analysis, comprising more than twice the livetime of the original published dataset, yielded results comparable to the original publication, however, with some distinct differences in the source morphology. A detailed analysis of an archival *XMM-Newton* observation yielded no apparent counterparts to the VHE emission in the X-ray regime. This information was used to derive an upper limit that challenges current models which rely on a purely leptonic γ-ray emission scenario. CO molecular line data from the NANTEN Galactic plane survey revealed a molecular cloud at a distance of 1.8 kpc that is strikingly consistent with the VHE morphology, particularly with the updated analysis results. With public H I data from the SGPS the line-of-sight distance to the SNR G335.2+00.1 could be constrained, assuming that a prominent density depression seen in the H I gas was created by the SNR shock. The projected distance between SNR G335.2+00.1 and HESS J1626−490 would then be only 8.1 pc, which makes a hadronic γ-ray emission scenario very likely. A detailed model for hadron transport and interaction confirms this conclusion, indicating a slightly larger distance between source and target of ∼30 pc, which is still compatible with the spectral resolution of the analyzed mm/cm radio data. Thus, HESS J1626−490 is now among the small but growing number of individual VHE γ-ray sources that correlate directly to dense molecular clouds in the vicinity of SNRs.

Now what can we do to learn even more about HESS J1626−490 or similar sources? With the improved angular resolution of next-generation Cherenkov Telescope arrays, it will be possible to study the morphology of the VHE signal and its connection to molecular gas in much greater detail. This is crucial for constraining the emission region of VHE γ-rays, which strongly influences any estimation of target mass and density. For the determination of diffuse X-ray fluxes and upper limits, a large effective area combined with a good angular resolution to effectively exclude point-like sources is needed. Therefore, a much deeper exposure (∼100 ks) with *XMM-Newton* would make

it possible to significantly improve the constraints on leptonic scenarios. However, for a more likely hadronic scenario, the flux expectations in the keV band are very low, which would certainly diminish the chances of such a proposal to be approved. To study the particle propagation in more detail, dedicated radio polarization observations in the MHz to GHz regime would help to determine the direction and level of turbulence of the magnetic field in the SNR. Furthermore, such measurements could be used to identify a potential additional synchrotron component, and thus the presence of relativistic electrons at the SNR shock. VHE γ-ray emission from molecular clouds may also exhibit localized peaks at their core regions with densities $>10^4$ cm^{-3} (Gabici and Aharonian 2007). To trace these regions molecular lines of NH_3, CS, or SiO can be used. Respective follow-up observations at mm and sub-mm wavelengths could be crucial for characterizing the environment of particle interaction.

5 Non-thermal emission from Globular Clusters

5.1 Introduction

Globular Clusters (GCs) are very old ($\sim 10^{10}$ years) gravitationally bound systems of stars comprising thousands to one million members. All GCs observed in the Milky Way or nearby galaxies seem to be stable, which implies the presence of some inner pressure countering the effects of gravitational collapse. Following Hut et al. (1992) this energy density might come from the potential energy of the numerous binary systems present in the cores of GCs, and that this energy might be transferred to the member stars in close stellar encounters, stabilizing their orbits. This process is assumed to be very efficient in the extremely dense cores of GCs, due to the strongly enhanced stellar encounter rate (Pooley and Hut 2006). Observational evidence for a rich abundance of close binary systems is provided by the detection of many X-ray binaries (XRBs) associated with GCs (e.g. Clark 1975).

Apart from the direct detection of binary systems also the search for millisecond pulsars (MSPs) could indicate the presence of close binary systems. At least in part, MSPs are believed to be "recycled" pulsars originating from binary systems, and spun up by mass accretion (Alpar et al. 1982). Therefore, a large population of close accreting binary systems would subsequently lead to numerous MSPs at later stages of the evolution. Indeed the abundance of radio MSPs per unit mass is greatly enhanced in the cores of GCs (Ransom 2008). Recently, observations with the *Fermi*/LAT telescope have shown that MSPs are also strong γ-ray emitters in the MeV to GeV regime, featuring hard spectra with cut-offs at a few GeV (Abdo et al. 2009). This emission is believed to originate from pulsed curvature radiation emitted by electrons directly in the pulsar magnetospheres (see e.g. Venter et al. 2009).

Furthermore, *Fermi* detected steady HE γ-ray emission from eight Galactic GCs (47 Tuc, ω Cen, M62, NGC 6388, Terzan 5, NGC 6440, M 28, and NGC 6652; Abdo et al. 2010c). The fact that in all these cases the emission does not show variability indicates that no individual MSP could be the origin of the observed signal. All the HE γ-ray spectra of these eight GCs are hard with spectral indices $0.7< \Gamma <1.7$), and a cut-off at a few GeV was measured for five of them (Abdo et al. 2010c). Therefore, these authors conclude that the γ-ray emission is due to magnetospheric emission from the whole population of MSPs present in the GCs. Based on this assumption using the flux in the GeV band, and when the distances to the clusters are known, the total number of

MSPs can be calculated for each individual GC (Abdo et al. 2010c). Even though the derived estimates are subject to large statistical uncertainties, the numbers of MSPs predicted from the γ-ray fluxes are much larger than the numbers of detected MSPs in the radio and X-ray regimes. This could be explained by wider beams at GeV energies with respect to lower frequency bands (see also Abdo et al. 2010b).

Due to the spectral cut-off at a few GeV, the magnetospheric emission does not extend to VHE γ-ray energies, which would also explain the non-detection of any individual MSP with current IACTs. Thus, in the context of magnetospheric emission from a large population of weak emitters, GCs also are unlikely candidates for VHE sources. So far, observations of GCs in the VHE regime only resulted in upper limits on M13, M15, M5 and 47 Tuc (Anderhub et al. 2009; McCutcheon 2009; Aharonian et al. 2009). However, the presence of relativistic electrons would give rise to VHE γ-ray emission via IC up-scattering of CMB photons (see Sect. 2.4.1). These electrons could be accelerated in the wind termination shocks of individual MSPs or in regions of colliding PWNe (Bednarek and Sitarek 2007). Such a scenario is very similar to a PWN, which is the most abundant class of Galactic VHE γ-ray emitters; but here the energy does not come from one single powerful pulsar but from a whole population of a few tens to a few hundred weak sources. In the case of VHE γ-ray emission due to the IC process, synchrotron radiation from the same population of leptons might be expected in the X-ray band. Therefore, the detection of non-thermal X-ray emission could help to confirm such a scenario.

Apart from relativistic leptons, VHE γ-ray emission could also originate from hadronic processes. As suggested by the recent detection of SN 1006 in VHE γ-rays (Acero et al. 2010), the remnants of type Ia supernovae, resulting from a white dwarfs merger, could produce hadronic CRs. The rate of such events is assumed to be very high in dense GC cores, due to the high probability for close stellar encounters (Shara and Hurley 2002). Another possibility for the production of hadronic CRs are remnants of short gamma-ray bursts (GRBs), resulting from a neutron stars merger (e.g. Nakar 2007). The relativistic shocks, expected to originate from such events, are very efficient particle accelerators, which would lower the requirements on the total kinetic energy with respect to type Ia SNRs (Atoyan et al. 2006). The detection of thermal X-rays would favor such a scenario, as shocks originating from sub-relativistic ejecta would heat the surrounding ISM (Domainko and Ruffert 2005, 2008).

In this chapter the results of a search for VHE γ-ray emission from 18 Galactic GCs, covered by the H.E.S.S. Galactic plane scan or dedicated observations, are presented (Sect. 5.2). Here Terzan 5 stands out as the only GC with a significant VHE γ-ray source in its direct vicinity (Sect. 5.2.1). Several GCs that are bright at MeV to GeV energies (including Terzan 5) were also observed with the X-ray telescopes *XMM-Newton* and *Chandra*. A weak and diffuse X-ray source, centered on Terzan 5, was detected with *Chandra* (Sect. 5.3.1). Three other GCs are searched for the presence of similar signals (Sect. 5.3.2), but the analyses resulted only in upper limits. Potential emission scenarios for VHE γ-rays and X-rays are explored in the respective sections.

In Sect. 5.4 the findings in both energy regimes are summarized, and potential common emission mechanisms are discussed.

5.2 Search for VHE γ-ray emission from Galactic Globular Clusters

To search for VHE γ-ray emission from Galactic GCs with H.E.S.S., the total available dataset of observation runs was used, including scans from the Galactic plane as well as dedicated observations. All three and four telescope runs that met the standard selection criteria on hardware performance and weather conditions were selected (see Aharonian et al. 2006d). Every GC that had a minimum exposure of 20 good quality runs, with offsets between 0.2° to 2.0° from the GC position was considered. Another *a priori* cut on the target list was applied by only accepting GCs with a minimum Galactic latitude of 1°, to avoid source confusion. Following Chaves (2009) the distribution of VHE γ-ray excess counts detected by H.E.S.S. can be approximated by a Gaussian profile centered at $b = -0.26°$ with a width of $\sigma = 0.4°$. Positions with $|b| > 1.0°$ are more than 2σ away from the center of the Gaussian, and the number of expected sources is of the order of 10^{-2}. The third cut on the target list requires an energy threshold of 800 GeV or lower. This cut basically rejects those GCs that were observed only at large zenith angles.

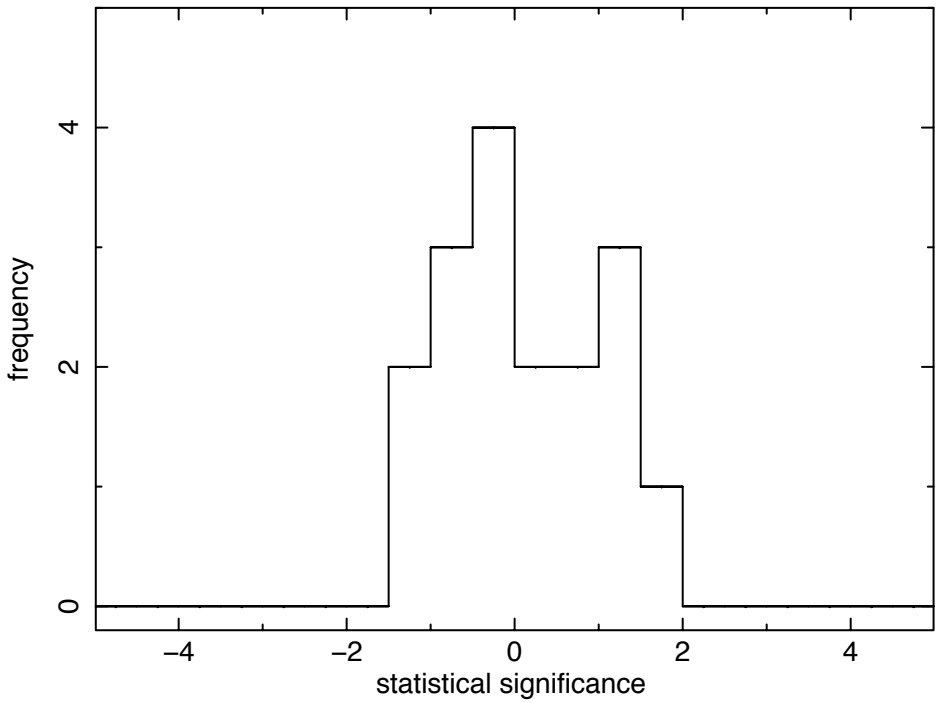

Figure 5.1: Distribution of statistical VHE γ-ray detection significances for all GCs, except Terzan 5. The mean of the distribution is 0.11σ.

A total of 18 GCs survived these cuts and were analyzed with the sensitive *model* analysis technique, which was already briefly described in Sect. 4.2. As the fluxes are expected to be very low, "hard" cuts for shower reconstruction were applied, which generally provide better results for weak sources (see Aharonian et al. 2006d). The positions listed in the GC catalog of Harris (1996) were used to perform a search for point-like ($r_{\mathrm{PSF}} = 0.07°$) VHE γ-ray emission from the direction of each GC. For background estimation the *reflected background* method was used (see Sect. 4.2). The statistical significance of VHE γ-ray emission from each GC, based on source and background counts as well as the area scaling factor, was calculated following Li and Ma (1983). All results are compiled in table 5.1. Most of these sources were not covered in dedicated observations, but lie just by chance in the FoV of Galactic plane scan runs or of observations targeted at nearby sources. Therefore, the GCs were observed at a wide variety of offsets in the range of 0.2° to 2.0°. To give comparable values for the effective exposure of each GC, the livetimes given in Tab. 5.1 were corrected for relative acceptance differences. Terzan 5 is the only source that shows significant excess emission and is therefore discussed separately in Sect. 5.2.1. The distribution of detection significances of all GCs except Terzan 5 has a mean of 0.15σ and is shown in Fig. 5.1. For all non-detected GCs, upper limits (at 95% confidence level) for the photon flux above 1 TeV were derived, following the approach of Feldman and Cousins (1998) and assuming a powerlaw spectrum with photon index -2.

5.2.1 A VHE γ-ray source near Terzan 5

Terzan 5 (stellar luminosity $L_{\mathrm{star}}=1.5\times10^5 L_\odot$, Harris 1996) is the Galactic GC with the largest population of known MSPs (33, see Ransom 2008). Furthermore, a high production rate for low-mass XRBs is expected in the extremely dense core of Terzan 5 (Ivanova et al. 2005). The GC is located at a distance of 5.5 kpc (Ortolani et al. 2007), only ∼1.7° above the Galactic plane (R.A.: $17^{\mathrm{h}}48^{\mathrm{m}}04\overset{\mathrm{s}}{.}0$, Dec.: -24°46′45″). Its core (r_{c}), half-mass, (r_{h}) and tidal radii (r_{t}) are 0.18′, 0.83′ and 4.6′, respectively (Harris 1996). Terzan 5 is also the brightest GC detected by *Fermi*/LAT, with an estimated total number of 180^{+100}_{-90} MSPs (Abdo et al. 2010c). It is therefore one of the most promising Galactic GCs for VHE γ-ray observations to test the scenario of leptonic emission related to MSPs. Furthermore, due to its high core density, Terzan 5 may also have been the site of recent catastrophic events, such as type Ia supernovae or short GRBs, which might also give rise to radiation in the VHE γ-ray band (see Sect. 5.1).

Terzan 5 was covered in the H.E.S.S. Galactic plane scan. Due to an indication of excess emission from the region around Terzan 5, a campaign of dedicated observations was conducted in 2009 and 2010. The analysis of H.E.S.S. data presented in this section is similar to the analysis described in the forthcoming H.E.S.S. publication (Acero et al. 2011) and yields consistent results. The total available dataset of runs, pointed within 2.5° of the core of Terzan 5, comprises a total livetime of 72.6 hours of good quality data. In contrast to the run selection criteria employed for the analysis of all other GCs (see Sect. 5.2), here also runs with offsets of more than 2.0° were accepted, to be consistent with the analysis presented in the forthcoming H.E.S.S. publication.

Table 5.1: Analysis results for GCs observed by H.E.S.S. passing the cuts

Name	Livetime (hours)	Significance (σ)	int. Flux (>1 TeV) (photons cm^{-2} s^{-1})
Terzan 5*	72.6	+7.3	$(3.2 \pm 0.6) \times 10^{-13}$
NGC104	16.4	+0.7	$<5.8\times10^{-14}$
FR1767	21.0	−0.1	$<1.4\times10^{-13}$
Pal6	29.8	−0.0	$<7.2\times10^{-14}$
NGC288	77.4	−0.8	$<2.4\times10^{-14}$
Terzan10	9.1	+2.0	$<2.6\times10^{-13}$
Djorg2	10.6	−1.0	$<8.4\times10^{-14}$
Terzan6	32.8	+0.1	$<9.7\times10^{-14}$
NGC6749	11.5	−0.5	$<1.3\times10^{-13}$
NGC6388	21.5	+1.2	$<1.8\times10^{-13}$
NGC6256	8.4	−0.3	$<3.3\times10^{-13}$
NGC6144	8.8	−1.0	$<1.5\times10^{-13}$
NGC362	8.5	+1.5	$<1.6\times10^{-13}$
Terzan4	10.7	+1.2	$<1.8\times10^{-13}$
NGC7078	13.9	+0.7	$<8.6\times10^{-14}$
HP1	8.1	−1.3	$<2.0\times10^{-13}$
NGC6715	30.5	+0.3	$<1.0\times10^{-13}$
FSR1735	26.9	−0.1	$<7.2\times10^{-14}$

* The quoted values for Terzan 5 are derived from the analysis presented in Sect. 5.2.1.

5.2.1.1 Characteristics of the VHE γ-ray signal detected by H.E.S.S.

Figure 5.2 shows a map of VHE γ-ray excess emission above an energy threshold of 200 GeV, as detected by H.E.S.S. The peak significance of the detected signal is 7.3σ pre-trials, which translates into a post-trial significance $>5\sigma$[1], taking into account the chance to encounter random fluctuations in the Galactic plane scan. The source is extended beyond the radius of the instrument's point spread function with a significance of $\sim4\sigma$ and features a fitted intrinsic width of $\sim0.1°$. The VHE γ-ray emission shows significant overlap with the area within the tidal radius of Terzan 5, but the center of gravity is offset from the GC core. A 2D-Gaussian fit to the excess map yields a position of R.A.: $17^{\mathrm{h}}47^{\mathrm{m}}40^{\mathrm{s}}$ ($\pm1.5'$), Dec.: -24°47′48″ ($\pm1.0'$), which is $2.4'$ offset from the core position of Terzan 5.

To derive a spectrum, a circular extraction region with a radius of 0.2°, centered on the 2D-Gaussian best-fit position, was chosen, which takes the point-spread-function as well as the intrinsic source extension into account (solid black circle in Fig. 5.2). A fit with a simple powerlaw model ($F(E) = N_0 \cdot E^{-\Gamma}$, χ^2/n.d.f. = 67/52) yields a

[1]Sources that are detected with post-trial significances of 5σ or more are considered as secure detections by the H.E.S.S. collaboration.

flux normalization at 1 TeV of $N_0 = (4.8 \pm 0.9) \cdot 10^{-13}\mathrm{cm}^{-2}\mathrm{s}^{-1}\mathrm{TeV}^{-1}$ and a photon index of $\Gamma = 2.7 \pm 0.3$ (Fig. 5.3). The energy interval used for spectral fitting was 0.2–84 TeV.

5.2.1.2 Origin of the VHE γ-ray emission

Possible scenarios for VHE γ-ray emission from GCs were already introduced in Sect. 5.1. Below, each possibility is discussed on the basis of the detected signal near Terzan 5. This discussion is part of the upcoming H.E.S.S. publication (Acero et al. 2011)[2].

Chance coincidence Before discussing possible emission scenarios giving rise to the observed VHE γ-ray signal from Terzan 5, first the possibility of a chance coincidence of an unrelated Galactic source with this GC is investigated. Following the same

[2]The content of Sect. 5.2.1.2 was developed in close cooperation with the corresponding authors of the HESS publication W. Domainko and Á.-C. Clapson.

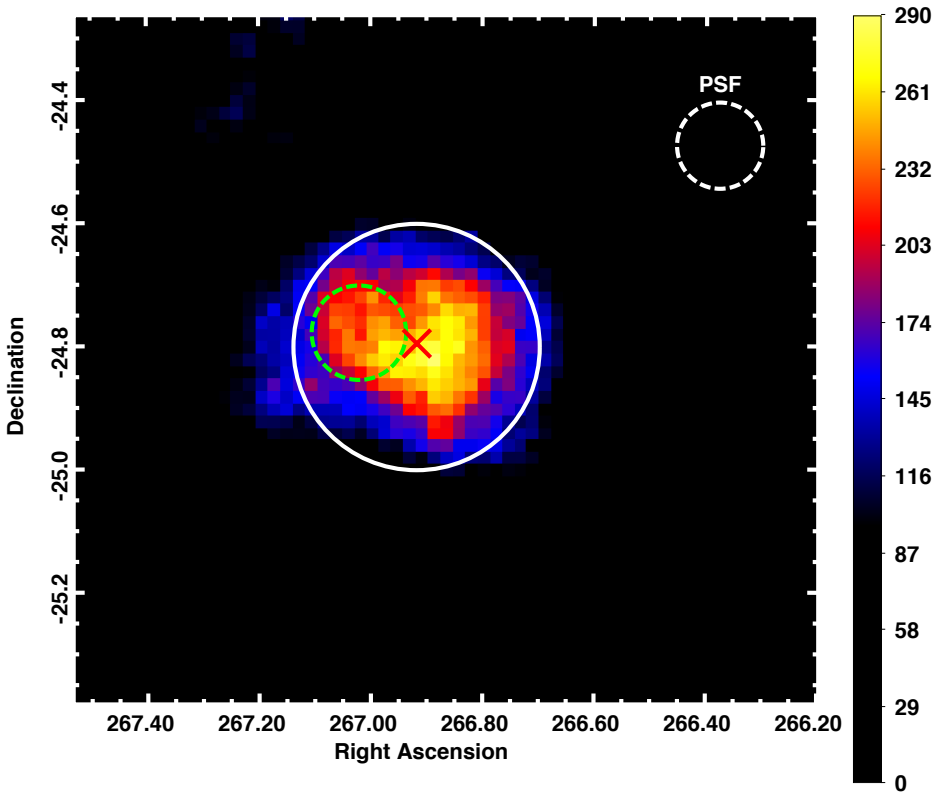

Figure 5.2: H.E.S.S. excess map of Terzan 5 above an energy threshold of 200 GeV. The dashed circle (green) shows the position and extension of the tidal radius of Terzan 5. The cross (red) denotes the fitted center of gravity of the VHE γ-ray emission. The white circles denote the instrument's point spread function (dashed) and the region used to extract the VHE γ-ray spectrum (solid), respectively.

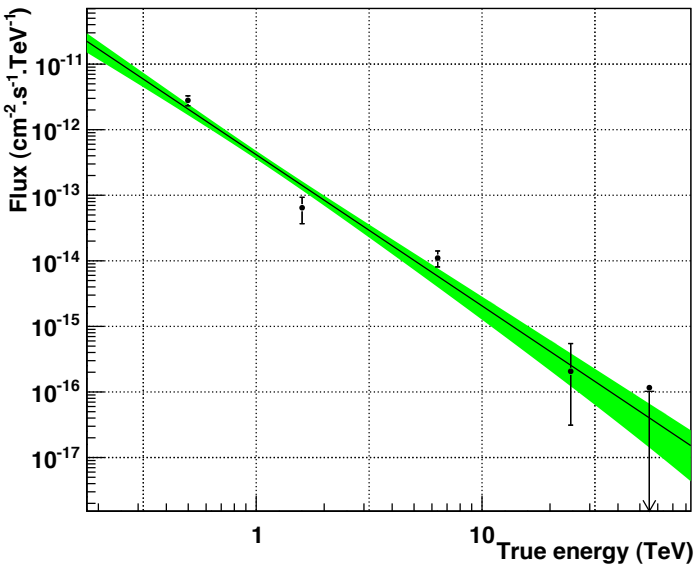

Figure 5.3: VHE γ-ray spectrum of Terzan 5. The solid line (black) denotes the best fit of a powerlaw model. The colored area (green) shows the 1 σ confidence region.

approach as in Sect. 5.2, the chance of finding a Galactic source can be determined from the distribution of VHE γ-ray excess counts as a function of Galactic latitude (see Chaves 2009). At a latitude of $b = 1.7°$, the expected number of counts at the position of Terzan 5 is negligible ($< 10^{-3}$). Therefore, a Galactic source coinciding by chance with Terzan 5 has to be an outlier of the distribution. Assuming that there is one such outlier, the probability to find this source within 0.1° of the position of Terzan 5 and over the longitude range covered by the H.E.S.S. Galactic plane scan ($-85° < l < 60°$) is $\sim 10^{-4}$. However, it has to be noted that this estimation may be biased, as the coverage of the scan is inhomogeneous, favoring regions much closer to the plane.

The characteristics (i.e. spectral index, angular extent, and flux) of the VHE γ-ray source detected close to Terzan 5 are compatible with PWNe, the most abundant class of sources in this energy regime. However, there is no known radio pulsar with a spin-down luminosity $> 10^{34}$ erg s^{-1}kpc^{-2} in the vicinity of Terzan 5 that could give rise to a detectable PWN. In the ATNF pulsar catalog (Manchester et al. 2005) there is only one such pulsar in the longitude band covered by H.E.S.S. and in the latitude range $1.5° < b < 2.0°$. Following Gonthier et al. (2004), the numbers of radio-loud and radio-quiet pulsars might be comparable. Therefore, one could assume the presence of one additional powerful pulsar in this region. Again, as discussed in the previous paragraph, the probability that one source is located within 0.1° of Terzan 5 is $\sim 10^{-4}$.

To conclude, it seems rather unlikely that the VHE γ-ray source detected in the vicinity of Terzan 5 is either due to chance, or arises from a PWN associated with an undetected powerful pulsar.

Leptonic scenario As mentioned in Sect. 5.1, leptonic γ-ray emission from GCs may arise either as the superposition of pulsed curvature radiation of electrons from individual MSPs (Venter et al. 2009) or from IC up-scattered photons by these leptons or by electrons accelerated in individual or colliding PWN shocks (e.g. Bednarek and Sitarek 2007). The γ-ray spectra in the case of curvature radiation are expected to feature cut-offs at a few GeV. Therefore, this process is compatible with the GC spectra observed with *Fermi*/LAT (Abdo et al. 2010c), but is not expected to be responsible for the VHE γ-ray emission from Terzan 5 detected by H.E.S.S. However, following Venter et al. (2009), this model might very well give rise to γ-ray emission in the VHE band due to IC up-scattering of stellar or CMB photons. Assuming a magnetic field strength of 10 μG and a distance of 5.9 kpc this model would need a population of 175±32 MSPs to result in the observed flux above 1 TeV, which is in agreement with the prediction based on the GeV flux measured by *Fermi*.

Compared to leptonic emission in the pulsars' magnetospheres, re-accelerated electrons in colliding PWN shocks would give rise to γ-ray emission on much larger spatial scales (a few arcmin, Bednarek and Sitarek 2007), which is more in agreement with the observed VHE γ-ray extension. Scaling their model with a distance of 5.9 kpc and assuming a population of 175 MSP with an individual spin-down power of 10^{34} erg s^{-1} each, the predicted flux is comparable to the observation. It has to be noted here, that none of the MSP models can predict the apparent offset of the VHE source from the GC core, as the IC intensity is supposed to follow the density distribution of the target photon field, which is centered and radially symmetric for GCs. However, an inhomogeneous diffusion of the re-accelerated electrons in the scenario described by Bednarek and Sitarek (2007) could give rise to the observed morphology. This might be due to an inhomogeneous distribution of matter in the surroundings of the GC. The analysis of molecular line radio data, tracing the ISM density, could provide proof for such an assumption.

Now that the first GC is potentially detected at VHE γ-ray energies, the question remains if this contradicts a general scenario for emission from GCs, as there have been only upper limits measured from other Galactic GCs before. The published upper limit for the integral VHE γ-ray flux of 47 Tuc is $I_{47\mathrm{Tuc}}(> 0.8\ \mathrm{TeV}) < 6.7 \times 10^{-13}\mathrm{cm}^{-2}\mathrm{s}^{-1}$ (99% confidence level, Aharonian et al. 2009). This can be compared to the measured integral flux from Terzan 5 of $I_{\mathrm{T5}}(> 0.8\ \mathrm{TeV}) = 2.8 \times 10^{-13}\mathrm{cm}^{-2}\mathrm{s}^{-1}$, which is below that limit. Therefore, Terzan 5 does not necessarily stand out among the Galactic GC populations. The scaling factor needed to compare these fluxes depends on the distances and the MSP populations of both GCs, which both may be subject to rather large uncertainties.

Hadronic scenario Following Atoyan et al. (2006), in an hadronic scenario the energy in CRs (E_{pp}) that is needed to explain the observed γ-ray luminosity L_γ can be estimated as

$$E_{pp} = L_\gamma \tau_{pp} \eta^{-1} (1 + S). \tag{5.1}$$

Here $\eta \approx 1/3$ is the fraction of the CR energy converted into neutral pions and $S \approx 5$ accounts for CR protons with energies outside the range probed by the H.E.S.S. observation. The cooling timescale due to inelastic proton–proton collisions (τ_{pp}) can be calculated as

$$\tau_{pp} = \left(K_{pp}\sigma_{pp} c\, n_{\mathrm{H}}\right)^{-1}, \tag{5.2}$$

with the inelasticity $K_{pp} \approx 0.5$, the total inclusive $pp \rightarrow \pi^0 + X$ cross section σ_{pp}, and the ambient ISM density n_{H} (Atoyan et al. 2006). According to the data collected by Dame et al. (2001), the molecular gas density at the location of Terzan 5 is negligible. Therefore, an ambient density $n_{\mathrm{H}} = 0.1$ cm^{-3} is assumed, which corresponds to the mean value in the Galactic plane (Dickey and Lockman 1990). The above assumptions yield a total CR energy requirement of $E_{pp} \approx 10^{51}$erg, which is a factor of 5 to 10 larger than expected from typical SNRs, and thus would require very high conversion efficiencies from the kinetic energy of the ejecta to CR acceleration.

A scenario where such high conversion efficiencies would be expected are remnants of short GRBs resulting from a neutron stars merger (see e.g. Nakar 2007). Following Atoyan et al. (2006), the transfer of the kinetic energy into CR acceleration is expected to be very efficient in the relativistic shocks present in the remnants of these extremely violent events. The age t of such a remnant can be estimated from its extension, as the CRs are subject to diffusion (see Sect. 2.5). With the radius of the remnant r and the diffusion coefficient D, the age of the GRB is

$$t = \frac{r^2}{2D}. \tag{5.3}$$

The apparent intrinsic source extension of $\sim$0.1° translates into a radius $r \approx 10$ pc at a distance of 5.9 kpc. The energy threshold of the VHE data analysis of 200 GeV yields a primary CR energy of $\sim$2 TeV. Using the diffusion coefficient for CR transport in the form $D_{\mathrm{ISM}}(E) = D_{10} \cdot (E/10\,\mathrm{GeV})^s$ (see Sect. 2.5.1) with $s = 0.5$ and $D_{10} = 0.3 \times 10^{27}\mathrm{cm}^2\mathrm{s}^{-1}$ (Atoyan et al. 2006), a GRB age of $t \approx 4 \times 10^3$ years is needed. This timescale can then be compared to the estimated rate of short GRBs in the Milky Way. The rate of short GRBs was measured as 10 Gpc^{-3}yr^{-1} with BATSE data (Nakar 2007). Furthermore, the density of Milky Way like galaxies in the local Universe is 10^{-2}Mpc^{-3} (Cole et al. 2001). To compare the total rate of such events with observations, the beaming factor $f_{\mathrm{b}} = \Omega_{\mathrm{b}}/4\pi$ has to be taken into account. Here Ω_{b} denotes the solid angle covered by the beam of the emitted radiation. For short GRBs f_{b} is estimated to be close to 100 (Nakar 2007). The quantities given above yield a total expected rate of short GRBs in one Milky Way-like galaxy of one event per 10^4 years. This timescale is a factor of $\sim$3 larger than the estimated age of the GRB, based on the VHE γ-ray extension of the source. However, the CR diffusion in the vicinity of Terzan 5 strongly influences the age estimation, but is a poorly known quantity and might differ from the above assumptions.

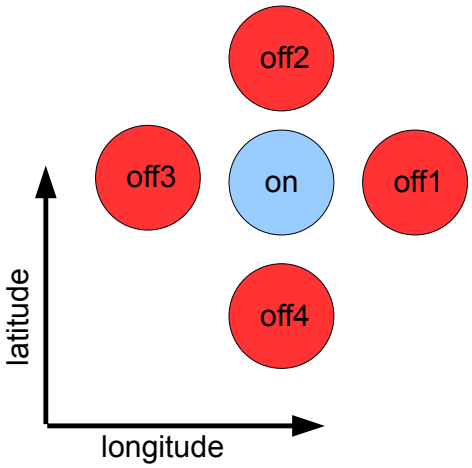

Figure 5.4: A scheme showing the arrangement of on and off positions around each GC. The offset positions are aligned to the Galactic coordinate system.

5.2.2 H.E.S.S. stacking analysis of Galactic GCs

Except for Terzan 5, no individual GC showed significant excess emission in the VHE γ-ray band. To determine whether the ensemble of the 17 non-detected GCs might be a population of weak emitters, a stacking analysis was performed. In addition to the point source analyses performed on the on-source positions, for each of the GCs the same analysis was also run for four offset positions[3]. These off-source regions are aligned to the Galactic coordinate system with offsets of 0.3° in each coordinate (see Fig. 5.4). This allows to compare the on-source results with background regions that feature a very similar Galactic distribution. Furthermore, systematic effects connected to the detected excess emission can be studied, such as a potential dependence of the flux on the distance to the Galactic plane. The off-regions are numbered such that region 2 is always farthest away from the plane, i.e. the absolute value of the b is largest, and region 4 is the closest to the plane. Region 1 and 3 are shifted by $\pm 0.3°$ in longitude, respectively. Fig. 5.4 thus shows the arrangement for GCs above the plane. To simplify the stacking, a "background livetime" t_{bg} was defined for each test position, that also includes the area scaling factor arising from the reflected background method:

$$t_{\mathrm{bg}} = t_{\mathrm{src}} \times \frac{A_{\mathrm{bg}}}{A_{\mathrm{src}}}. \tag{5.4}$$

Here t_{src} is the total exposure of the test position and A_{src}, A_{bg} are the areas of the extraction regions for source and background estimation, respectively. To determine the significance of the stacked signal, the source and background counts as well as the source and background livetimes $(t_{\mathrm{src}}, t_{\mathrm{bg}})$ each were summed over all contributing sources. Like for individual sources, the total significance of the stack was calculated

[3]for both on and off positions an extraction radius of 0.1° was used

following Li and Ma (1983) but using now the total stacked values for source and background counts and the ratio of the total livetimes $\alpha = t_{\mathrm{src,tot}}/t_{\mathrm{bg,tot}}$. The stack comprises runs with a total livetime of ∼346 hours, and the resulting significances for the five test positions are given in Tab. 5.2. Judging from these values the signals from each of the test positions are compatible with zero emission. Comparing off-regions 2 and 4, there is also no evidence for a dependence of the excess signal on the distance to the Galactic plane.

To identify the most promising candidates in the sample, for each GC a weight was calculated as

$$w = \frac{\sqrt{t_{\mathrm{src,tot}}}}{d}, \tag{5.5}$$

where d denotes the distance to the GC, as listed in the catalog of Harris (1996). These weights are motivated by the fact that the significance scales with the square root of the excess counts, which are proportional to $d^{-2} \cdot t_{\mathrm{src,tot}}$. Of course, depending on the assumed VHE γ-ray emission mechanism, other properties of the GCs may play a role, such as the total number of MSPs (see Sect. 5.1). However, as the potential emission scenario for GCs is not settled yet, these weights were defined without any additional parameters. Table. 5.1 lists the GCs ordered according to decreasing weights. In Fig. 5.5 the cumulative significance of the stack is shown, depending on the number of contributing sources, by following the order given by the weights. Therefore, the most promising datasets are stacked first. The rather featureless behavior of the stacked significance with increasing source count might indicate that a subset of contributing sources that provide a significantly stronger signal compared to the rest does not exist. This conclusion, however, strongly depends on the ordering scheme of the sources, and could change if more information is available on the actual emission scenario.

Table 5.2: Total stacked significances for on and off positions

Test position	stacked significance
on	1.7 σ
off1	0.2 σ
off2	1.9 σ
off3	-0.8 σ
off4	2.3 σ

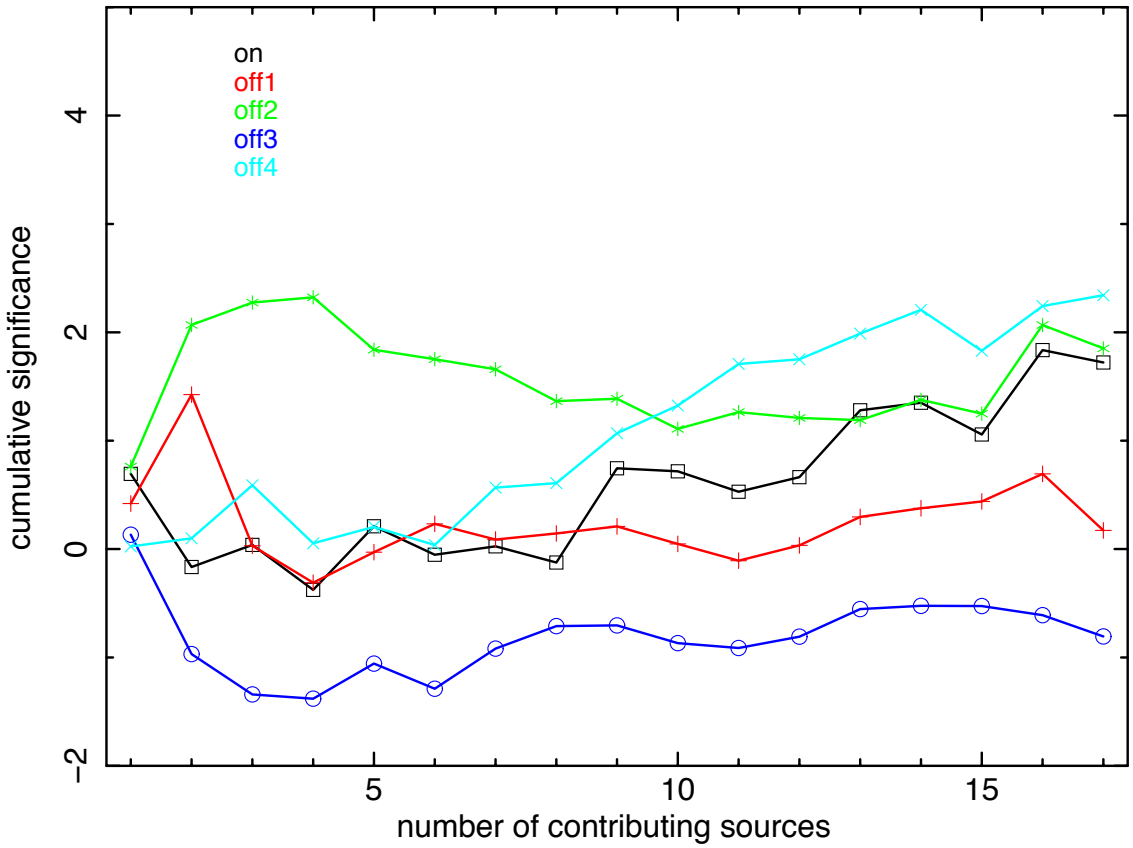

Figure 5.5: Cumulative significance of the stack as a function of the number of contributing sources. The order of the GCs follows Tab. 5.1 (see also text).

5.3 Search for non-thermal X-ray emission from Galactic GCs

The analysis of X-ray data of GCs was motivated by the possible association of VHE γ-ray emission with Terzan 5. For instance, the detection of diffuse synchrotron emission in the X-ray band could confirm the interpretation of the VHE signal as leptonic emission from relativistic electrons. However, the presence of extended emission from GCs, arising from a wide variety of thermal and non-thermal processes, is already very well established. To distinguish any potential synchrotron signal from such contributions might be challenging. In this section first the various emission mechanisms are introduced, that are discussed in the context of extended X-ray emission from GCs. This is followed by an analysis of observational data of six GCs, presented in sects. 5.3.1 and 5.3.2.

GCs are expected to contain intracluster gas originating from the mass loss of evolved stars. Since GCs move through the Galactic halo medium with typical velocities of $\sim$200 km s^{-1}, bow shocks should form in front of them in the direction of their proper motion (Krockenberger and Grindlay 1995). These shocks have the ability to both accelerate particles and heat the gas behind them. In this scenario, electrons accel-

erated at the bow shock could produce diffuse non-thermal X-ray emission because of either IC scattering on ambient photon fields (Krockenberger and Grindlay 1995) or non-thermal bremsstrahlung resulting from the deflection of the electrons by ISM nuclei (Okada et al. 2007, henceforth Ok07). Also, diffuse thermal X-ray emission can be emitted from shock-heated material trailing behind the moving GC. For a detailed discussion of the bow shock scenario, see Ok07.

The first unresolved diffuse X-ray emission from GCs (47 Tuc, ω Cen, and M 22) was reported by Hartwick et al. (1982) using the *Einstein* observatory, which was later confirmed by Krockenberger and Grindlay (1995) with *ROSAT*. Recently, using *Chandra* data, Ok07 detected significant diffuse X-ray emission from the GCs 47 Tuc, NGC 6752, M 5, and ω Cen. They find that the diffuse source at the position of ω Cen is likely to be a background cluster of galaxies. A similar extra-Galactic nature is proposed for the source coincident with 47 Tuc by Yuasa et al. (2009). The remaining potentially GC-associated diffuse X-ray emission, from M 5 and NGC 6752, could arise from different scenarios. The emission in M 5 features an arclike morphology and exhibits a thermal spectrum (kT<0.1 keV), possibly from shock-heated gas. The clumpy structure seen near NGC 6752 presents a hard non-thermal spectrum ($\Gamma \sim 2$) and a radio counterpart, maybe from non-thermal bremsstrahlung emission by shock-accelerated electrons hitting nearby gas clouds (Ok07).

Non-thermal emission in the X-ray band may also be associated with compact objects, either directly, as detected from isolated low-mass X-ray binary systems (see for instance Wijnands et al. 2005, for such a candidate system in Terzan 5), or as secondary emission from the population of high-energy particles they would generate. This was modeled for millisecond pulsars by Venter and de Jager (2008, henceforth VJ08) for the synchrotron radiation mechanism. The second case may translate into larger physical scales, due to the diffusion of the energetic particles away from their source. The populations of compact objects in GCs may provide an opportunity to test these scenarios. Apparent extended X-ray emission from the direction of GCs might also arise from a population of faint unresolved point-like sources below the detection limit of the observing instrument.

5.3.1 Detection of diffuse X-ray emission from Terzan 5

Especially the GC Terzan 5 poses an interesting target to search for extended non-thermal X-ray emission, due the detection of a VHE γ-ray signal possibly related to this source (see Sect. 5.2.1). In this section the results from our already published analysis are presented (Eger et al. 2010). We analyzed an archival *Chandra* observation to search for a diffuse emission component associated with Terzan 5 above the Galactic background. The X-ray signal was characterized using spatially resolved spectral analyses, after a careful study of the diffuse Galactic background. The detected signal is discussed in the context of various emission scenarios.

5.3.1.1 Chandra observation and data preparation

To search for extended diffuse X-ray emission from Terzan 5, we analyzed the ACIS data of an archival 40 ks *Chandra* observation (ObsID 3798), which was originally performed to characterize the faint X-ray point-source population of this GC (Heinke et al. 2006, henceforth H06). Only the ACIS-S3 chip was switched on, so we were only able to search for diffuse X-ray emission at angular distances $<4'$ from the cluster core. A comprehensive study of diffuse X-ray emission seen from a number of Galactic GCs was performed by Ok07. However, these authors excluded Terzan 5 from their work because the only available *Chandra* dataset at that time suffered from serious pile-up effects due to a bright binary outburst in the field of view (FoV). In this work we analyzed data from a newer observation where such an event did not occur.

For the X-ray analysis we used the CIAO software version 4.1 (Fruscione et al. 2006), supported by tools from the FTOOLS package (Blackburn et al. 1993) and XSPEC version 12.5.0 for spectral modeling (Arnaud 1996). The `event1` data were reprocessed with the latest position and energy calibration (CTI correction, v4.1.3) using bad pixel files generated by `acis_run_hotpix`. The good-time-interval (GTI) file supplied by the standard processing, which was used by H06, screens out a $\sim$4.0 ks interval of strong background flaring at the end of the observation. To remove an additional time period of 4.3 ks with a slightly increased background level, we used the light curve in the 0.5–7.0 keV energy band after the core region of the cluster and additional bright sources were removed from the data. A screening threshold of 1.0 cts/s yielded a net exposure of 31.0 ks. We chose these stricter criteria with respect to H06 because understanding the background is crucial for analyzing faint extended sources.

5.3.1.2 Extraction regions

To detect and remove point-like X-ray sources from the event-list, we ran `wavdetect` on the GTI-screened dataset in three energy bands (0.5–2.0 keV, 2.0–7.0 keV and 0.5–7.0 keV). H06 used `pwdetect` for the detection within r_h and `wavdetect` for outer regions. In this work we only analyzed areas outside r_h, so results should be comparable. We estimated a point-source detection limit of $\sim 2\times10^{-15}$ erg cm^{-2} s^{-1} in the 0.5–7.0 keV band. For the most part our results are compatible with the sources listed by H06 (their table 2). However, the shorter exposure time compared to the analysis of H06 led to a higher point-source detection threshold. Therefore we did not detect the faintest seven sources from H06 that we introduced manually into our source list. Sources were removed from the dataset using the 3σ radius of the point spread function. Additionally, all events within r_h were disregarded.

To measure the level of diffuse X-ray emission around Terzan 5, we extracted spectra from eight concentric annular regions centered on the cluster core with radii from $1.1'$ to $3.9'$ (Fig. 5.6). Each ring has a width of $0.4'$. We chose rings with equal width over rings with constant area to have comparable statistical quality in the spectra since

the surface brightness decreases with distance from the GC. For the spectral analysis, we chose the 1–7 keV energy band. Widening the band in either direction led to lower signal-to-noise ratios. At lower energies an increased contribution to the signal from soft thermal Galactic diffuse emission is expected. At energies above 7–8 keV the charged particle-induced background component increases significantly for instruments onboard *Chandra*. For the extraction of spectra, we employed the same methods as already described in Sect. 4.3.3. To subtract the NXB, we used a background dataset provided by the calibration database, where the detector was operated in stowed position. The background spectrum for each ring was extracted from the respective region in this NXB dataset. To account for the time dependence of the NXB, we scaled the background by the ratio of the source and background count rates in the 9–12 keV energy band for each spectrum (as described by Markevitch et al. 2003).

To produce an image of diffuse X-ray emission above the particle background from the direction of Terzan 5, we extracted counts in the 1–7 keV energy band and refilled the excluded source regions and the region inside r_h with `dmfilth` using the photon distributions from rings around the excluded areas. We subtracted the particle background using the corresponding image from the stowed dataset after correction for the different exposures. The resulting image was corrected for relative exposure and adaptively smoothed with `asmooth`. We required a minimum significance of 3σ for the kernel size of the smoothing algorithm. The resulting smoothing radii were a few arcminutes, so that no details smaller than that scale can be seen in the smoothed image. Figure 5.6 shows the resulting image together with all extraction regions that we used in this work.

Even though a significant contribution from thermal Galactic diffuse emission is expected, the spectra from the single rings were fit well enough by an absorbed power-law model for a preliminary flux estimate. The resulting fit parameters are given in Table 5.3. We found significant diffuse excess emission above the NXB in all rings and derived the surface brightness for each region by dividing the model flux by the effective extraction area, which is the geometric ring area inside the FoV minus excluded regions and bad pixels. Due to limited statistics, we fixed the column density at a default value of $N_H = 1{\times}10^{22}$ cm^{-2}. Therefore, we list the observed surface fluxes in Table 5.3, as opposed to the intrinsic fluxes we provide for all other spectra. The diffuse surface flux shows a clear radial dependence (Fig. 5.7), which indicates that a significant part of the excess is connected to the cluster. At distances greater than $\sim$170″ from the GC core, the observed surface flux seems to reach a base level of $F_{x,surf} \approx 1.5{\times}10^{-18}$ erg cm^{-2} s^{-1}arcsec^{-2} (1–7 keV). In the following section we derive the unabsorbed surface flux for the outer region by applying a more realistic physical model.

5.3.1.3 Galactic diffuse background

Terzan 5 is close to the Galactic plane where diffuse Galactic emission becomes an important component. However, the *Chandra* blank-sky datasets are composed of observations towards high Galactic latitudes, which would underestimate the sky back-

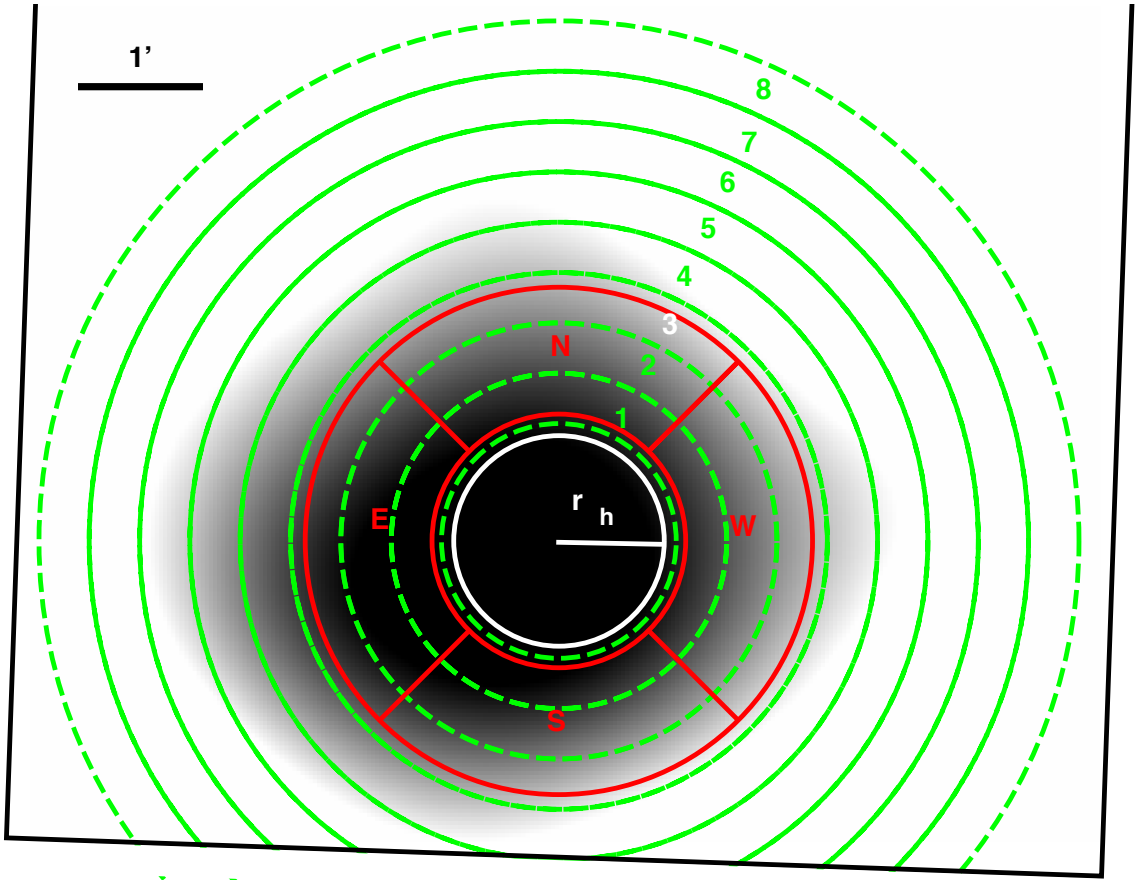

Figure 5.6: Smoothed, exposure corrected and NXB subtracted *Chandra* image of diffuse X-ray emission in the 1–7 keV band around Terzan 5. Excluded regions from point sources and the region inside r_h (white circle labeled r_h) were refilled (see text). The wings seen towards the north, east and west are only marginally significant and might be artifacts of the smoothing algorithm. The FoV for this observation is drawn as a box (black). Shown are the eight annular extraction regions (dashed green lines, numbered 1 to 8) and the four pie-shaped regions (solid red lines, labeled N, E, S and W). The color scaling is linear and chosen such that the Galactic diffuse level is saturated as white. Thus only emission above the Galactic diffuse level appears in gray scales.

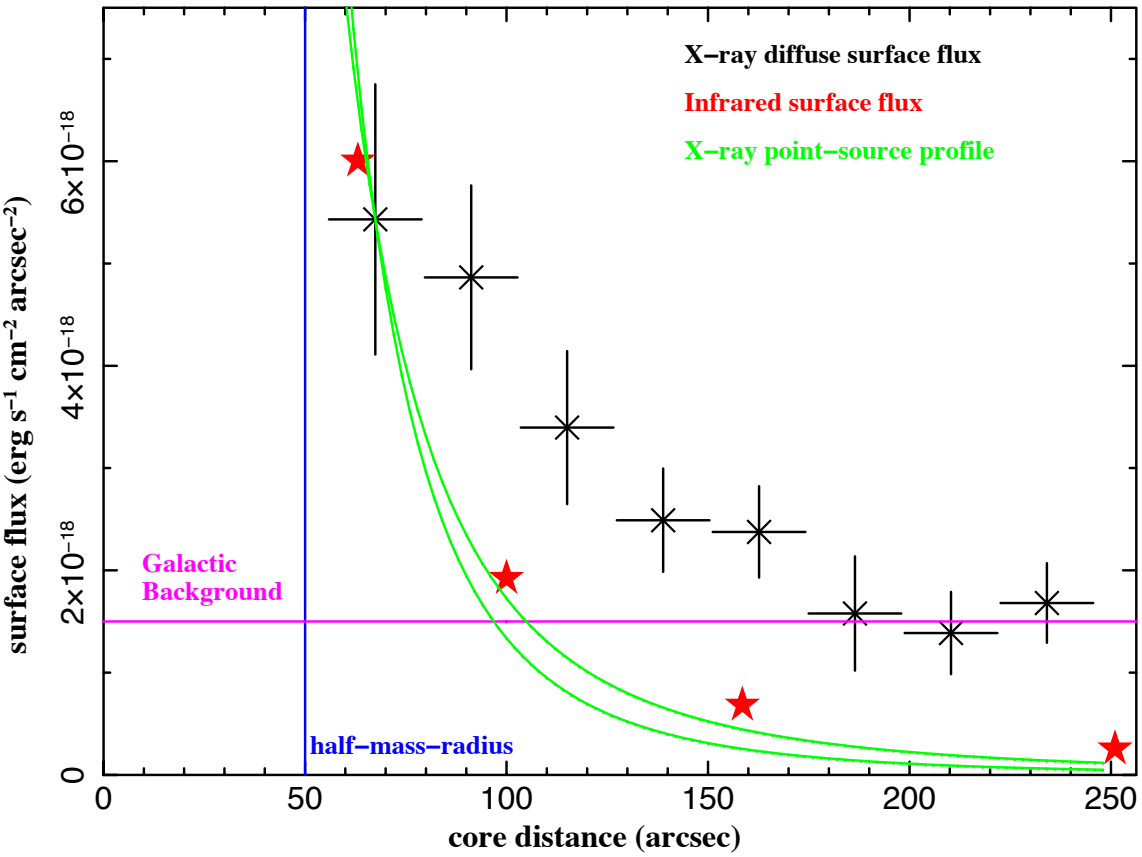

Figure 5.7: Radial dependence of the observed diffuse X-ray surface flux above the particle background in the 1–7 keV band as seen with *Chandra* (black crosses with error bars). Stars (red) denote the infrared surface brightness profile from Trager et al. (1995). The solid curves (green) show the X-ray point-source distribution described by a generalized King profile (Heinke et al. 2006) for the two extreme cases q =1.43±0.11. All profiles are scaled to match the first diffuse X-ray data point, using an exponential fit in the case of the infrared data. The vertical (blue) and the horizontal (magenta) line denote r_h (Harris 1996) and the Galactic diffuse background level, respectively.

ground in our case. To test whether the spectrum observed from the outer three rings is compatible with thermal Galactic diffuse emission, we used a more physically reasonable model. Similar to Kaneda et al. (1997) and Ebisawa et al. (2005), who modeled the diffuse Galactic ridge emission as observed with *ASCA* and *Chandra*, respectively, we describe the Galactic diffuse component using a two-temperature (2-T) non-equilibrium ionization model (NEI) (Masai 1984). To improve the statistical quality, we combined the outer three (175″–246″) rings into a single spectrum. The spectrum was adaptively binned to a minimum of 20 excess counts per bin. As background we again used the spectrum extracted from the same region in the NXB dataset. We fitted a 2-T NEI model to the outer spectrum, freezing most of the parameters to the best-fit values from Table 8 in Ebisawa et al. (2005). We left the surface brightnesses of the two components and the N_H free to vary to account for the difference in flux and column density between the region around Terzan 5 and the area observed by Ebisawa et al. (2005). In addition, we allowed the Si-abundance of the soft component as a free fit parameter, because otherwise the low-ionized Si line at ∼1.8 keV (Kaneda et al. 1997; Ebisawa et al. 2005) was underestimated.

The spectrum of the outer region together with the model fit is shown in Fig. 5.8 (*Top*). To be able to compare our results to the analysis of Ebisawa et al. (2005), we chose an energy range of 0.7–10 keV in this specific case. The best-fit values are given in Table 5.3 (*Outer* region). The total intrinsic surface flux of the two components is a factor of three lower than the value for the Galactic region observed by Ebisawa et al. (2005). This relation is in good agreement with the ratio between the column densities for both regions, which is ∼4 (Dickey and Lockman 1990). Assuming that the Galactic column density seen from a certain direction is directly related to the expected flux from a diffuse Galactic component, we conclude that at least ∼3/4 of the total excess above particle background observed from the outer region comes from Galactic diffuse emission.

5.3.1.4 Diffuse excess emission connected to Terzan 5

In this section we focus on the diffuse emission observed from the inner five rings (55″–175″). In addition to the radial dependence of the diffuse excess emission, Fig. 5.7 shows the infrared surface brightness profile (Trager et al. 1995) and the X-ray point-source distribution (King profile from Heinke et al. 2006). Both profiles are scaled to match the first diffuse X-ray data point, using an exponential fit in the case of the infrared data.

To investigate the nature of the diffuse excess emission observed from the inner region in more detail and to improve the statistical quality, we extracted the combined spectrum from the inner five rings (55–175″). As a first step we fitted the same 2-T NEI model to the NXB subtracted inner spectrum, binned to a minimum of 20 excess counts per bin, as was done for the outer region in the previous section. The resulting surface fluxes of the two components are listed in Table 5.3 (*Inner* region). Following the same argument as in the previous section, we estimate that in this case only ∼1/3

Table 5.3: Extraction regions and results from spectral fitting

Region	Distance range[1] (arcsec)	Angular range[2] (deg)	Excess counts[3]	NEI: $F_{x,surf}$[4] (10^{-7} erg cm^{-2} s^{-1} sr^{-1})	NEI: kT[5] (keV)	PL: $F_{x,surf}$[6] (10^{-7} erg cm^{-2} s^{-1} sr^{-1})	PL: Γ[7]	χ^2_ν(d.o.f.)[8]
Ring 1	55–79	0–360	195.2±26.5	–	–	1.01±0.25	1.8±0.4	–/1.3(15)
Ring 2	79–103	0–360	278.6±31.1	–	–	0.91±0.17	2.1±0.5	–/0.7(26)
Ring 3	103–126	0–360	274.8±33.3	–	–	0.64±0.14	2.2±0.6	–/1.2(27)
Ring 4	126–150	0–360	259.9±34.2	–	–	0.47±0.09	3.0±0.8	–/0.9(24)
Ring 5	150–174	0–360	276.7±35.3	–	–	0.44±0.08	2.9±0.7	–/1.4(26)
Ring 6	174–198	0–360	192.7±34.7	–	–	0.30±0.10	2.8±0.8	–/0.9(19)
Ring 7	198–222	0–360	227.5±36.2	–	–	0.26±0.08	3.6±1.2	–/1.2(22)
Ring 8	222–246	0–360	240.3±37.5	–	–	0.31±0.07	3.5±1.2	–/1.0(23)
Inner	55–174	0–360	1273.5±115.8	1.34±0.14 (soft)	0.59 (soft)	1.17±0.16	0.9±0.5	1.1(52)/1.3(50)
		0–360		5.36±0.80 (hard)	5.0 (hard)	–	–	
Outer	175–246	0–360	825.3±62.5	0.58±0.19 (soft)	0.59 (soft)	–	–	1.2(36)/–
		0–360		2.1±0.7 (hard)	5.0 (hard)	–	–	
North	60–120	45–135	191.0±26.4	–	–	1.44±0.63	1.5±1.0	–/1.0(45)
East	60–120	135–225	176.1±26.7	–	–	2.10±0.70	0.6±0.7	–/0.9(44)
South	60–120	225–315	230.1±27.0	–	–	2.46±0.72	0.8±0.7	–/0.8(47)
West	60–120	315–45	165.2±27.1	–	–	2.10±0.75	1.7±1.1	–/1.0(45)

[1]Inner and outer radii of the region. [2]Angular range of the region. [3]Excess counts after background subtraction. [4]Intrinsic 0.7–10.0 keV surface flux of the two thermal components. [5]Temperatures of the two thermal components. [6]Surface flux (1–7 keV) resulting from an absorbed power-law fit. [7]Spectral index resulting from an absorbed power-law fit. [8]Reduced χ^2 (d.o.f) for both models.

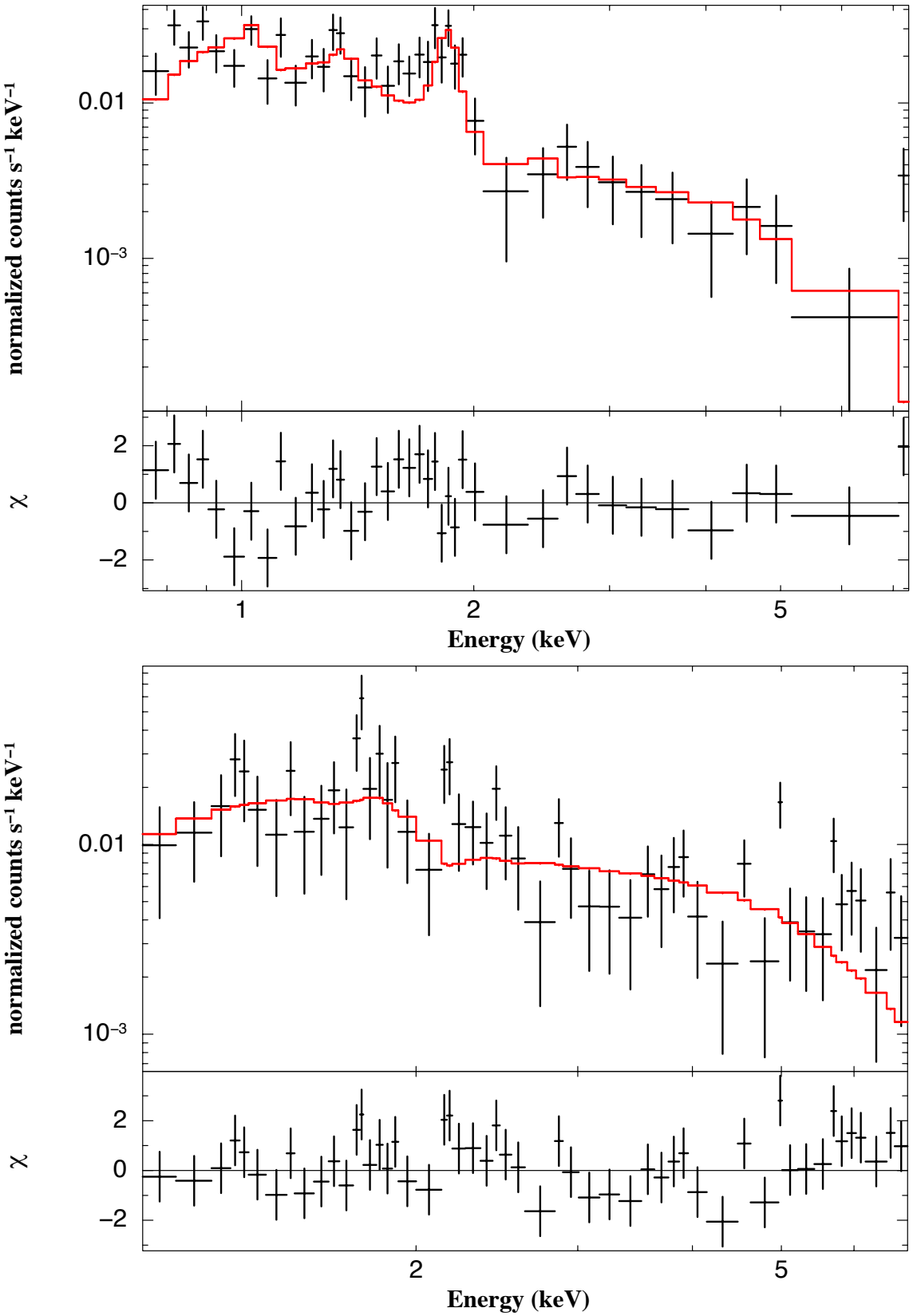

Figure 5.8: *Top*: *Chandra* spectrum from the outer annulus (175″–246″) with a 2-temperature non-equilibrium ionization model fit (stepped red line). All parameters are fixed to the values from Ebisawa et al. (2005) except for the surface brightnesses of the two components. *Bottom*: *Chandra* spectrum from the inner annulus (55″–175″) with the spectrum from the outer annulus subtracted as background. The fit is an absorbed power-law model (red stepped line). The parameters for both fits are given in Table 5.3.

of the total observed emission is of diffuse Galactic origin. Together with the surface brightness showing a clear radial dependence with respect to the core of Terzan 5, we conclude that a significant part of the observed flux is connected to the GC.

As an estimate for the Galactic diffuse background component, we subtracted the outer (175–246″, see previous section) from the inner spectrum. Figure 5.8 (*Bottom*) shows the resulting excess spectrum from the inner region, binned to a minimum of 20 excess counts per bin, together with an absorbed power-law model fit. The spectral parameters are collected in Table 5.3 (*Inner* region). Fitting a thermal plasma (MEKAL, χ^2_ν = 1.4(50)) or a thermal bremsstrahlung model (BREMSS, χ^2_ν = 1.4(50)) to the spectrum resulted in temperatures of kT>17 keV and kT>25 keV, respectively. The most prominent feature of the Galactic thermal emission observed from the outer region is an emission line, centered at ∼1.8 keV. Introducing a Gaussian line at that energy or an additional thermal component to the excess spectrum from the inner annulus does not significantly improve the fit (χ^2_ν = 1.2). Therefore, we conclude that the spectrum from the outer region describes the Galactic diffuse background component sufficiently. The total unabsorbed diffuse excess flux in the 1–7 keV band measured from the inner region above the Galactic background is $F_X = (5.5\pm0.8)\times10^{-13}$ erg cm^{-2} s^{-1}. Assuming a distance of 5.5 kpc the intrinsic luminosity is $L_X = (2.0\pm0.3)\times10^{33}$ erg s^{-1}.

We found no indication of a variation in the spectral index with increasing radius, when subdividing the inner region into two or more sub-regions. Furthermore, there is no evidence of a directional variation in the index and flux. Table 5.3 (*north, east, south*, and *west* regions) illustrates the result for directional dependence of spectra extracted from pie-shaped regions towards the north, east, south and west with respect to the cluster center (Fig. 5.6). Their inner and outer radii are 60″ and 120″, respectively. The latter value was chosen such that the southern region is not truncated by the border of the FoV. As background we again used the spectrum from the outer annulus. A similar result was achieved when the regions were rotated by 45°.

5.3.1.5 Origin of the diffuse emission

The present results indicate GC-centered diffuse hard X-ray excess emission above Galactic background, which extends significantly beyond r_h. In this section we briefly discuss standard thermal and non-thermal emission scenarios, leaving out more exotic possibilities, as described by, e.g., Domainko and Ruffert (2005). Throughout this section we use a distance to Terzan 5 of 5.5 kpc. The larger distance estimate (8.7 kpc) would increase the energy requirements for the models by a factor of 2.5.

Contribution from unresolved point sources The luminosity of unresolved point sources inside r_h has been estimated by Heinke et al. (2006) to 8×10^{32} erg s^{-1}. They furthermore determined the spatial surface distribution of X-ray sources in Terzan 5 to $S(r) \propto (1 + (r/r_c)^2)^{(1-3q)/2}$ with q =1.43. From this distribution we expect to find in the 1–3 arcmin annulus only 9% of the luminosity of unresolved point sources

within r_h. The expected 7×10^{31} erg s^{-1} is much lower than the measured emission $(2.0\pm0.3)\times10^{33}$ erg s^{-1}, so we conclude that the contribution from unresolved point sources is negligible.

Synchrotron radiation One possibility for producing non-thermal emission by relativistic electrons is synchrotron radiation (SR), which would radiate at a frequency $\nu_{\rm syn}=120\,(\gamma/10^4)^2\,(B/1\mu{\rm G})\,\sin(\phi)$ MHz, where B is the strength of the magnetic field, γ the Lorentz factor of the electrons, and ϕ the pitch angle between the magnetic field and the electron velocity (Ok07). Following Ok07, electrons with an energy of $\sim10^{14}$ eV would be needed to produce SR emission in the keV regime for typical Galactic magnetic field strengths of a few μG. The population of MSPs in the center of Terzan 5 was suggested as a continuous source of such highly energetic electrons (Bednarek and Sitarek 2007; Venter et al. 2009). These particles propagate to the observed extent of the diffuse emission of $3'$ (4.8 pc) on a timescale of $t_{\rm diff}=3\times10^3\,B_{1\mu{\rm G}}$ years, assuming Bohm diffusion (VJ08). The cooling of electrons with energies of $\sim10^{14}$ eV in GCs is dominated by SR emission with typical cooling times of $t_{\rm cool}\approx3\times10^4\,B_{1\mu{\rm G}}^{-2}$ years (VJ08). Assuming an injection spectrum with index -1, SR cooling, which depends linearly on the energy of the electrons, should change the index to -2. Since no such steepening of the spectrum is observed at the 2σ level, $t_{\rm diff}\lesssim t_{\rm cool}$ is required, which would limit the magnetic field strength to ~1 μG or it would indicate a faster diffusion of electrons. In this scenario, the population of highly energetic electrons has to radiate the observed X-ray luminosity (2×10^{33} erg s^{-1}) on a timescale of $t_{\rm cool}$, and thus would require a total energy in these electrons of $1.8\times10^{45}\,B_{1\mu{\rm G}}^{-2}$ erg. Associated IC radiation in the TeV energy range should be detectable in spatial coincidence in the case of low magnetic field strengths $B\lesssim$ few μG, providing a possibility to test this scenario (VJ08).

Inverse Compton emission Non-thermal X-ray emission in GCs can also be produced by IC up-scattering of starlight photons by mildly relativistic electrons (Krockenberger and Grindlay 1995). The bow shock of the GC could provide these electrons (Ok07). The power of IC radiation $P_{\rm IC}$ emitted by a single electron is given by $P_{\rm IC}=4/3\,\sigma_T\,c\,\gamma^2\,u_{\rm rad}$, where σ_T is the Thomson cross section, c is the speed of light, γ the energy of the electrons, and $u_{\rm ph}$ the density of the target photon field (Krockenberger and Grindlay 1995). Therefore the intensity of IC emission is directly related to the energy density of the target photon field. GCs exhibit a very high stellar density in their core region, which decreases rapidly in their outskirts, resulting in a centrally peaked photon field as indicated with the distribution of the infrared surface brightness in Fig. 5.7. The diffuse X-ray emission presented in this work exhibits a surface brightness profile that is roughly similar to this measure of the density of the photon field. This fact is consistent with an IC emission scenario. The energy density $u_{\rm rad}$ of the stellar photon field scaling with $u_{\rm rad}\approx L_{\rm star}/(4\pi r^2 c)$ is about 40 eV/cm^3 and 5 eV/cm^3, at distances of $1'$ and $3'$ from the center of the GC, respectively. For the quantitative estimate of the total energy in electrons we adopt the model of Krockenberger and Grindlay (1995), giving 5×10^{49} ($u_{\rm rad}$/ 40 eV cm^{-3}) erg. In this scenario

the X-ray emission should be accompanied by potentially detectable SR in the radio band.

Non-thermal bremsstrahlung One additional emission process of non-thermal X-rays is non-thermal bremsstrahlung, which is produced when energetic electrons are deflected by protons and nuclei. In this scenario the flux of the emission should follow the distribution of target material. The Galactic density profile of ISM perpendicular to the Galactic plane at the relevant galactocentric distances of 1–3 kpc was constrained as a single Gaussian with a full width at half maximum of less than 200 pc and virtually no gas above 400 pc (Lockman 1984). At a distance of 5.5 kpc, Terzan 5 would be at an offset above the disk of 160 pc and thus in an ambient gas density of a few times 0.1 cm^{-3}. The total energy in non-thermal electrons required for the emission of $2{\times}10^{33}$ erg s^{-1} of diffuse X-ray emission would be about $9{\times}10^{49}(\mathrm{n_H}/0.1\ \mathrm{cm}^{-3})$ erg if an electron energy of 20 keV is assumed (Ok07). In contrast to the asymmetric morphology detected by Ok07 for GCs in a bow shock scenario, we did not find evidence of a non-uniform shape of the excess emission from Terzan 5. This scenario could be tested by searching for the presence of target material in the environment of the GC. Target material in the form of molecular clouds could be probed by carefully examining molecular emission lines that are Doppler-shifted by the relative Galactic rotation velocity at the physical location of Terzan 5.

Thermal contribution The very high fitted temperature (> 15 keV) of the diffuse X-ray emission suggests a non-thermal origin. However, at least a thermal contribution to the total excess cannot be excluded at this point. If thermal bremsstrahlung is presumed as the emission mechanism, the temperature of the plasma can be estimated from the X-ray luminosity, the volume of the emission region, and the density of the plasma (Krockenberger and Grindlay 1995). With the radius of the emission region set to 5 pc (which corresponds to $188''$ at a distance of 5.5 kpc), this leads to

$$\left(\frac{T}{10^7\,\mathrm{K}}\right) \approx \left(\frac{L_\mathrm{X}^\mathrm{th}}{1.3\times10^{33}(n_\mathrm{H}/0.1\,\mathrm{cm}^{-3})^2}\right)^2 . \tag{5.6}$$

Assuming that the observed emission is entirely thermal, i.e., $L_\mathrm{X}^\mathrm{th} = L_\mathrm{X}$, an upper bound for the temperature of the plasma can be derived. It appears that this upper bound strongly depends on the plasma density. For a typical density at the GC position of 0.1 cm^{-3} (see Sect. 3.4), the upper bound on the temperature is about 10^7 K ($\approx$ 1 keV). Only for densities lower than 0.05 cm^{-3} can the temperature exceed 15 keV.

To heat plasma to such high temperatures, strong shocks would be indispensable. The remnants of catastrophic events may release such strong shocks (see, e.g., Acero et al. (2007) for a remnant of a type IA supernova and Domainko and Ruffert (2005) for remnants of compact binary mergers). It was proposed that Terzan 5 may host the required mergers; e.g., Shara and Hurley (2002) for white dwarf mergers and Grindlay et al. (2006) for neutron star – neutron star mergers. However, even supernova remnants may have difficulty producing such high temperatures, because even the hot,

thermal plasma in the young remnant of the type Ia supernova SN 1006 reaches a temperature of about 2 keV (e.g. Acero et al. 2007), significantly cooler than the temperature found for the thermal fit to the diffuse emission in Terzan 5.

If the diffuse X-ray emission is indeed thermal, it could also originate in principle from a background galaxy cluster that by chance coincides with the core of Terzan 5. Since galaxy clusters with temperatures >10 keV are very rare (e.g. Reiprich and Böhringer 2002), such a correlation appears rather unlikely.

From the available data, a contribution from thermal emission processes to the measured excess flux cannot be ruled out, but it is not likely to represent the dominant fraction.

5.3.2 Search for extended X-ray emission from other GeV-bright GCs

Terzan 5 is the brightest GC at GeV energies as seen by *Fermi* (Abdo et al. 2010c) and is so far the only GC with a possibly associated VHE γ-ray source (Sect. 5.2.1, Acero et al. 2011). Furthermore, it features diffuse and hard X-ray emission that extends beyond the half-mass-radius, which might arise from a different origin as the diffuse emission seen from a few other Galactic GCs (see previous section). Fortunately, all the GCs that are associated with γ-ray sources detected by *Fermi* were also observed with *Chandra* and/or *XMM-Newton*. The data from other X-ray observatories, such as *Suzaku*, are not suited to study diffuse emission near GCs, due to their larger PSFs. These regions are populated by many point sources, most of them related to the GCs, which have to be removed from the datasets before a reliable study of the remaining diffuse emission can be performed. To date, only *XMM-Newton* and *Chandra* feature a sufficiently high angular resolution for this task.

Some of these X-ray data were already analyzed by Okada et al. (2007) who searched for extended and diffuse X-ray emission from GCs in a very similar way as done in the analysis of *Chandra* data of Terzan 5 presented in this work. Even though these authors did detect significant diffuse X-ray emission from six GCs, the observed signals do not feature the same characteristics as the signal detected from Terzan 5 (i.e. centered on the core, extending beyond $r_{\rm h}$, hard).

To complete the search for diffuse X-ray emission from GCs where published *Fermi* results are available (see Abdo et al. 2010c), in this work the public X-ray data of the remaining seven GCs were considered. Most of the *XMM-Newton* observations were performed in *timing* mode, where the spatial photon information along one direction is sacrificed in favor of better timing resolution. These observations were conducted to study the characteristics of variable point-sources in the GC cores, but are not suited to analyze the spatially resolved diffuse emission. The one remaining *XMM-Newton* EPIC observation in *imaging* mode (NGC 6388) was affected by single mirror reflections from a bright source outside the FoV. Thus, none of the available public *XMM-Newton* data were suited to study faint diffuse X-ray emission around the GCs considered here.

Table 5.4: *XMM-Newton* and *Chandra* observations of GeV-bright GCs

source	observations[(1)]	analysis[(2)]	comments
47 Tuc	ACIS-I,S	Ok07	r_h too large compared to FoV
ω Cen	ACIS-I, EPIC	Ok07	r_h too large compared to FoV
M 62	**ACIS-S**	Sect. 5.3.2	
NGC 6388	**ACIS-S**, EPIC	Sect. 5.3.2	EPIC: single mirror reflections
Terzan 5	**ACIS-S**	Sect. 5.3.1	
NGC 6440	ACIS-S, EPIC	Ok07	
NGC 6441	ACIS-S, EPIC-TI	Sect. 5.3.2	Bright point-like source
NGC 6541	**ACIS-S**	Sect. 5.3.2	
NGC 6624	ACIS-S, EPIC-TI	Sect. 5.3.2	ACIS only grating observations
M 28	ACIS-S	Ok07	
NGC 6652	ACIS-S, EPIC-TI	Sect. 5.3.2	ACIS only very low exposure
NGC 6752	ACIS-S	Ok07	
M 15	ACIS-S, EPIC-TI	Sect. 5.3.2	Bright point-like source

[(1)]Names of the instruments/modes onboard *XMM-Newton* (EPIC) and *Chandra* (ACIS) used for the observations (for more information on these instruments see Sect. 3.4). EPIC-TI means that the camera was not operated in imaging but in timing mode. The data analyzed in this work are highlighted in boldface. [(2)]This column indicates whether the respective data were considered in this work or were analyzed by Okada et al. (2007, Ok07).

With *Chandra* one of the GCs (NGC 6624) was only observed with grating observations, which is also not suited for the purpose of this work. Furthermore, two ACIS observations (NGC 6441 and M 15) show one or more very bright point-like sources in the cores of the GCs. Even though only regions outside of the half-mass-radius of the GCs will be considered in the following analyses, sufficiently bright point sources in the core can still contaminate these regions due to the broad wings of the PSF. The ACIS-S data of NGC 6652 provide only a very short exposure (<10 ks), and thus were also not used in this work. Therefore, apart from the ACIS-S data of Terzan 5 (see Sect. 5.3.1), three ACIS-S datasets (NGC 6388: ObsID 5505, M 62: ObsID 2677, and NGC 6541: ObsID 3779) remain and are suited to search for faint diffuse X-ray emission around the GCs. Table 5.4 lists all the available *XMM-Newton* and *Chandra* data, where these observations are highlighted in boldface.

In the analysis of these three ACIS-S datasets, the same methods were employed as for the *Chandra* observation of Terzan 5 (for a detailed description see Sect. 5.3.1). To search for diffuse X-ray emission on the same spatial scales as seen from Terzan 5, the same annular extraction regions were used, with the same radii in units of the half-mass-radii r_h. For each of the three GCs the radii of the annuli r_i were calculated as

$$r_\mathrm{i} = r_\mathrm{i,T5} \cdot \frac{r_\mathrm{h}}{r_\mathrm{h,T5}}. \tag{5.7}$$

Here $r_{\mathrm{i,T5}}$ denotes the radius of the respective region used for Terzan 5, and r_{h}, $r_{\mathrm{h,T5}}$ are the half-mass-radii of the analyzed GC and that of Terzan 5, respectively. Figure 5.9 shows the measured surface fluxes (1–7 keV) from the three GCs as black data points. None of the observed GCs shows a significant enhancement of excess emission towards smaller radii. Based on the excess surface fluxes measured from Terzan 5 above the Galactic background, for each of these GCs a predicted flux can be calculated by scaling by the relative distance and other parameters that are supposed to influence the expected emission. Assuming that the MSP population is directly related to the observed X-ray emission, here the relative photon flux measured by *Fermi* was used (Abdo et al. 2010c) as the only scaling factor. This takes into account both the relative distance as well as number of MSPs. The expected X-ray excess surface flux in each annulus (F_{X}), calculated by rescaling the Terzan 5 measurement ($F_{\mathrm{X,T5}}$) then is:

$$F_{\mathrm{X}} = F_{\mathrm{X,T5}} \cdot \frac{F_{\mathrm{GeV}}}{F_{\mathrm{GeV,T5}}}, \tag{5.8}$$

where F_{GeV}, $F_{\mathrm{GeV,T5}}$ denote the *Fermi* flux measured from the considered GC and from Terzan 5, respectively. For NGC 6541 only an upper limit for this value is available, which will be used for the scaling instead. Table 5.5 lists the input parameters used for the scaling to calculate the predicted X-ray fluxes.

Based on the estimated excess surface flux, an expected total surface flux can be calculated by adding the level of Galactic diffuse emission. As in the Terzan 5 measurement, to estimate the latter the surface flux measured from the outer three annuli was used. In Fig. 5.9 the estimated total flux is plotted in red, where the values together with their respective uncertainties were scaled from the Terzan 5 data. From these flux levels it can be seen that in a scenario related to MSPs, also the expected values are quite low for these three GCs. With the statistical quality of the available X-ray data the presence of diffuse X-ray emission, similar to what was observed from Terzan 5, can therefore be neither confirmed nor ruled out in such a scenario. Terzan 5 may just stand out due to its large population of MSPs and its relatively small distance to Earth.

Table 5.5: GC fluxes measured by *Fermi*

source	photon flux* (10^{-8}ph cm^{-2} s^{-1})
M 62	$2.7^{+1.0+1.9}_{-0.9-0.8}$
NGC 6388	$1.6^{+1.0+2.0}_{-0.6-0.6}$
Terzan 5	$7.6^{+1.7+3.4}_{-1.5-2.2}$
NGC 6541	< 1.1

*Abdo et al. (2010c), first errors indicate systematic, second errors indicate statistical uncertainties.

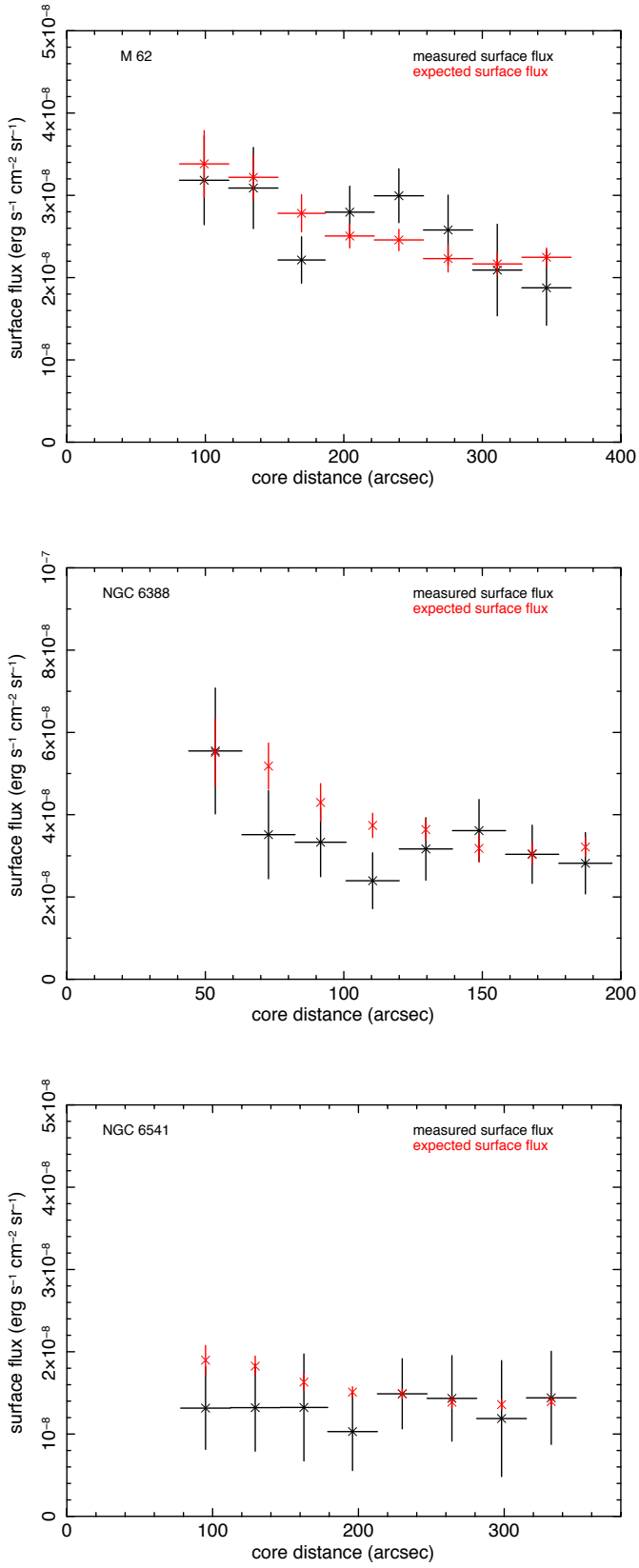

Figure 5.9: Diffuse X-ray surface flux (1–7 keV, black) as measured with *Chandra* from the three GCs M 62 (*top*), NGC 6388 (*middle*), and NGC 6541 (*bottom*). The red data points indicate the expected fluxes, based on the detected X-ray surface fluxes from Terzan 5, scaled by relative distance and number of MSPs, as seen by *Fermi*.

5.4 Conclusion and outlook

This chapter presented X-ray and VHE γ-ray analyses of various Galactic GCs. In both wavelength regimes Terzan 5 stands out as the only GC where significant excess emission could be detected. The possible emission scenarios that could give rise to the observed signal were discussed in detail for both X-ray and γ-ray wavelengths and are here also summarized briefly. Furthermore, it is highlighted in which cases the emission seen in both energy regimes could be connected.

Terzan 5 is not the first GC where diffuse X-ray emission was detected in direct vicinity. Ok07 detected significant extended X-ray emission from six GCs and attributed these signals to either thermal plasma emission or non-thermal bremsstrahlung, both arising from a bow shock as the GC moves through the Galactic halo medium. In these cases the X-ray signal was either displaced from the GC center in the direction of proper motion, or features an arc-like morphology. In contrast, the emission seen from Terzan 5 appears to be radially symmetric and centered on the GC core. The above radiation mechanisms are also discussed in the context of Terzan 5, but judging from the energetics, a synchrotron emission scenario seems to be preferred (see Sect. 5.3.1). In this case, depending on the magnetic field strength, detectable VHE γ-ray emission could be expected. To establish such a common scenario involving both the X-ray and the VHE fluxes measured from Terzan 5, additional observations at radio continuum wavelengths are required. Based on such observations, it would be possible to judge whether the observed X-ray signal is the tail of an IC peak, which suggests only moderate electron energies, or if the synchrotron spectrum indeed extends to these energies.

The analyses of *Chandra* data of other GCs that were detected by *Fermi*/LAT do not show diffuse X-ray emission on a similar scale as observed from Terzan 5. Assuming that the emission in both X-rays and HE γ-rays is connected to the population of MSPs, this result might not be surprising, as the expected X-ray fluxes could be too low to be detected with the available X-ray datasets. Judging from the very low expected flux levels, a positive detection of diffuse X-ray emission from these GCs, on a similar scale as seen from Terzan 5, might be challenging for current X-ray observatories.

The results from VHE γ-ray observations of Galactic GCs with H.E.S.S. are strikingly similar to the ones obtained at X-ray wavelengths. Despite a systematic search for excess emission from 18 clusters, Terzan 5 turns out to be the only GC with a detected source in direct vicinity. However, the origin of this signal is not settled yet. The two possible VHE γ-ray emission scenarios discussed in this chapter are IC scattering of relativistic electrons originating from MSPs, and hadronic emission from a GRB remnant (see Sect. 5.2.1.2). In the former case, the emission seen in X-rays could indeed be related to the VHE γ-ray signal, if interpreted as synchrotron radiation. However, the apparent offset of the γ-ray emission with respect to the GC center is challenging to explain with simple models. In the case of a GRB remnant, thermal X-ray emission originating from the sub-relativistic ejecta would be expected, which so far was not detected with the available *Chandra* data. However, as the VHE emission

is offset by a few arcminutes from the GC core, the thermal X-ray emission might be just beyond the limited FoV of the *Chandra* observations. In such a case the diffuse non-thermal X-ray signal, centered on the core, would most likely not be related to the VHE γ-ray signal. Future sensitive X-ray observations (e.g. with *XMM-Newton*) pointed towards the center of gravity of the VHE γ-ray signal could shed new light on this scenario. Another approach to test the viability of an hadronic scenario would arise from the analysis of high-resolution molecular line data, which would trace the amount of available target material in the vicinity of Terzan 5.

A search for VHE γ-ray signals from other galactic GCs covered by the currently available H.E.S.S. dataset resulted only in upper limits. However, this might not come as a surprise when assuming a scenario related to MSPs. Terzan 5 may just stand out as a relatively nearby GC featuring one of the largest MSP populations among all galactic GCs. Also, due to its extremely high rate of close stellar encounters, the probability of a recent short GRB originating from a neutron stars merger is very high for Terzan 5 in particular. Other GCs, such as 74 Tuc or NGC 6388, could be just beyond the reach of current IACTs and only the next generation of ground based γ-ray telescopes might be able to firmly detect these potential source candidates.

6 Summary

The aim of this thesis was not only to present detailed multi-wavelength studies of unidentified TeV γ-ray sources, but also to demonstrate the powerful synergies that arise from combining information from various electromagnetic energy regimes. To motivate a multi-wavelength approach in exploring sources of highly energetic γ-rays, first a number of relevant non-thermal astrophysical radiation mechanisms were introduced, as well as the respective wavelength domains where these processes are observable (chapter 2). Already here the gain from multi-wavelength approaches becomes clear, which basically arises from two different reasons. On the one hand, the same underlying population of relativistic particles may be visible at different wavelength regimes due to two or more competing radiation mechanisms. For instance, this is the case if the relativistic particles are dominated by leptons which radiate at radio to X-ray wavelengths via synchrotron emission, and via the inverse Compton process at the high-energy γ-ray regime. On the other hand, if the γ-ray emission process is highly dependent on the astrophysical environment of the cosmic-ray source, a multi-wavelength study would be essential to characterize parameters such as the structure and composition of the interstellar medium, its density or the ambient magnetic field. A good example of such a case are cosmic rays escaping from supernova remnant shocks, and their subsequent interaction with nearby molecular clouds.

In chapter 3 all observatories that were used for the astrophysical studies presented in chapters 4 and 5 are introduced. The scientific background information for each telescope is emphasized in the respective sections. Here the particular insights that can be gained from observations at the respective wavelength to improve our understanding of sources of cosmic rays are highlighted. Furthermore, the capabilities of the telescopes are described in detail, to underline their strong points and limitations when used in the context of astroparticle physics.

In the course of this thesis, multi-wavelength studies of two very different kinds of Galactic cosmic-ray sources are presented. These are the very-high-energy (VHE) γ-ray source HESS J1626−490, which most likely can be associated with a molecular cloud illuminated by a nearby supernova remnant, and globular clusters (GCs) which might represent a new class of sources producing VHE photons. The analyses of multi-wavelength data of these sources are presented in chapters 4 and 5, respectively. Below, the obtained results are summarized briefly.

The VHE γ-ray source HESS J1626−490 was discovered during the H.E.S.S. Galactic plane scan in 2008. As no obvious counterpart at lower energies could be identified, the nature of this source remained a mystery. In this work the H.E.S.S. data of

HESS J1626−490 were re-analyzed, using a significantly larger dataset together with a more sensitive analysis method than employed for the original detection. We carried out a detailed analysis of an X-ray observation performed with the *XMM-Newton* space telescope to search for a counterpart in the 0.5–10 keV energy band. We classified all detected point sources and characterized the properties of diffuse X-ray emission in a region compatible with the γ-ray signal. In particular we found that the flux and spectral shape of diffuse emission from this region is compatible with the expected diffuse Galactic background emission. Neither any of the detected point-sources nor the upper limit for potential diffuse excess emission fulfill the energetic requirements to be considered as the synchrotron counterpart of the observed TeV γ-ray source. This result makes a purely leptonic scenario as origin for the non-thermal emission rather unlikely. Hence, an alternative explanation for the VHE γ-ray signal was explored. To search for dense molecular clouds coincident with the γ-ray emission region, we analyzed ^{12}CO ($J = 1-0$) data from the NANTEN Galactic plane scan. We found a good morphological match between dense molecular gas at a kinematic distance of $\sim$2.0 kpc and the γ-ray signal detected with H.E.S.S. This molecular cloud could provide target material for hadronic cosmic rays to produce neutral pions which subsequently decay into γ-rays. However, the mass and density of this cloud are not sufficient to explain the observed VHE γ-ray signal if the cloud is only embedded in the sea of background cosmic rays with an energy density similar to the one observed at Earth. Therefore, a local accelerator in the vicinity of the molecular cloud is needed for a hadronic scenario to be viable. An analysis of H I data from the Southern Galactic Plane Survey suggests that the supernova remnant SNR G335.2+00.1 is located at a very similar line-of-sight distance as the molecular cloud detected with NANTEN, and is therefore a good candidate for the local source of cosmic rays illuminating the molecular gas. A detailed modeling of cosmic ray propagation and interaction confirms that SNR G335.2+00.1 indeed could provide a sufficiently high density of relativistic protons at the location of the molecular cloud to produce the VHE γ-ray signal detected with H.E.S.S. To improve our understanding of the environment of HESS J1626−490 and to trace the densest regions of the molecular cloud, rotational line observations of heavier molecules such as NH_3, CS, or SiO would help. Furthermore, to search for an additional leptonic component present in the shock of SNR G335.2+00.1 and to measure the degree of orientation of the magnetic field, radio polarization observations would provide further insights.

The second class of sources investigated in this work are Globular clusters (chapter 5). Even though these gravitationally bound systems of evolved stars have been proposed as potential sources of high and VHE γ-rays already a few years ago, they have attracted particular attention only recently. In December 2010, the *Fermi*/LAT collaboration reported the detection of quite a number of Galactic GCs in the MeV to GeV energy regime. This emission was attributed to curvature radiation from electrons in the magnetospheres of the numerous millisecond pulsars (MSPs) present in the dense cores of the GCs. However, also inverse Compton emission from electrons, that have been accelerated by the individual pulsars or in colliding pulsar wind nebulae, is discussed in the context of HE or even VHE γ-ray emission from GCs. In such a case, very similar

to individual pulsar wind nebulae, synchrotron radiation in the radio to X-ray regime would be expected. In this work H.E.S.S. data of 18 Galactic GCs were investigated to search for the presence of γ-ray emission with an energy above 800 GeV. Furthermore, X-ray observations of those GCs considered in the recent *Fermi*/LAT publication were analyzed. Qualitatively, the results from both the X-ray and VHE γ-ray studies are very similar. Terzan 5 is the only cluster that could be associated to a significant signal detected in either of the two wavelength regimes. If the VHE γ-ray source in the vicinity of Terzan 5 is indeed connected to this GC, this would make Terzan 5 the first GC detected in that energy regime. Furthermore, Terzan 5 is also by far the brightest GC detected by *Fermi*/LAT, which is strikingly consistent with the results presented here and might suggest a common emission scenario, e.g. related to MSPs. Indeed, Terzan 5 hosts the largest population of individually detected MSPs among all Galactic GCs. However, there are also other potential scenarios predicting the observed VHE γ-ray signal from Terzan 5, such as non-thermal emission from hadrons produced in a catastrophic event like a type Ia supernova or a short gamma-ray burst. Thus, the origin of the VHE γ-ray signal seen from the vicinity of Terzan 5 is not settled yet, and further multi-wavelength investigations as well as VHE γ-ray observations with future instruments are required to explore the nature of this source. Finally, in this work also a potential connection between the X-ray and VHE γ-ray emission detected from Terzan 5 is discussed. A connection seems likely in a scenario related to MSPs, where the γ-rays are thought to originate from inverse Compton up-scattering by relativistic electrons. Here, the non-thermal X-ray emission could be attributed to synchrotron radiation from the same lepton population. Indeed, the latter seems to be the most likely origin of the X-ray signal, judging only from energetic considerations. However, there are also alternative interpretations of the observed X-ray emission, such as inverse Compton emission from mildly relativistic electrons or non-thermal bremsstrahlung. In these cases the X-ray and VHE γ-ray emission would not be directly connected. The observational facts presented in this work could be seen as one of many steps in exploring the non-thermal processes in the cores of GCs. Most likely only future, more detailed observations will yield the decisive clues.

7 Zusammenfassung

Ziel dieser Arbeit war es nicht nur detaillierte Multi-wellenlängen Studien unidentifizierter TeV-Gammastrahlungsquellen vorzustellen, sondern auch zu demonstrieren wie mächtig eine solche Analyse von Breitband-Daten sein kann um mehr über diese Objekte zu lernen als es mit einzelnen Datensatz getrennt voneinander möglich wäre. Um einen Multi-wellenlängen Ansatz zu motivieren werden in der vorliegenden Dissertation zunächst die relevanten nicht-thermischen Strahlungsmechanismen vorgestellt. Hier wird insbesondere darauf eingegangen bei welchen Wellenlängen die einzelnen Prozesse beobachtbar sind (Kapitel 2). Bereits hier werden die Vorteile einer Analyse von Breitband-Daten ersichtlich, welche im Wesentlichen auf zwei Gründen beruhen. Zum einen kann die selbe Population hochenergetischer Teilchen aufgrund von mehreren konkurrierenden Mechanismen Licht in sehr unterschiedlichen Energiebereichen erzeugen. Dies ist zum Beispiel der Fall, wenn die relativistische Teilchenpopulation hauptsächlich aus Leptonen besteht, die Synchrotronstrahlung im Radio- bis Röntgenbereich emittieren, und über inverse Compton-Streuung Photonen mit Energien von bis zu mehreren TeV erzeugen. Zum anderen kann der Prozess der Emission von Gammastrahlung sehr stark von der astrophysikalischen Umgebung der Quelle der kosmischen Strahlung abhängen. In solchen Fällen ist ebenfalls eine Untersuchung der Region in einem breiten Wellenlängen-Bereich nötig um nicht nur die erzeugte Gammastrahlung sondern auch Parameter wie Masse und Dichte des Interstellaren Mediums zu messen. Ein gutes Beispiel dafür sind hochenergetische Protonen, die in den Schocks von Supernovaüberresten beschleunigt werden, aus diesen entkommen und mit kalter und dichter Materie in benachbarten Molekülwolken wechselwirken.

In Kapitel 3 werden zunächst alle Observatorien eingeführt, deren Daten für die astrophysikalischen Studien in den Kapiteln 4 und 5 genutzt wurden. Die vielleicht wichtigsten Teile dieses Kapitels enthalten den wissenschaftlichen Hintergrund ("scientific background") für das jeweilige Teleskop. Diese Abschnitte heben die konkreten Aspekte hervor, die mit dem entsprechenden Teleskop untersucht werden und zum Verständnis von Quellen höchstenergetischer Gammastrahlung beitragen können. Desweiteren werden die Eigenschaften der verschiedenen Observatorien im Detail beschrieben, um deren Stärken und Schwächen besonders im Kontext der Astroteilchenphysik herauszustellen.

In dieser Dissertation werden Multiwellenlängen Studien zu zwei sehr verschiedenartigen Quellen kosmischer Strahlung vorgestellt. Diese sind die TeV-Gammastrahlungsquelle HESS J1626−490, die mit einer Molekülwolke assoziiert ist, die von einem nahen Supernovaüberrest beleuchtet wird, und Kugelsternhaufen (KH), die möglicherweise

eine neue Klasse von Quellen höchstenergetischer Gammastrahlung darstellen. Im Folgenden sind die Ergebnisse der Studien zu beiden Quelltypen kurz zusammengefasst.

Die Gammastrahlungsquelle HESS J1626−490 wurde mit H.E.S.S. während der Durchmusterung der Galaktischen Ebene im Jahr 2008 entdeckt. Da zunächst kein Gegenstück bei niedrigeren Energien gefunden werden konnte, wurde HESS J1626−490 zusammen mit einer Reihe weiterer Quellen als "nicht identifiziert" eingestuft. Für diese Arbeit wurden die H.E.S.S.-Daten erneut analysiert, da ein weitaus umfangreicherer Datensatz zur Verfügung stand, ebenso wie eine fortschrittlichere und sensitivere Methode zur Datenanalyse. Weiterhin wurden Röntgendaten des Weltraumteleskops *XMM-Newton* untersucht, um nach einem möglichen Gegenpart bei Energien zwischen 0.5 keV und 10.0 keV zu suchen. Alle detektierten Punktquellen in diesem Energieband wurden gemäß ihres Spektrums und den Eigenschaften ihres Gegenparts bei infraroten Wellenlängen klassifiziert. Desweiteren wurde nach einer ausgedehnten und diffusen Komponente im Röntgenbereich gesucht, die mit HESS J1626−490 in Verbindung stehen könnte. Der Fluss keiner der detektieren Punktquellen und auch nicht das Niveau möglicher diffuser Emission erfüllen die energetischen Anforderungen um mit HESS J1626−490 in Verbindung zu stehen. Dieses Ergebnis schließt ein Emissionsszenario, das auf rein leptonischen Prozessen beruht, nahezu aus. Um nach Molekülwolken zu suchen, die konsistent sind mit der Emissionsregion der Gammastrahlung, wurden ^{12}CO ($J = 1 - 0$)-Daten des NANTEN-Radioteleskops analysiert. Dabei wurde eine gute morphologische Übereinstimmung zwischen dem γ-Signal und molekularem Gas bei einer kinematischen Entfernung von ~ 2 kpc gefunden. Diese Molekülwolke könnte das nötige Targetmaterial für hadronische kosmische Strahlung liefern um neutrale Pionen zu erzeugen, die wiederum in je zwei Photonen zerfallen. Allerdings ist die Masse und Dichte der Molekülwolke nicht ausreichend um das mit H.E.S.S. beobachtete Signal zu erklären, falls die Materie lediglich in den "See" aus dem Hintergrund komischer Strahlung eingebettet ist. Daher ist für ein solches Szenario ein lokaler Beschleuniger in der Nähe der Molekülwolke nötig. Eine Untersuchung von H I-Daten des Southern Galactic Plane Survey lässt den Schluss zu, dass der Supernovaüberrest SNR G335.2+00.1 bei einer sehr ähnlichen Entfernung zu uns liegt wie die Molekülwolke. Eine detaillierte Modellierung der Diffusion und Interaktion relativistischer Protonen zeigt, dass SNR G335.2+00.1 in der Tat die nötige Dichte an kosmischer Strahlung am Ort der Molekülwolke liefern könnte um den beobachteten Fluss an Gammastrahlung zu erklären. Beobachtungen der Rotationslinien schwererer Moleküle wie NH_3, CS oder SiO werden helfen unser Verständnis der Umgebung von HESS J1626−490 zu verbessern, und um die dichtesten Bereiche der Molekülwolke zu identifizieren. Weiterhin würden Messungen der Polarisation des Signals im Radiokontinuum von SNR G335.2+00.1 es ermöglichen die Ordnung des Magnetfelds zu quantifizieren, und um nach einer etwaigen zusätzlichen leptonischen Komponente am Schock zu suchen.

Die zweite Klasse von Quellen, die in dieser Arbeit untersucht wurde, sind KH (Kapitel 5). Obwohl diese gebundenen Systeme weit entwickelter stellarer Populationen schon lange as potenzielle Quellen hochenergetischer Gammastrahlung diskutiert wurden, haben sie erst vor Kurzem besondere Aufmerksamkeit erlangt. Im Dezember

2010 berichtete die *Fermi*/LAT-Kollaboration von der Entdeckung gleich mehrerer KH im MeV- bis GeV-Energiebereich. Die Emission wurde der Zyklotronstrahlung relativistischer Elektronen in den Magnetosphären von Millisekundenpulsaren (MSPe) in den dichten Kernen von KH zugeschrieben. Allerdings wurde auch inverse Compton-Streuung relativistischer Elektronen, die an individuellen Pulsarwindnebeln (PWN) oder auch in den Kollisionszonen benachbarter PWN beschleunigt werden, als möglicher Strahlungsprozess vorgeschlagen. Hier wäre auch Synchrotronstrahlung bis hin zu Wellenlängen im Röntgenbereich zu erwarten. In dieser Arbeit wurden H.E.S.S.-Daten von 18 Galaktischen KH untersucht, um nach einem Signal bei Energien zwischen 800 GeV und 10 TeV zu suchen. Außerdem wurden Röntgenbeobachtungen von denjenigen KH analysiert, die auch von der *Fermi*/LAT-Kollaboration untersucht wurden. Qualitativ sind die Ergebnisse der Studien bei beiden Wellenlängen sehr ähnlich. Der KH Terzan 5 ist das einzige Objekt, das ein signifikantes Signal sowohl im Röntgen- als auch im TeV-Gammabereich aufweist. Falls die detektierte TeV-Gammastrahlungsquelle tatsächlich mit Terzan 5 in Verbindung steht würde dies KH als neue Klasse von Quellen in diesem Energiebereich etablieren. Die Tatsache, dass Terzan 5 auch im GeV-Regime der hellste KH ist, könnte ein gemeinsames Emissionsszenario nahelegen, wie zum Beispiel MSPe. Allerdings ließe sich das mit H.E.S.S. detektierte TeV-Signal auch durch andere Szenarien, wie z.B. den Überrest einer Typ Ia Supernova oder eines kurzen Gammastrahlungsausbruchs erklären. Daher ist der Ursprung des TeV-Signals von Terzan 5 noch nicht abschließend geklärt. Weitere Breitband-Studien und Beobachtungen mit künftigen Gammastrahlungsobservatorien werden nötig sein um die Natur dieser Quelle zu erforschen. In dieser Arbeit wurde auch ein möglicher Zusammenhang zwischen der Emission von Terzan 5 im Röntgenbereich und dem Signal im TeV-Bereich diskutiert. Ein solcher Zusammenhang scheint plausibel in einem Szenario, das in Verbindung mit MSPe steht. Hier könnte die nicht-thermische Röntgenemission aus Synchrotronstrahlung der relativischen Leptonpopulation herrühren. Jedoch kommen auch andere Prozesse für die Erzeugung der diffusen Röntgenstrahlung in Frage, wie inverse Compton-Streuung von Eletronen geringerer Energie als im Falle der Synchrotronstrahlung, oder durch nich-thermische Bremsstrahlung. In diesen Fällen stünde die Emission höchstenergetischer Gammastrahlung in keinem direkten Zusammenhang mit dem Röntgen-Signal. Letztlich lassen sich zu diesem Zeitpunkt noch keine gesicherten Aussagen über die nicht-thermischen Vorgänge in den Kernen von KH treffen. Möglicherweise werden erst künftige, detailliertere Beobachtungen die entscheidenden Hinweise liefern.

Acknowledgements

Es heißt, dass die Danksagungen zu den meist gelesenen Kapiteln einer Dissertation gehören. Um dieser Beachtung gerecht zu werden, versuche ich hier alle Menschen zu erwähnen, die mich während meiner Zeit als Doktorand am ECAP in besonderer Weise begleitet haben. Es war eine tolle Zeit, und das soll auch an dieser Stelle zum Ausdruck kommen.

Neben mir selbst hatte sicherlich **Prof. Christian Stegmann** den größten Einfluss auf das Gelingen der vorliegenden Arbeit. Vielen Dank, Christian, für den großen wissenschaftlichen Freiraum, den ich während meiner Arbeit hier am ECAP genießen durfte. Auch möchte ich mich für deine Unterstützung bedanken, und für die vielen guten Ratschläge, die für mich stets sehr wichtig waren.

Gleich vierfacher Dank gilt unserem "Altdoktoranden" und meinem ehemaligen Zimmergenossen **Dr. Fabian M. Schöck**. 1.) Als Hauptverantwortlicher mich in die Erlanger HESS Gruppe zu integrieren hast du ganze Arbeit geleistet! 2.) Für die besonderen Einblicke in die Funktionsweise der HESS Kollaboration (insbesondere während der zahlreichen Kollaborationstreffen) bin ich dir ebenfalls zu großem Dank verpflichtet. 3.) Ohne dein geballtes Fachwissen, und auch die Fähigkeit dieses zu vermitteln, wären mir bis heute die physikalischen Vorgänge am *termination shöck* völlig unklar. 4.) Vor allem aber danke ich dir für die tolle Atmosphäre in unserem Büro während der viel zu kurzen Zeit, in der wir dieses teilten. ;-)

Furthermore, I would like to thank **Gavin Rowell** for gladly sharing his knowledge on the interpretation of molecular and atomic line observations. The multi-wavelength study presented in this thesis would certainly not have been possible without your support. Also, I would like to thank the members of the Nagoya NANTEN group **Yasuo Fukui** and **Akiko Kawamura** for providing the excellent and very crucial ^{12}CO dataset, which significantly improved the scientific value of this work.

Thanks to my collegues from Heidelberg **Wilfried Domainko** and **Ándre-Claude Clapson** for the very productive collaboration during our work on Globular Clusters. The scientific results presented in this work certainly profited a lot from our numerous dedicated discussions. Also thank you for inviting me to Heidelberg, which was a very pleasant and fruitful meeting.

Vielen Dank an meine Kollegen in Erlangen, die dafür sorgen, dass ich meine Arbeit am Institut sehr genieße. Sowohl in fachlicher als auch in persönlicher Hinsicht war für mich das kollegiale Verhältnis eine Bereicherung. Einige seien im Folgenden mit kurzem Kommentar erwähnt: **Michi** (Danke für bereichernde Diskussionen über rein

physikalische aber auch interdisziplinäre Themen.), **Markus** (Danke für die unzähligen "HESS Standards" mit allem, was dazugehört, und für die vielen kritischen Einwände, die uns oft scheinbar bekannte Sachverhalte neu überdenken ließ.), **Kathrin** (Danke für das gewissenhafte Korrekturelesen meiner Arbeit, für deine erfrischende Art und vor allem für die tolle Zeit in Namibia!), **Anneli** und **Kora** (die Frauenpower der neuen Generation, die das "Machtgefüge" innerhalb der Gruppe ins Wanken brachte :-)), **Anton, Arnim** und **Daniel** (die ultimativen Technik Gurus, geballte Kompetenz, ohne euch läuft hier nichts), **Bernhard** (mein "längjähriger" Zimmernachbar; vielen Dank für die vielen Diskussionen, die mir fundierte Einsichten in zahlreiche Themen der Gamma-Astronomie gewährten), **Sebastian** (wir verheirateten Physiker müssen eben zusammenhalten!), **Ira** (Danke für das gewissenhafte Lesen meiner Arbeit und die vielen konstruktiven Kommentare!)

Dank ganz anderer Natur gilt meiner Mutter **Gisela Eger**. Vielen Dank für deine langjährige Unterstützung während meiner, leider nicht immer finanziell sehr ertragreichen, schulischen und universitären Ausbildung. Dies war zwar während meiner Promotion nicht mehr nötig aber so weit wäre ich ja sonst nie gekommen. Für mich persönlich jedoch war etwas anderes noch viel wichtiger. Vielen Dank, Mama, für dein unumstößliches Vertrauen in die Richtigkeit meiner Entscheidungen mein Leben zu gestalten. Ohne diesen starken persönlichen Rückhalt wäre für mich sicher vieles nicht so leicht oder gar nicht möglich gewesen.

Ganz lieber Dank gilt meiner Frau **Rosi**. Speziell bezüglich meiner Promotion danke ich Dir für Deine unzähligen guten Ratschläge, Dein stets offenes Ohr auch für wissenschaftliche Fragestellungen und den starken Rückhalt, den Du mir bietest! Vielleicht schaffen wir es ja tatsächlich einmal eine unserer Dienstreisen zu verbinden!

Funding agencies and public domain data:
The XMM-Newton project is supported by the Bundesministerium für Wirtschaft und Technologie/Deutsches Zentrum für Luft- und Raumfahrt (BMWI/DLR, FKZ 50 OX 0001) and the Max-Planck Society.
This dissertation makes use of data products from the Two Micron All Sky Survey, which is a joint project of the University of Massachusetts and the Infrared Processing and Analysis Center/California Institute of Technology, funded by the National Aeronautics and Space Administration and the National Science Foundation.
The NANTEN project is financially supported from JSPS (Japan Society for the Promotion of Science) Core-to-Core Program, MEXT Grant-in-Aid for Scientific Research on Priority Areas, and SORST-JST (Solution Oriented Research for Science and Technology: Japan Science and Technology Agency).
This research has made use of data obtained from the Chandra Data Archive and software provided by the Chandra X-ray Center (CXC) in the application packages CIAO and ChIPS.
This work is supported by the Bundesministerium für Bildung und Forschung (BMBF).

List of Figures

List of Tables

Bibliography

Abdo, A. A., Ackermann, M., Ajello, M., Allafort, A., Antolini, E., Atwood, W. B., Axelsson, M., Baldini, L., Ballet, J., Barbiellini, G., Bastieri, D., Baughman, B. M., Bechtol, K., Bellazzini, R., Belli, F., Berenji, B., Bisello, D., Blandford, R. D., Bloom, E. D., Bonamente, E., Bonnell, J., Borgland, A. W., Bouvier, A., Bregeon, J., Brez, A., Brigida, M., Bruel, P., Burnett, T. H., Busetto, G., Buson, S., Caliandro, G. A., Cameron, R. A., Campana, R., Canadas, B., Caraveo, P. A., Carrigan, S., Casandjian, J. M., Cavazzuti, E., Ceccanti, M., Cecchi, C., Çelik, Ö., Charles, E., Chekhtman, A., Cheung, C. C., Chiang, J., Cillis, A. N., Ciprini, S., Claus, R., Cohen-Tanugi, J., Conrad, J., and Corbet, R. et al. (2010a). Fermi Large Area Telescope First Source Catalog. *ApJS*, 188:405–436.

Abdo, A. A., Ackermann, M., Ajello, M., Atwood, W. B., Axelsson, M., Baldini, L., Ballet, J., Barbiellini, G., Baring, M. G., Bastieri, D., Baughman, B. M., Bechtol, K., Bellazzini, R., Berenji, B., Bignami, G. F., Blandford, R. D., Bloom, E. D., Bonamente, E., Borgland, A. W., Bregeon, J., Brez, A., Brigida, M., Bruel, P., Burnett, T. H., Caliandro, G. A., Cameron, R. A., Camilo, F., Caraveo, P. A., Carlson, P., Casandjian, J. M., Cecchi, C., Çelik, Ö., Charles, E., Chekhtman, A., Cheung, C. C., Chiang, J., Ciprini, S., Claus, R., Cognard, I., Cohen-Tanugi, J., Cominsky, L. R., Conrad, J., Corbet, R., and Cutini, S. et al. (2009). A Population of Gamma-Ray Millisecond Pulsars Seen with the Fermi Large Area Telescope. *Science*, 325:848.

Abdo, A. A., Ackermann, M., Ajello, M., Atwood, W. B., Axelsson, M., Baldini, L., Ballet, J., Barbiellini, G., Baring, M. G., Bastieri, D., and et al. (2010b). The First Fermi Large Area Telescope Catalog of Gamma-ray Pulsars. *ApJS*, 187:460–494.

Abdo, A. A., Ackermann, M., Ajello, M., Baldini, L., Ballet, J., Barbiellini, G., Bastieri, D., Bellazzini, R., Blandford, R. D., Bloom, E. D., Bonamente, E., Borgland, A. W., Bouvier, A., Brandt, T. J., Bregeon, J., Brigida, M., Bruel, P., Buehler, R., Buson, S., Caliandro, G. A., Cameron, R. A., Caraveo, P. A., Carrigan, S., Casandjian, J. M., Charles, E., Chaty, S., Chekhtman, A., Cheung, C. C., Chiang, J., Ciprini, S., Claus, R., Cohen-Tanugi, J., Conrad, J., Decesar, M. E., Dermer, C. D., de Palma, F., Digel, S. W., Silva, E. D. C. E., and Drell, P. et al. (2010c). A population of gamma-ray emitting globular clusters seen with the Fermi Large Area Telescope. *A&A*, 524:A75+.

Acero, F., Aharonian, F., Akhperjanian, A. G., Anton, G., Barres de Almeida, U., Bazer-Bachi, A. R., Becherini, Y., Behera, B., Beilicke, M., Bernlöhr, K., Bochow,

A., Boisson, C., Bolmont, J., Borrel, V., Brucker, J., Brun, F., Brun, P., Bühler, R., Bulik, T., Büsching, I., Boutelier, T., Chadwick, P. M., Charbonnier, A., Chaves, R. C. G., Cheesebrough, A., Conrad, J., Chounet, L., Clapson, A. C., Coignet, G., Dalton, M., Daniel, M. K., Davids, I. D., Degrange, B., Deil, C., Dickinson, H. J., Djannati-Ataï, A., Domainko, W., O'C. Drury, L., Dubois, F., Dubus, G., Dyks, J., Dyrda, M., Egberts, K., Eger, P., Espigat, P., Fallon, L., Farnier, C., and Fegan, S. et al. (2010). First detection of VHE γ-rays from SN 1006 by HESS. *A&A*, 516:A62+.

Acero, F., Aharonian, F., Akhperjanian, A. G., Anton, G., Barres de Almeida, U., Bazer-Bachi, A. R., Becherini, Y., Behera, B., Beilicke, M., Bernlöhr, K., Bochow, A., Boisson, C., Bolmont, J., Borrel, V., Brucker, J., Brun, F., Brun, P., Bühler, R., Bulik, T., Büsching, I., Boutelier, T., Chadwick, P. M., Charbonnier, A., Chaves, R. C. G., Cheesebrough, A., Conrad, J., Chounet, L., Clapson, A. C., Coignet, G., Dalton, M., Daniel, M. K., Davids, I. D., Degrange, B., Deil, C., Dickinson, H. J., Djannati-Ataï, A., Domainko, W., O'C. Drury, L., Dubois, F., Dubus, G., Dyks, J., Dyrda, M., Egberts, K., Eger, P., Espigat, P., Fallon, L., Farnier, C., and Fegan, S. et al. (2011). Very-high-energy gamma-ray emission from the direction of the Galactic globular cluster Terzan 5. *in prep.*

Acero, F., Ballet, J., and Decourchelle, A. (2007). The gas density around SN 1006. *A&A*, 475:883–890.

Aharonian, F., Akhperjanian, A., Beilicke, M., Bernlöhr, K., Börst, H., Bojahr, H., Bolz, O., Coarasa, T., Contreras, J., Cortina, J., Denninghoff, S., Fonseca, V., Girma, M., Götting, N., Heinzelmann, G., Hermann, G., Heusler, A., Hofmann, W., Horns, D., Jung, I., Kankanyan, R., Kestel, M., Kettler, J., Kohnle, A., Konopelko, A., Kornmeyer, H., Kranich, D., Krawczynski, H., Lampeitl, H., and Lopez, M. et al. (2002). An unidentified TeV source in the vicinity of Cygnus OB2. *A&A*, 393:L37–L40.

Aharonian, F., Akhperjanian, A. G., Anton, G., Barres de Almeida, U., Bazer-Bachi, A. R., Becherini, Y., Behera, B., Bernlöhr, K., Boisson, C., Bochow, A., Borrel, V., Braun, I., Brion, E., Brucker, J., Brun, P., Bühler, R., Bulik, T., Büsching, I., Boutelier, T., Chadwick, P. M., Charbonnier, A., Chaves, R. C. G., Cheesebrough, A., Chounet, L.-M., Clapson, A. C., Coignet, G., Dalton, M., Daniel, M. K., Davids, I. D., Degrange, B., Deil, C., Dickinson, H. J., Djannati-Ataï, A., Domainko, W., O'C. Drury, L., Dubois, F., Dubus, G., Dyks, J., Dyrda, M., Egberts, K., Emmanoulopoulos, D., Espigat, P., Farnier, C., Feinstein, F., Fiasson, A., Förster, A., Fontaine, G., Füßling, M., and Gabici, S. et al. (2009). HESS upper limit on the very high energy γ-ray emission from the globular cluster 47 Tucanae. *A&A*, 499:273–277.

Aharonian, F., Akhperjanian, A. G., Aye, K.-M., Bazer-Bachi, A. R., Beilicke, M., Benbow, W., Berge, D., Berghaus, P., Bernlöhr, K., Boisson, C., Bolz, O., Borgmeier, C., Braun, I., Breitling, F., Brown, A. M., Gordo, J. B., Chadwick, P. M., Chounet, L.-M., Cornils, R., Costamante, L., Degrange, B., Djannati-Ataï, A., Drury, L. O., Dubus, G., Ergin, T., Espigat, P., Feinstein, F., Fleury, P., Fontaine, G., Funk, S., Gallant, Y. A., Giebels, B., Gillessen, S., Goret, P., Hadjichristidis, C., Hauser,

M., and Heinzelmann, G. et al. (2005a). A New Population of Very High Energy Gamma-Ray Sources in the Milky Way. *Science*, 307:1938–1942.

Aharonian, F., Akhperjanian, A. G., Aye, K.-M., Bazer-Bachi, A. R., Beilicke, M., Benbow, W., Berge, D., Berghaus, P., Bernlöhr, K., Boisson, C., Bolz, O., Braun, I., Breitling, F., Brown, A. M., Bussons Gordo, J., Chadwick, P. M., Chounet, L.-M., Cornils, R., Costamante, L., Degrange, B., Djannati-Ataï, A., O'C. Drury, L., Dubus, G., Emmanoulopoulos, D., Espigat, P., Feinstein, F., Fleury, P., Fontaine, G., Fuchs, Y., Funk, S., Gallant, Y. A., Giebels, B., and Gillessen, S. et al. (2005b). Discovery of extended VHE gamma-ray emission from the asymmetric pulsar wind nebula in MSH 15-52 with HESS. *A&A*, 435:L17–L20.

Aharonian, F., Akhperjanian, A. G., Barres de Almeida, U., Bazer-Bachi, A. R., Behera, B., Beilicke, M., Benbow, W., Bernlöhr, K., Boisson, C., Bolz, O., Borrel, V., Braun, I., Brion, E., Brown, A. M., Bühler, R., Bulik, T., Büsching, I., Boutelier, T., Carrigan, S., Chadwick, P. M., Chounet, L.-M., Clapson, A. C., Coignet, G., Cornils, R., Costamante, L., Dalton, M., Degrange, B., Dickinson, H. J., Djannati-Ataï, A., Domainko, W., Drury, L. O., Dubois, F., Dubus, G., Dyks, J., Egberts, K., Emmanoulopoulos, D., Espigat, P., Farnier, C., Feinstein, F., Fiasson, A., Förster, A., Fontaine, G., Funk, S., Füßling, M., Gallant, Y. A., Giebels, B., Glicenstein, J. F., Glück, B., Goret, P., and Hadjichristidis, C. et al. (2008a). HESS very-high-energy gamma-ray sources without identified counterparts. *A&A*, 477:353–363.

Aharonian, F., Akhperjanian, A. G., Barres de Almeida, U., Bazer-Bachi, A. R., Behera, B., Beilicke, M., Benbow, W., Bernlöhr, K., Boisson, C., Bolz, O., Borrel, V., Braun, I., Brion, E., Brown, A. M., Bühler, R., Bulik, T., Büsching, I., Boutelier, T., Carrigan, S., Chadwick, P. M., Chounet, L.-M., Clapson, A. C., Coignet, G., Cornils, R., Costamante, L., Dalton, M., Degrange, B., Dickinson, H. J., Djannati-Ataï, A., Domainko, W., O'C. Drury, L., Dubois, F., Dubus, G., Dyks, J., Egberts, K., Emmanoulopoulos, D., Espigat, P., Farnier, C., Feinstein, F., Fiasson, A., Förster, A., Fontaine, G., and Funk, S. et al. (2008b). Exploring a SNR/molecular cloud association within HESS J1745-303. *A&A*, 483:509–517.

Aharonian, F., Akhperjanian, A. G., Bazer-Bachi, A. R., Behera, B., Beilicke, M., Benbow, W., Berge, D., Bernlöhr, K., Boisson, C., Bolz, O., Borrel, V., Braun, I., Brion, E., Brown, A. M., Bühler, R., Bulik, T., Büsching, I., Boutelier, T., Carrigan, S., Chadwick, P. M., Chounet, L.-M., Clapson, A. C., Coignet, G., and Cornils, R. et al. (2008c). Discovery of very high energy gamma-ray emission coincident with molecular clouds in the W 28 (G6.4-0.1) field. *A&A*, 481:401–410.

Aharonian, F., Akhperjanian, A. G., Bazer-Bachi, A. R., Beilicke, M., Benbow, W., Berge, D., Bernlöhr, K., Boisson, C., Bolz, O., Borrel, V., Braun, I., Breitling, F., Brown, A. M., Chadwick, P. M., Chounet, L.-M., Cornils, R., Costamante, L., Degrange, B., Dickinson, H. J., Djannati-Ataï, A., Drury, L. O., Dubus, G., Emmanoulopoulos, D., Espigat, P., Feinstein, F., Fontaine, G., Fuchs, Y., Funk, S.,

Gallant, Y. A., Giebels, B., Gillessen, S., Glicenstein, J. F., Goret, P., Hadjichristidis, C., Hauser, D., Hauser, M., and Heinzelmann, G. et al. (2006a). Discovery of very-high-energy γ-rays from the Galactic Centre ridge. *Nature*, 439:695–698.

Aharonian, F., Akhperjanian, A. G., Bazer-Bachi, A. R., Beilicke, M., Benbow, W., Berge, D., Bernlöhr, K., Boisson, C., Bolz, O., Borrel, V., Braun, I., Brion, E., Brown, A. M., Bühler, R., Büsching, I., Boutelier, T., Carrigan, S., Chadwick, P. M., Chounet, L.-M., Coignet, G., Cornils, R., Costamante, L., Degrange, B., Dickinson, H. J., Djannati-Ataï, A., Drury, L. O., Dubus, G., Egberts, K., Emmanoulopoulos, D., Espigat, P., Farnier, C., Feinstein, F., Ferrero, E., Fiasson, A., Fontaine, G., Funk, S., Funk, S., Füßling, M., Gallant, Y. A., Giebels, B., Glicenstein, J. F., Glück, B., Goret, P., Hadjichristidis, C., Hauser, D., Hauser, M., Heinzelmann, G., Henri, G., Hermann, G., Hinton, J. A., Hoffmann, A., Hofmann, W., Holleran, M., Hoppe, S., Horns, D., and Jacholkowska, A. et al. (2007a). Detection of extended very-high-energy γ-ray emission towards the young stellar cluster Westerlund 2. *A&A*, 467:1075–1080.

Aharonian, F., Akhperjanian, A. G., Bazer-Bachi, A. R., Beilicke, M., Benbow, W., Berge, D., Bernlöhr, K., Boisson, C., Bolz, O., Borrel, V., Braun, I., Brion, E., Brown, A. M., Bühler, R., Büsching, I., Carrigan, S., Chadwick, P. M., Chounet, L.-M., Coignet, G., Cornils, R., Costamante, L., Degrange, B., Dickinson, H. J., Djannati-Ataï, A., O'C. Drury, L., Dubus, G., Egberts, K., Emmanoulopoulos, D., Espigat, P., Feinstein, F., Ferrero, E., Fiasson, A., Fontaine, G., Funk, S., Funk, S., Füßling, M., Gallant, Y. A., Giebels, B., Glicenstein, J. F., Glück, B., Goret, P., Hadjichristidis, C., and Hauser, D. et al. (2007b). Primary particle acceleration above 100 TeV in the shell-type supernova remnant RX J1713.7-3946 with deep HESS observations. *A&A*, 464:235–243.

Aharonian, F., Akhperjanian, A. G., Bazer-Bachi, A. R., Beilicke, M., Benbow, W., Berge, D., Bernlöhr, K., Boisson, C., Bolz, O., Borrel, V., Braun, I., Brown, A. M., Bühler, R., Büsching, I., Carrigan, S., Chadwick, P. M., Chounet, L.-M., Coignet, G., Cornils, R., Costamante, L., Degrange, B., Dickinson, H. J., Djannati-Ataï, A., Drury, L. O., Dubus, G., Egberts, K., Emmanoulopoulos, D., Espigat, P., Feinstein, F., Ferrero, E., Fiasson, A., Filipovic, M. D., Fontaine, G., Fukui, Y., Funk, S., Funk, S., Füßling, M., Gallant, Y. A., Giebels, B., Glicenstein, J. F., Goret, P., Hadjichristidis, C., Hauser, D., Hauser, M., Heinzelmann, G., Henri, G., Hermann, G., Hinton, J. A., Hiraga, J. S., Hoffmann, A., Hofmann, W., Holleran, M., Hoppe, S., Horns, D., Ishisaki, Y., Jacholkowska, A., de Jager, O. C., Kendziorra, E., Kerschhaggl, M., Khélifi, (2007c). H.E.S.S. Observations of the Supernova Remnant RX J0852.0-4622: Shell-Type Morphology and Spectrum of a Widely Extended Very High Energy Gamma-Ray Source. *ApJ*, 661:236–249.

Aharonian, F., Akhperjanian, A. G., Bazer-Bachi, A. R., Beilicke, M., Benbow, W., Berge, D., Bernlöhr, K., Boisson, C., Bolz, O., Borrel, V., Braun, I., Breitling, F., Brown, A. M., Chadwick, P. M., Chounet, L.-M., Cornils, R., Costamante, L., Degrange, B., Dickinson, H. J., Djannati-Ataï, A., Drury, L. O., Dubus, G., Em-

manoulopoulos, D., Espigat, P., Feinstein, F., Fontaine, G., Fuchs, Y., Funk, S., Gallant, Y. A., Giebels, B., Gillessen, S., Glicenstein, J. F., Goret, P., Hadjichristidis, C., Hauser, M., Heinzelmann, G., Henri, G., Hermann, G., Hinton, J. A., Hofmann, W., Holleran, M., Horns, D., and Jacholkowska, A. et al. (2006b). The H.E.S.S. Survey of the Inner Galaxy in Very High Energy Gamma Rays. *ApJ*, 636:777–797.

Aharonian, F., Akhperjanian, A. G., Bazer-Bachi, A. R., Beilicke, M., Benbow, W., Berge, D., Bernlöhr, K., Boisson, C., Bolz, O., Borrel, V., Braun, I., Brown, A. M., Bühler, R., Büsching, I., Carrigan, S., Chadwick, P. M., Chounet, L.-M., Cornils, R., Costamante, L., Degrange, B., Dickinson, H. J., Djannati-Ataï, A., O'C. Drury, L., Dubus, G., and HESS Collaboration (2006c). Energy dependent γ-ray morphology in the pulsar wind nebula HESS J1825-137. *A&A*, 460:365–374.

Aharonian, F., Akhperjanian, A. G., Bazer-Bachi, A. R., Beilicke, M., Benbow, W., Berge, D., Bernlöhr, K., Boisson, C., Bolz, O., Borrel, V., Braun, I., Breitling, F., Brown, A. M., Bühler, R., Büsching, I., Carrigan, S., Chadwick, P. M., Chounet, L.-M., Cornils, R., Costamante, L., Degrange, B., Dickinson, H. J., Djannati-Ataï, A., O'C. Drury, L., Dubus, G., Egberts, K., Emmanoulopoulos, D., Espigat, P., Feinstein, F., Ferrero, E., Fiasson, A., Fontaine, G., Funk, S., Funk, S., Gallant, Y. A., Giebels, B., Glicenstein, J. F., and Goret, P. et al. (2006d). Observations of the Crab nebula with HESS. *A&A*, 457:899–915.

Aharonian, F., Buckley, J., Kifune, T., and Sinnis, G. (2008d). High energy astrophysics with ground-based gamma ray detectors. *Reports on Progress in Physics*, 71(9):096901–+.

Aharonian, F. A. (1991). Very high and ultra-high-energy gamma-rays from giant molecular clouds. *ApSS*, 180:305–320.

Aharonian, F. A., Akhperjanian, A. G., Bazer-Bachi, A. R., Beilicke, M., Benbow, W., Berge, D., Bernlöhr, K., Boisson, C., Bolz, O., Borrel, V., Braun, I., Breitling, F., Brown, A. M., Chadwick, P. M., Chounet, L.-M., Cornils, R., Costamante, L., Degrange, B., Dickinson, H. J., Djannati-Ataï, A., O'C. Drury, L., Dubus, G., Emmanoulopoulos, D., Espigat, P., Feinstein, F., Fontaine, G., Fuchs, Y., and Funk, S. et al. (2005c). A possible association of the new VHE γ-ray source HESS J1825-137 with the pulsar wind nebula G 18.0 0.7. *A&A*, 442:L25–L29.

Aharonian, F. A. and Atoyan, A. M. (1996). On the emissivity of $\pi\hat{}0\hat{}$-decay gamma radiation in the vicinity of accelerators of galactic cosmic rays. *A&A*, 309:917–928.

Aharonian, F. A., Atoyan, A. M., and Kifune, T. (1997). Inverse Compton gamma radiation of faint synchrotron X-ray nebulae around pulsars. *MNRAS*, 291:162–176.

Aharonian, F. A., Drury, L. O., and Voelk, H. J. (1994). GeV/TeV gamma-ray emission from dense molecular clouds overtaken by supernova shells. *A&A*, 285:645–647.

Alpar, M. A., Cheng, A. F., Ruderman, M. A., and Shaham, J. (1982). A new class of radio pulsars. *Nature*, 300:728–730.

Anderhub, H., Antonelli, L. A., Antoranz, P., Backes, M., Baixeras, C., Balestra, S., Barrio, J. A., Bastieri, D., Becerra González, J., Becker, J. K., Bednarek, W., Berger, K., Bernardini, E., Biland, A., Bock, R. K., Bonnoli, G., Bordas, P., Borla Tridon, D., Bosch-Ramon, V., Bose, D., Braun, I., Bretz, T., Britvitch, I., Camara, M., Carmona, E., Commichau, S., Contreras, J. L., Cortina, J., Costado, M. T., Covino, S., Curtef, V., Dazzi, F., DeAngelis, A., DeCea del Pozo, E., de los Reyes, R., and DeLotto, B. et al. (2009). Search for VHE γ-ray Emission from the Globular Cluster M13 with the Magic Telescope. *ApJ*, 702:266–269.

Ardavan, H. (1973). Dynamical Evolution of an Expanding Gas Cloud. *ApJ*, 184:435–452.

Arnaud, K. A. (1996). XSPEC: The First Ten Years. In *ASP Conf. Ser. 101: Astronomical Data Analysis Software and Systems V*, page 17.

Arnaud, M., Neumann, D. M., Aghanim, N., Gastaud, R., Majerowicz, S., and Hughes, J. P. (2001). Measuring cluster temperature profiles with XMM/EPIC. *A&A*, 365:L80–L86.

Atoyan, A., Buckley, J., and Krawczynski, H. (2006). A Gamma-Ray Burst Remnant in Our Galaxy: HESS J1303-631. *ApJL*, 642:L153–L156.

Baade, W. and Zwicky, F. (1934). Cosmic Rays from Super-novae. *Proceedings of the National Academy of Science*, 20:259–263.

Bałucińska-Church, M., Humphrey, P. J., Church, M. J., and Parmar, A. N. (2000). A study of the dipping low mass X-ray binary X 1624-490 from the broadband BeppoSAX observation. *A&A*, 360:583–591.

Bamba, A., Yamazaki, R., Ueno, M., and Koyama, K. (2003). Small-Scale Structure of the SN 1006 Shock with Chandra Observations. *ApJ*, 589:827–837.

Bednarek, W. and Sitarek, J. (2007). High-energy γ-rays from globular clusters. *MNRAS*, 377:920–930.

Bell, A. R. (2004). Turbulent amplification of magnetic field and diffusive shock acceleration of cosmic rays. *MNRAS*, 353:550–558.

Berezhko, E. G., Ksenofontov, L. T., and Völk, H. J. (2002). Emission of SN 1006 produced by accelerated cosmic rays. *A&A*, 395:943–953.

Berezhko, E. G. and Völk, H. J. (2006). Theory of cosmic ray production in the supernova remnant RX J1713.7-3946. *A&A*, 451:981–990.

Berezinskii, V. S., Bulanov, S. V., Dogiel, V. A., and Ptuskin, V. S. (1990). *Astrophysics of cosmic rays*.

Berge, D., Funk, S., and Hinton, J. (2007). Background modelling in very-high-energy γ-ray astronomy. *A&A*, 466:1219–1229.

Bernlohr, K. (2000). Impact of atmospheric parameters on the atmospheric Cherenkov technique*. *Astroparticle Physics*, 12:255–268.

Blackburn, J. K., Greene, E. A., and Pence, W. (1993). FTOOLS: A FITS Data Processing and Analysis Software Package. In *American Astronomical Society Meeting Abstracts #182*, volume 25 of *Bulletin of the American Astronomical Society*, pages 816–+.

Blumenthal, G. R. and Gould, R. J. (1970). Bremsstrahlung, synchrotron radiation, and compton scattering of high-energy electrons traversing dilute gases. *Rev. Mod. Phys.*, 42(2):237–270.

Bock, D., Large, M. I., and Sadler, E. M. (1999). SUMSS: A Wide-Field Radio Imaging Survey of the Southern Sky. I. Science Goals, Survey Design, and Instrumentation. *AJ*, 117:1578–1593.

Brand, J. and Blitz, L. (1993). The Velocity Field of the Outer Galaxy. *A&A*, 275:67–+.

Carey, S. J. (2008). MIPSGAL: A View of the Cold and Dusty in the Inner Galactic Plane with the Spitzer Space Telescope. In *American Astronomical Society Meeting Abstracts #212*, volume 40 of *Bulletin of the American Astronomical Society*, pages 255–+.

Carrigan, S., Hinton, J. A., Hofmann, W., and et al. (2008). Establishing a connection between high-power pulsars and very-high-energy gamma-ray sources. In *International Cosmic Ray Conference*, volume 2 of *International Cosmic Ray Conference*, pages 659–662.

Carter, J. A. and Read, A. M. (2007). The XMM-Newton EPIC background and the production of background blank sky event files. *A&A*, 464:1155–1166.

Caselli, P., Vastel, C., Ceccarelli, C., van der Tak, F. F. S., Crapsi, A., and Bacmann, A. (2008). Survey of ortho-H_2D^+ ($1_{1,0}$-$1_{1,1}$) in dense cloud cores. *A&A*, 492:703–718.

Casse, M. and Paul, J. A. (1980). Local gamma rays and cosmic-ray acceleration by supersonic stellar winds. *ApJ*, 237:236–243.

Chaves, R. C. G. (2009). Extending the H.E.S.S. Galactic Plane Survey. *ArXiv e-prints*.

Churchwell, E., Babler, B. L., Meade, M. R., Whitney, B. A., Benjamin, R., Indebetouw, R., Cyganowski, C., Robitaille, T. P., Povich, M., Watson, C., and Bracker, S. (2009). The Spitzer/GLIMPSE Surveys: A New View of the Milky Way. *PASP*, 121:213–230.

Clark, G. W. (1975). X-ray binaries in globular clusters. *ApJL*, 199:L143–L145.

Cole, S., Norberg, P., Baugh, C. M., Frenk, C. S., Bland-Hawthorn, J., Bridges, T., Cannon, R., Colless, M., Collins, C., Couch, W., Cross, N., Dalton, G., De Propris, R., Driver, S. P., Efstathiou, G., Ellis, R. S., Glazebrook, K., Jackson, C., Lahav, O., Lewis, I., Lumsden, S., Maddox, S., Madgwick, D., Peacock, J. A., Peterson, B. A., Sutherland, W., and Taylor, K. (2001). The 2dF galaxy redshift survey: near-infrared galaxy luminosity functions. *MNRAS*, 326:255–273.

Dame, T. M., Hartmann, D., and Thaddeus, P. (2001). The Milky Way in Molecular Clouds: A New Complete CO Survey. *ApJ*, 547:792–813.

De Luca, A. and Molendi, S. (2004). The 2-8 keV cosmic X-ray background spectrum as observed with XMM-Newton. *A&A*, 419:837–848.

de Naurois, M. and Rolland, L. (2009). A high performance likelihood reconstruction of γ-rays for imaging atmospheric Cherenkov telescopes. *Astroparticle Physics*, 32:231–252.

Dermer, C. D. (1986). Secondary production of neutral pi-mesons and the diffuse galactic gamma radiation. *A&A*, 157:223–229.

Dickey, J. M. and Lockman, F. J. (1990). H I in the Galaxy. *ARAA*, 28:215–261.

Dickman, R. L. (1978). The ratio of carbon monoxide to molecular hydrogen in interstellar dark clouds. *ApJS*, 37:407–427.

Domainko, W. and Ruffert, M. (2005). Long-term remnant evolution of compact binary mergers. *A&A*, 444:L33–L36.

Domainko, W. and Ruffert, M. (2008). Remnants of compact binary mergers. *Advances in Space Research*, 41:518–522.

Domingo-Santamaría, E. and Torres, D. F. (2006). Hadronic processes within collective stellar winds. *A&A*, 448:613–622.

Drury, L. O. (1983). An introduction to the theory of diffusive shock acceleration of energetic particles in tenuous plasmas. *Reports on Progress in Physics*, 46:973–1027.

D'Urso, D. (2007). The Physics of Ultra High Energy Cosmic Rays (Review). In N. R. Napolitano & M. Paolillo, editor, *1st Workshop of Astronomy and Astrophysics for Students*, pages 11–+.

Ebisawa, K., Tsujimoto, M., Paizis, A., Hamaguchi, K., Bamba, A., Cutri, R., Kaneda, H., Maeda, Y., Sato, G., Senda, A., Ueno, M., Yamauchi, S., Beckmann, V., Courvoisier, T., Dubath, P., and Nishihara, E. (2005). Chandra Deep X-Ray Observation of a Typical Galactic Plane Region and Near-Infrared Identification. *ApJ*, 635:214–242.

Eger, P., Domainko, W., and Clapson, A. (2010). Chandra detection of diffuse X-ray emission from the globular cluster Terzan 5. *A&A*, 513:A66+.

Eger, P., Rowell, G., Kawamura, A., Fukui, Y., Rolland, L., and Stegmann, C. (2011). A multi-wavelength study of the unidentified TeV gamma-ray source HESS J1626-490. *A&A*, 526:A82+.

Feldman, G. J. and Cousins, R. D. (1998). Unified approach to the classical statistical analysis of small signals. *PhysicalReviewD*, 57:3873–3889.

Fermi, E. (1949). On the Origin of the Cosmic Radiation. *Physical Review*, 75:1169–1174.

Fruscione, A., McDowell, J. C., Allen, G. E., Brickhouse, N. S., Burke, D. J., Davis, J. E., Durham, N., Elvis, M., Galle, E. C., Harris, D. E., Huenemoerder, D. P., Houck, J. C., Ishibashi, B., Karovska, M., Nicastro, F., Noble, M. S., Nowak, M. A., Primini, F. A., Siemiginowska, A., Smith, R. K., and Wise, M. (2006). CIAO: Chandra's data analysis system. In *Society of Photo-Optical Instrumentation Engineers (SPIE) Conference Series*, volume 6270 of *Society of Photo-Optical Instrumentation Engineers (SPIE) Conference Series*.

Funk, S., Hermann, G., Hinton, J., Berge, D., Bernlöhr, K., Hofmann, W., Nayman, P., Toussenel, F., and Vincent, P. (2004). The trigger system of the H.E.S.S. telescope array. *Astroparticle Physics*, 22:285–296.

Gabici, S. and Aharonian, F. A. (2007). Gamma ray signatures of ultra high energy cosmic ray accelerators: electromagnetic cascade versus synchrotron radiation of secondary electrons. *ApSS*, 309:465–469.

Gabici, S., Aharonian, F. A., and Casanova, S. (2009). Broad-band non-thermal emission from molecular clouds illuminated by cosmic rays from nearby supernova remnants. *MNRAS*, 396:1629–1639.

Gabici, S., Casanova, S., Aharonian, F. A., and Rowell, G. (2010). Constraints on the cosmic ray diffusion coefficient in the W28 region from gamma-ray observations. In S. Boissier, M. Heydari-Malayeri, R. Samadi, & D. Valls-Gabaud , editor, *SF2A-2010: Proceedings of the Annual meeting of the French Society of Astronomy and Astrophysics. Eds.: S. Boissier, M. Heydari-Malayeri, R. Samadi and D. Valls-Gabaud, p.313*, pages 313–+.

Gabriel, C., Guainazzi, M., Metcalfe, L., Ibarra, A., Ojero, E., and Saxton, R. (2006). The Scientific Analysis System (SAS) and its Evolution Through the Different Stages of the XMM-Newton Project. *IAU Special Session*, 6.

Gaensler, B. M. and Slane, P. O. (2006). The Evolution and Structure of Pulsar Wind Nebulae. *ARAA*, 44:17–47.

Gaetz, T. J., Jerius, D., Edgar, R. J., Van Speybroeck, L. P., Schwartz, D. A., Markevitch, M. L., Taylor, S. C., and Schulz, N. S. (2000). Orbital verification of the CXO high-resolution mirror assembly alignment and vignetting. In J. E. Truemper & B. Aschenbach, editor, *Society of Photo-Optical Instrumentation Engineers*

(SPIE) Conference Series, volume 4012 of *Society of Photo-Optical Instrumentation Engineers (SPIE) Conference Series*, pages 41–52.

Gaisser, T. K. (1990). *Cosmic rays and particle physics*.

Gallant, Y. A. for the H. E. S. S. Collaboration (2010). Recent H.E.S.S. Results. In *AAS/High Energy Astrophysics Division #11*, volume 42 of *Bulletin of the American Astronomical Society*, pages 738–+.

Garmire, G. P., Bautz, M. W., Ford, P. G., Nousek, J. A., and Ricker, Jr., G. R. (2003). Advanced CCD imaging spectrometer (ACIS) instrument on the Chandra X-ray Observatory. In J. E. Truemper & H. D. Tananbaum, editor, *Society of Photo-Optical Instrumentation Engineers (SPIE) Conference Series*, volume 4851 of *Society of Photo-Optical Instrumentation Engineers (SPIE) Conference Series*, pages 28–44.

Georgy, C., Meynet, G., Walder, R., Folini, D., and Maeder, A. (2009). The different progenitors of type Ib, Ic SNe, and of GRB. *A&A*, 502:611–622.

Gonthier, P. L., Van Guilder, R., and Harding, A. K. (2004). Role of Beam Geometry in Population Statistics and Pulse Profiles of Radio and Gamma-Ray Pulsars. *ApJ*, 604:775–790.

Green, A. J., Cram, L. E., Large, M. I., and Ye, T. (1999). The Molonglo Galactic Plane Survey. I. Overview and Images. *ApJS*, 122:207–219.

Green, D. A. (2005). Some statistics of Galactic SNRs. *Memorie della Societa Astronomica Italiana*, 76:534–+.

Green, D. A. (2009). A revised Galactic supernova remnant catalogue. *Bulletin of the Astronomical Society of India*, 37:45–+.

Greisen, K. (1966). End to the cosmic-ray spectrum? *Phys. Rev. Lett.*, 16(17):748–750.

Grindlay, J., Portegies Zwart, S., and McMillan, S. (2006). Short gamma-ray bursts from binary neutron star mergers in globular clusters. *Nature Physics*, 2:116–119.

Güdel, M., Audard, M., Magee, H., Franciosini, E., Grosso, N., Cordova, F. A., Pallavicini, R., and Mewe, R. (2001). The XMM-Newton view of stellar coronae: Coronal structure in the Castor X-ray triplet. *A&A*, 365:L344–L352.

Guseinov, O. H., Ankay, A., and Tagieva, S. O. (2004). Observational Data on Galactic Supernova Remnants: III. The Supernova Remnants Within l = 270ˆo - 360ˆo. *Serbian Astronomical Journal*, 169:65–+.

Hands, A. D. P., Warwick, R. S., Watson, M. G., and Helfand, D. J. (2004). X-ray source populations in the Galactic plane. *MNRAS*, 351:31–56.

Harris, W. E. (1996). A Catalog of Parameters for Globular Clusters in the Milky Way. *AJ*, 112:1487–+.

Hartwick, F. D. A., Grindlay, J. E., and Cowley, A. P. (1982). Evidence for extended X-ray emission from globular clusters. *ApJL*, 254:L11–L13.

Heinke, C. O., Wijnands, R., Cohn, H. N., Lugger, P. M., Grindlay, J. E., Pooley, D., and Lewin, W. H. G. (2006). Faint X-Ray Sources in the Globular Cluster Terzan 5. *ApJ*, 651:1098–1111.

Hillas, A. M., Akerlof, C. W., Biller, S. D., Buckley, J. H., Carter-Lewis, D. A., Catanese, M., Cawley, M. F., Fegan, D. J., Finley, J. P., Gaidos, J. A., Krennrich, F., Lamb, R. C., Lang, M. J., Mohanty, G., Punch, M., Reynolds, P. T., Rodgers, A. J., Rose, H. J., Rovero, A. C., Schubnell, M. S., Sembroski, G. H., Vacanti, G., Weekes, T. C., West, M., and Zweerink, J. (1998). The Spectrum of TeV Gamma Rays from the Crab Nebula. *ApJ*, 503:744–+.

Hinton, J. (2009). Ground-based gamma-ray astronomy with Cherenkov telescopes. *New Journal of Physics*, 11(5):055005–+.

Hinton, J. A. (2004). The status of the HESS project. *New Astronomy Reviews*, 48:331–337.

Hinton, J. A. and Hofmann, W. (2009). Teraelectronvolt Astronomy. *ARAA*, 47:523–565.

Holler, M., Schoeck, F. M., Eger, P., and Stegmann, C. (2011). Spatially resolved XMM-Newton analysis and a model of the nonthermal emission of G09+0.1. *in preparation.*

Hoppe, S., Lemoine-Goumard, M., and Vink, J. (2008). Discovery of gamma-ray emission from the shell-type supernova remnant RCW 86 with H.E.S.S. In F. A. Aharonian, W. Hofmann, & F. Rieger, editor, *American Institute of Physics Conference Series*, volume 1085 of *American Institute of Physics Conference Series*, pages 332–335.

Hut, P., McMillan, S., Goodman, J., Mateo, M., Phinney, E. S., Pryor, C., Richer, H. B., Verbunt, F., and Weinberg, M. (1992). Binaries in globular clusters. *PASP*, 104:981–1034.

Ivanova, N., Fregeau, J. M., and Rasio, F. A. (2005). Binary Evolution and Neutron Stars in Globular Clusters. In F. A. Rasio & I. H. Stairs, editor, *Binary Radio Pulsars*, volume 328 of *Astronomical Society of the Pacific Conference Series*, pages 231–+.

Jansen, F., Lumb, D., Altieri, B., Clavel, J., Ehle, M., Erd, C., Gabriel, C., Guainazzi, M., Gondoin, P., Much, R., Munoz, R., Santos, M., Schartel, N., Texier, D., and Vacanti, G. (2001). Xmm-newton observatory. i. the spacecraft and operations. *A&A*, 365:L1–L6.

Kahn, F. D. and Woltjer, L. (1967). Supernovae and interstellar gas dynamics. In H. van Woerden, editor, *Radio Astronomy and the Galactic System*, volume 31 of *IAU Symposium*, pages 117–+.

Kaneda, H., Makishima, K., Yamauchi, S., Koyama, K., Matsuzaki, K., and Yamasaki, N. Y. (1997). Complex Spectra of the Galactic Ridge X-Rays Observed with ASCA. *ApJ*, 491:638–+.

Katz, B. and Waxman, E. (2008). In which shell-type SNRs should we look for gamma-rays and neutrinos from P-P collisions? *JCAp*, 1:18–+.

Koyama, K., Petre, R., Gotthelf, E. V., Hwang, U., Matsuura, M., Ozaki, M., and Holt, S. S. (1995). Evidence for shock acceleration of high-energy electrons in the supernova remnant SN1006. *Nature*, 378:255–258.

Kraushaar, W. L., Clark, G. W., Garmire, G. P., Borken, R., Higbie, P., Leong, V., and Thorsos, T. (1972). High-Energy Cosmic Gamma-Ray Observations from the OSO-3 Satellite. *ApJ*, 177:341–+.

Krockenberger, M. and Grindlay, J. E. (1995). Discovery of Diffuse X-Ray Emission in 47 Tucanae. *ApJ*, 451:200–+.

Krumholz, M. R. (2011). Star Formation in Molecular Clouds. *ArXiv e-prints*.

Kuchar, T. A. and Bania, T. M. (1990). H I emission-absorption experiments toward Galactic H II regions. *ApJ*, 352:192–206.

Kulsrud, R., M. (2005). *Plasma Physics for Astrophysics*. Princeton Series in Astrophysics, Princeton University Press, 2005.

Leahy, D. A. and Tian, W. W. (2008). The Distances of SNR W41 and Overlapping H II Regions. *AJ*, 135:167–172.

LeBohec, S. for the VERITAS Collaboration (2009). VERITAS Observation of the E>200GeV Gamma-ray Sky. In *American Astronomical Society Meeting Abstracts #214*, volume 214 of *American Astronomical Society Meeting Abstracts*, pages 302.05–+.

Li, T. and Ma, Y. (1983). Analysis methods for results in gamma-ray astronomy. *ApJ*, 272:317–324.

Lockman, F. J. (1984). The H I halo in the inner galaxy. *ApJ*, 283:90–97.

López Moya, M. (2010). Scientific Highlights and Status of the MAGIC Telescope. In C. Cecchi, S. Ciprini, P. Lubrano, & G. Tosti, editor, *American Institute of Physics Conference Series*, volume 1223 of *American Institute of Physics Conference Series*, pages 99–108.

Makarov, V. V. (2003). The 100 Brightest X-Ray Stars within 50 Parsecs of the Sun. *AJ*, 126:1996–2008.

Manchester, R. N., Hobbs, G. B., Teoh, A., and Hobbs, M. (2005). The Australia Telescope National Facility Pulsar Catalogue. *AJ*, 129:1993–2006.

Mariş, I. C., Blümer, J., Roth, M., Schmidt, T., Schüssler, F., Unger, M., and Pierre AUGER Collaboration (2007). The UHECR energy spectrum measured at the Pierre Auger Observatory. *Astronomische Nachrichten*, 328:617–+.

Markevitch, M., Bautz, M. W., Biller, B., Butt, Y., Edgar, R., Gaetz, T., Garmire, G., Grant, C. E., Green, P., Juda, M., Plucinsky, P. P., Schwartz, D., Smith, R., Vikhlinin, A., Virani, S., Wargelin, B. J., and Wolk, S. (2003). Chandra Spectra of the Soft X-Ray Diffuse Background. *ApJ*, 583:70–84.

Masai, K. (1984). X-ray emission spectra from ionizing plasmas. *ApSS*, 98:367–395.

Matheson, H. and Safi-Harb, S. (2005). The plerionic supernova remnant G21.5-0.9: In and out. *Advances in Space Research*, 35:1099–1105.

Matsunaga, K., Mizuno, N., Moriguchi, Y., Onishi, T., Mizuno, A., and Fukui, Y. (2001). Detection of Eight Molecular Supershells in the Southern Milky Way with NANTEN. *PASJ*, 53:1003–1016.

McClure-Griffiths, N. M., Dickey, J. M., Gaensler, B. M., Green, A. J., Haverkorn, M., and Strasser, S. (2005). The Southern Galactic Plane Survey: H I Observations and Analysis. *ApJS*, 158:178–187.

McCutcheon, M. (2009). VERITAS Observations of Globular Clusters. *ArXiv e-prints*.

Metzger, A. E., Parker, R. H., Gilman, D., Peterson, L. E., and Trombka, J. I. (1974). Observation of a cosmic gamma-ray burst on Apollo 16. I - Temporal variability and energy spectrum. *ApJL*, 194:L19–L25.

Michelson, P. F., Atwood, W. B., and Ritz, S. (2010). Fermi Gamma-ray Space Telescope: high-energy results from the first year. *Reports on Progress in Physics*, 73(7):074901–+.

Minkowski, R. (1957). Optical investigations of radio sources (Introductory Lecture). In H. C. van de Hulst, editor, *Radio astronomy*, volume 4 of *IAU Symposium*, pages 107–+.

Mizuno, A. and Fukui, Y. (2004). Physical properties of molecular clouds as revealed by NANTEN CO survey: from the galactic center to the galactic warp. In D. Clemens, R. Shah, & T. Brainerd, editor, *Milky Way Surveys: The Structure and Evolution of our Galaxy*, volume 317 of *Astronomical Society of the Pacific Conference Series*, pages 59–+.

Morrison, P. (1958). On gamma-ray astronomy. *Il Nuovo Cimento (1955-1965)*, 7:858–865. 10.1007/BF02745590.

Nakar, E. (2007). Short-hard gamma-ray bursts. *PhysRep*, 442:166–236.

Okada, Y., Kokubun, M., Yuasa, T., and Makishima, K. (2007). Chandra Detections of Diffuse X-Ray Emission from Globular Clusters. *PASJ*, 59:727–.

Onishi, T., Mizuno, N., Mizuno, A., Fukui, Y., and Nanten Team (2005). New View of Molecular Gas Distribution of the Southern Sky: CO Surveys with NANTEN. In *Protostars and Planets V*, pages 8301–+.

Ortolani, S., Barbuy, B., Bica, E., Zoccali, M., and Renzini, A. (2007). Distances of the bulge globular clusters Terzan 5, Liller 1, UKS 1, and Terzan 4 based on HST NICMOS photometry. *A&A*, 470:1043–1049.

Pittard, J. M. and Dougherty, S. M. (2006). Radio, X-ray, and γ-ray emission models of the colliding-wind binary WR140. *MNRAS*, 372:801–826.

Pollock, A. M. T. (1987). New evidence at X-ray and COS-B gamma-ray frequencies for non-thermal phenomena in Wolf-Rayet stars. *A&A*, 171:135–139.

Pooley, D. and Hut, P. (2006). Dynamical Formation of Close Binaries in Globular Clusters: Cataclysmic Variables. *ApJL*, 646:L143–L146.

Ptuskin, V. S., Rogovaya, S. I., Zirakashvili, V. N., Chuvilgin, L. G., Khristiansen, G. B., Klepach, E. G., and Kulikov, G. V. (1993). Diffusion and drift of very high energy cosmic rays in galactic magnetic fields. *A&A*, 268:726–735.

Ptuskin, V. S. and Zirakashvili, V. N. (2005). On the spectrum of high-energy cosmic rays produced by supernova remnants in the presence of strong cosmic-ray streaming instability and wave dissipation. *A&A*, 429:755–765.

Ransom, S. M. (2008). Pulsars in Globular Clusters. In E. Vesperini, M. Giersz, & A. Sills, editor, *IAU Symposium*, volume 246 of *IAU Symposium*, pages 291–300.

Reach, W. T., Rho, J., Tappe, A., Pannuti, T. G., Brogan, C. L., Churchwell, E. B., Meade, M. R., Babler, B., Indebetouw, R., and Whitney, B. A. (2006). A Spitzer Space Telescope Infrared Survey of Supernova Remnants in the Inner Galaxy. *AJ*, 131:1479–1500.

Reich, P., Testori, J. C., and Reich, W. (2001). A radio continuum survey of the southern sky at 1420 MHz. The atlas of contour maps. *A&A*, 376:861–877.

Reimer, A., Pohl, M., and Reimer, O. (2006). Nonthermal High-Energy Emission from Colliding Winds of Massive Stars. *ApJ*, 644:1118–1144.

Reimer, A. and Reimer, O. (2009). Massive stars in colliding wind systems: the high-energy gamma-ray perspective. In D. Bastieri & R. Rando, editor, *American Institute of Physics Conference Series*, volume 1112 of *American Institute of Physics Conference Series*, pages 43–53.

Reiprich, T. H. and Böhringer, H. (2002). The Mass Function of an X-Ray Flux-limited Sample of Galaxy Clusters. *ApJ*, 567:716–740.

Reynolds, S. P. (2008). Supernova Remnants at High Energy. *ARAA*, 46:89–126.

Reynolds, S. P. (2010). Particle acceleration in supernova-remnant shocks. *ApSS*, pages 374–+.

Romero, G. E., Benaglia, P., and Torres, D. F. (2000). On the nature of the galactic population of 3EG sources. In M. L. McConnell & J. M. Ryan, editor, *American Institute of Physics Conference Series*, volume 510 of *American Institute of Physics Conference Series*, pages 509–512.

Russeil, D. (2003). Star-forming complexes and the spiral structure of our Galaxy. *A&A*, 397:133–146.

Sanders, D. B., Clemens, D. P., Scoville, N. Z., and Solomon, P. M. (1986). Massachusetts-Stony Brook Galactic plane CO survey. I - (b,V) maps of the first Galactic quadrant. *ApJS*, 60:1–296.

Schöck, F. M., Büsching, I., de Jager, O. C., Eger, P., and Vorster, M. J. (2010). Spatially resolved XMM-Newton analysis and a model of the nonthermal emission of MSH 15-52. *A&A*, 515:A109+.

Sedov, L. I. (1959). *Similarity and Dimensional Methods in Mechanics*.

Shara, M. M. and Hurley, J. R. (2002). Star Clusters as Type Ia Supernova Factories. *ApJ*, 571:830–842.

Shetty, R., Glover, S. C., Dullemond, C. P., and Klessen, R. S. (2011). Modelling CO emission - I. CO as a column density tracer and the X factor in molecular clouds. *MNRAS*, pages 11–+.

Skrutskie, M. F., Cutri, R. M., Stiening, R., Weinberg, M. D., Schneider, S., Carpenter, J. M., Beichman, C., Capps, R., Chester, T., Elias, J., Huchra, J., Liebert, J., Lonsdale, C., Monet, D. G., Price, S., Seitzer, P., Jarrett, T., Kirkpatrick, J. D., Gizis, J. E., Howard, E., Evans, T., Fowler, J., Fullmer, L., Hurt, R., Light, R., Kopan, E. L., Marsh, K. A., McCallon, H. L., Tam, R., Van Dyk, S., and Wheelock, S. (2006). The Two Micron All Sky Survey (2MASS). *AJ*, 131:1163–1183.

Slane, P. O. (2010). The Structure and Evolution of Pulsar Wind Nebulae. In *Bulletin of the American Astronomical Society*, volume 42 of *Bulletin of the American Astronomical Society*, pages 605–+.

Spitzer, Jr., L. (1960). Particle Diffusion across a Magnetic Field. *Physics of Fluids*, 3:659–661.

Strong, A. W., Moskalenko, I. V., Reimer, O., Digel, S., and Diehl, R. (2004). The distribution of cosmic-ray sources in the Galaxy, γ-rays and the gradient in the CO-to-H_2 relation. *A&A*, 422:L47–L50.

Strüder, L., Briel, U., Dennerl, K., Hartmann, R., Kendziorra, E., Meidinger, N., Pfeffermann, E., Reppin, C., Aschenbach, B., Bornemann, W., Bräuninger, H., Burkert, W., Elender, M., Freyberg, M., Haberl, F., Hartner, G., Heuschmann, F., Hippmann, H., Kastelic, E., Kemmer, S., Kettenring, G., Kink, W., Krause, N., Müller, S., Oppitz, A., Pietsch, W., Popp, M., Predehl, P., Read, A., Stephan, K. H., Stötter, D., Trümper, J., Holl, P., Kemmer, J., Soltau, H., Stötter, R., Weber, U., Weichert, U., von Zanthier, C., Carathanassis, D., Lutz, G., Richter, R. H., Solc, P., Böttcher, H., Kuster, M., Staubert, R., Abbey, A., Holland, A., Turner, M., Balasini, M., Bignami, G. F., La Palombara, N., Villa, G., Buttler, W., Gianini, F., Lainé, R., Lumb, D., and Dhez, P. (2001). The european photon imaging camera on xmm-newton: The pn-ccd camera. *A&A*, 365:L18–L26.

Tian, W. W., Leahy, D. A., and Wang, Q. D. (2007). Radio and X-ray images of the SNR G18.8+0.3 interacting with molecular clouds. *A&A*, 474:541–547.

Trager, S. C., King, I. R., and Djorgovski, S. (1995). Catalogue of Galactic globular-cluster surface-brightness profiles. *AJ*, 109:218–241.

Turner, M. J. L., Abbey, A., Arnaud, M., Balasini, M., Barbera, M., Belsole, E., Bennie, P. J., Bernard, J. P., Bignami, G. F., Boer, M., Briel, U., Butler, I., Cara, C., Chabaud, C., Cole, R., Collura, A., Conte, M., Cros, A., Denby, M., Dhez, P., Di Coco, G., Dowson, J., Ferrando, P., Ghizzardi, S., Gianotti, F., Goodall, C. V., Gretton, L., Griffiths, R. G., Hainaut, O., Hochedez, J. F., Holland, A. D., Jourdain, E., Kendziorra, E., Lagostina, A., Laine, R., La Palombara, N., Lortholary, M., Lumb, D., Marty, P., Molendi, S., Pigot, C., Poindron, E., Pounds, K. A., Reeves, J. N., Reppin, C., Rothenflug, R., Salvetat, P., Sauvageot, J. L., Schmitt, D., Sembay, S., Short, A. D. T., Spragg, J., Stephen, J., Strüder, L., Tiengo, A., Trifoglio, M., Trümper, J., Vercellone, S., Vigroux, L., Villa, G., Ward, M. J., Whitehead, S., and Zonca, E. (2001). The european photon imaging camera on xmm-newton: The mos cameras : The mos cameras. *A&A*, 365:L27–L35.

Uchiyama, Y., Takahashi, T., and Aharonian, F. A. (2002). Flat Spectrum X-Ray Emission from the Direction of a Molecular Cloud Associated with SNR RX J1713.7-3946. *PASJ*, 54:L73–L77.

Venter, C. and de Jager, O. C. (2008). Estimates for Very High Energy Gamma Rays from Globular Cluster Pulsars. In F. A. Aharonian, W. Hofmann, & F. Rieger, editor, *American Institute of Physics Conference Series*, volume 1085 of *American Institute of Physics Conference Series*, pages 277–280.

Venter, C., De Jager, O. C., and Clapson, A. (2009). Predictions of Gamma-Ray Emission from Globular Cluster Millisecond Pulsars Above 100 MeV. *ApJL*, 696:L52–L55.

Vincent, P. (2005). H.E.S.S. Phase II. In *International Cosmic Ray Conference*, volume 5 of *International Cosmic Ray Conference*, pages 163–+.

Vink, J. (2004). A Review of X-ray Observations of Supernova Remnants. *Nuclear Physics B Proceedings Supplements*, 132:21–30.

Voelk, H. J. and Forman, M. (1982). Cosmic rays and gamma-rays from OB stars. *ApJ*, 253:188–198.

Voges, W., Aschenbach, B., Boller, T., Bräuninger, H., Briel, U., Burkert, W., Dennerl, K., Englhauser, J., Gruber, R., Haberl, F., Hartner, G., Hasinger, G., Kürster, M., Pfeffermann, E., Pietsch, W., Predehl, P., Rosso, C., Schmitt, J. H. M. M., Trümper, J., and Zimmermann, H. U. (1999). The rosat all-sky survey bright source catalogue. *A&A*, 349:389–405.

Weekes, T. C., Cawley, M. F., Fegan, D. J., Gibbs, K. G., Hillas, A. M., Kowk, P. W., Lamb, R. C., Lewis, D. A., Macomb, D., Porter, N. A., Reynolds, P. T., and Vacanti, G. (1989). Observation of TeV gamma rays from the Crab nebula using the atmospheric Cerenkov imaging technique. *ApJ*, 342:379–395.

Weisskopf, M. C., Brinkman, B., Canizares, C., Garmire, G., Murray, S., and Van Speybroeck, L. P. (2002). An Overview of the Performance and Scientific Results from the Chandra X-Ray Observatory. *PASP*, 114:1–24.

White, R. L. (1985). Synchrotron emission from chaotic stellar winds. *ApJ*, 289:698–708.

Whiteoak, J. B. Z. and Green, A. J. (1996). The MOST supernova remnant catalogue (MSC). *A&AS*, 118:329–380.

Wijnands, R., Heinke, C. O., Pooley, D., Edmonds, P. D., Lewin, W. H. G., Grindlay, J. E., Jonker, P. G., and Miller, J. M. (2005). The Hard Quiescent Spectrum of the Neutron Star X-Ray Transient EXO 1745-248 in the Globular Cluster Terzan 5. *ApJ*, 618:883–890.

Woltjer, L. (1972). Supernova Remnants. *ARAA*, 10:129–+.

Xiang, J., Lee, J. C., and Nowak, M. A. (2007). Using the X-Ray Dust Scattering Halo of 4U 1624-490 to Determine Distance and Dust Distributions. *ApJ*, 660:1309–1318.

Yuasa, T., Nakazawa, K., and Makishima, K. (2009). The origin of an extended X-ray emission apparently associated with the globular cluster 47 Tucanae. *ArXiv e-prints*.

Zatsepin, G. T. and Kuz'min, V. A. (1966). Upper Limit of the Spectrum of Cosmic Rays. *Soviet Journal of Experimental and Theoretical Physics Letters*, 4:78–+.